Asymmetric Magnetohydrodynamic Waves of the Solar Atmosphere

Matthew Mark Allcock

Professor Robertus Erdélyi

The University Of Sheffield.

University of Sheffield

School of Mathematics and Statistics

A thesis submitted in partial fulfilment of the requirements for the degree of

Doctor of Philosophy

September 2020

To Fred Allcock, who would have hated to read this.

Acknowledgements

Thank you to my examiners, Prof. Misha Ruderman and Dr. Elena Khomenko, whose comments have improved this thesis. I am grateful for the financial support of the University Prize Scholarship from the University of Sheffield. Thank you to my academic supervisor, Prof. Robertus Erdélyi, for support throughout my undergraduate and postgraduate journey.

Thank you to everyone who has contributed to my office being a pleasant place to spend many hours a day for the last four years. Thank you and good luck to those who are still on their PhD journey: Anwar, Farhad, Fionnlagh, Noemi, and Vinh. Thank you to those who have already moved on: Alex, Chris, Ellie, Freddie, Marianna, Mihai, Norbert, Rachael, Rahul, Stuart, and Tamas. Thank you to those in the rest of the School of Mathematics and Statistics who have been no less important: Callum, Drew, Fay, Hope, and Poppy.

Thank you to my family who have had a major role in getting me to this point. In particular, thank you to Becky, who has been by my side throughout. Finally, thank you to my Sheffield household who have felt like a family and treated me as such: Miriam, Ellie, and Fay.

Declaration of Authorship

I hereby declare that except where specific reference is made to the work of others, the contents of this dissertation are original and have not been submitted in whole or in part for consideration for any other degree or qualification in this, or any other university. This dissertation is my own work and contains nothing which is the outcome of work done in collaboration with others, except as specified in the text. This dissertation contains fewer than 80,000 words including appendices, bibliography, footnotes, tables and equations.

Matthew Mark Allcock
September 2020

Abstract

Over 50 years of solar magnetohydrodynamic wave theory has focussed on waveguides in symmetric plasma environments. Yet the Sun's inhomogeneous atmosphere supports waveguides held in asymmetric equilibrium. In this thesis, we break this symmetry by studying a slab waveguide model embedded in an asymmetric external plasma with three approaches:

- Eigenvalue problem: We derive the dispersion relation and show that asymmetric eigenmodes have mixed properties of the traditional sausage and kink modes.
- Ray theory: We demonstrate how a ray theoretic approach can be used to derive this dispersion relation, giving an intuitive description of asymmetric leaky modes.
- Initial value problem: An initial perturbation of an asymmetric slab evolves, in general, through a series of three phases: the *initial phase*, the period before collective modes are excited; the *impulsive phase*, where leaky modes can dominate; and the *stationary phase*, where trapped modes dominate for an indefinite time period. We show that, in general, the impulsive phase for a slab is significantly shorter than for a magnetic flux tube. We then show that an asymmetric slab of cold plasma does not have a stationary phase because the principal kink mode in an asymmetric slab is leaky.

Next, we derive two magneto-seismology techniques to estimate the magnetic field strength in asymmetric solar waveguides. We apply this novel technique to a series of solar chromospheric fibrils as a proof of concept with estimated values of the Alfvén speed that agree with estimates using traditional techniques.

List of Publications

Parts of this thesis are based on the following publications:

- Allcock, M., and Erdélyi, R., (2017), 'Magnetohydrodynamic Waves in an Asymmetric Magnetic Slab', *Solar Phys.*, volume 292, 35.
- Allcock, M., and Erdélyi, R., (2018), 'Solar Magnetoseismology with Magnetoacoustic Surface Waves in Asymmetric Magnetic Slab Waveguides', *Astrophys. J.*, volume 855, 90.
- Zsámberger, N. K., Allcock, M., and Erdélyi, R., (2018), 'Magneto-acoustic Waves in a Magnetic Slab Embedded in an Asymmetric Magnetic Environment: The Effects of Asymmetry', *Astrophys. J.*, volume 853, 136.
- Allcock, M., Shukhobodskaia, D., Zsámberger, N. K., and Erdélyi, R., (2019), 'Magnetohydrodynamic waves in multi-layered asymmetric waveguides: solar magneto-seismology theory and application', Frontiers in Astronomy and Space Sciences, volume 6, 48.

Contents

CHAPTER 1
Introduction

1.1 The Sun

The Sun is hot. It is so hot that thermal energy overcomes the electromagnetic force between subatomic particles so that they struggle to form neutral atoms. Instead the hottest regions of the Sun are composed of a fully ionised soup of electrons and nuclei known as *plasma*. Due to the dissociation of charges in a plasma, it can conduct electricity and therefore has an associated magnetic field. This magnetic field interacts with the fluid in a nonlinear coupling between the magnetic field and the plasma motion. This coupling can be described mathematically by the theory of *magnetohydrodynamics (MHD)*.

The Sun's atmosphere, particularly the most extended region, known as the *corona*, is dominated by a complex, dynamic, and inhomogeneous magnetic field. This magnetic field contributes to the astronomical energy that drives many of the most energetic events in the solar system, including jets, eruptions, and flares. These dynamic solar events, as well as convectional buffeting from the bubbling interior Sun, drive waves in the solar atmosphere which can be guided by the inhomogeneous magnetic field. What differentiates these waves from waves in fluids, such as sound waves in air, is the contribution of the magnetic field to the waves' restoring force. These waves are known as *magnetohydrodynamic waves*. MHD waves whose restoring force is a combination of the pressure gradient and the magnetic force, but not other forces such as gravity and Coriolis which are neglected in this thesis, are known as *magneto-acoustic waves*.

Observations of MHD waves in the Sun's atmosphere can be used to approximate plasma parameters, such as the magnetic field strength, that are difficult to measure using traditional methods that involve analysis of light spectra (Nakariakov and Verwichte, 2005; De Moortel and Nakariakov, 2012).

This is accomplished by comparing observations of MHD waves in the solar atmosphere to theoretical results from studying MHD wave propagation in model waveguides that approximate those in the solar atmosphere. This emerging field is inspired by the Earth seismology and is known as *solar magneto-seismology* (SMS) (Erdélyi, 2006). A brief history of SMS is given in Section 5.1.2. Accurate approximations of plasma parameters in the solar atmosphere are useful for a number of reasons. For numerical solutions to accurately model the solar conditions, we need realistic input parameters. On a more fundamental level, cataloguing realistic solar parameters can provide evidence for or against various hypothetical mechanisms leading to, for example, instability, magnetic reconnection, and waves. Some of these phenomena contribute to the onset of solar flares and coronal mass ejections, which pose a significant threat to modern society on Earth (Cabinet Office, 2015). SMS is introduced and discussed in more depth in Chapter 5.

Improvements in the spatial-resolution of solar telescopes have driven a new era of solar physics. Of particular interest to this thesis are observations of MHD waves. Some of the first identifications of MHD waves came from non-thermal broadening of transition region and coronal spectral lines (Doschek et al., 1976; Zirker, 1993). Later, slow MHD waves were observed in coronal plumes (DeForest and Gurman, 1998; Ofman et al., 1999, 2000), and in coronal loops (Nakariakov et al., 2000; Robbrecht et al., 2001). Fast MHD waves were famously imaged in coronal loops at the end of the millennium with the TRACE solar observatory (Aschwanden et al., 1999; Nakariakov et al., 1999). In more recent years, improvements in spatial resolution of observational instrumentation have suggested that these waves are not one-dimensional oscillations like those along a guitar string, but instead they have complex structure in three-dimensions. The precise form of this structure is dictated by the parameters of the inhomogeneous plasma. One characteristic of this structuring is *asymmetry* - the difference in plasma parameters on each side of a structure. This asymmetry of MHD waveguides is the focus of this thesis. In order to motivate the study of asymmetric MHD waves, we first introduce the mathematical framework of MHD.

1.2 Magnetohydrodynamics

1.2.1 The equations of ideal magnetohydrodynamics

The Sun's plasma, just like all ordinary matter in the Universe, is made up of particles[1], but MHD waves are a *macroscopic* phenomenon. This means that MHD waves have characteristic length-scales much larger than the *mean free path*, that is, the average distance a particle will travel before colliding with another[2]. This means that the *Knudsen number*, the dimensionless parameter defined by the ratio of the mean free path to a characteristic length scale, in the Sun is much less than unity. Additionally, we assume that the length-scales of interest are much larger than the Debeye length, so that the fluid can be treated as a charge-neutral plasma rather than merely a collection of charged particles. This motivates the *continuum assumption*, where the fluid is considered to *fill up* the space in which it is contained, so that small-scale inhomogeneities caused by particle dynamics are negligible. This means that we have a coherent notion of fluid velocity, $\mathbf{v}(\mathbf{x}, t)$, density, $\rho(\mathbf{x}, t)$, and pressure, $p(\mathbf{x}, t)$, as functions of continuous position, $\mathbf{x}$, and time, t.

The universe gifts us fundamental laws that are obeyed by all classical mechanics systems upon which we can build our framework. Firstly, the *conservation of mass* tells us that the change in mass in a fixed volume is due only to mass entering or leaving the volume. The rate of change of density in a fixed volume V is

$$\frac{d}{dt}\iiint_V \rho \, d\mathbf{x} = \iiint_V \frac{\partial \rho}{\partial t} \, d\mathbf{x} \tag{1.1}$$

and the rate of mass flux into this volume, whose bounding surface we denote by S, which has infinitesimal surface normal component $d\mathbf{s}$, is

$$-\iint_S \rho\mathbf{v} \, d\mathbf{s} = \iiint_V -\nabla \cdot (\rho\mathbf{v}) \, d\mathbf{x}, \tag{1.2}$$

by use of the divergence theorem. Equations (1.1) and (1.2) must be equal for any volume V so the integrands must be equal, that is

$$\frac{\partial \rho}{\partial t} + \nabla \cdot (\rho\mathbf{v}) = 0, \tag{1.3}$$

known as the *continuity equation*.

[1] Atomic or subatomic particles, depending on the temperature, and hence ionisation, of the solar plasma.

[2] The mean free path in the Sun ranges from approximately 1 cm in the solar interior to 1 km in the sparse corona.

Secondly, the *conservation of momentum* tells us that the momentum in a volume V that moves with the fluid is only changed by forces exerted on the fluid. The rate of change of momentum in this volume is

$$\frac{d}{dt}\iiint_V \rho\mathbf{v}\ d\mathbf{x} = \iiint_V \rho\frac{D\mathbf{v}}{Dt}\ d\mathbf{x}, \tag{1.4}$$

where $D/Dt = \partial/\partial t + \mathbf{v}\cdot\nabla$ is the derivative observed when moving with the fluid, known as the *material derivative*. The forces acting upon the fluid are either *surface forces* (such as the pressure gradient force and viscosity) that act on an internal or external surface, or *body forces*, $\mathbf{b}$, (such as the gravitational and magnetic forces) that act on the whole volume. The surface forces form a stress tensor σ, so that the total force exerted on a volume of fluid is

$$\iint_S \sigma\cdot d\mathbf{s} + \iiint_V \mathbf{b}\ d\mathbf{x} = \iiint_V (\nabla\cdot\sigma + \mathbf{b})\ d\mathbf{x}, \tag{1.5}$$

using the divergence theorem. Equations (1.4) and (1.5) must be equal for any volume V so the integrands must be equal, that is

$$\rho\frac{D\mathbf{v}}{Dt} = \nabla\cdot\sigma + \mathbf{b}. \tag{1.6}$$

Motivated by the large role they play in the dynamics of small to medium scale solar phenomena, in this thesis we focus on the effects of magnetic and pressure forces and neglect other forces such as gravity and viscosity. Denoting the magnetic field and permeability by $\mathbf{B}$ and μ, respectively, the magnetic force felt by a (non-relativistic) fluid element is $(\nabla\times\mathbf{B})\times\mathbf{B}/\mu$. By neglecting viscosity, we can write the stress tensor as $\sigma = -pI$, where I is the 3×3 identity matrix. This reduces Equation (1.6) to the *momentum equation*, namely

$$\rho\frac{D\mathbf{v}}{Dt} = -\nabla p + \frac{1}{\mu}(\nabla\times\mathbf{B})\times\mathbf{B}. \tag{1.7}$$

Finally, *conservation of entropy* occurs during processes that are *adiabatic* and *reversible*. The entropy per unit mass, s, for an *ideal fluid* is given by

$$s = C_v \ln\left(\frac{p}{\rho^\gamma}\right) + \text{const}, \tag{1.8}$$

where C_v and γ are the specific heat at constant volume and the adiabatic index, respectively. Entropy is conserved when moving with the fluid, which, using Equation (1.8), can be written in the form

$$\frac{D}{Dt}\left(\frac{p}{\rho^\gamma}\right) = 0, \tag{1.9}$$

which we call the *energy equation* because it can also be interpreted as the fundamental law of conservation of energy.

Equations (1.3), (1.9), and the three components of (1.7) are a system of five equations that relate eight unknowns (ρ, p, and three components of $\mathbf{v}$ and $\mathbf{B}$). Three additional equations are required to close the system. To establish these additional equations, we use *Ohm's Law*, which asserts that the current density, $\mathbf{j}$, is proportional to the total electric field when moving with the fluid,

$$\mathbf{j} = \frac{1}{\eta}(\mathbf{E} + \mathbf{v} \times \mathbf{B}), \tag{1.10}$$

where η is the magnetic diffusivity and $\mathbf{E}$ is the electric field. In this thesis, we are concerned with plasmas where resistive effects, including magnetic reconnection and diffusion, are neglected. Therefore, we omit the left hand side of this equation to give

$$\mathbf{E} + \mathbf{v} \times \mathbf{B} = 0. \tag{1.11}$$

Faraday's law of electromagnetism relates the gradient of the electric field to the change in magnetic field:

$$\nabla \times \mathbf{E} = -\frac{\partial \mathbf{B}}{\partial t}. \tag{1.12}$$

Combining Equations (1.11) and (1.12) gives us the *induction equation* (for an ideal plasma)

$$\frac{\partial \mathbf{B}}{\partial t} = \nabla \times (\mathbf{v} \times \mathbf{B}). \tag{1.13}$$

Equations (1.3), (1.7), (1.9), and (1.13) constitute a complete set of equations that describe the evolution of an ideal plasma and are known as the *ideal MHD equations*.

In addition, *Gauss' Law*, which states that $\nabla \cdot \mathbf{B} = 0$, puts a constraint on the choice of initial magnetic field. Integrating Equation (1.13) with respect to time shows us that initial satisfaction of Gauss' Law ensures its satisfaction for all later time.

1.2.2 Ideal magnetohydrodynamic behaviour

The ideal plasma assumption approximates the plasma to be perfectly conducting. Ideal plasmas behave in unique and surprisingly simple ways that will be discussed in this subsection. We will briefly discuss the decomposition of the Lorentz force into magnetic tension and pressure, the conservation of magnetic flux, and the conservation of magnetic field lines.

Magnetic field lines, or just *field lines*, are lines parallel to the magnetic field, $\mathbf{B}$. The local field line density is proportional to the local strength of the magnetic field. Magnetic field lines are fictitious and are conceived of merely for ease of understanding and visualisation.

1.2.2.1 Magnetic tension and pressure

The Lorentz force in the momentum Equation (1.7) can be decomposed using a vector calculus identity into

$$\frac{1}{\mu}(\nabla \times \mathbf{B}) \times \mathbf{B} = \frac{1}{\mu}(\mathbf{B} \cdot \nabla)\mathbf{B} - \nabla\left(\frac{\mathbf{B}^2}{2\mu}\right). \tag{1.14}$$

The first term on the right hand side is the *magnetic tension* force which acts normal to $\mathbf{B}$. It acts to *straighten out* curved magnetic field lines and its strength is proportional to the field line's curvature. The second term on the right-hand side is the *magnetic pressure* force which acts along a negative gradient in magnetic field strength. It acts to *spread out* magnetic field lines in the sense that magnetic field lines that are close together will have a force pulling them apart.

1.2.2.2 Magnetic flux conservation

The magnetic flux through a surface S which moves with the plasma and is bounded by a simple closed curve C is

$$\Psi = \iint_S \mathbf{B} \cdot d\mathbf{s}. \tag{1.15}$$

The magnetic flux can change in two ways: when the magnetic field $\mathbf{B}$ changes with S held fixed, and when the flux swept out by the C is moved with the plasma. Combining these, the rate of change of flux is

$$\frac{d\Psi}{dt} = \iint_S \frac{\partial \mathbf{B}}{\partial t} \cdot d\mathbf{s} + \oint_C \mathbf{B} \cdot \mathbf{v} \times d\mathbf{l}, \tag{1.16}$$

where $d\mathbf{l}$ is an element parallel to curve C. Using Stokes' Theorem on the second term on the right hand side, this equation becomes

$$\frac{d\Psi}{dt} = \iint_S \left[\frac{\partial \mathbf{B}}{\partial t} - \nabla \times (\mathbf{v} \times \mathbf{B})\right] \cdot d\mathbf{s}. \tag{1.17}$$

Using the induction equation, Equation (1.13) it is clear that the change in the magnetic flux vanishes. Therefore, magnetic flux is conserved in an ideal plasma.

This result has the important corollary that the magnetic field lines are frozen to the plasma. That is, wherever the magnetic field moves, the plasma follows, and *vice versa*. In other words, plasma elements that initially occupy the same field line will always do so in ideal MHD. This is known as *Alfvén's frozen flux theorem*.

1.3 Waves in the solar atmosphere

1.3.1 Magnetohydrodynamic waves in a homogeneous plasma

Whilst the Sun's atmosphere is in reality inhomogeneous, it is instructive to first study the MHD waves that propagate in a homogeneous plasma. We start with the ideal MHD equations derived in Section 1.2.1,

$$\frac{\partial \rho}{\partial t} + \nabla \cdot (\rho \mathbf{v}) = 0, \tag{1.18}$$

$$\rho \frac{D\mathbf{v}}{Dt} = -\nabla p + \frac{1}{\mu}(\nabla \times \mathbf{B}) \times \mathbf{B}, \tag{1.19}$$

$$\frac{D}{Dt}\left(\frac{p}{\rho^{\gamma}}\right) = 0, \tag{1.20}$$

$$\frac{\partial \mathbf{B}}{\partial t} = \nabla \times (\mathbf{v} \times \mathbf{B}). \tag{1.21}$$

Consider a stationary homogeneous plasma with equilibrium magnetic field given by $\mathbf{B_0} = (0, 0, B_0)$, without loss of generality. Each physical quantity can be written as a sum of its equilibrium quantity and a perturbation from that equilibrium, namely, $f = f_0 + f'$, where f is a placeholder for variables $\rho, p, \mathbf{v}$, and $\mathbf{B}$. The equilibrium plasma is stationary and homogeneous, so $\mathbf{v}_0 = 0$, and each equilibrium variable is uniform in space. By considering just small perturbations from equilibrium, *i.e.* $f' \ll f_0$ for each physical quantity, we can remove the non-linearity from the governing equations. Substituting this form of the variables into the ideal MHD equations and neglecting terms of quadratic order or higher in small perturbations gives us the linearised ideal

MHD equations

$$\frac{\partial \rho'}{\partial t} + \rho_0(\nabla \cdot \mathbf{v}') = 0, \tag{1.22}$$

$$\rho_0 \frac{\partial \mathbf{v}'}{\partial t} = -\nabla p' + \frac{1}{\mu}(\nabla \times \mathbf{B}') \times \mathbf{B}_0, \tag{1.23}$$

$$\frac{\partial p'}{\partial t} - c_0^2 \frac{\partial \rho'}{\partial t} = 0, \tag{1.24}$$

$$\frac{\partial \mathbf{B}'}{\partial t} = \nabla \times (\mathbf{v}' \times \mathbf{B}_0), \tag{1.25}$$

where $c_0 = \sqrt{\gamma p_0/\rho_0}$ is the *sound speed*. This system of equations can be combined into the generalised wave equation

$$\frac{\partial^2 \mathbf{v}}{\partial t^2} = c_0^2 \nabla(\nabla \cdot \mathbf{v}) + \frac{1}{\mu\rho_0}(\nabla \times (\nabla \times (\mathbf{v} \times \mathbf{B}_0))) \times \mathbf{B}_0, \tag{1.26}$$

where we have dropped the apostrophe on $\mathbf{v}$ for brevity. The form of this equation motivates a search for solutions of the form

$$\mathbf{v}(\mathbf{x}, t) = \widehat{\mathbf{v}} e^{i(\mathbf{k}\cdot\mathbf{x} - \omega t)}, \tag{1.27}$$

corresponding to *plane-waves* with wavenumber vector $\mathbf{k}$, circular frequency ω, and amplitude $\widehat{\mathbf{v}}$ that is spatially uniform. This reduces Equation (1.26) to an eigenvalue problem with eigenfrequency ω^2, namely

$$\omega^2 \widehat{\mathbf{v}} = c_0^2 \mathbf{k}(\mathbf{k} \cdot \widehat{\mathbf{v}}) + \frac{1}{\mu\rho_0}(\mathbf{k} \times (\mathbf{k} \times (\widehat{\mathbf{v}} \times \mathbf{B}_0))) \times \mathbf{B}_0. \tag{1.28}$$

With the aim of first studying a limiting solution, the ratio of the first term to the second term on the right hand side of the above equation is

$$\frac{|c_0^2 \mathbf{k}(\mathbf{k} \cdot \widehat{\mathbf{v}})|}{|\frac{1}{\mu\rho_0}(\mathbf{k} \times (\mathbf{k} \times (\widehat{\mathbf{v}} \times \mathbf{B}_0))) \times \mathbf{B}_0|} = \frac{c_0^2}{v_A^2}, \tag{1.29}$$

where $v_A = B_0/\sqrt{\mu\rho_0}$ is the *Alfvén speed*. When the sound speed dominates the Alfvén speed[3], and assuming that $\mathbf{k} \cdot \widehat{\mathbf{v}} \neq 0$ so that the fluid is compressible, taking the dot product of $\mathbf{k}$ and Equation (1.28) leads to $\omega = \pm k c_0$. These solutions correspond to forwards and backwards propagating *sound waves*. They are longitudinal waves that propagate isotropically in a homogeneous fluid.

[3]This is known as the *high beta limit*. Here, beta refers to the plasma beta parameter defined as the ratio of kinetic pressure to magnetic pressure and can be written as $\beta = \frac{2c_0^2}{\gamma v_A^2}$

When neither the sound speed or Alfvén speed dominates, we can write Equation (1.28) in component form as

$$\begin{pmatrix} \omega^2 - k_x^2 c_0^2 - (k_x^2 + k_z^2) v_A^2 & 0 & -k_x^2 k_z^2 c_0^2 \\ 0 & \omega^2 - k_z^2 v_A^2 & 0 \\ -k_x k_z c_0^2 & 0 & \omega^2 - k_z^2 c_0^2 \end{pmatrix} \begin{pmatrix} \widehat{v}_x \\ \widehat{v}_y \\ \widehat{v}_z \end{pmatrix} = 0, \tag{1.30}$$

where, without loss of generality, we have let $\mathbf{k} = (k_x, 0, k_z)$. For there to exist non-trivial solutions to this equation, the determinant of the matrix must vanish, that is

$$(\omega^2 - k_z^2 v_A^2) \left[\omega^4 - \omega^2 k^2 (c_0^2 + v_A^2) + k^2 k_z^2 c_0^2 v_A^2 \right] = 0, \tag{1.31}$$

where we have defined $k^2 = k_x^2 + k_z^2$.

The first set of solutions to Equation (1.31) are $\omega = \pm k_z v_A$. These solutions correspond to forward and backwards propagating *Alfvén waves*[4]. They are transverse oscillations of the magnetic field that can propagate in any direction apart from perpendicular to the magnetic field and transport energy parallel to the magnetic field. They are described as purely magnetic waves because they are not associated with a density perturbation.

The second set of solutions to Equation (1.31) are

$$\omega^2 = \frac{1}{2} k^2 (c_0^2 + v_A^2) \left(1 \pm \sqrt{1 - 4 c_T^2 \frac{k_z^2}{k^2}} \right), \tag{1.32}$$

where $c_T = c_0^2 v_A^2 / \sqrt{c_0^2 + v_A^2}$ is known as the *tube speed* or *cusp speed*, so called because it is the phase speed of slow waves in a thin magnetic flux tube (see Section 1.3.2.3). These solutions are *magneto-acoustic waves*, which are oscillations restored by a combination of both the pressure gradient and Lorentz forces. The solutions with the higher frequency (and hence faster phase speed) are known as *fast magneto-acoustic waves* and the solutions with the lower frequency are known as *slow magneto-acoustic waves*. Physically, perturbations in the fast mode are restored by the pressure gradient and Lorentz forces working in phase, whereas perturbations in the slow mode are restored by the forces working in anti-phase, leading to a less strong restoring force for slow modes.

1.3.2 Magnetohydrodynamic waves in inhomogeneous plasma

To progress towards an understanding of MHD waves in the solar atmosphere, we now study MHD waves in simple inhomogeneous plasma configurations. In

[4]Named after *Hannes Alfvén*, whose original derivation of this solution earned him the Nobel prize in Physics (Alfvén, 1942).

this subsection, we review the theory of linear MHD waves propagating along simple inhomogeneous structures: a tangential interface (Section 1.3.2.1), a symmetric slab (Section 1.3.2.2), and a magnetic flux tube (Section 1.3.2.3).

1.3.2.1 Tangential interface

MHD wave propagation along a tangential interface, where the magnetic field is tangential to the interface, was studied by Nye and Thomas (1976). Here, we follow a popular version of the derivation by Roberts (1981*a*). Consider a plasma at equilibrium with piecewise uniform magnetic field, $\mathbf{B}_0(x) = (0, 0, B_0(x))$, given by

$$B_0(x) = \begin{cases} B_- & \text{if } x \leq 0, \\ B_+ & \text{if } x > 0. \end{cases} \tag{1.33}$$

The interface between the two regions is at $x = 0$, without loss of generality. Given a magnetic field that is initially tangent to the interface, the magnetic field must be tangent to the interface for all time due to ideal magnetic flux conservation (see Section 1.2.2.2).

To derive the dispersion relation, first we seek plane wave solutions to the linearised ideal MHD equations, Equations (1.22)-(1.25) by assuming that parameters behave like $f(x) = \widehat{f}e^{i(kz-\omega t)}$, where k and ω are the wavenumber and angular frequency of the waves that propagate in the z-direction. They are then combined to show that the transverse velocity perturbation, $\widehat{v}_x$, satisfies a Helmholtz differential equation for each of the two plasma regions, denoted by subscript $-$ and $+$, namely

$$\widehat{v}_x'' - m_\pm^2 \widehat{v}_x = 0, \quad \text{where} \quad m_\pm^2 = \frac{(\omega_{A\pm}^2 - \omega^2)(\omega_\pm^2 - \omega^2)}{(c_\pm^2 + v_{A\pm}^2)(\omega_{T\pm}^2 - \omega^2)}, \tag{1.34}$$

where $' = \mathrm{d}/\mathrm{d}x$ and $\omega_{A\pm} = kv_{A\pm}$, $\omega_\pm = kc_\pm$, and $\omega_{T\pm} = kc_{T\pm}$, are each region's respective Alfvén, sound, and tube frequency. Solutions to this equation are a linear combination of exponential functions, $e^{\pm m_\pm x}$, if $m_\pm^2 > 0$, or trigonometric functions, $\cos m_\pm x$ and $\sin m_\pm x$, if $m_\pm^2 < 0$. We restrict our model to waves trapped by the slab by imposing the boundary condition $\widehat{v}_x \to 0$ as $|x| \to \infty$. This ensures that $m_\pm^2 > 0$, leading to solutions of the form

$$\widehat{v}_x(x) = \begin{cases} Ae^{m_- x}, & \text{if } x \leq 0, \\ Be^{-m_+ x}, & \text{if } x > 0, \end{cases} \tag{1.35}$$

where A and B are constant with respect to x. This equation describes the distribution of oscillation amplitudes across the waveguide and is known as

an *eigenfunction*[5]. The boundary conditions across the interface are that the velocity and total (gas plus magnetic) pressure are continuous[6]. Applying these boundary conditions leads to a system of linear algebraic equations in the unknowns A and B. The requirement that there exist non-trivial solutions is that the determinant of this system be zero. This gives us the dispersion relation, namely

$$\rho_+ m_-(\omega^2 - \omega_{A+}^2) + \rho_- m_+(\omega^2 - \omega_{A-}^2) = 0. \tag{1.36}$$

The solutions to this equation correspond to *surface* magneto-acoustic modes. These are modes whose eigenfunction decays exponentially away from the interface and owe their existence to the interface. The radicals in $m_\pm$ resist the use of analytical methods to find the solutions, unless further approximations are made (see Section 2.3.1).

There also exist Alfvén modes, which are sometimes referred to as *shear Alfvén modes* in the slab geometry, which we decoupled from the magneto-acoustic modes due to our choice of ansatz. Alfvén modes propagate along the magnetic field and perturb it tangentially to the interface, without perturbing the density. Since the perturbations are tangential to the interface, each magnetic isosurface, defined as a surface of constant magnetic field, is free to oscillate independently (in ideal MHD). These Alfvén modes are local modes in that they only oscillate a strict subset of the whole domain, therefore, they do not owe their existence to the interface, and are therefore not discussed in any more detail here.

1.3.2.2 Symmetric slab

MHD wave propagation along a symmetric magnetic slab was studied by McKenzie (1970). It was later studied by Roberts (1981*b*) and Edwin and Roberts (1982), whose derivation we follow here. Consider a plasma at equilibrium with piecewise uniform magnetic field given by

$$B_0(x) = \begin{cases} B_i & \text{if } |x| \leq x_0, \\ B_e & \text{if } |x| > x_0. \end{cases} \tag{1.37}$$

Here, the word *symmetric* refers to the reflectional symmetry of the waveguide over the $x = 0$ plane. We refer to eigenmodes of symmetric waveguides

[5]We use the term *eigenmode* to refer to the whole solution, *i.e.* an eigenfrequency and its associated eigenfunction. Eigenmodes are also known as *normal modes*.

[6]These boundary conditions are equivalent to the familiar *kinematic* and *dynamic* boundary conditions on a free surface (Goedbloed and Poedts, 2004).

as *symmetric modes*. Any waveguide or eigenmode that is not symmetric is referred to as *asymmetric*[7].

Following the same derivation as in Section 1.3.2.1, we can derive the dispersion relation for transverse eigenmodes of a symmetric slab, namely

$$D_s(\omega)D_k(\omega) = 0, \tag{1.38}$$

where

$$D_s(\omega) = \rho_e m_i(\omega_{\mathrm{Ae}}^2 - \omega^2)\tanh m_i x_0 + \rho_i m_e(\omega_{\mathrm{Ai}}^2 - \omega^2), \tag{1.39}$$

$$D_k(\omega) = \rho_e m_i(\omega_{\mathrm{Ae}}^2 - \omega^2)\coth m_i x_0 + \rho_i m_e(\omega_{\mathrm{Ai}}^2 - \omega^2), \tag{1.40}$$

where m_i and m_e are defined in the fashion equivalent to Equation (1.34). Therefore, either $D_s = 0$ or $D_k = 0$. Solutions to $D_s = 0$ are the eigenfrequencies of *sausage modes* and solutions to $D_k = 0$ are the eigenfrequencies of *kink modes*. For sausage modes, the boundaries of the slab oscillate in anti-phase and for kink modes, they oscillate in phase.

Whilst the sign of m_e^2 must be negative to ensure that the perturbation is attenuated away from the slab, the sign of m_i^2 can be positive or negative. If $m_i^2 > 0$, then the velocity perturbation within the slab is a linear combination of exponential functions. Modes of this type are known as *surface modes*. If $m_i^2 < 0$, then the velocity perturbation within the slab is a linear combination of trigonometric functions. Modes of this type are known as *body modes*.

Exponential functions are monotonic, so there is only one way in which an internally exponential function can satisfy the continuity conditions at the interfaces. This means that for both sausage and kink varieties, there exists only one surface mode. On the other hand, trigonometric functions are periodic, so there is an infinite number of ways in which an internally trigonometric function can satisfy the continuity conditions at the interfaces. This means that for both sausage or kink varieties, there exist an infinite number of body modes, each with a different integer number of nodes and anti-nodes within the slab.

There also exist Alfvén modes that behave in the same way as the tangential interface because they perturb the plasma tangentially to the interfaces.

[7]Some publications have used the terms *symmetric mode* and *anti-symmetric mode* to refer to the sausage and kink eigenmodes of a symmetric slab or tube. This is motivated by the symmetry/anti-symmetry of the eigenfunctions over the axis of the waveguide. In this thesis, we use the terms *sausage mode* and *kink mode* instead of *symmetric mode* and *anti-symmetric mode* to avoid confusion.

1.3.2.3 Magnetic flux tube

MHD wave propagation along a magnetic flux tube was first studied mathematically by Defouw (1976) and Ryutov and Ryutova (1976). Later, Edwin and Roberts (1983) studied the same problem in the format followed here. Consider a plasma at equilibrium, in cylindrical geometry $\mathbf{r} = (r, \phi, z)$, with magnetic field $\mathbf{B}_0(\mathbf{r}) = (0, 0, B_0(r))$ that is piecewise uniform in the radial direction, given by

$$B_0(r) = \begin{cases} B_i & \text{if } r \leq r_0, \\ B_e & \text{if } r > r_0. \end{cases} \tag{1.41}$$

We seek solutions of the form $f(\mathbf{r}) = \widehat{f}(r)e^{i(kz+m\phi-\omega t)}$. Note that this form necessitates that $m \in \mathbb{Z}$, to maintain azimuthal continuity in each variable. Then, dropping the hat for brevity, the perturbation in total pressure, p_T, inside the tube obeys the equation

$$p_T'' + \frac{1}{r}p_T' - (m_i^2 + \frac{m^2}{r^2})p_T = 0. \tag{1.42}$$

Outside of the tube, an equivalent equation, with subscripts e is satisfied. For $m_i^2 > 0$, this is the modified Bessel's equation of integer order m and for $m_i^2 < 0$, it is Bessel's equation of integer order m. Requiring that the perturbations approach zero far from the tube outside means that for $r > r_0$,

$$p_T(r) = AK_m(m_e r), \tag{1.43}$$

where K_m is the modified Bessel function of the second kind with $m_e^2 > 0$, and A is a constant to be determined. Inside the tube, we require that the perturbation remain finite as $r \to 0$, so for $r > r_0$,

$$p_T(r) = BI_m(m_i r), \tag{1.44}$$

where I_m is the modified Bessel function of the first kind and B is a constant to be determined. Either $m_i^2 > 0$ or $m_i^2 < 0$. If $m_i^2 < 0$, then Equation (1.44) can be formulated in terms of the Bessel function of the first kind, J_m, because $I_m(iz) \propto J_m(z)$. Also, each modified Bessel function of integer order, when considered as functions of their order, are even functions (*i.e.* $I_{-n}(z) = I_n(z)$ and $K_{-n}(z) = K_n(z)$), modes with negative orders are identical modes to their positive order counterparts. Applying the boundary conditions of continuity in normal velocity and total pressure using Equations (1.44) and (1.43) leads

to the dispersion relation for magneto-acoustic waves in a magnetic flux tube, namely

$$\rho_i(\omega_{Ai}^2 - \omega^2)m_e\frac{K'_m(m_e r_0)}{K_m(m_e r_0)} = \rho_e(\omega_{Ae}^2 - \omega^2)m_i\frac{I'_m(m_i r_0)}{I_m(m_i r_0)}, \tag{1.45}$$

Similar to the symmetric slab, eigenmodes for which $m_i^2 > 0$ are surface modes and eigenmodes for which $m_i^2 < 0$ are body modes. Body modes can have any positive integer number of radial nodes and anti-nodes within the tube. The integer m is half the number of azimuthal nodes. In particular, modes for which $m = 0$ have no azimuthal nodes and therefore correspond to axisymmetric perturbations. These are known as sausage modes. Modes for which $m = 1$ have two azimuthal nodes and are known as kink modes. Modes for which $m > 1$ are known as *fluting modes*.

There also exist torsional Alfvén modes which oscillate individual magnetic isosurfaces. As with the magneto-acoustic modes, they can oscillate with any even number of azimuthal nodes. They perturb plasma orthogonal to, and therefore do not perturb, the tube boundary.

1.4 Thesis outline

The remainder of this thesis is structured as follows:

- **Chapter 2**: We establish and solve the eigenvalue problem for MHD waves propagating along a magnetic slab waveguide where the external plasma is asymmetric. This is the simplest MHD waveguide that demonstrates asymmetry. The dispersion relation is derived and is solved analytically under certain approximations, and numerically. The eigenmodes can exist as a generalisation of the traditional sausage and kink modes. Two implications for solar observations are discussed. First, we establish the existence of quasi-symmetric eigenmodes. These are modes that have symmetric amplitudes on the waveguide interfaces even though they propagate along asymmetric waveguides, which could lead to misidentification of eigenmodes. Secondly, we discuss the difficulty of distinguishing an asymmetric MHD wave from a superposition of symmetric MHD waves in solar atmospheric structures.

- **Chapter 3**: We introduce ray optics as a mathematical model of MHD wave propagation. We introduce the ambiguities that arise in MHD ray

optics due to the anisotropy of the magnetic field. Then we derive the dispersion relation for the asymmetric slab using ray optics. This approach provides an intuitive notion of lateral wave leakage as transmission of wave power due to partial internal reflection.

- **Chapter 4**: We establish and solve the initial value problem (IVP) of MHD waves propagating along a magnetic slab waveguide. First, we solve the IVP under the assumption that the plasma is incompressible. Along the way, we revisit and correct a major error in a related paper by Rae and Roberts (1981) that solves an initial value problem of surface MHD waves on a tangential interface. Finally, we solve the more difficult IVP under the zero-beta assumption, showing that the perturbed waveguide evolves through three phases: the initial phase, the impulsive phase, and the stationary phase. We show that the impulsive phase is much shorter for a slab waveguide than a cylindrical waveguide.

- **Chapter 5**: We derive two new inversion techniques that use the symmetry of asymmetric MHD waves to diagnose parameters of the background plasma that are otherwise impossible to measure. We coin these techniques the *amplitude ratio method* and the *minimum perturbation shift method*. This is the first time that a solar magneto-seismology technique has employed the asymmetry of MHD waves. By diagnosing the Alfvén speed in five chromospheric fibrils, we perform a first use of the amplitude ratio method on solar observations. Our results corroborate with previous analyses of chromospheric fibrils that use different methods.

- **Chapter 6**: A summary and discussion of the conclusions of this thesis.

- **Chapter 7**: A discussion of possible further work that would build upon this thesis.

CHAPTER 2

Eigenvalue problem

2.1 Chapter introduction

The aim of this chapter is to investigate the physics of asymmetric MHD waves as an eigenvalue problem (EVP). To isolate the behaviour introduced when symmetry is broken, it is instructive to analyse a simple model that supports asymmetric MHD waves. That way, any novel behaviour can be unambiguously attributed to the asymmetry of the model rather than another factor. The simplest model of an asymmetric waveguide is an asymmetric magnetic slab[1], breaking the symmetry of the symmetric magnetic slab analysed in Section 1.3.2.2 and by Roberts (1981*b*).

The EVP approach to MHD wave problems was first employed by Alfvén (1942) to derive the theoretic existence and propagation speed of magnetically driven waves in the fluid, the result that awarded him the Nobel Prize in Physics in 1970. He showed that in a homogeneous plasma there are three types of waves that propagate, as shown in Section 1.3.1. The wave with intermediate speed became known as the *Alfvén wave*. This theoretical result sparked the search for Alfvén waves across several areas of plasma physics, from experimental, with early detection in magnetised mercury (Lundquist, 1949), sodium (Lehnert, 1954), and bismuth (Hess and Hinsch, 1973), to geophysics, with a surprisingly early detection of Alfvén waves in the Earth's ionosphere, driven by a nuclear weapon test (Berthold et al., 1960).

More relevant to the present thesis is that the discovery of Alfvén waves got the solar physics world asking the question: *are there Alfvén waves on the Sun?* The difficulty in establishing a confident affirmative answer to this question is that, in structured plasma like that of the solar atmosphere, MHD

[1]More precisely, the simplest model of an asymmetric MHD waveguide is an interface between different plasmas; the asymmetric slab is the simplest asymmetric waveguide that can oscillate in a collective body mode (see Section 2.2.3).

waves demonstrate mixed properties (Goossens et al., 2009, 2012, 2019). By this we mean that, in general, they can propagate both vorticity (like Alfvén waves do) and compression (like magneto-acoustic waves do). In some circumstances, such as when the plasma is cold, the fast kink magneto-acoustic wave is almost completely incompressible, and therefore produces a similar observational signature to Alfvén wave. These nearly incompressible kink modes have rather confusingly become known as *Alfvénic* and have ubiquitous presence in the solar atmosphere (Tomczyk et al., 2007). This explains the erroneous detection of Alfvén waves in the corona (Tomczyk et al., 2007), which are more likely to have been kink waves (Van Doorsselaere, Nakariakov and Verwichte, 2008; Erdélyi and Taroyan, 2008). More likely observations of Alfvén waves have since been made in X-ray jets (Cirtain et al., 2007) and in magnetic bright points (Jess et al., 2009). A review of the theory and observations of solar Alfvén waves was conducted by Mathioudakis et al. (2013).

After the detection of ubiquitous MHD waves in the solar atmosphere, whether they be Alfvén, Alfvénic, or another kind entirely, comes the question: *do they contribute to the heating of the corona?* This question must be answered in two parts: (1) *is there enough energy transported in these waves to heat the corona?* and (2) *is there a mechanism for converting this wave energy into thermal energy?* Withbroe and Noyes (1977), amongst others, have shown that an energy input of $10^2 - 10^4$ W m^{-2} is required to balance the thermal losses from radiation and solar wind in order to maintain the corona's high temperatures of approximately 2 MK. Many acclaimed Alfvén wave observational studies have estimated the energy density transported by the observed MHD waves to be sufficient. This has been backed up by numerical studies that show that sufficient energy can be found in, for example, high-frequency torsional Alfvén waves (Srivastava et al., 2017). A number of mechanisms for dissipating this wave energy into the coronal environment have been proposed, including phase mixing (Heyvaerts and Priest, 1983) and resonant absorption (Ionson, 1978), that can significantly shorten the time-scale for energy dissipation by resistive or viscous processes. MHD waves remain a strong candidate for explaining the unexpectedly high coronal temperatures but the matter is far from settled. The current status of MHD wave heating is reviewed by a number of papers (Mathioudakis et al., 2013; De Moortel and Browning, 2015).

A selection of MHD waveguides have been investigated with an EVP approach. The first non-uniform plasma system that was investigated with an EVP was the tangential interface between semi-infinite plasma regions with

distinct parameters (Zajtsev and Stepanov, 1975; Roberts, 1981*a*; see Section 1.3.2.1). They showed the existence of trapped MHD surface waves that can be either *fast* or *slow*, depending on the phase difference between the pressure gradient and magnetic restoring forces. The contact discontinuity, where the magnetic field intersects the interface, was shown by Vickers et al. (2018) to contain most of its oscillatory power in modes that leak energy laterally away from the interface. Two parallel tangential interfaces, in the form of a symmetric slab waveguide, were shown by Roberts (1981*b*) and Edwin and Roberts (1982) to oscillate in both surface and body modes, depending on whether the spatial signature of the wave is evanescent or oscillatory within the slab (see Section 1.3.2.2).

Modelling the cylindrical nature of coronal loops, focus moved towards cylindrical waveguides. This began with an investigation by Defouw (1976); Ryutov and Ryutova (1976); Edwin and Roberts (1983) into the oscillatory modes of straight cylindrical flux tubes of infinite length (see Section 1.3.2.3). They showed the existence of *fluting modes*, which have azimuthal wavenumber $m \geq 2$, in addition to the already familiar sausage ($m = 0$) and kink ($m = 1$) modes. Inhomogeneities in the solar atmosphere are such that it is unlikely that the axisymmetry of a circular cross-sectional cylinder will be sufficient to model coronal loops. To accommodate the diversion from axisymmetry, elliptical cross-sectional tubes were investigated by Gu and Qiu (1980), Ruderman (2003), Erdélyi and Morton (2009), and Morton and Ruderman (2011). The sausage mode (and other even-ordered azimuthal modes) differs from its counterpart in circular cross-sectional tubes only by it's phase speed, whereas the kink mode (and other odd-ordered azimuthal modes) splits into two modes with axial displacement polarized along the major and minor axes.

Other EVP investigations of MHD waves have studied the effect of curvature, including a curved magnetic slab (Verwichte et al., 2006*a*,*b*) and a semi-toroidal loop (Van Doorsselaere et al., 2004). The semi-toroidal loop is a mathematical model that approximates coronal loops well. It was shown that curvature has no first-order effect on the frequency and damping time of kink quasi-mode oscillations. This result has justifiably made the solar physics community more comfortable applying the more simple theory of MHD waves in straight waveguide models to curved solar structures. The effects of curvature on coronal loop kink oscillations is reviewed by Van Doorsselaere et al. (2009).

Loop systems above active regions are often observed to oscillate collectively and even single coronal loops have been hypothesised to have a multi-stranded fine structure (Aschwanden et al., 2000), motivating the study of mathematical models of adjacent flux tubes. Luna et al. (2008) showed numerically that a system of two adjacent flux tubes of equal parameters oscillates in four trapped eigenmodes: two where the tubes oscillate in phase and two in anti-phase. Van Doorsselaere, Ruderman and Robertson (2008) generalised this to a system of two distinct flux tubes. This is discussed in more detail as an example of an asymmetric MHD waveguide in Section 2.5.

What this chapter does to build upon previous studies is to focus on the features of asymmetric MHD eigenmodes by building up from the simplest asymmetric MHD waveguide. In particular, we determine how asymmetry of MHD waveguides is manifested in MHD waves, the effects of varying the asymmetry, and how this affects observational wave signatures in the solar atmosphere.

In Section 2.2, we introduce the general asymmetric slab model and derive the dispersion relation for its trapped eigenmodes. Since the dispersion relation for the general model is not analytically solvable to the best of our knowledge, we consider a simplification with non-magnetised external plasma, which yields analytical solutions under certain approximations in Section 2.3.1 and numerical solutions more generally in Section 2.3.2. We study the fully general eigenmodes in Section 2.4. We briefly overview the insights from other asymmetric waveguides including multi-layered plasma, distinct adjacent flux tubes, and non axisymmetric flux tubes in Section 2.5. We cover the conclusions of this chapter in Section 2.6.

Section 2.3 is based on Allcock and Erdélyi (2017) and Section 2.4 is based on my contribution to Zsámberger et al. (2018).

2.2 Asymmetric slab

2.2.1 Model description

Figure 2.1 illustrates the construction of the mathematical model of an asymmetric slab, where a three-dimensional, unbounded, inviscid plasma is separated into three regions by two parallel planar interfaces at $x = \pm x_0$. The

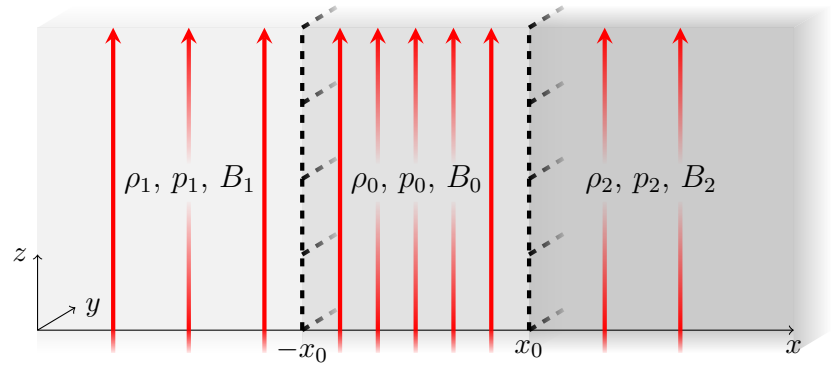

Figure 2.1: The equilibrium state inside the slab, ($|x| \leq x_0$) and outside the slab, ($x < -x_0$ and $x > x_0$). The red arrows illustrate magnetic field lines, $B(x)\widehat{\mathbf{z}}$, and the dashed black lines indicate the boundaries of the slab.

equilibrium magnetic field is in the z-direction and has magnitude

$$B(x) = \begin{cases} B_1 & \text{if } x < -x_0, \\ B_0 & \text{if } |x| \leq x_0, \\ B_2 & \text{if } x > x_0, \end{cases} \tag{2.1}$$

where B_j, for $j = 0, 1, 2$, are constant. Within each region, denoted by subscripts 0, 1, and 2, the plasma is uniform and the equilibrium plasma pressure, density, and temperature are denoted by p_j, ρ_j, and T_j, respectively, for $j = 0, 1, 2$. This defines an *isolated* waveguide, by which we mean there are no adjacent waveguides that can affect or be affected by the oscillations.

To ensure that the model is in equilibrium, the total pressure in each external region must balance the total pressure in the internal region, therefore

$$p_1 + \frac{B_1^2}{2\mu_0} = p_0 + \frac{B_0^2}{2\mu_0} = p_2 + \frac{B_2^2}{2\mu_0}, \tag{2.2}$$

where μ_0 is the permeability of free space. We can rewrite Equation (2.2) as

$$\rho_i \left(c_i^2 + \frac{\gamma}{2} v_{Ai}^2\right) = \rho_j \left(c_j^2 + \frac{\gamma}{2} v_{Aj}^2\right), \quad \text{for} \quad i, j = 0, 1, 2, \tag{2.3}$$

where we define the sound and Alfvén speeds in each region by $c_j = \sqrt{\gamma p_j / \rho_j}$ and $v_{Aj} = B_j / \sqrt{\mu \rho_j}$, respectively, for $j = 0, 1, 2$. The adiabatic index[2] is denoted by γ.

2.2.2 The dispersion relation

In the derivation of the dispersion relation, we decompose the linearised ideal MHD equations into Fourier components then combine them into an ordinary

[2]The adiabatic index is assumed uniform across the whole domain under the single-fluid approximation.

differential equation (ODE) for the transverse velocity perturbation for each of the three plasma regions. After finding the general solution to each of these ODEs, we match the solutions across each interface at $\pm x_0$. The condition for the existence of non-trivial solutions will specify discrete eigenfrequencies for a given wavenumber. This is the *dispersion relation*. In mathematical terms, we convert a set of partial differential equations into ordinary differential equations, then into algebraic equations, then into a single equation. Taking it from a form that we cannot solve into a form that we can.

2.2.2.1 Derivation

We begin with the ideal MHD equations, linearised around a static equilibrium with subscripts j, Equations (1.22)-(1.25). Taking the partial derivative with respect to time of Equation (1.23) and eliminating $\mathbf{B}$ using Equation (1.25), gives

$$\frac{\partial^2 v_x}{\partial t^2} = \frac{\partial}{\partial x}\left[(c_j^2 + v_{Aj}^2)\nabla\cdot\mathbf{v} - v_{Aj}^2\frac{\partial v_z}{\partial z}\right] + v_{Aj}^2\frac{\partial^2 v_x}{\partial z^2} \tag{2.4}$$

$$\frac{\partial^2 v_y}{\partial t^2} = \frac{\partial}{\partial y}\left[(c_j^2 + v_{Aj}^2)\nabla\cdot\mathbf{v} - v_{Aj}^2\frac{\partial v_z}{\partial z}\right] + v_{Aj}^2\frac{\partial^2 v_y}{\partial z^2} \tag{2.5}$$

$$\frac{\partial^2 v_z}{\partial t^2} = c_j^2\frac{\partial}{\partial z}(\nabla\cdot\mathbf{v}). \tag{2.6}$$

Seeking solutions of the form $f(\mathbf{x},t) = \widehat{f}(x)\exp\{i(ly+kz-\omega t)\}$, where $\mathbf{k} = (0,l,k)$ is the wavenumber vector and ω is the angular frequency, for $\mathbf{v}$ in Equation (2.5) gives

$$(k^2v_{Aj}^2 - \omega^2)\widehat{v}_y = l((c_j^2 + v_{Aj}^2)(i\widehat{v}_x' - l\widehat{v}_y - k\widehat{v}_z) + kv_{Aj}^2\widehat{v}_z), \tag{2.7}$$

where $' = d/dx$. If the component of the wavenumber in the y-direction is zero, *i.e.* $l = 0$, then this equation reduces to

$$(k^2v_{Aj}^2 - \omega^2)\widehat{v}_y(x) = 0, \tag{2.8}$$

which yield two solutions. Firstly, $\omega^2 = k^2v_{Aj}^2$ is a solution corresponding to shear Alfvén waves with different phase speed for each magnetic iso-surface (in this case the isosurfaces are surfaces parallel to the yz-plane). The second solution is $\widehat{v}_y(x) = 0$ for all x and therefore $v_y = 0$, *i.e.* waves without perturbation component along the slab and perpendicular to the magnetic field. These solutions correspond to magneto-acoustic modes. Thus we have a decoupling of the Alfvén modes from the magneto-acoustic modes.

Focusing from here on magneto-acoustic modes, we seek solutions of the Fourier form

$$\mathbf{v}(\mathbf{x},t) = (\widehat{v}_x(x)\mathrm{e}^{i(kz-\omega t)}, 0, \widehat{v}_z(x)\mathrm{e}^{i(kz-\omega t)}). \tag{2.9}$$

This restricts the investigation to magneto-acoustic waves propagating parallel to the equilibrium magnetic field, with velocity perturbation amplitude $\widehat{v}_x(x)$ in the x-direction, and $\widehat{v}_z(x)$ in the z-direction. With this ansatz, Equation (2.5) degenerates and Equations (2.4) and (2.6) become

$$-\omega^2\widehat{v}_x = (c_j^2 + v_{\mathrm{Aj}}^2)(\widehat{v}_x'' + ik\widehat{v}_z') - v_{\mathrm{Aj}}^2 ik\widehat{v}_z' - v_{\mathrm{Aj}}^2 k^2\widehat{v}_x, \tag{2.10}$$

$$-\omega^2\widehat{v}_z = c_j^2 ik(\widehat{v}_x' + ik\widehat{v}_z). \tag{2.11}$$

These equations can be combined to give an ordinary differential equation for $\widehat{v}_x$, namely

$$\widehat{v}_x'' - m_j^2\widehat{v}_x = 0, \quad \text{where} \quad m_j^2 = \frac{(k^2v_{\mathrm{Aj}}^2 - \omega^2)(k^2c_j^2 - \omega^2)}{(c_j^2 + v_{\mathrm{Aj}}^2)(k^2c_{\mathrm{Tj}}^2 - \omega^2)}. \tag{2.12}$$

This is identical to the corresponding equation governing, for example, a tangential interface or a symmetric slab, derived in Sections 1.3.2.1 and 1.3.2.2 by Roberts (1981*a*) and Edwin and Roberts (1982).

Solutions of Equations (2.12) are a linear combination of hyperbolic functions or trigonometric functions depending on the sign of the non-zero term m_j^2. Given that the trigonometric functions are identical to hyperbolic functions with imaginary sign, we progress from here with hyperbolic functions only, without loss of generality. We restrict our model to waves trapped by the slab by imposing the boundary condition $\widehat{v}_x \to 0$ as $|x| \to \infty$. Thus, the general solution for the velocity perturbation in the x-direction is

$$\widehat{v}_x(x) = \begin{cases} A(\cosh m_1 x + \sinh m_1 x), & \text{if } x < -x_0, \\ B\cosh m_0 x + C\sinh m_0 x, & \text{if } |x| \le x_0, \\ D(\cosh m_2 x - \sinh m_2 x), & \text{if } x > x_0, \end{cases} \tag{2.13}$$

where A, B, C, and D are arbitrary constants (with respect to x). The remaining boundary conditions are continuity of velocity and total pressure across the slab boundaries at $x = \pm x_0$.

With the aim of finding an expression for the total pressure perturbation, the Equations (1.22) and (1.24) can be combined to give

$$\frac{\partial p}{\partial t} = -\rho_j c_i^2 \nabla\cdot\mathbf{v}. \tag{2.14}$$

Using the above equation and the z-component of Equation (1.25), the perturbation in total pressure (plasma pressure, p, plus magnetic pressure, $B_j B_z/\mu$) across the whole domain has amplitude

$$\widehat{p}_T(x) = \frac{\Lambda_j}{m_j}\widehat{v}_x'(x), \tag{2.15}$$

where

$$\Lambda_j = \frac{i\rho_j(\omega^2 - \omega_{Aj}^2)}{m_j\omega}, \quad \text{for} \quad j = 0, 1, 2. \tag{2.16}$$

Ensuring continuity of velocity and total pressure across the slab boundaries gives four coupled algebraic equations, namely

$$\begin{pmatrix} c_1 - s_1 & -c_0 & s_0 & 0 \\ 0 & c_0 & s_0 & s_2 - c_2 \\ \Lambda_1(c_1 - s_1) & \Lambda_0 s_0 & -\Lambda_0 c_0 & 0 \\ 0 & \Lambda_0 s_0 & \Lambda_0 c_0 & -\Lambda_2(s_2 - c_2) \end{pmatrix} \begin{pmatrix} A \\ B \\ C \\ D \end{pmatrix} = \begin{pmatrix} 0 \\ 0 \\ 0 \\ 0 \end{pmatrix}, \tag{2.17}$$

where $c_j = \cosh m_j x_0$ and $s_j = \sinh m_j x_0$ for $j = 0, 1, 2$, for brevity. The condition for the existence of non-trivial solutions to this system of equations is that the determinant of the matrix is zero. Applying this condition gives us the dispersion relation for an asymmetric slab, namely

$$(\Lambda_0^2 + \Lambda_1\Lambda_2) + \Lambda_0(\Lambda_1 + \Lambda_2)\coth 2m_0x_0 = 0. \tag{2.18}$$

By expanding each Λ_j, we can write this dispersion relation in familiar variables as

$$\begin{aligned} &m_0^2(\omega^2 - \omega_{A1}^2)(\omega^2 - \omega_{A2}^2) + \frac{\rho_0}{\rho_1}m_1\frac{\rho_0}{\rho_2}m_2(\omega^2 - \omega_{A0}^2)^2 \\ &+ m_0(\omega^2 - \omega_{A0}^2)\left[\frac{\rho_0}{\rho_1}m_1(\omega^2 - \omega_{A2}^2) + \frac{\rho_0}{\rho_2}m_2(\omega^2 - \omega_{A1}^2)\right]\coth 2m_0x_0 = 0. \end{aligned} \tag{2.19}$$

2.2.2.2 First-order asymmetric slab

There is a key qualitative difference between waves propagating along symmetric and asymmetric magnetic slabs. The dispersion relation governing an asymmetric slab is a single equation, whereas the dispersion relation governing a symmetric slab (Roberts, 1981*a*) consists of two independent equations, corresponding to the sausage and kink eigenmodes. This corresponds to mixed properties of the asymmetric eigenmodes.

Under the approximation that the densities and temperatures of the external plasma are approximately the same, the dispersion relation, Equation (2.19), can be factorised to give the approximate dispersion relation

$$[\Lambda_0(\Lambda_1+\Lambda_2)+2\Lambda_1\Lambda_2\tanh m_0x_0]\,[\Lambda_0(\Lambda_1+\Lambda_2)+2\Lambda_1\Lambda_2\coth m_0x_0]=0. \tag{2.20}$$

To show this, define each bracket as the functions

$$D_s(\omega) := \Lambda_0(\Lambda_1+\Lambda_2)+2\Lambda_1\Lambda_2\tanh m_0x_0, \tag{2.21}$$

$$D_k(\omega) := \Lambda_0(\Lambda_1+\Lambda_2)+2\Lambda_1\Lambda_2\coth m_0x_0. \tag{2.22}$$

Their product is

$$\begin{aligned} D_s(\omega)D_k(\omega) =& [\Lambda_0(\Lambda_1+\Lambda_2)+2\Lambda_1\Lambda_2\tanh m_0x_0] \\ & [\Lambda_0(\Lambda_1+\Lambda_2)+2\Lambda_1\Lambda_2\coth m_0x_0] \\ =&\Lambda_0^2(\Lambda_1+\Lambda_2)^2+2\Lambda_0(\Lambda_1+\Lambda_2)\Lambda_1\Lambda_2(\tanh m_0x_0+\coth m_0x_0) \\ & +4\Lambda_1^2\Lambda_2^2 \\ =&4\Lambda_1\Lambda_2\left[(\Lambda_0^2F+\Lambda_1\Lambda_2)+\Lambda_0(\Lambda_1+\Lambda_2)\coth(2m_0x_0)\right], \end{aligned} \tag{2.23}$$

where

$$F=\frac{(\Lambda_1+\Lambda_2)^2}{4\Lambda_1\Lambda_2}. \tag{2.24}$$

When the plasma parameters on each side of the slab are approximately equal, *i.e.* $\Lambda_2=\Lambda_1(1+\epsilon L)$, with $\epsilon\ll 1$ and $L\approx 1$, F becomes

$$F=\frac{(2+\epsilon L)^2}{4(1+\epsilon L)}=1+\mathcal{O}(\epsilon^2). \tag{2.25}$$

Therefore,

$$(\Lambda_0^2+\Lambda_1\Lambda_2)+\Lambda_0(\Lambda_1+\Lambda_2)\coth(2m_0x_0)=\frac{1}{4\Lambda_1\Lambda_2}D_s(\omega)D_k(\omega)+\mathcal{O}(\epsilon^2). \tag{2.26}$$

Therefore, to linear order of waveguide asymmetry, if the dispersion relation, Equation (2.18) is satisfied, then either $D_s(\omega)=0$ or $D_k(\omega)=0$, which completes the proof of Equation (2.20).

The expressions for the variables Λ_i for $i=0,1,2$ in Equations (2.16) can be employed to yield the approximately symmetric dispersion relation

$$(\omega^2-\omega_{A0}^2)\left(\frac{\rho_0}{\rho_1}\frac{m_1}{(\omega^2-\omega_{A1}^2)}+\frac{\rho_0}{\rho_2}\frac{m_2}{(\omega^2-\omega_{A2}^2)}\right)+2m_0\begin{pmatrix}\tanh\\ \coth\end{pmatrix}(m_0x_0)=0. \tag{2.27}$$

This equation is now in a form similar to the dispersion relation corresponding to MHD waves along a symmetric magnetic slab,

$$\rho_i m_e(\omega^2-\omega_{\mathrm{Ai}}^2)+\rho_e m_i(\omega^2-\omega_{\mathrm{Ae}}^2)\begin{pmatrix}\tanh\\ \coth\end{pmatrix}(m_ix_0)=0, \tag{2.28}$$

where internal and external parameters are denoted by subscripts i and e.

2.2.3 Asymmetric eigenmodes

There is a rich spectrum of MHD eigenmodes on an asymmetric magnetic slab. The key distinctions of these modes from the eigenmodes of a symmetric slab are discussed in this subsection. To aid the reader's understanding, we have created over a hundred three-dimensional animations of symmetric and asymmetric eigenmodes in a magnetic slab, available at Allcock and Erdélyi (2018*a*). The videos visualise the oscillations in the slab boundaries, magnetic field, density, and velocity field. The eigenmodes in visualised are:

- Alfvén modes:
  - Oscillating on a single magnetic isosurface.
  - Oscillating on multiple magnetic isosurfaces.
- Symmetric slab:
  - Fast and slow, sausage and kink surface modes.
  - Fast and slow, 1st, 2nd, and 3rd order sausage and kink body modes.
- Asymmetric slab:
  - Fast and slow, sausage and kink surface modes.
  - Fast and slow, 1st, 2nd, and 3rd order sausage and kink body modes.

That is 33 different eigenmodes visualised with 12 different camera angles and a corresponding dispersion diagram.

The dispersion relation for a symmetric slab, Equation (2.28), consists of two decoupled equations that correspond to the two types of eigenmodes supported by the slab: the *sausage* and *kink* MHD waves. In an asymmetric slab, the sausage and kink modes are modified by the external density difference, causing an asymmetry of the oscillation amplitude on each side of the slab (for visualisation see Figures 2.2a and 2.2b). We call these asymmetric *quasi-sausage* and *quasi-kink* eigenmodes. In a symmetric slab, sausage modes are characterised by an undisplaced slab axis in the centre of the slab. In an asymmetric slab, this undisplaced position is shifted towards the side of greatest external density for quasi-kink modes and towards the side of lowest external density for quasi-sausage modes. For symmetric kink modes, the width of the perturbed slab remains constant along the slab, but this characteristic is lost in an asymmetric slab. This highlights the mixed nature of these modes.

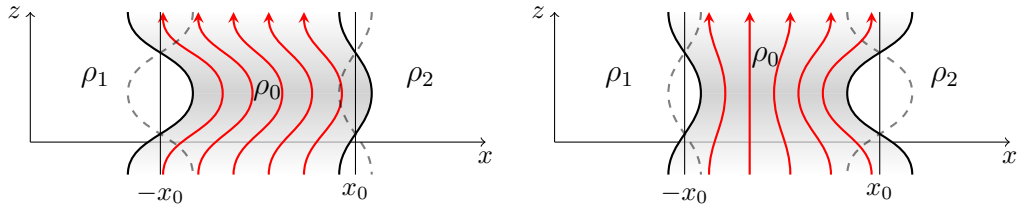

(a) Quasi-kink (b) Quasi-sausage

Figure 2.2: Quasi-kink and quasi-sausage modes with external density ordering $\rho_1 > \rho_2$. The red arrows illustrate the perturbed magnetic field, the thick solid black lines illustrate the perturbed slab boundaries, and the dashed lines illustrate the future position of the slab boundaries after half a period.

Additionally, this shows that it is the phase of the boundary oscillations that is a more fundamental distinguishing characteristic of sausage and kink modes. For this reason, when we refer to *quasi-sausage* and *quasi-kink* modes of an asymmetric slab, we refer strictly to modes which oscillate the waveguide boundaries in *anti-phase* and *in-phase*, respectively.

A key characteristic of kink modes of a symmetric waveguide (slab or tube) is that they are, to a first approximation when the wavelength is much longer than the waveguide is wide, incompressible (Goossens et al., 2009). That is, the density perturbations are small compared to the perturbations in other parameters, such as velocity and magnetic field strength[3]. This is largely a result of the waveguide's cross-sectional width remaining constant throughout the oscillation. However, quasi-kink modes do not preserve the cross-sectional width. Therefore, they are, in general, compressible. The compressibility of a kink-like eigenmode is a similar result to Verwichte et al. (2006*a*), who showed that the kink mode of a curved slab waveguide does not preserve cross-sectional width and is therefore compressible.

The differences between symmetric and asymmetric eigenmodes are summarised in Table 2.1.

Sausage and kink modes are further categorised into *surface* and *body* modes. Surface modes are waves more enhanced at the slab boundaries, whereas body waves are characterised by oscillations permeating spatially throughout the slab, having their maximum amplitude within the slab. Mathematically, surface waves correspond to exponential solutions of Equation (2.13) within the slab. This occurs when $m_0^2 > 0$, which occurs when the phase speed,

[3]This is why transverse kink modes of symmetric waveguides are also described as *Alfvénic*.

ω/k, satisfies

$$\frac{\omega}{k} < c_{\mathrm{T}} \quad \text{or} \quad \min\{c_0, v_{\mathrm{A}}\} < \frac{\omega}{k} < \max\{c_0, v_{\mathrm{A}}\}. \tag{2.29}$$

Body waves correspond to trigonometric solutions of Equation (2.13) within the slab. Most notably, this means that there can be any number of nodes within the slab where the plasma is unperturbed, so that there exist an infinite set of body eigenmodes. They exist when $m_0^2 < 0$, which occurs when

$$c_{\mathrm{T}} < \frac{\omega}{k} < \min\{c_0, v_{\mathrm{A}}\} \quad \text{or} \quad \max\{c_0, v_{\mathrm{A}}\} < \frac{\omega}{k}. \tag{2.30}$$

For a surface mode (Figures 2.3a and 2.3b), the wave power distribution across the slab has a single minimum. The displacement of this minimum from the centre of the slab is a consequence of the asymmetry in the external plasma. The intensity of the maximum amplitudes on the left and right boundaries of the slab is different, reflecting the asymmetry in the external plasma.

Body modes are also affected by the asymmetric external environment (Figures 2.3c and 2.3d). Local maxima and minima in wave power are shifted towards the external plasma of higher density for a quasi-kink body mode and towards the external plasma of lower density for a quasi-sausage mode. However, this is a much weaker effect than for surface modes because the eigenfrequencies of body waves do not depend strongly on the parameters of the external plasma, and therefore they do not depend strongly on the asymmetry of the waveguide, as shown in Sections 2.3.1 and 2.3.2. The same can be said for the eigenfunctions of body modes. These results agree with the intuition that because the majority of the wave power is confined to within the slab, rather than its boundaries, the body modes don't *feel* the external plasma as much as surface waves do.

Mode type	Boundary oscillations	Constant width	Axis displacement	Unperturbed position	Approximately incompressible
Symmetric sausage	Anti-phase	No	No	Centre	No
Quasi-sausage	Anti-phase	No	Yes	Shifted	No
Symmetric kink	In-phase	Yes	Yes	-	Yes
Quasi-kink	In-phase	No	Yes	-	No

Table 2.1: The qualitative differences between symmetric and asymmetric surface modes.

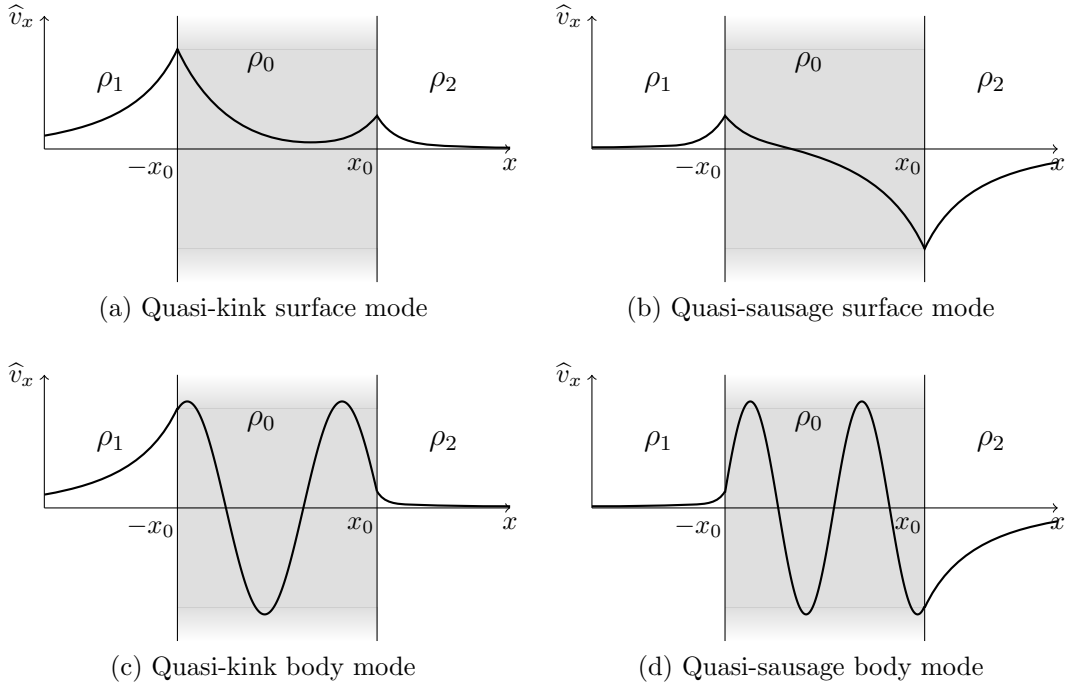

(a) Quasi-kink surface mode

(b) Quasi-sausage surface mode

(c) Quasi-kink body mode

(d) Quasi-sausage body mode

Figure 2.3: The transverse velocity perturbation amplitude, $\widehat{v}_x$ as a function of the transverse spatial coordinate, x, for quasi-sausage and quasi-kink modes in an isolated magnetic slab with external density ordering $\rho_1 > \rho_2$. The vertical black lines illustrate the boundaries (at $\pm x_0$) of the slab (shaded region).

2.3 Asymmetric slab in a non-magnetic environment

Much of the interesting physics due to waveguide asymmetry is exhibited by a magnetic slab with non-magnetic external plasma.

By letting $B_1 = B_2 = 0$, the plasma in the asymmetric external regions is non-magnetic. Then the dispersion relation, Equation (2.19), simplifies to

$$m_0^2\omega^4 + \frac{\rho_0}{\rho_1}m_1\frac{\rho_0}{\rho_2}m_2(\omega^2-\omega_{\mathrm{A0}}^2)^2 + m_0\omega^2(\omega^2-\omega_{A0}^2)\left(\frac{\rho_0}{\rho_1}m_1+\frac{\rho_0}{\rho_2}m_2\right)\coth 2m_0x_0 = 0, \tag{2.31}$$

and the dispersion relation for a slab with first order asymmetry simplifies to

$$(\omega^2-\omega_{\mathrm{A0}}^2)\left(\frac{\rho_0}{\rho_1}m_1+\frac{\rho_0}{\rho_2}m_2\right)+2\omega^2m_0\begin{pmatrix}\tanh\\ \coth\end{pmatrix}(m_0x_0)=0. \tag{2.32}$$

2.3.1 Analytical solutions

Analytical solutions to the dispersion relation can only be made under further assumptions about the plasma. In this section, incompressible (Sec-

tion 2.3.1.2), zero-beta (Section 2.3.1.3), thin slab (Section 2.3.1.4), and wide slab (Section 2.3.1.5) approximations are explored. First, we deal with spurious solutions in Section 2.3.1.1.

2.3.1.1 Spurious solutions

There are three sets of spurious roots to the dispersion relation given by $\omega = \pm k v_{A0}$, $\omega = \pm k c_0$, and $\omega = \pm k c_{T0}$. To treat these cases we refer back to the ODE for $\widehat{v}_x(x)$ within the slab, Equation (2.12).

When $\omega = \pm k c_{T0}$, m_0 is singular, in which case the solution to Equation (2.12) is $\widehat{v}_x(x) = 0$ within the slab. From Equation(2.11), it follows that $\widehat{v}_z \propto \widehat{v}_x'$, we therefore also have $\widehat{v}_z(x) = 0$. Given that we are assuming ideal plasma so that the magnetic flux is frozen to the plasma, this means that there is no magnetic field perturbation either. Therefore, $\omega = \pm k c_{T0}$ is a spurious solution.

When $\omega = \pm k c_0$, we have $m_0 = 0$, therefore Equation (2.12) has general solution $\widehat{v}_x(x) = Bx + C$ for constants B and C. Equation (2.11) further shows that $\widehat{v}_x' = 0$. Therefore, $B = 0$ and $\widehat{v}_x(x) = C$. The z-component of Equation (1.25) tells us that $\widehat{b}_z \propto \widehat{v}_x'$ and so $\widehat{b}_z = 0$, therefore the magnetic pressure perturbation is zero. It can be shown that the plasma pressure is

$$\widehat{p}(x) = -\frac{i\rho_0 c_0^2}{\omega}\left[\frac{Cx(k^2 v_A^2 - \omega^2)}{c_0^2} + C_2\right], \tag{2.33}$$

within the slab, for constant C_2. To balance total pressure over each interface we must have $C = 0$. This means that $v_x(x) = 0$ within the slab and therefore across the whole domain. Therefore the pressure outside the slab is zero (since it is proportional to $\widehat{v}_x' = 0$), and by matching pressure, it is zero within the slab. Therefore this solution is the trivial solution rather than a wave.

On the other hand, when $\omega = k v_A$, the total pressure amplitude, $\widehat{P}(x)$, is such that

$$\widehat{P}(x) = \widehat{v}_x'(x)\begin{cases}\Lambda_1/m_1, & \text{if } x < -x_0,\\ \Lambda_0/m_0, & \text{if } |x| \le x_0,\\ \Lambda_2/m_2, & \text{if } x > x_0,\end{cases} \tag{2.34}$$

where

$$\Lambda_0 = -\frac{i\rho_0(k^2 v_A^2 - \omega^2)}{m_0\omega}, \quad \Lambda_1 = \frac{i\rho_1\omega}{m_1}, \quad \text{and} \quad \Lambda_2 = \frac{i\rho_2\omega}{m_2}. \tag{2.35}$$

(the derivation for this still holds). Note that the singularity due to the division by m_0^2 is regularised by the factor of $k^2 v_A^2 - \omega^2$ in Λ_0. Therefore, since $\widehat{v}_x' = B$ is constant in the slab, then so is $\widehat{P}$. When we match the total pressure over

the boundaries we find that the slab must be symmetric. Therefore $B = 0$ to ensure that the velocity profile is symmetric. Therefore $\widehat{v}'_x = B = 0$, so there is no pressure perturbation. In particular, there is no pressure perturbation outside the slab, which implies that there is no velocity perturbation outside the slab, because they both depend on the same constants. Therefore by continuity of velocity and the fact that it is constant within the slab, the velocity perturbation is zero everywhere. Therefore there is no wave.

2.3.1.2 Limiting case - incompressible

Compressibility is essential for the propagation of sound waves. Consider the dispersion relation, Equation (2.31), in the limit of incompressibility, that is, when $\gamma \to \infty$. In this limit, the sound speeds become unbounded and the tube speed in the slab behaves like $c_{T0} \to v_{A0}$. This means that $m_j \to k$ for $j = 0, 1, 2$, so that the dispersion relation reduces to

$$\omega^4 + \frac{\rho_0^2}{\rho_1\rho_2}(\omega^2 - \omega_{A0}^2)^2 + \omega^2(\omega^2 - \omega_{A0}^2)\left(\frac{\rho_0}{\rho_1} + \frac{\rho_0}{\rho_2}\right)\coth 2kx_0 = 0. \tag{2.36}$$

This is a special case of a dispersion relation previously derived by Ruderman (1992), who found solitons propagating on a system of N tangential discontinuities. Equation (2.36) is a quadratic equation in ω^2 which has solutions

$$\omega^2 = k^2 v_{A0}^2 \left[\frac{2 + \sigma \pm \sqrt{\sigma^2 - 4\frac{\rho_1\rho_2}{\rho_0^2}}}{2\left(1 + \sigma + \frac{\rho_1\rho_2}{\rho_0^2}\right)}\right], \tag{2.37}$$

where

$$\sigma = \left(\frac{\rho_1}{\rho_0} + \frac{\rho_2}{\rho_0}\right)\coth 2kx_0. \tag{2.38}$$

These solutions hold for all $kx_0 > 0$ and describe surface modes with sub-Alfvénic phase speed. The solution found by the plus (minus) on the numerator is the sausage (kink) eigenfrequency. Since $\coth\theta > 1$ for all positive θ, and therefore $\sigma^2 - 4\rho_1\rho_2/\rho_0^2 > 0$, these eigenfrequencies are real, as we would expect from spectral theory.

Figures 2.4a-2.4d illustrate that in a thin ($kx_0 \ll 1$) incompressible slab, the phase speeds of these modes approach zero or the Alfvén speed. In a symmetric wide incompressible slab, the phase speeds converge to the same speed (Figure 2.4a), whereas in an asymmetric slab, the phase speeds converge to different speeds (Figures 2.4b-2.4d) that depend upon the values of the external densities. This observation is mirrored by both fast and slow surface

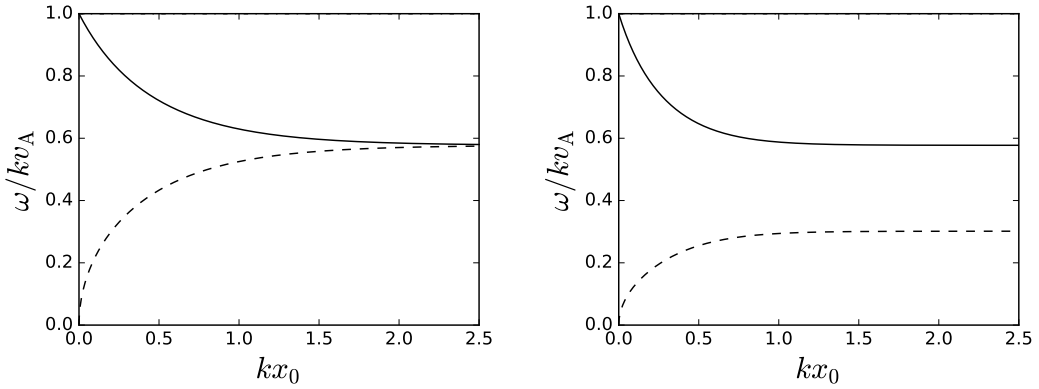

(a) $\rho_1/\rho_0 = 2$, $\rho_2/\rho_0 = 2$

(b) $\rho_1/\rho_0 = 10$, $\rho_2/\rho_0 = 2$

(c) $\rho_1/\rho_0 = 10$, $\rho_2/\rho_0 = 0.1$

(d) $\rho_1/\rho_0 = 100$, $\rho_2/\rho_0 = 0.1$

Figure 2.4: The behaviour of the modes in an incompressible slab. The fast surface modes and all the body modes degenerate leaving two sub-Alfvénic surface modes. (a) A symmetric slab, (b)-(d) asymmetric slabs.

modes in the more general solutions of a compressible slab solved numerically to give Figure 2.8a.

One might ask whether the notion of incompressible asymmetric modes is coherent given that the cross-sectional width variation appears to be associated with density perturbation. It is true that incompressible quasi-sausage and quasi-kink modes do not preserve cross-sectional width, however, they do this in a way that does not perturb density. This is achieved by virtue of a significant longitudinal velocity component. The longitudinal velocity allows plasma to flow from sections of the waveguide that have been narrowed by the wave to widened sections.

2.3.1.3 Limiting case - low-beta

The case when the magnetic pressure strongly dominates the gas pressure within the slab, *i.e.* $\beta := 2\mu_0 p_0/B_0^2 \ll 1$, is known as the *low-beta approximation*. This approximation is equivalent to the Alfvén speed dominating the sound speed in the slab and provides a good approximation of the solar coronal environment. In this section, the results are to quadratic order in β.

Under this speed ordering, $m_0^2 \approx k^2 - \omega^2/v_\mathrm{A}^2$. After a numerical investigation, it is clear that the frequency of waves in this approximation satisfies $\omega^2 \ll k^2 v_\mathrm{A}^2$, in which case $m_0^2 \approx k^2$ provides a valid approximation. This means that $m_0^2 > 0$ and the solutions are surface modes. For a symmetric slab of low-beta plasma (*e.g.* Roberts 1981*b*), the dispersion relation reduces to a quadratic expression in ω^2 whose solutions are the fast sausage and kink surface modes given by

$$\omega^2 = k^2 c_\mathrm{e}^2 \left(\frac{\sqrt{1 + \gamma^2 \begin{pmatrix} \tanh^2 \\ \coth^2 \end{pmatrix} (kx_0)} - 1}{\frac{1}{2}\gamma^2 \begin{pmatrix} \tanh^2 \\ \coth^2 \end{pmatrix} (kx_0)} \right), \tag{2.39}$$

where c_e is the external sound speed, along with a spurious solution.

Unfortunately, for the more general case of an asymmetric slab of low-beta plasma, the dispersion relation does not reduce to an analytically solvable equation. However, we find numerically that there are two fast surface modes. The quasi-sausage surface mode is not present for small kx_0, but becomes a solution at an intermediate value of kx_0 with phase speed $\omega^2/k^2 = \min(c_1^2, c_2^2)$. The quasi-kink surface mode is present for all values of kx_0. Qualitatively, the solutions for a low-beta plasma are analogous to the fast quasi-sausage and quasi-kink mode solutions, discussed later in Sections 2.3.1.4 and 2.3.1.5.

2.3.1.4 Limiting case - thin slab

Consider the case where the wavelength, λ, is much greater than the width of the slab, $2x_0$, *i.e* $2x_0/\lambda = kx_0/\pi \ll 1$, or equivalently $kx_0 \ll 1$.

First, consider the quasi-sausage surface modes, which are governed by the tanh version of Equation (2.32), for $m_0^2 > 0$. In the thin slab limit, this equation reduces to

$$(\omega^2 - \omega_{\mathrm{A}0}^2)\left(\frac{\rho_0}{\rho_1}m_1 + \frac{\rho_0}{\rho_2}m_2\right) - 2\omega^2 m_0^2 x_0 = 0. \tag{2.40}$$

Clearly, $\omega^2 = k^2 v_{\mathrm{A}}^2$ is a solution, but as noted in Section 2.3.1.1, it is spurious. The other solution for ω^2 behaves like $\omega^2 \to k^2 c_{\mathrm{T}0}^2$ as $kx_0 \to 0$. To first order in kx_0, this solution is a slow quasi-sausage surface mode given by

$$\omega^2 = k^2 c_{\mathrm{T}0}^2 \left[1 - \frac{2(kx_0)(c_0^2 - c_{\mathrm{T}0}^2)}{(c_0^2 + v_{\mathrm{A}0}^2)\left(\frac{\rho_0}{\rho_1}\frac{\sqrt{c_1^2 - c_{\mathrm{T}0}^2}}{c_1} + \frac{\rho_0}{\rho_2}\frac{\sqrt{c_2^2 - c_{\mathrm{T}}^2}}{c_2}\right)}\right], \tag{2.41}$$

which is less than $k^2 c_{\mathrm{T}0}^2$ and exists only when $c_1 > c_{\mathrm{T}0}$ and $c_2 > c_{\mathrm{T}0}$.

It is interesting to note that if $c_1 = c_2 = c_{\mathrm{e}}$ (and therefore $\rho_1 = \rho_2 = \rho_{\mathrm{e}}$ by Equation (2.3)), then there exists a second solution to Equation (2.40). By letting $\omega^2 = k^2 c_{\mathrm{e}}^2(1 + \nu)$ for some $\nu \ll 1$ in Equation (2.40), we find the solution to be

$$\omega^2 = k^2 c_{\mathrm{e}}^2 \left(1 - \left[\frac{\rho_{\mathrm{e}}}{\rho_0}\frac{c_{\mathrm{e}}^2(c_0^2 - c_{\mathrm{e}}^2)(kx_0)}{(c_0^2 + v_{\mathrm{A}0}^2)(c_{\mathrm{T}0}^2 - c_{\mathrm{e}}^2)}\right]^2\right) \tag{2.42}$$

in the thin slab limit. This is a fast sausage surface mode, and it degenerates (as a solution in the thin slab limit) as c_1 and c_2 become distinct. This mode can still exist with a phase speed below the cut-off at $\min(c_1, c_2)$ (see Section 2.3.2.2).

Next, consider quasi-kink surface mode solutions in the thin slab limit, which are governed by the coth version of Equation (2.32), for $m_0^2 > 0$. As $kx_0 \to 0$, we have $m_0 x_0 \to 0$, so $\coth m_0 x_0 \to 1/m_0 x_0$. This simplifies the dispersion relation to

$$\omega^2 = \frac{k^2 x_0 v_{\mathrm{A}0}^2\left(\frac{\rho_0}{\rho_1}m_1 + \frac{\rho_0}{\rho_2}m_2\right)}{\left(\frac{\rho_0}{\rho_1}m_1 x_0 + \frac{\rho_0}{\rho_2}m_2 x_0\right) + 2} \approx \frac{1}{2}k^2 v_{\mathrm{A}0}^2\left(\frac{\rho_0}{\rho_1} + \frac{\rho_0}{\rho_2}\right)kx_0. \tag{2.43}$$

This is a slow quasi-kink surface mode that behaves like $\omega/k \to 0$ in the thin slab limit.

For body waves in the thin slab approximation, following the same procedure as for surface waves turns out to be fruitless, so we must reconsider our assumptions. Unfortunately, letting $m_0 x_0 \to 0$ as $kx_0 \to 0$, whilst valid for surface modes, is not valid for body modes. Instead, we must consider the scenario where $m_0 x_0$ remains finite as $kx_0 \to 0$. This can occur only if $|m_0^2| \to \infty$ as $kx_0 \to 0$. To ensure that $|m_0^2| \to \infty$, we are restricted to solutions that behave like $\omega^2 \to k^2 c_{\mathrm{T}0}^2$ as $kx_0 \to 0$. Considering Equation (2.32), this can only be the case when $m_0^2 < 0$, *i.e.* only for body modes. To find these solutions, set $\omega^2 = k^2 c_{\mathrm{T}0}^2 (1 + \nu (kx_0)^2)$ for some $\nu > 0$ that is to be determined. To see why this form has been chosen, a substitution into the definition of m_0^2 demonstrates that $|m_0^2| \to \infty$ and $m_0 x_0$ remains bounded as $kx_0 \to 0$, as required. Using this ansatz, Equation (2.27) has a countably infinite set of quasi-sausage body solutions which, in the thin slab limit, behave like

$$\omega^2 = k^2 c_{\mathrm{T}0}^2 \left[1 + \frac{c_{\mathrm{T}0}^4 (kx_0)^2}{c_0^2 v_{\mathrm{A}0}^2 \pi^2 j^2} \right], \quad \text{for} \quad j = 1, 2, \ldots . \tag{2.44}$$

There are also quasi-kink body solutions that, in the thin slab limit, behave like

$$\omega^2 = k^2 c_{\mathrm{T}0}^2 \left[1 + \frac{c_{\mathrm{T}0}^4 (kx_0)^2}{c_0^2 v_{\mathrm{A}0}^2 \pi^2 (j - \frac{1}{2})^2} \right], \quad \text{for} \quad j = 1, 2, \ldots . \tag{2.45}$$

Equations (2.44) and (2.45) show us that to quadratic order in kx_0 the quasi-sausage and quasi-kink body modes do not depend on the external environment parameters. The effects of external density and temperature are felt in the higher order terms, which explains why Equations (2.44) and (2.44) are identical to the corresponding solutions in a thin symmetric slab derived by Roberts 1981*b*. This also explains theoretically why body modes only weakly depend on the asymmetry of the external plasma, as discussed in the context of solar atmospheric magnetic field diagnostics in Chapter 5.

2.3.1.5 Limiting case - wide slab

The wide slab approximation the limit of the slab width being is much larger than the wavelength, *i.e.* when $kx_0 \gg 1$. To understand the properties of the eigenfrequencies in a wide asymmetric slab, it is instructive to return to the dispersion relation in lambda notation, Equation (2.18). For surface modes in the slab, the wide slab approximation implies that $m_0 x_0 \gg 1$, therefore $\coth m_0 x_0 \approx 1$ (this is verified *a posteriori* by Roberts, 1981*b*). Under this approximation, Equation (2.18), becomes

$$(\Lambda_0 + \Lambda_1)(\Lambda_0 + \Lambda_2) = 0, \tag{2.46}$$

which gives us two families of solutions, one satisfying $\Lambda_0 + \Lambda_1 = 0$ and the other satisfying $\Lambda_0 + \Lambda_2 = 0$. These are equivalent to

$$\rho_0 m_j(\omega^2 - \omega_{\rm A0}^2) + \rho_j m_0 \omega^2 = 0, \tag{2.47}$$

for $j = 1, 2$, respectively. This equation is the same as the dispersion relation governing surface waves along a single interface between a magnetized and a non-magnetized plasma, Equation(1.36) for $v_{A1} = v_{A2} = 0$. Hence, the surface mode solutions of a wide asymmetric slab are precisely those that propagate along each interface independently. This corroborates our intuition that, as the slab width increases, the interfaces have diminishing influence on each other. In the wide slab limit, the interfaces have no influence on each other at all, allowing each to oscillate independently with its own characteristic frequency.

Unfortunately, the body waves have no parallel in the single interface model because body waves in a slab owe their existence to both of the two interfaces. In the wide slab limit, body waves behave like $\omega^2 \to k^2 c_0^2$ as $kx_0 \to \infty$. To see this, substitute the ansatz $\omega^2 = k^2 c_0^2 (1 + \nu/(kx_0)^2)$ into the dispersion relation, Equation (2.32), to retrieve the family of quasi-sausage body modes given by

$$\omega^2 = k^2 c_0^2 \left[1 - \frac{\pi^2 (j - \frac{1}{2})^2 c_0^2}{(v_{A0}^2 - c_0^2)(kx_0)^2}\right], \quad j = 1, 2, \ldots \tag{2.48}$$

in the wide slab limit. Similarly, there exist quasi-kink body modes given by

$$\omega^2 = k^2 c_0^2 \left[1 - \frac{\pi^2 j^2 c_0^2}{(v_{A0}^2 - c_0^2)(kx_0)^2}\right], \quad j = 1, 2, \ldots \tag{2.49}$$

in the wide slab limit. These solutions are valid only when $v_{A0} > c_0$.

This analysis may be repeated for $v_{A0} < c_0$ to find that, in the wide slab limit, there exist quasi-sausage body modes given by

$$\omega^2 = k^2 v_{\rm A0}^2 \left[1 - \frac{\pi^2 (j - \frac{1}{2})^2 v_{A0}^2}{(c_0^2 - v_{A0}^2)(kx_0)^2}\right], \quad \text{for} \quad j = 1, 2, \ldots \tag{2.50}$$

and quasi-kink body modes of the form

$$\omega^2 = k^2 v_{A0}^2 \left[1 - \frac{\pi^2 j^2 v_{\rm A0}^2}{(c_0^2 - v_{A0}^2)(kx_0)^2}\right], \quad \text{for} \quad j = 1, 2, \ldots. \tag{2.51}$$

These solutions demonstrate that, to quadratic order in $1/kx_0$, the wide slab body modes are independent of the external plasma parameters. Therefore, Equations (2.48)-(2.51) are identical to the body mode solutions in a wide symmetric slab (Roberts, 1981*b*). Equations (2.41)-(2.45), (2.48) and (2.49) also appear in Li et al. (2013) for a symmetric magnetic slab with shear flow when the shear flow speed is set to zero.

2.3.2 Numerical solutions

Numerical methods are required to investigate solutions to the asymmetric slab dispersion relation, Equation (2.31), without having to rely on further approximations. Focus is placed on the additional physics that arises from the asymmetry of the external plasma.

2.3.2.1 Description of numerical procedure

To solve Equation (2.31) numerically, view the left-hand-side as a function $D(\omega)$ of the wave frequency, ω, and wavenumber k. This function is known as a *dispersion function*. This means that for a given wavenumber value, we are solving a simple root-finding problem, where the aim is to find the zeros of the dispersion function. To accomplish this, we use the *secant method*. The Secant method is a standard root-finding procedure that is equivalent to the Newton-Raphson method utilising a finite difference approximation to the derivative of the dispersion function. This method is chosen because the derivative of the dispersion function is not easily derived analytically. The cost is that the secant method has an order of convergence of the golden ratio, $\psi \approx 1.618$, which is smaller than the order of convergence of the Newton-Raphson method, which is 2.

For a range of values of the non-dimensionalised half slab width, kx_0, we use the secant method to iterate towards the many zeroes of the dispersion function. The algorithm is most unstable for very large and very small values of kx_0 due to the different sheets of the function being very close together (small kx_0) or the solution curves having approximately zero gradient (large kx_0). Therefore, a middle value of kx_0 is first used with a range of initial values. Then, working outwards form the middle, the initial values for the secant method applied to the next values of kx_0 are the roots found from the previous step. This process is continued until zeroes of the dispersion function are found for the whole range of kx_0 values.

2.3.2.2 Dispersion diagrams

Figure 2.5 illustrates the solutions to the dispersion relation, Equation (2.31), for two orderings of the characteristic speeds. Figure 2.5a illustrates the spectrum of modes we would expect to find in the corona and Figure 2.5b illustrates the spectrum of modes we would expect to find in the photosphere.

In both coronal and photospheric conditions, there are slow sausage and kink surface modes (illustrated by the lowest red lines) and an infinite sequence

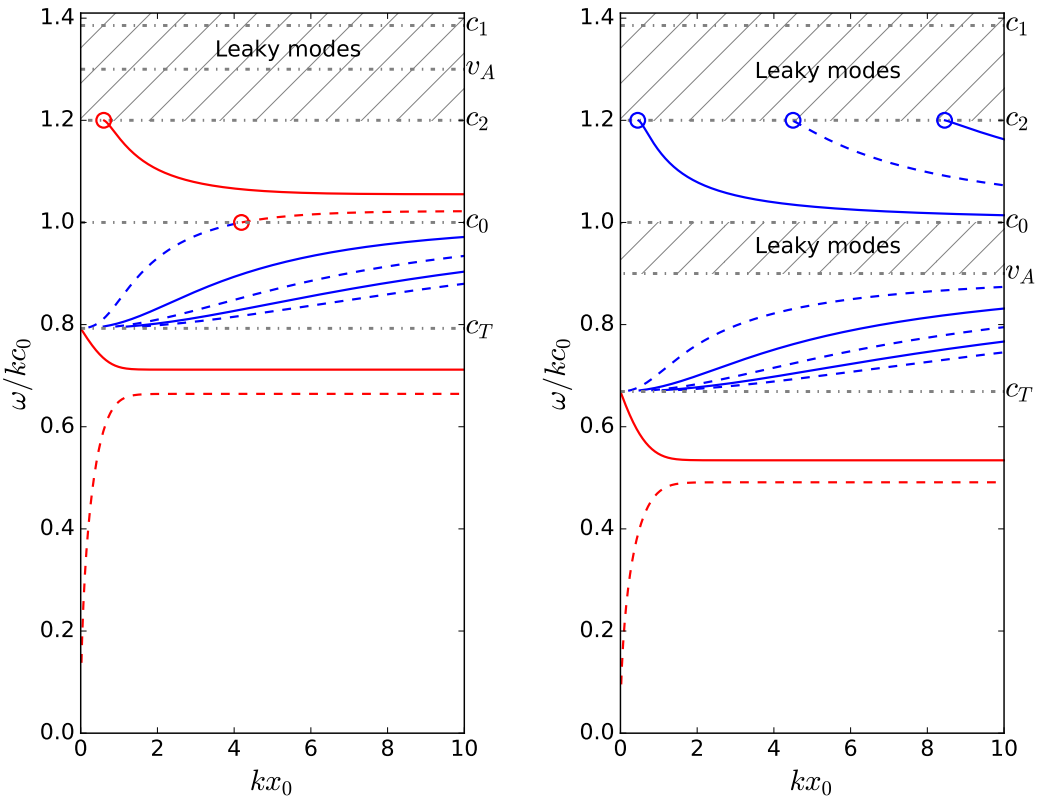

(a) $v_{A0} > c_0$ (b) $v_{A0} < c_0$

Figure 2.5: Dispersion diagram for the dispersion relation, Equation (2.31). The surface (body) modes are in plotted red (blue) and the sausage (kink) modes are represented by solid (dashed) lines. The density ratios are $\rho_1/\rho_0 = 1.5$ and $\rho_2/\rho_0 = 2$, and the characteristic speed orderings are $c_2 = 1.2c_0$ and (a) $v_{A0} = 1.3c_0$ and (b) $v_{A0} = 0.9c_0$.

of slow sausage and kink body modes (illustrated by the slowest blue lines). Each sausage body mode propagates faster than its corresponding kink mode, which agrees with the analytical solutions in Equations (2.44), (2.45), (2.48)-(2.51).

In coronal conditions, there exist fast sausage and kink surface modes with phase speeds between c_0 and $\min c_1, c_2$. Figure 2.5a shows that the minimum of c_1 and c_2 becomes a new cut-off, causing the fast kink surface mode to transform into a slow kink first-order body mode for smaller values of kx_0. In Section 2.3.2.3, the precise value of this critical wavenumber is determined and the eigenfunction is analysed across this transition.

In photospheric conditions, there exists an infinite sequence of fast sausage and kink body modes with phase speeds between c_0 and $\min c_1, c_2$. For values of the slab width below a cut-off value (that is unique for every order of body mode), these modes cease to be trapped by the slab and leak energy into the surrounding plasma. In Section 2.3.2.4, the precise value of these cut-off values is determined.

2.3.2.3 critical wavenumber for kink mode transformation

First, we derive an analytical expression for the critical wavenumber, over which the slow kink first-order body mode transitions into a fast kink surface mode. To do this, let $\omega^2 = k^2 c_0^2(1+\nu)$ for some $\nu \ll 1$. Then we have

$$m_0^2 = -\frac{\nu k^2 c_0^2 (v_A^2 - c_0^2(1+\nu))}{(c_0^2 + v_A^2)(c_T^2 - c_0^2(1+\nu))}, \tag{2.52}$$

which, when terms of quadratic and higher order in ν are neglected, reduces to

$$m_0^2 = \frac{\nu k^2 (v_A^2 - c_0^2)}{c_0^2}, \tag{2.53}$$

and therefore,

$$\tanh(2m_0 x_0) = 2kx_0 \sqrt{\frac{\nu(v_A^2 - c_0^2)}{c_0^2}}. \tag{2.54}$$

Substituting these into the dispersion relation for quasi-kink modes, neglecting terms of quadratic and higher order in ν, and solving for kx_0 gives us the critical value for the 1st fast kink body mode as

$$kx_0 = \frac{c_0^2 \left(\frac{\rho_2}{\rho_0} c_2 \sqrt{c_1^2 - c_0^2} + \frac{\rho_1}{\rho_0} c_1 \sqrt{c_2^2 - c_0^2} \right)}{2(v_A^2 - c_0^2)\sqrt{(c_1^2 - c_0^2)(c_2^2 - c_0^2)}}. \tag{2.55}$$

Across this transitional value, the eigenfunction changes functional form inside the slab from trigonometric to exponential function (see Figure 2.6).

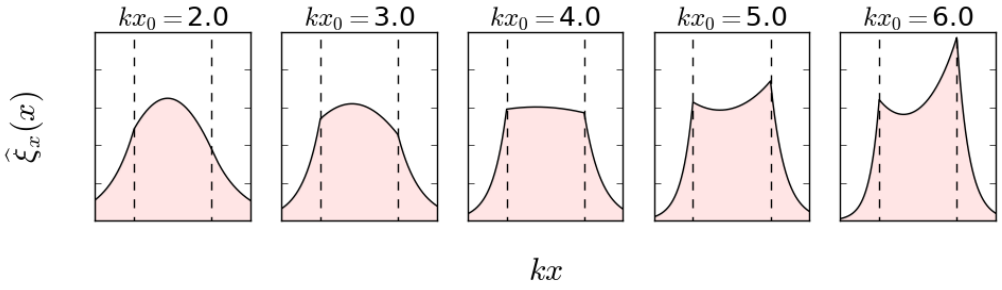

Figure 2.6: The eigenfunction of the transitional kink mode. The critical wavenumber occurs between $kx_0 = 4$ and $kx_0 = 5$.

2.3.2.4 Fast mode cut-off

If $c_1 = c_2$, we have a symmetric slab and therefore no fast mode cut-off. Let $c_1 \neq c_2$ and let $\omega = \min(kc_1, kc_2)$. Without loss of generality, consider the case where $c_1 < c_2$ so that $m_1 = 0$. Therefore,

$$m_0^2 = \frac{k^2(c_0^2 - c_1^2)(v_A^2 - c_1^2)}{(c_0^2 + v_A^2)(c_T^2 - c_1^2)} = k^2 m^2, \quad \text{and} \quad m_2^2 = k^2\left(1 - \frac{c_1^2}{c_2^2}\right). \tag{2.56}$$

Substituting these expressions in the dispersion relation and solving for kx_0 gives the fast mode cut-off values

$$kx_0 = \frac{1}{2m}\tanh^{-1}\left(\frac{1}{mc_1^2}\frac{\rho_0}{\rho_2}\sqrt{1 - \frac{c_1^2}{c_2^2}}(c_1^2 - v_{A0}^2)\right). \tag{2.57}$$

For surface modes, $m_0^2 > 0$, therefore the argument of the $\tanh^{-1}$ term is real, so that Equation (2.57) admits a single solution. This corresponds to the cut-off value for the fast sausage surface mode in Figure 2.5a.

For body modes, $m_0^2 < 0$, therefore the argument of the $\tanh^{-1}$ term is imaginary. Defining $n \in \mathbb{R}$ as $n = im$ and utilising the fact that $\tanh^{-1}(ix) = i\tan^{-1}(x)$, we can rewrite Equation (2.57) as

$$kx_0 = \frac{1}{2n}\left[\tan_p^{-1}\left(\frac{1}{nc_1^2}\frac{\rho_0}{\rho_2}\sqrt{1 - \frac{c_1^2}{c_2^2}}(v_{A0}^2 - c_1^2)\right) + j\pi\right], \tag{2.58}$$

for $j \in \mathbb{Z}$ and $\tan_p^{-1}$ refers to the principal value of the inverse tan function, *i.e.* the value in the range $(-\pi/2, \pi/2)$. This infinite set of solutions corresponds to the infinite set of fast sausage and kink body modes, each of which has a cut-off, as seen in Figure 2.5b.

When the slab is symmetric, the cut-off for both the fast sausage surface mode and the fast sausage first-order body mode are zero. See this by setting

$c_1 = c_2$ in the argument of $\tanh^{-1}$ and $\tan_p^{-1}$ in Equations (2.57) and (2.58), respectively. This means that the modes cease to have a cut-off at all and exist for all values of the slab width, kx_0, which corroborates with the results of Roberts (1981*b*).

2.3.2.5 Varying the degree of asymmetry

First, consider a magnetised slab with symmetric non-magnetic external plasma, as described by Roberts (1981*b*) and summarised in Section 1.3.2.2. Figures 2.7a-2.7c illustrate how varying the ratio of external to internal density affects the propagation speeds of the slow kink and sausage surface modes. An increase in the density ratio, ρ_e/ρ_0, causes a decrease in the propagation speed of the slow modes. The fast surface modes demonstrate an identical behaviour (not shown). The body modes are weakly dependent on the external density, so that the propagation speed decreases only negligibly as the density ratio increases.

More generally, consider an asymmetric slab whose equilibrium conditions are given by Figure 2.1. Figures 2.8a-2.8e illustrate the behaviour of the slow surface modes as the external density on one side of the slab is varied while holding fixed the other external density. The slice where $\rho_1/\rho_0 = 2$ corresponds to a symmetric slab, where the usual behaviour is observed: that the phase speeds of the two slow surface modes converge to a speed that is slower than the tube speed, c_{T0}, as the slab width increases. However, as the external densities become distinct, the phase speeds of these modes no longer converge to the same value in the wide slab limit. This can also be seen in Figures 2.5a and 2.5b.

For a wide slab width, $kx_0 \gg 1$, Figure 2.8e illustrates that the eigenfrequencies of the slow surface modes possess a wave phenomenon known as *avoided crossing*. An avoided crossing occur when the phase speeds of two wave modes avoid intersecting when a parameter of the system is varied. This occurs when there are constraints preventing two solution from being equal and it demonstrates a transferral of properties between the two modes. Analysis of this phenomenon can be used to give insight into the modal structure. There is rich literature regarding avoided crossings for the eigensolutions of a wide range of physical processes including coupled spring oscillations in classical mechanics (Novotny, 2010) and energy level repulsion in quantum physics (Naqvi and Brown, 1972). In MHD wave theory, the subject has been covered only briefly, for example, between fast and slow magneto-acoustic gravity

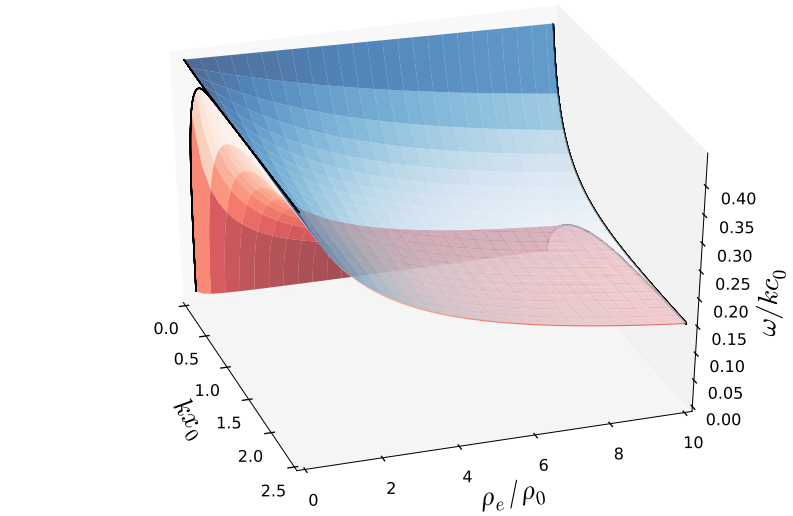

(a)

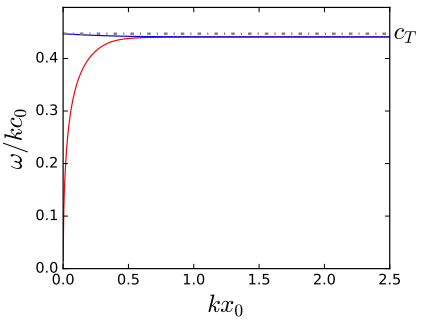

(b) $\frac{\rho_e}{\rho_0} = 0.1$

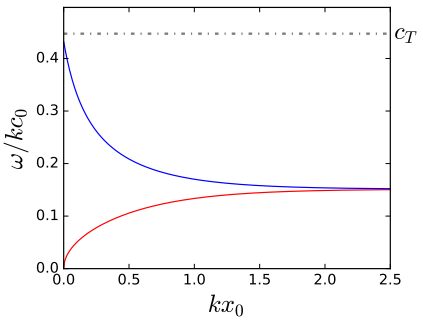

(c) $\frac{\rho_e}{\rho_0} = 10$

Figure 2.7: The effect of varying the ratio, ρ_e/ρ_0, of the slab density to the symmetric external density, on the dispersion of the slow surface modes of a magnetic slab in a symmetric external plasma. The red and blue surfaces correspond to the kink and sausage modes, respectively. Panels (b) and (c) are slices of panel (a) at specific values of ρ_e/ρ_0. These slices are superimposed onto panel (a) as black lines. The characteristic speed orderings are $v_{A0} = 0.5c_0$, $c_e = c_0$.

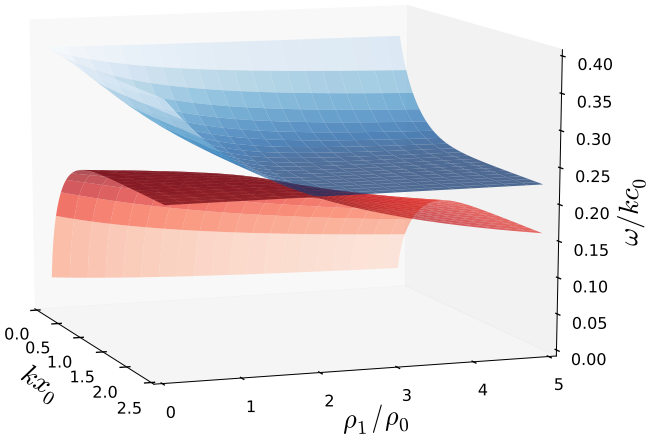

(a)

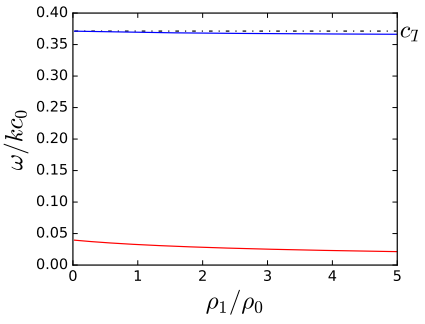

(b) $kx_0 = 0.01$

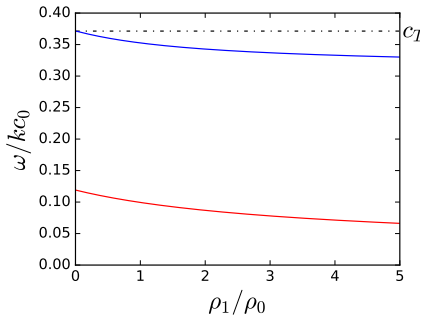

(c) $kx_0 = 0.1$

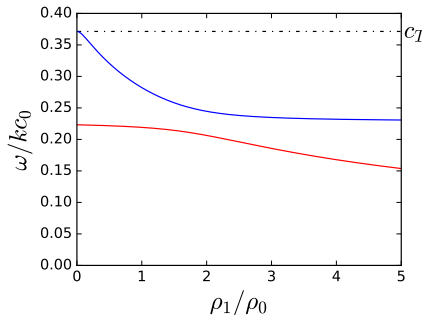

(d) $kx_0 = 1$

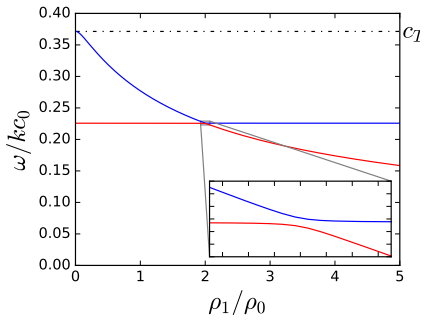

(e) $kx_0 = 3$

Figure 2.8: (a) The slow quasi-sausage (blue) and quasi-kink (red) surface mode solutions of the dispersion relation (Equation (2.19)) are plotted showing the variation of the dispersion as the ratio of one external density to the internal density is changed. The other density ratio is held fixed at $\rho_2/\rho_0 = 2$. The characteristic speed orderings are $c_2 = 0.7c_0$, $v_A = 0.4c_0$, and c_1 varies to satisfy equilibrium pressure balance, given by Equation (2.3). Panels (b)-(e) are slices of panel (a) for specific values of the non-dimensional slab width, kx_0.

waves in a magnetically stratified plasma by Abdelatif (1990) and Mather and Erdélyi (2016).

In the present study, the avoided crossing occurs between quasi-kink and quasi-sausage surface solutions to the asymmetric slab. This explains why the dispersion relation does not decouple into two equations (Section 2.2.2.2). Figure 2.9 demonstrates that during the transition across the avoided crossing, the quasi-sausage and quasi-kink modes exchange the slab boundary upon which the largest perturbation occurs. For example, the left plots of Figure 2.9b show that the quasi-sausage mode has its highest amplitude on the interface of highest local phase-speed (equivalently, lowest external density). The quasi-kink mode demonstrates the opposite behaviour. The central plots show the special case of a symmetric slab, where $\rho_1 = \rho_2$, demonstrating the spatial antisymmetry and symmetry in the symmetric sausage and kink mode, respectively. As the left external density, ρ_1, dominates the right external density, ρ_2, the right plots of Figure 2.9b show that, again, the quasi-sausage mode has its higher amplitude on the interface of higher local phase-speed, but this is now on the other interface. By the term *local phase speed*, we are referring to the phase-speed that a slow surface mode propagating along that interface would have if the other interface were not there. Each interface of an asymmetric magnetic slab has a distinct local phase-speed and they are inversely proportional to the density in the non-magnetic region (Roberts, 1981*a*).

When they exist, the fast quasi-sausage and quasi-kink surface modes demonstrate an identical behaviour (not shown). As demonstrated analytically in Equations (2.44), (2.45) and (2.48)-(2.51), the body modes are not dependent on internal or external densities to quadratic order in kx_0. This means that body modes demonstrate only a weak dependence on the external densities, and an avoided crossing does not occur between these modes.

2.3.3 Analogy to coupled spring and mass oscillator

One particularly interesting characteristic of asymmetric eigenmodes is that the interface which oscillates with the highest amplitude is different for sausage and kink modes. This characteristic changes across the avoided crossing, as shown in Figure (2.9). To investigate this further, we propose an analogy with a coupled mechanical simple harmonic oscillation system[4].

[4]More information on coupled simple harmonic oscillators can be found in Novotny (2010).

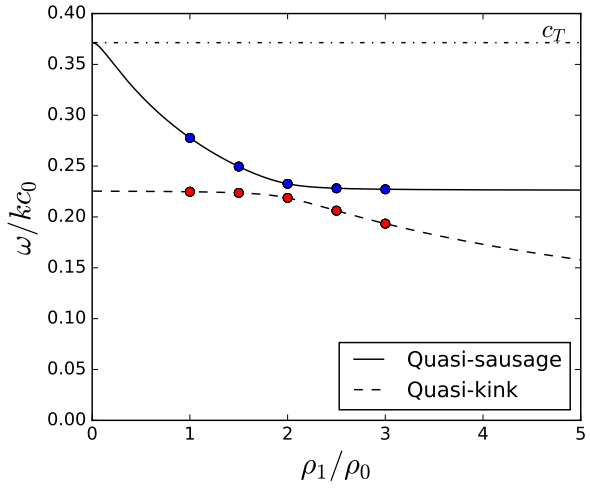

(a)

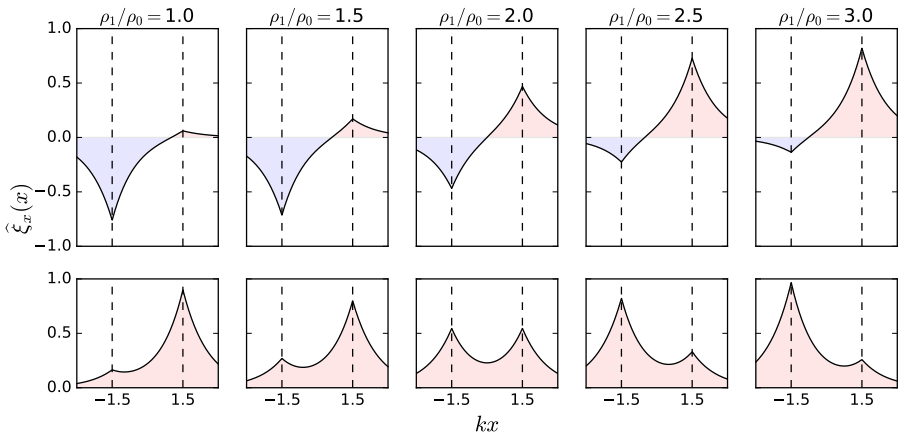

(b)

Figure 2.9: (a) The slow surface mode solutions of the dispersion relation, Equation (2.19), are plotted showing the variation of the dispersion as the ratio of one external density to the internal density is changed. The other density ratio is held fixed at $\rho_2/\rho_0 = 2$ and the non-dimensionalised slab width $kx_0 = 1.5$. The characteristic speed orderings are $c_2 = 0.7c_0$, $v_\mathrm{A} = 0.4c_0$, and c_1 varies to satisfy equilibrium pressure balance, given by Equation (2.3). The parameters at each blue and red dot in panel(a) are used to plot the spatial variation of the transverse displacement perturbation, $\widehat{\xi}_x$, given by panel (b). The upper (lower) plots in panel (b) correspond to the quasi-sausage (quasi-kink) mode solutions.

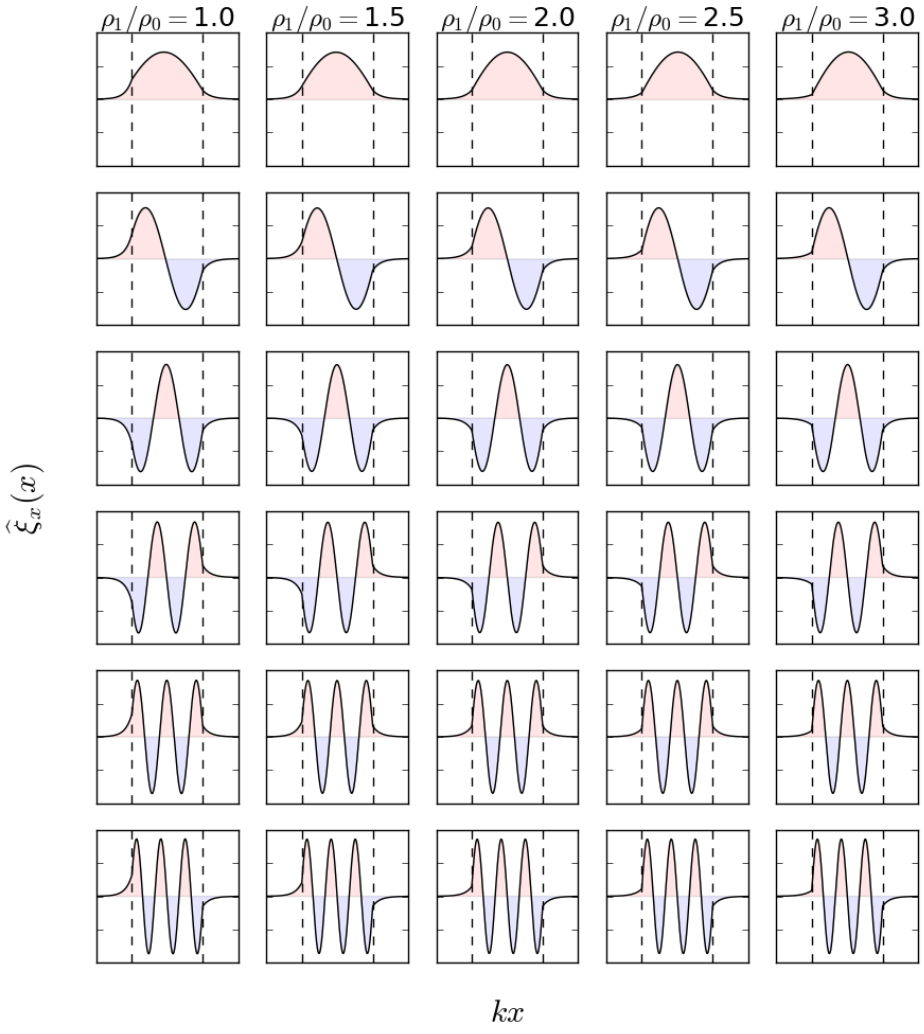

Figure 2.10: The variation (or lack of) of the first three slow sausage and kink body eigenfunctions as the asymmetry in the background plasma is varied. The first, third, and fifth rows are kink modes and the second, fourth, and sixth rows are sausage modes. The density ratio ρ_1/ρ_0 is varied while the other density ratio is held fixed at $\rho_2/\rho_0 = 2.0$. Therefore, the middle column of panels for which $\rho_1/\rho_0 = 2.0$ corresponds to a symmetric slab.

Consider a system of two identical masses of mass m between two fixed walls, with light springs connecting the left wall to the left mass, the masses together, and the right mass to the right wall (Figure 2.11a). The springs have spring constants k_1, k_0, and k_2, respectively. The coordinates x_1 and x_2, which give the displacements of the two masses at time t, uniquely specify the system. Applying Newton's Second Law of Motion gives a coupled system of differential equations

$$m\frac{d^2}{dt^2}\begin{pmatrix}x_1\\x_2\end{pmatrix} = \begin{pmatrix}-k_1-k_0 & k_0\\ k_0 & -k_2-k_0\end{pmatrix}\begin{pmatrix}x_1\\x_2\end{pmatrix}. \tag{2.59}$$

Looking for wave solutions of the form $x_1(t) = \widehat{x}_1 e^{-i\omega t}$, and similar for $x_2(t)$, and defining $\omega_j = k_j/m$ for $j = 0, 1, 2$, gives

$$\begin{pmatrix}\omega_1^2+\omega_0^2-\omega^2 & -\omega_0^2\\ -\omega_0^2 & \omega_2^2+\omega_0^2-\omega^2\end{pmatrix}\begin{pmatrix}\widehat{x}_1\\\widehat{x}_2\end{pmatrix} = \begin{pmatrix}0\\0\end{pmatrix}. \tag{2.60}$$

For non-trivial solutions to exist, the matrix must be singular. For this to occur, its determinant must vanish, *i.e.*

$$(\omega_1^2+\omega_0^2-\omega^2)(\omega_1^2+\omega_0^2-\omega^2)-\omega_0^4 = 0, \tag{2.61}$$

which has solutions

$$\omega_\pm^2 = \frac{1}{2}\left[\omega_2^2-\omega_1^2+2\omega_0^2 \pm \sqrt{(\omega_2^2-\omega_2^2)+\omega_0^4}\right]. \tag{2.62}$$

Thus, there are two eigenfrequences of the system. This is to be expected because the system has two degrees of freedom: the one-dimensional movement of each of the two masses. The eigenfunctions (*i.e.* the values of $\widehat{x}_1$ and $\widehat{x}_2$) associated with these eigenfrequencies are found by substituting the eigenfrequencies back into Equation (2.60). Thus, we find that the ratio of the oscillation amplitudes of each mass is

$$\frac{\widehat{x}_1}{\widehat{x}_2} = -\frac{1}{\omega_0^2}(\omega_2^2+\omega_0^2-\omega_\pm^2) \tag{2.63}$$

$$= -\frac{1}{2W}\left[1 \pm \sqrt{1+4W^2}\right]. \tag{2.64}$$

where $W = \omega_0^2/(\omega_2^2-\omega_1^2)$. Without loss of generality, let $\omega_2 > \omega_1$ so that $W > 0$. Then, considering Equation 2.64, the eigenmode with eigenfrequency ω_+ gives $\widehat{x}_1/\widehat{x}_2 < 0$, *i.e.* the masses oscillate in anti-phase. This is known as the *breathing mode* and is equivalent to the sausage mode of the MHD slab model. The eigenmode with eigenfrequency ω_- gives $\widehat{x}_1/\widehat{x}_2 > 0$, *i.e.* the

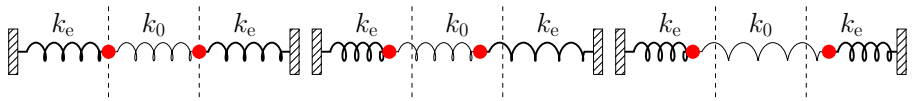

(a) Symmetric equilibrium (b) Symmetric sloshing (c) Symmetric breathing

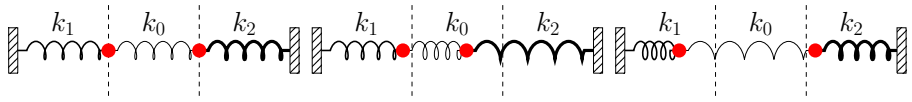

(d) Asymmetric equilibrium (e) Asymmetric sloshing (f) Asymmetric breathing

Figure 2.11: A coupled mechanical oscillator gives an analogy to the eigenmodes of symmetric and asymmetric magnetic slabs. Spring constants are denoted k, with a thicker spring corresponding to a higher spring constant. Figures (a) and (d) show the symmetric and asymmetric spring systems in equilibrium. Figures (b) and (c) show the normal modes of a symmetric system. Figures (e) and (f) show the normal modes of an asymmetric system with spring constants $k_2 > k_1$. In each panel, the vertical dashed lines give the positions of the red masses at equilibrium.

masses oscillate in phase. This is known as the *sloshing mode* and is equivalent to the kink modes of the MHD slab model.

Comparing with the magnetic slab model, the three springs here correspond to the three regions of plasma, and the masses to the plasma interfaces. The breathing mode has highest amplitude on the mass connected to the external spring with lowest spring constant and the sloshing mode has highest amplitude on the mass connected to the external spring with highest spring constant (shown analytically in Appendix A). A higher spring constant in this model is analogous to a lower density plasma in the magnetic slab model. This is because a higher spring constant in an uncoupled spring-mass system gives a higher characteristic frequency. This gives motivation as to why the surface modes of the asymmetric magnetic slab have higher amplitudes on different sides for quasi-sausage and quasi-kink modes.

2.4 Asymmetric slab in a magnetic environment

Now we return to the general model for a magnetic slab, that is, a magnetic slab with asymmetric external environment.

The eigenfrequencies of the magnetic slab with asymmetric external environment are illustrated in Figure 2.12 and are broadly similar to the slab in a non-magnetic environment. The main difference is in the existence of slow

surface and slow body modes for a single set of waveguide parameters. This is true for conditions intermediate between those typical for the corona and photosphere. This can be seen in Figure 2.12b, where there is a family of slow body modes. A deeper analysis of the magnetic slab with asymmetric external environment is given by Zsámberger et al. (2018).

2.4.1 Implications for observations

Accurate mode identification is a key aspect of SMS. Different modes can differ in characteristics such as damping rate, phase and group speed, and, most relevant to this Thesis, response to waveguide asymmetry. Therefore, inaccurate mode identification can lead to significant error in diagnosis of background parameters. This subsection warns observational solar physicists of two possible ways in which errors in mode identification could be made due to waveguide asymmetry.

2.4.1.1 Quasi-symmetric eigenmodes

It is possible for asymmetric MHD waves to have similar observational qualities to symmetric MHD waves. This can occur when the restoring force (that is, the sum of the pressure gradient and Lorentz forces) of MHD perturbations is equal at both interfaces. This can occur in an asymmetric slab when the asymmetry in the pressure gradient force is precisely balanced by the asymmetry in the Lorentz force. We describe an eigenmode with this property as a *quasi-symmetric* mode. Equivalently, we define quasi-symmetric modes to be eigenmodes which have equal amplitude on each boundary of the slab[5]. This is equivalent to setting $\widehat{v}_x(-x_0) = -\widehat{v}_x(x_0)$ for quasi-sausage modes and $\widehat{v}_x(-x_0) = \widehat{v}_x(x_0)$ for quasi-kink modes. The aim in this subsection is to prove that the necessary and sufficient condition for the existence of quasi-symmetric eigenmodes of an asymmetric magnetic slab is

$$\frac{\rho_1}{m_1}(k^2 v_{A1}^2 - \omega^2) = \frac{\rho_2}{m_2}(k^2 v_{A2}^2 - \omega^2), \tag{2.65}$$

for a given frequency, ω, and wavenumber, k.

To show that Equation (2.65) is sufficient for there to exist quasi-symmetric modes, consider an asymmetric magnetic slab with parameters that satisfy

[5]If we further specify that the penetration depth of perturbations in the external plasma be equal on each side of the slab, so that the eigenfunction is symmetric, then it must be the case that the external parameters are equal and we have a symmetric slab.

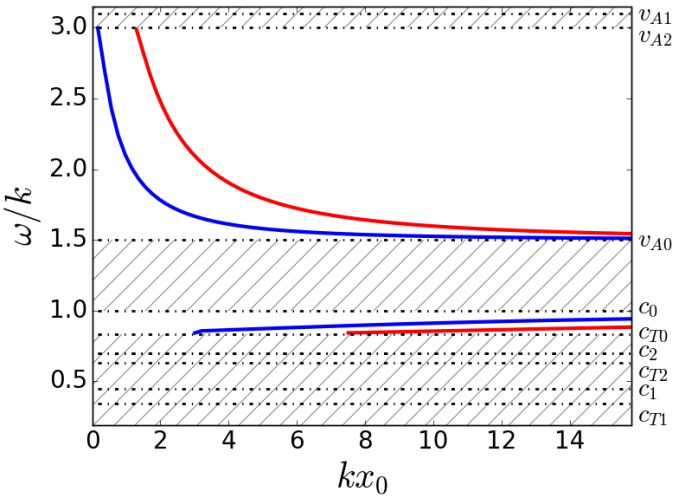

(a) $v_{A0} > c_0$

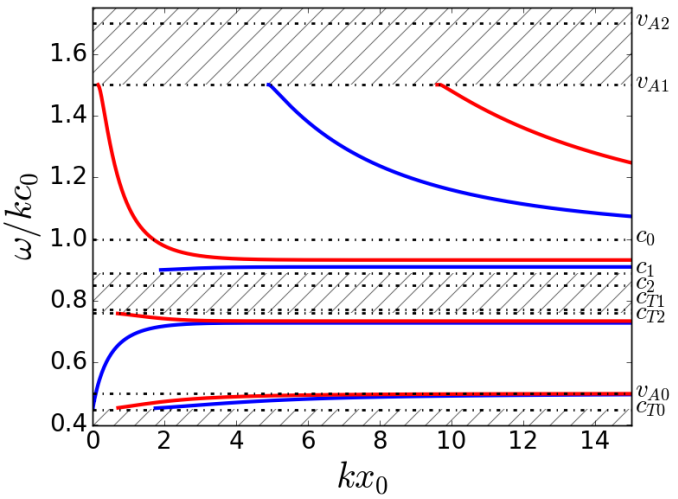

(b) $v_{A0} < c_0$

Figure 2.12: The dispersion diagram for the an asymmetric magnetic slab with external magnetic field. The solutions are found by numerical solution of the dispersion relation, Equation (2.19), for given waveguide parameters. The red lines illustrate quasi-sausage modes and the blue lines illustrate quasi-kink modes. Panel (a) shows the existence of a family of slow body modes and fast surface modes. Panel (b) shows the existence of a family of slow body modes, a slow quasi-sausage and quasi-kink surface mode, a fast quasi-kink surface mode, and a family of fast body modes, the slowest of which being a first order fast quasi-sausage mode that exists as a body mode for slab waveguides thinner than a critical width, and as a surface mode for wider slabs. Note that the slow modes are still trapped for small values of kx_0.

Equation (2.65). Under this supposition, the transverse velocity perturbation solution for quasi-sausage modes reduces to

$$\widehat{v}_x(x) = \begin{cases} A(\cosh m_1 x + \sinh m_1 x) & \text{if } x < -x_0, \\ C \sinh m_0 x & \text{if } |x| \leq x_0, \\ D(\cosh m_2 x - \sinh m_2 x) & \text{if } x > x_0, \end{cases} \tag{2.66}$$

where

$$A = \frac{-Cs_0}{c_1 - s_1}, \quad D = \frac{Cs_0}{c_2 - s_2}, \quad C \text{ is arbitrary.} \tag{2.67}$$

We have denoted $c_j = \cosh m_j x_0$ and $s_j = \sinh m_j x_0$, for $j = 1, 2$, for brevity. The solution within the slab, $|x| \leq x_0$, is an odd function of x, therefore $\widehat{v}_x(x_0) = -\widehat{v}_x(-x_0)$. Therefore Equation (2.65) is a sufficient condition for the existence of quasi-symmetric modes. For quasi-kink modes, a similar proof is followed, where we find that $\widehat{v}_x(x)$ is an even function within the slab.

To show that Equation (2.65) is necessary for there to exist quasi-symmetric modes, consider an asymmetric magnetic slab which supports quasi-symmetric modes. The transverse velocity perturbation solution is given by

$$\widehat{v}_x(x) = \begin{cases} A(\cosh m_1 x + \sinh m_1 x) & \text{if } x < -x_0, \\ B \cosh m_0 x + C \sinh m_0 x & \text{if } |x| \leq x_0, \\ D(\cosh m_2 x - \sinh m_2 x) & \text{if } x > x_0, \end{cases} \tag{2.68}$$

where

$$A = \frac{1}{c_1 - s_1}(Bc_0 - Cs_0), \tag{2.69}$$

$$D = \frac{1}{c_2 - s_2}(Bc_0 + Cs_0), \tag{2.70}$$

$$B = \frac{\Lambda_0 c_0 + \Lambda_1 s_0}{\Lambda_0 s_0 + \Lambda_1 c_0} C = -\frac{\Lambda_0 c_0 + \Lambda_2 s_0}{\Lambda_0 s_0 + \Lambda_2 c_0} C, \tag{2.71}$$

$$C \text{ is arbitrary,} \tag{2.72}$$

for quasi-sausage modes, and

$$A = \frac{1}{c_1 - s_1}(Bc_0 - Cs_0), \tag{2.73}$$

$$D = \frac{1}{c_2 - s_2}(Bc_0 + Cs_0), \tag{2.74}$$

$$C = \frac{\Lambda_0 s_0 + \Lambda_1 c_0}{\Lambda_0 c_0 + \Lambda_1 s_0} B = -\frac{\Lambda_0 s_0 + \Lambda_2 c_0}{\Lambda_0 c_0 + \Lambda_2 s_0} B, \tag{2.75}$$

$$B \text{ is arbitrary,} \tag{2.76}$$

for quasi-kink modes. Given the supposition that the slab supports quasi-symmetric modes, we have, for quasi-sausage modes,

$$\widehat{v}_x(-x_0) = -\widehat{v}_x(x_0), \tag{2.77}$$

$$\implies \left(\frac{\Lambda_0 c_0 + \Lambda_1 s_0}{\Lambda_0 s_0 + \Lambda_1 c_0}\right) c_0 - s_0 = -\left(\frac{\Lambda_0 c_0 + \Lambda_1 s_0}{\Lambda_0 s_0 + \Lambda_1 c_0}\right) c_0 - s_0, \tag{2.78}$$

$$\implies \Lambda_0 c_0 + \Lambda_1 s_0 = 0. \tag{2.79}$$

Similarly, taking the second expression for B, we deduce that

$$\Lambda_0 c_0 + \Lambda_2 s_0 = 0. \tag{2.80}$$

By subtracting Equation (2.80) from Equation (2.79), it follows that $\Lambda_1 = \Lambda_2$, which is equivalent to Equation (2.65). This concludes the proof that Equation (2.65) is a necessary condition for the existence of quasi-symmetric quasi-sausage modes. For quasi-kink modes, a similar proof can be followed to show that $\widehat{v}_x(x_0) = \widehat{v}_x(-x_0)$ implies Equation (2.65). This completes the proof that Equation (2.65) is a necessary and sufficient condition for the existence of quasi-symmetric modes.

The main consequence of this result is that one can not conclude from an observation of a MHD wave that appears symmetric (*i.e.* that the boundary oscillations have equal amplitudes) that the underlying waveguide is symmetric. This fallacy could lead to incorrect mode identification and therefore erroneous diagnosis of the background plasma.

Is it possible to differentiate between a symmetric and a quasi-symmetric eigenmode? Theoretically, the answer to this question is *yes*. Quasi-symmetric modes have symmetric amplitudes at the boundaries but they have asymmetric penetration depths into the external plasmas (see Figure 2.13). In theory, one could track the attenuation of the oscillation amplitude of plasma away from the slab on each side. If the attenuation is asymmetric, the mode is likely to be quasi-symmetric and the underlying waveguide asymmetric. In practice, however, this will prove difficult. Although we currently have the required spatial resolution for measuring the spatial attenuation of MHD waves in isolated waveguides, solar structures are unlikely to be sufficiently isolated to allow for good measurements of spatial attenuation.

2.4.1.2 Asymmetric mode or a superposition of symmetric modes?

A second implication that asymmetric eigenmodes have for mode identification in solar observations is that a waveguide oscillating in an asymmetric mode could be indistinguishable from a superposition of symmetric eigenmodes.

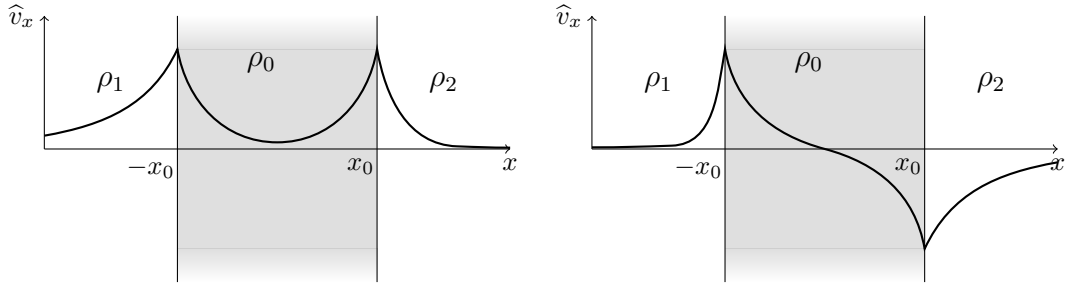

(a) Quasi-symmetric quasi-sausage mode (b) Quasi-symmetric quasi-kink mode

Figure 2.13: The eigenfunctions of a quasi-symmetric modes. The (absolute) oscillation amplitude is equal on each boundary so such a mode could be misidentified as a symmetric mode. An example of a difference between a quasi-symmetric mode and its symmetric counterpart is that quasi-symmetric modes have asymmetric penetration depth.

Consider how one has traditionally identified sausage and kink eigenmodes of a symmetric waveguide. To identify sausage modes, it has been presumed sufficient to identify oscillation in the cross-sectional width. To identify kink modes, previous studies have presumed it to be sufficient to identify perturbation of the waveguide axis (for example, Morton et al., 2012). The mixed characteristics of sausage and kink modes in asymmetric waveguides (see Table 2.1) tell us that these two characteristics are necessary but not sufficient for identification of the respective modes.

To appreciate the potential misidentification, consider a hypothetical observation of a waveguide in the solar atmosphere from which oscillations can be identified in both the cross-sectional width and the axis (for example, Figure 5.7b). A naive approach would be to assume that the waveguide is symmetric, so that the only explanation for the cross-sectional oscillation is a symmetric sausage mode and the only explanation for the axial oscillation is a symmetric kink mode. One might then conclude that the observation is a superposition of a sausage mode and a kink mode. However, as can be seen in Table 2.1, if the waveguide is instead asymmetric (and the asymmetry need only be small, such that it might not be directly observable) then both the oscillation in cross-sectional width and the axial oscillation could be due to asymmetric eigenmodes. Therefore, the correct identification could be a quasi-sausage mode, quasi-kink mode, or superposition of both types. More information is required in order to confidently identify a mode.

One possible resolution to this problem is to measure the background parameters on each side of the waveguide to determine the degree of asymmetry

before identifying the modes. If the waveguide is determined to be symmetric, symmetric modes can be identified. If not, the more general asymmetric modes can be identified.

One problem with this approach is that determining the key background parameters, the density and magnetic field strength, is often very difficult and estimates will have an associated uncertainty large enough that it would often not be possible to rule out the possibility of asymmetry. Another problem with this approach is that even relatively small degrees of waveguide asymmetry can cause significant asymmetry in the eigenmodes. For example, the second panel of Figure 2.9b shows a case where the ratio of the external densities is only $\rho_2/\rho_1 = 2/1.5 = 1.33$ (*i.e.* a relative difference of 33%), yet the asymmetry in the eigenfunctions, measured, for example, by the ratio of the oscillation amplitudes at each interface, is approximately $|\widehat{\xi}_x(x_0)/\widehat{\xi}_x(-x_0)| \approx 4$ for quasi-kink modes and 0.25 for quasi-sausage modes, *i.e.* a relative difference of approximately 400%, easily sufficient to show up in observations. This is an increase in the relative difference of a factor of 12.

A second resolution is to independently measure the propagation speeds of the cross-sectional width oscillation and axial oscillation. Distinct eigenmodes propagate at distinct phase-speeds[6]. If, in fact, the observation is of a superposition of symmetric sausage and kink eigenmodes, then each eigenmode will propagate at a distinct phase speed. Specifically, the cross-sectional oscillation will propagate at a different speed to the axial oscillation, and the oscillations will become out of phase. Whereas, if the oscillations in cross-sectional width and axis are both due to a single asymmetric eigenmode, then they will both share the same propagation speed and remain in phase. If different propagation speeds between these oscillations can be identified, then it will more likely be a superposition of symmetric modes than asymmetric modes.

One problem with this approach is that often only a small number of periods are observed before either the wave is damped or the waveguide disappears from observational view or breaks up[7]. When only a small number of periods are observed, there are often either too few periods to observe the cross-sectional width oscillations breaking phase with axial oscillations, or errors in the phase-speed measurements too large to determine a difference. A second problem is that for some equilibrium parameters, the phase speeds of the symmetric sausage and kink eigenmodes are very similar so would require

[6]This is an example of the uniqueness of eigenvalues in Sturm-Liouville systems (see, for example, Boyce and DiPrima, 2012).

[7]A notable exception to this are decayless kink oscillations (Nisticò et al., 2013).

many periods before breaking phase. For example, this is true for body modes in most parameter regimes and for surface modes in a wide slab.

2.5 Other asymmetric waveguides

For completion, we briefly discuss studies of other MHD waveguides that display asymmetric properties.

2.5.1 Further study of asymmetric slab waveguides

Since the development of the theory of asymmetric slab MHD waveguides in the papers on which this chapter is based (Allcock and Erdélyi, 2017; Zsámberger et al., 2018), there have been further advancements. Zsámberger and Erdélyi (2020) studied an asymmetric slab with magnetised external plasma environment in a variety of limiting cases, with effectively the same results as were derived in this chapter without an external magnetic field. Oxley et al. (2020*b*) and Oxley et al. (2020*a*) studied a bounded asymmetric slab. The boundaries in the longitudinal direction create nodes of the MHD eigenmodes, which in this case are standing rather than propagating. They characterise the eigenmodes and derive an initial application of this waveguide for magnetoseismology.

2.5.2 Multi-layered plasma

Shukhobodskaia and Erdélyi (2018) and Allcock et al. (2019) studied a waveguide formed by an arbitrary number of parallel tangential discontinuities. This model generalises the asymmetric slab waveguide studied in depth in this chapter. The eigenfunctions, *i.e.* the distribution of wave amplitude transversely across the waveguide for each eigenmode, are not at all simple. For trapped modes, the eigenfunction must be evanescent in the external plasma regions. However, the eigenfunction can be either evanescent or spatially oscillatory in each internal region. This allows for parts of the waveguide to oscillate like a body mode and other parts like a surface mode. Each pair of interfaces can oscillate in phase or in anti-phase, each internal region can oscillate like a body or a surface mode, and each eigenmode can be of either fast or slow variety, depending on the phase of the pressure gradient and magnetic restoring forces. Each combination corresponds to a distinct mode. An additional interface increases the number of distinct eigenmodes by a factor of approximately

four[8]. The precise combination of eigenmodes driven in a physical system is dependent on the distribution of the driver across the waveguide as well as the plasma parameters.

This work corroborates with the work of Ruderman (1992), who studied soliton propagation along a waveguide formed by an arbitrary number of tangential discontinuities, with magnetic field in each plasma region in an arbitrary tangential direction.

Plasma with multiple layers is present in several parts of the solar atmosphere. Gravitational stratification, as well as other currently unknown effects, stratify the solar atmosphere into approximately radial layers. Large gradients between plasma of different parameters are present, for example, between the chromosphere and the corona. Inhomogeneities in the lower solar atmosphere can form waveguides that have an approximately multi-layered structure. For example, the atmosphere above elongated magnetic bright points and clusters of elongated sunspots or sunspots with several light bridges (and corresponding overlying light walls) can form horizontally layered systems.

Where these models of multi-layered waveguides might fail is in the assumption that the whole waveguide oscillates collectively. For this to occur, the wavelength must be the same order as the characteristic length scale of the waveguide, otherwise, each interface will oscillate independently. For example, the atmosphere above granules in quiet Sun regions is structured with magnetic bright points and has length scale around the size of granules, which is on the order of 1 Mm (Rast, 2003). MHD oscillations in these structures also have wavelength on the order of 1 Mm (Jafarzadeh et al., 2017). Therefore, it is likely that a multi-layered waveguide formed of several magnetic bright points and adjacent over-granule atmosphere will oscillate collectively. On the other hand, a structure with characteristic length-scale of 1 Mm, oscillating with wavelength 1 km is unlikely to oscillate collectively. In this case we would expect oscillations to be locally distributed, perhaps manifested as surface modes localised to the interfaces between the plasma regions.

[8]Due to the infinite number of body modes, the set of eigenmodes of a multi-layered waveguide with more than one interface has cardinality $\aleph_0$ (*aleph-null*, the cardinality of the natural numbers). In particular, these sets are the same cardinal size. Instead, we can use the *number density* to get a feel for the number of eigenmodes. The number density of a set gives the asymptotic proportion of elements of the set compared to the natural numbers from 1 to n as $n \to \infty$. It is in the number density sense that an additional interface increases the size of distinct eigenmodes by a factor of approximately four.

2.5.3 Non-stationary plasma

Barbulescu and Erdélyi (2018) studied the onset of the Kelvin-Helmholtz instability (KHI) in asymmetric magnetic slab waveguides. The KHI owes its existence to velocity shear and, for a given model, there exists a critical difference in flow speed between different fluid regions such that any greater difference will trigger instability. In their model, Barbulescu and Erdélyi (2018) induced a uniform flow in the slab and showed that increased asymmetry in the external plasma is associated with a decrease in the critical flow speed. This mechanism works counter to the stabilising effect due to the magnetic field tangential to the interface.

This multi-layered flowing plasma model has application in the flank of CME ejecta as they rapidly flows through the sparse coronal environment (Foullon et al., 2011).

2.5.4 Adjacent waveguides

As mentioned in the introduction to this chapter, Luna et al. (2008) showed numerically that a system of two adjacent flux tubes of equal parameters oscillates in four trapped eigenmodes: two where the tubes oscillate in phase and two in anti-phase. As expected, the tubes oscillate independently when the distance between them significantly exceeds the wavelength. The tubes in this model are equal in spatial scale and plasma parameters, so this constitutes a symmetric model. Van Doorsselaere, Ruderman and Robertson (2008) generalised this model to a system of unequal tubes.

It is possible that our present limits on spatial resolution obscure the multi-stranded fine structure of coronal loops. There is no reason for these strands to be equal in size or plasma parameters. Therefore, we might expect strands of different parameters to form a coronal loop that oscillates collectively as an asymmetric waveguide. If this is the case, the asymmetric adjacent flux tube model of Van Doorsselaere, Ruderman and Robertson (2008) will be particularly useful.

2.6 Chapter conclusions

In this chapter, we have investigated a simple asymmetric slab model of layered solar atmospheric waveguides using an EVP approach. We derived the dispersion relation, Equation (2.19), for linear oscillations of this waveguide.

In contrast to that of a symmetric slab the dispersion relation for an asymmetric slab does not decouple into separate equations for kink and sausage modes. Instead, all the eigenmodes are described by the single transcendental equation. Despite this, the eigenmodes can still be categorised into distinct *quasi-kink* and *quasi-sausage* modes depending on whether the boundary oscillations are in phase or in anti-phase, respectively. By generalising the MHD slab model, we have shown that it is the in phase or anti-phase relationship between oscillations at the waveguide boundaries that is the fundamental distinction between sausage mode and kink modes, rather than other often-used proxies such as axial displacement and cross-sectional width variation.

There are some key difference between quasi-kink and quasi-sausage modes and their symmetric counterparts (summarised in Table 2.1). In particular, *quasi-kink modes* do not preserve the cross-sectional width and are, in general compressible. This is in stark contrast to the often observed symmetric kink modes, which are practically incompressible, to the point where they are often indistinguishable from Alfvén modes in observations when the spatial resolution is low, leading to there adoption of the name Alfvénic. Both quasi-sausage and quasi-kink modes perturb the axis of the waveguide. This is in contrast to the symmetric modes, of which only kink modes perturb the waveguide axis. The mixed nature of the eigenmodes leads to the presence of avoided crossing phenomena between quasi-sausage and quasi-kink modes in the dispersion diagrams of asymmetric waveguides.

These differences between the symmetric and asymmetric eigenmodes could lead to misidentification of observed MHD oscillations in the solar atmosphere. If one were to observe an MHD wave with axial displacement, it could be a kink mode of a symmetric waveguide, or a quasi-kink or quasi-sausage mode of an asymmetric waveguide. Further analysis, such as the measurement of different phase-speeds for the axial perturbation and the intensity perturbation, is required to make a confident mode identification. For this reason, we should use several observational proxies so that ambiguity can be reduced.

Another mechanism for wave misidentification is due to the possible existence of quasi-symmetric eigenmodes. These are modes that appear symmetric *i.e.* the oscillation amplitudes on each interface are equal. This special type of asymmetric eigenmode can exist if and only if a condition, Equation (2.65), on the background parameters is satisfied. Misidentification can occur if one were to observe a wave with symmetric boundary oscillations and deduce from this that the underlying waveguide must be symmetric. From this information

alone, the waveguide could be symmetric or asymmetric and the wave could be a symmetric mode or a quasi-symmetric mode. Further analysis, for example measurement of the penetration depth of the wave into the surrounding plasma, would be needed to make confident mode identification. Although, in practice, the penetration depth of MHD waves is difficult to measure due to the presence of neighbouring inhomogeneities that obscure the wave's evanescence.

The dispersion relation for asymmetric eigenmodes is analytically solvable under further approximations to the plasma. We derived analytical solutions in the limits of incompressible plasma, zero-beta plasma, thin slab, and wide slab. One of the key results from this is that while asymmetric surface modes are strongly dependent on the external plasma parameters, asymmetric body modes are independent of the external plasma parameters to leading order in the slab width. In particular, surface modes are strongly dependent on the waveguide asymmetry, whereas body modes are not. This has the implication that the magneto-seismology techniques developed in Chapter 5 are useful for surface modes.

Asymmetric eigenfunctions have unequal oscillation amplitudes on each interface (unless it is the eigenfunction of a quasi-symmetric mode). We found that the side of the waveguide which oscillates with the largest amplitude is different for quasi-sausage and quasi-kink modes. This is a surprising result because one might naively expect the largest amplitude to be on the side with lowest density in the external plasma because of the lower density would be expected to give less resistance to perturbation. Establishing an analogy with an asymmetric spring-mass coupled oscillator makes this property less surprising. Like those of an asymmetric slab, the eigenfunctions of the sloshing and breathing modes (analogous to quasi-kink and quasi-sausage modes) a spring-mass oscillator have largest amplitude on different masses.

CHAPTER 3

Ray theory

3.1 Chapter introduction

In this section, we give an introduction to MHD ray theory, use ray theory to characterise guided and leaky modes of MHD waveguides, and provide an alternative derivation of the dispersion relation for MHD slab waveguides. The significance of this approach is that it could present a method of deriving a dispersion relation in cases where the differential equation approach is intractable.

Ray theory (also known as ray optics or geometric optics) is an approach to studying wave propagation that models waves as continuous lines, known as *rays*. It is extensively used in electromagnetic wave theory but has largely been neglected in MHD and solar physics. It provides a mathematically tractable description of phenomena such as reflection and refraction, but is inadequate to describe phenomena such as diffraction which require a wave-based approach.

Due to the dominance of its use in electromagnetism, ray theory is mostly encountered in isotropic media, that is, media for which wave propagation is independent of propagation direction. While MHD wave propagation is inherently anisotropic due to the magnetic field, isotropic ray theory remains instructive for MHD because some limiting cases in MHD exhibit isotropic wave propagation.

The seminal text for ray theory is Born and Wolf (1999), which covers electromagnetic wave propagation in both isotropic and anisotropic media. Also, Veiras et al. (2010) gives a particularly intuitive description of electromagnetic wave propagation in uniaxial crystals which demonstrates the type of optical anisotropy that is a most similar to MHD media. The authors define a crystal axis as a direction along which propagating light suffers no birefringent, that is, rays are refracted in one, rather than many, direction. Uniaxial crystals are crystals which have one crystal axis. Light propagation along the plane perpendicular to the single crystal axis in a uniaxial crystal is isotropic. In

this sense, the magnetic field direction is to MHD waves as the crystal axis is to light waves.

The slab waveguide, the centrepiece of this thesis, is a prototypical model for guiding electromagnetic waves. The electromagnetic slab waveguide is formed by dielectric layers and is used in, for example, integrated optical circuits and optical fibres (Ramo et al., 1984). Modes analogous to MHD body modes, that is, modes which are spatially oscillatory within the waveguide, are guided by right-handed electromagnetic slabs. They are termed *right-handed* because the electric field vector, magnetic field vector, and wavevector form a right-handed orthogonal set (Ramo et al., 1984). Modes analogous to MHD surface modes, that is, modes that are evanescent within the waveguide where the wave energy is confined to the interfaces, are guided by left-handed electromagnetic slabs (Wang and Li, 2008; Ashour, 2013; Shadrivov et al., 2003). Left-handed optical waveguides are more esoteric than right-handed optical waveguides because of the engineering complexity of meta-materials that are required to construct such waveguides.

Hu and Menyuk (2009) give an overview of the theory and applications of electromagnetic slab waveguides. They focus on leaky modes, giving a particularly intuitive description of energy leakage as the result of partial internal reflection leading to energy being transmitted to the external region. Minimising energy leakage is key to avoiding energy losses in optical communication infrastructure. They also expand the theory of the W-type slab waveguide, which is constructed by two adjacent slab waveguides. Marcuse (1974) generalises the theory of optical slab waveguides to an asymmetric slab, analogous to the asymmetric slab MHD waveguide modelled in this thesis.

Severe inhomogeneities exists across a broad range of length scales in the solar atmosphere, from the global scale at the transition region between the chromosphere and the corona, to the smallest scales that we can currently resolve in magnetic bright points in inter-granular lanes. When waves are incident on these structures, the wave's energy is partially reflected and partially transmitted, with the remainder of the energy dissipated into the background plasma or converted to a different MHD wave mode. Ray theory is an appropriate model for the reflection and transmission of MHD waves.

The basic theory of MHD ray theory has been established for some time. McKenzie (1970) calculated the reflection and transmission coefficients for MHD waves incident on the magnetopause. Verzariu (1973) extended this

by calculating the transmitted energy and Wolfe and Kaufmann (1975) comparing to instances of large perturbations of the magnetopause by oscillations in the solar wind. The ray theory behind these results is particularly well explained by Walker (2004). Nonlinear MHD ray theory has recently been investigated by Núñez (2018) and Núñez (2020).

MHD waves have long been a considered mechanism for plasma heating. Wave heating of plasma in the Sun's corona would require energy to be efficiently transported from the solar interior and dissipated at a given height, but there is no wave mode that is both efficient at energy transportation and energy dissipation. One possibility is that mode conversion occurs between a mode with efficient energy transportation to a mode with efficient energy dissipation (Parnell and De Moortel, 2012). To incorporate mode conversion to MHD ray theory, Schunker and Cally (2006) developed a *generalized ray theory*. This theory has also been used in helioseismology. Cally (2006) numerically investigated the mode conversion of MHD waves in the Sun's interior at the position of equipartition between the sound and Alfvén speeds and the acoustic cut-off position.

Lee and Kim (2002) utilise a numerical method known as *invariant embedding* to solve a system of nonlinear boundary value differential equations to derive expressions for the reflection and transmission coefficients (that is, the amplitude modulation factor that a wave undergoes upon reflection or transmission) of MHD waves when propagating through arbitrary non-uniform regions. They then use this to derive a relationship between the reflection and transmission coefficients and the damping time of MHD waves.

Using ray theory of MHD waves normally incident on a multi-layered plasma model of the interface between the solar wind and Earth's magnetosphere, Leonovich et al. (2003) estimated that 40% of the wave energy flux incident on the magnetosphere is transmitted into the magnetosphere. This is enough to explain the energy in moderate geomagnetic sub-storms.

This chapter uses ray theory to determine the discrete spectrum of eigenfrequencies of MHD waveguides. This is manifested by imposing the condition that rays that are internally reflected from the boundaries of the waveguide must have equal phase to rays that travel the same distance without reflection. This technique has been employed in standard electromagnetic ray theory (Born and Wolf, 1999). In MHD, it has been explored for simple waveguides such as a symmetric slab waveguide modelling waves guided by a coronal hole (Davila, 1985).

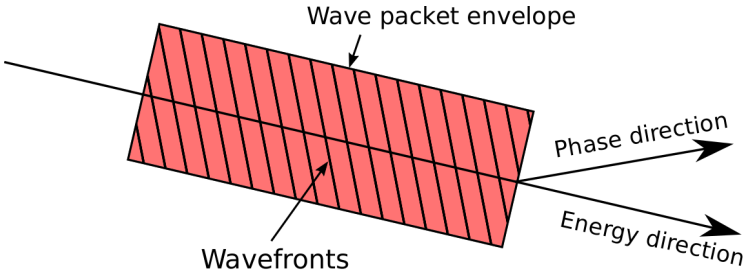

Figure 3.1: In an anisotropic fluid, wave packets and wavefronts can travel in different directions.

3.2 Anisotropic ray theory

There are two notions of a wave's direction: phase velocity and group velocity. The phase velocity, $\mathbf{v_{ph}} = \omega/|k|\widehat{\mathbf{k}}$ is the velocity with which each peak and trough travels and the group velocity, $\mathbf{v_g} = \partial\omega/\partial\mathbf{k}$, is the velocity with which the envelope of a wave packet travels. In general, these directions are different. However, in the ray theory of isotropic media, there is an unambiguous notion of direction of the wave. This can be proven as follows.

Using the quotient rule, we can show that the group and phase velocities are related by

$$\mathbf{v_g} = \mathbf{v_{ph}} + k\nabla_k v_{ph}, \tag{3.1}$$

where $v_{ph} = |\mathbf{v_{ph}}|$ and $\nabla_k = (\partial/\partial k_x, \partial/\partial k_y)$. Let's restrict the domain to the xy-plane for ease of algebra and define the angle that $\mathbf{k}$ makes with the x-axis to be θ. Now, by the chain rule,

$$\frac{\partial}{\partial\theta} = -k_y\frac{\partial}{\partial k_x} + k_x\frac{\partial}{\partial k_y}. \tag{3.2}$$

Therefore, taking the magnitude of the cross product of Equation (3.1) with $\mathbf{k}$ leads to

$$|\mathbf{k}\times\mathbf{v_g}| = \frac{\partial v_{ph}}{\partial\theta}. \tag{3.3}$$

Therefore, if the medium is isotropic, *i.e.* if the right-hand side of the above equation is zero, then the group velocity is parallel to $\mathbf{k}$ and hence is parallel to the phase velocity, which concludes the proof. The proof for a general three-dimensional domain is similar but each direction is uniquely determined by two angles, rather than one.

When the medium is anisotropic, then the phase speed is dependent on the angle of propagation, therefore it is possible for the group speed to have a component perpendicular to the phase speed (see Figure 3.1). For anisotropic ray theory, a natural question to ask is: along which direction does the ray

travel? The answer to this is dependent on the purpose. Of course, ray theory is merely a model of reality; its importance is in virtue of its utility rather than its truthfulness, *per se*. So we are free to choose which is most useful. Ray theory using the phase direction, *i.e.* the direction normal to wavefronts, is known as *geometric optics* and ray theory using the group direction, *i.e.* the direction along which the wave energy propagates, is known as *Hamiltonian optics*. For our purpose, which is to derive the dispersion relation for guided MHD waves, we will be required to impose a condition of matching the phase of two reflected waves. This motivates the use of the phase direction for MHD rays. Therefore, geometrical optics is more suitable for the present purpose. This disambiguation is laid out more fully for electromagnetic ray theory by Hashimoto (1988) and for MHD ray theory by Walker (1977).

A third characteristic speed is the *ray velocity*, which is the speed of the energy ray, defined by $v_r = v_{ph}/\cos\alpha$, where α is the angle between the group velocity and the phase velocity. In other words, the ray velocity is phase velocity measured in the group velocity direction, so that the phase velocity is the component on the ray velocity in the phase direction. For an isotropic fluid, $\alpha = 0$, therefore making the ray velocity equal to the phase velocity.

A key principle for ray theory is Fermat's Principle of Least Time, which states that the path taken by an energy ray between two points is that which takes least time for the ray to cover. We can use this to define the energy ray path. Then we can use this definition to determine a relationship between the phase angles of incident, reflection, and transmitted rays when a ray is incident on a planar interface as follows.

Fermat's principle applied to paths connecting points A and B can be written as

$$\delta T = \delta \int_A^B \frac{1}{v_r}\, ds = 0, \tag{3.4}$$

where s is the arc length measured along the path from A to B and T is the time for the energy ray to travel between A and B (Born and Wolf, 1999). The symbol δ denotes a small change in a quantity. When the domain is divided by an interface parallel to the z-axis, with uniform plasma on each side, making a change of variables $p = s\cos\alpha$ leads to $dp = \cos\alpha\ ds$ in each uniform region. Therefore,

$$T = \int_A^O \frac{1}{v_r}\, ds + \int_O^B \frac{1}{v_r}\, ds = \int_A^{O'} \frac{1}{v_{ph}}\, dp + \int_{O'}^{B'} \frac{1}{v_{ph}}\, dp, \tag{3.5}$$

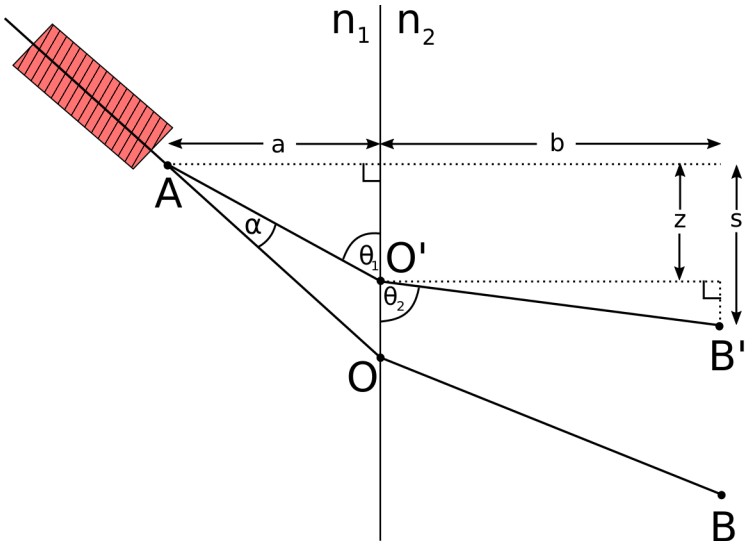

Figure 3.2: An isotropic ray is incident on a planar interface between two plasmas with refractive indices n_1 and n_2, respectively. The energy ray path is from point A to B via O. The phase ray path, which propagates at an angle α to the energy ray path, is from point A to B' via O'. The phase ray path makes an angle of θ_1 with the interface.

which has effectively changed the contour of the integral from the energy ray path to the phase ray path. Using the notation defined in Figure 3.2, T can be written as

$$T = \frac{\sqrt{z^2 + a^2}}{v_{ph1}} + \frac{\sqrt{b^2 + (s-z)^2}}{v_{ph2}}. \tag{3.6}$$

Each region is homogeneous, so the ray is a straight line in each region. Therefore,

$$\frac{dT}{dz} = \frac{z}{v_{ph1}\sqrt{z^2 + a^2}} - \frac{s-z}{v_{ph2}\sqrt{b^2 + (s-z)^2}}. \tag{3.7}$$

By noticing that

$$\cos\theta_1 = \frac{z}{\sqrt{z^2 + a^2}} \quad \text{and} \quad \cos\theta_2 = \frac{s-z}{\sqrt{b^2 + (s-z)^2}}, \tag{3.8}$$

we can write

$$\frac{dT}{dz} = \frac{1}{v_{ph1}}\cos\theta_1 - \frac{1}{v_{ph2}}\cos\theta_2. \tag{3.9}$$

By Fermat's Principle, this must vanish, hence,

$$\frac{1}{v_{ph1}}\cos\theta_1 = \frac{1}{v_{ph2}}\cos\theta_2. \tag{3.10}$$

This is Snell's law, which we have shown to still hold for the phase ray in anisotropic media.

If we instead position point B (and hence point B') on the same side of the interface as point A, then Equation (3.10) reduces to $\theta_i = \theta_r$, known as the *Law of Reflection*, which we have shown holds for the phase ray. Snell's law does not hold for the energy ray but the law of reflection does.

3.3 Low-beta ray theory of a slab waveguide

In general, magneto-acoustic waves are anisotropic, that is, they propagate with different speed depending on their propagation angle. The phase speeds of fast and slow magneto-acoustic waves are given by

$$v_{\text{ph}}^2 = \frac{\omega^2}{k^2} = \frac{1}{2}\left[(v_A^2 + c_0^2) \pm \sqrt{(v_A^2 + c_0^2)^2 - 4v_A^2 c_0^2 \frac{k_z^2}{k^2}}\right]. \tag{3.11}$$

When kinetic pressure is negligible compared to the magnetic pressure, *i.e.* $v_A \gg c_0$, then the fast speed is approximately v_A, and the slow speed is approximately 0. That is, the fast mode propagates isotropically at the Alfvén speed and the slow mode degenerates. Clearly, the group velocity is also $\mathbf{v_g} = v_A\widehat{\mathbf{k}}$, where $\widehat{\mathbf{k}} = \mathbf{k}/k$, so is equal to the phase velocity. Hence, there is an unambiguous ray direction. Therefore, the ray theory of isotropic optical waveguides is isomorphic to low-beta MHD ray theory.

Consider an asymmetric slab MHD waveguide of low-beta plasma. Since MHD wave propagation in low-beta plasma is isotropic, the dispersion relation for guided low-beta MHD waves along an asymmetric slab can be derived in the same way as for guided electromagnetic waves in an asymmetric dielectric slab waveguide. The derivations differ only by notation.

Ramo et al. (1984) used ray theory to show that the eigenfrequencies, ω, of (transverse electric mode[1]) electromagnetic waves guided by an asymmetric dielectric waveguide satisfy the dispersion relation (their Equation 7 in Chapter 14.7)

$$\tan hd = \frac{h(q+p)}{h^2 - pq}, \tag{3.12}$$

where d is the width of the waveguide, waves propagate in proportion to $e^{i\beta z}$

[1]In general, guided electromagnetic waves propagate in a superposition of transverse electric modes and transverse magnetic modes. The transverse electric modes have no electric field in the direction of propagation, and the transverse magnetic modes have no magnetic field in the direction of propagation. The transverse electric mode is analogous to the MHD modes due to their polarisation with respect to the slab boundaries.

in the z-direction, and[2]

$$q^2 := \beta^2 - k_1^2, \quad h^2 := k_0^2 - \beta^2, \quad p^2 := \beta^2 - k_2^2. \tag{3.13}$$

The rays in each dielectric medium i travel at speed $\omega/k_i = v_i$. Therefore, $q^2 = \beta^2 - \omega^2/v_1^2$, $h^2 = \omega^2/v_0^2 - \beta^2$, and $p^2 = \beta^2 - \omega^2/v_2^2$. Therefore, Equation (3.12) is equivalent to

$$\Lambda_0(\Lambda_1 + \Lambda_2) + (\Lambda_0^2 + \Lambda_1\Lambda_2)\tanh d\Lambda_0 = 0, \tag{3.14}$$

where $\Lambda_i = \sqrt{\beta^2 - \omega^2/v_i^2}$ and we have used $\tan i\theta = i\tanh\theta$. Equation (3.14) is isomorphic to the dispersion relation for guided low-beta MHD modes (see Allcock and Erdélyi, 2017) of an asymmetric slab by setting the phase speeds of the rays to be the Alfvén speed, $v_i = v_{Ai}$, for $i = 0, 1, 2$.

3.4 Finite-beta ray theory of a slab waveguide

Next, we relax the low-beta condition. This allows for anisotropic wave propagation. This is most clearly illustrated in the Friedrichs diagrams which demonstrate how the phase and group speeds of MHD waves depend on the angle of propagation (see, for example, Goedbloed and Poedts, 2004; Priest, 2014). In this section, we use MHD ray theory to derive the dispersion for a finite beta asymmetric slab.

Consider a small-amplitude magnetoacoustic phase ray propagating incident on the interface between plasma regions 0 and 2 at an angle of θ_i. The velocity perturbation associated with this incident wave can be written $\mathbf{v_i} = (v_{ix}, 0, v_{iz})$ as we have already shown that the magnetoacoustic modes have no component perpendicular to the magnetic field and parallel to the slab boundaries. Only the Alfvén mode perturbs the plasma in this direction, and that mode is decoupled from the magnetoacoustic modes. In general, the incident ray will be partially reflected and partially transmitted. Each of these waves can be decomposed into a linear superposition of plane waves, whose transverse velocity components have the form

$$v_{ix} = \widehat{v}_{ix} e^{i(\mathbf{k_i}\cdot\mathbf{x} - \omega t)}, \tag{3.15}$$

$$v_{rx} = \widehat{v}_{rx} e^{i(\mathbf{k_r}\cdot\mathbf{x} - \omega t)}, \tag{3.16}$$

$$v_{tx} = \widehat{v}_{tx} e^{i(\mathbf{k_t}\cdot\mathbf{x} - \omega t)}, \tag{3.17}$$

[2]Note that we have changed the subscripts to be in keeping with the notation in this thesis.

where subscripts i, r, t refer to the *incident*, *reflected*, and *transmitted* waves. Let the angles that the incident, reflected, and transmitted rays make with the interface be θ_i, θ_r, and θ_t, respectively.

The interfaces between the plasmas are free surfaces with tangential magnetic field, so the dynamic and kinematic boundary conditions are equivalent to the normal velocity component and total pressure perturbation being continuous at the interface (Goedbloed and Poedts, 2004). Continuity of normal velocity at $x = 0$ gives

$$\widehat{v}_{ix} e^{i(k_{iz} z - \omega t)} + \widehat{v}_{rx} e^{i(k_{rz} z - \omega t)} = \widehat{v}_{tx} e^{i(k_{tz} z - \omega t)}. \tag{3.18}$$

The Law of Reflection tells us that $\theta_r = \theta_i$. The incident, reflected, and transmitted ways must have equal phase at the interface $x = 0$, known as the phase matching condition. This implies that the frequency on each side must be equal. Thus, Snell's Law tells us that the tangential components of the wave-vector components obey

$$k_i \cos\theta_i = k_r \cos\theta_r = k_t \cos\theta_t. \tag{3.19}$$

Therefore, by the Law of Reflection $k_r = k_i$. In particular, $k_{rx} = -k_{ix}$ and $k_{rz} = k_{iz}$. Therefore, Equation (3.18) reduces to

$$\widehat{v}_{ix} + \widehat{v}_{rx} = \widehat{v}_{tx}. \tag{3.20}$$

The total pressure perturbation for a ray with wave-vector $\mathbf{k} = (k_x, 0, k_z)$ is derived as follows. The linearised perturbation in magnetic pressure is $p_m = B_0 b_{iz}/\mu_0$, where B_0 and b_{iz} are the equilibrium and z-component of the magnetic field in the slab region and μ_0 is the magnetic permeability. Using the z-component of the induction equation,

$$\widehat{b}_{iz} = \frac{B_0}{\omega} k_{ix} \widehat{v}_x, \tag{3.21}$$

where $b_{iz} = \widehat{b}_{iz} e^{i(\mathbf{k_i}\cdot\mathbf{x} + \omega t)}$. The energy and continuity equations can be combined to

$$\frac{\partial p}{\partial t} = -\rho_0 c_0^2 \nabla \cdot \mathbf{v}. \tag{3.22}$$

A Fourier decomposition of this equation yields

$$\widehat{p} = -\frac{\rho_0 c_0^2}{\omega}(k_x \widehat{v}_x + k_z \widehat{v}_z). \tag{3.23}$$

The z-component of the momentum equation is

$$\frac{\partial^2 v_z}{\partial t^2} = c_0^2 \frac{\partial}{\partial z}(\nabla \cdot \mathbf{v}), \tag{3.24}$$

which, when taking Fourier forms, reduces to

$$\widehat{v}_z = -\frac{ic_0^2 k_z}{k_z c_0^2 - \omega^2} k_x \widehat{v}_x. \tag{3.25}$$

Equations (3.21), (3.23), and (3.25) combine to give an expression for the total pressure perturbation, namely

$$\widehat{p}_T = \widehat{p} + \widehat{p}_m = \frac{\Lambda_0}{m_0} i k_x \widehat{v}_x, \tag{3.26}$$

where, as defined in Allcock and Erdélyi (2017),

$$\Lambda_j = \frac{i\rho_j(\omega^2 - k_z^2 v_{Aj}^2)}{\omega m_j}, \quad m_j^2 = \frac{(k_z^2 v_{Aj}^2 - \omega^2)(k_z^2 c_j^2 - \omega^2)}{(c_j^2 + v_{Aj}^2)(k_z^2 c_{Tj}^2 - \omega^2)}. \tag{3.27}$$

Equation (3.11) can be rearranged to give

$$k_x^2 = -\frac{(k_z^2 v_{A0}^2 - \omega^2)(k_z^2 c_0^2 - \omega^2)}{(c_0^2 + v_{A0}^2)(k_z^2 c_{T0}^2 - \omega^2)}. \tag{3.28}$$

Therefore, $k_{rx} = -k_{ix} = -im_0$ and $k_{tx} = im_2$. Hence, the condition of continuity of total pressure at the interface is equivalent to

$$\Lambda_0(\widehat{v}_{ix} - \widehat{v}_{rx}) = \Lambda_2 \widehat{v}_{tx}. \tag{3.29}$$

Equations (3.20) and (3.29) can be solved simultaneously to find

$$\widehat{v}_{ix} = \frac{1}{2}\widehat{v}_{tx}\left(1 + \frac{\Lambda_2}{\Lambda_0}\right) \tag{3.30}$$

$$\widehat{v}_{rx} = \frac{1}{2}\widehat{v}_{tx}\left(1 - \frac{\Lambda_2}{\Lambda_0}\right). \tag{3.31}$$

The ratio of these is the reflection coefficient, namely

$$r_2 := \frac{\widehat{v}_{rx}}{\widehat{v}_{ix}} = \frac{\Lambda_0 - \Lambda_2}{\Lambda_0 + \Lambda_2}. \tag{3.32}$$

Total internal reflection occurs for $\theta_i < \theta_c$, where $\cos\theta_c = k_t/k_i$. In this case,

$$k_{tx}^2 = k_t^2 \sin^2\theta_t \tag{3.33}$$

$$= k_t^2(1 - \cos^2\theta_t) \tag{3.34}$$

$$= k_t^2 - k_i^2 \cos^2\theta_i \tag{3.35}$$

$$< k_t^2 - k_i^2 \cos^2\theta_c \tag{3.36}$$

$$= k_t^2 - k_i^2\left(\frac{k_t^2}{k_i^2}\right) \tag{3.37}$$

$$= 0. \tag{3.38}$$

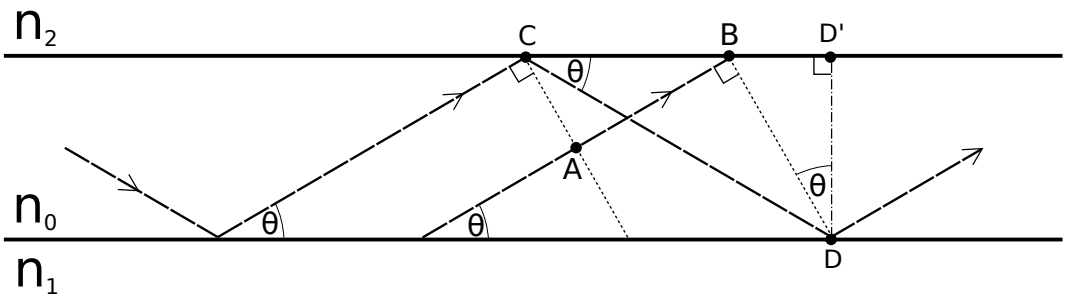

Figure 3.3: Ray paths (dashed) travelling in an asymmetric slab made up of three plasma regions of different refractive indices n_0, n_1, and n_3. The dotted lines indicate the wavefronts of the waves at specific points.

Therefore, k_{tx}, and hence Λ_2, is imaginary. Therefore, define L_2 by $\Lambda_2 = iL_2$, with $L_2 \in \mathbb{R}$ so that we can write

$$r_2 = \frac{\Lambda_0 - iL_2}{\Lambda_0 + iL_2}. \tag{3.39}$$

The variable Λ_0 can be real or imaginary. First, we consider the case when Λ_0 is real.

3.4.1 Body modes

When Λ_0 is real, k_{ix} is real, therefore Equation (3.17) tells us that this corresponds to spatially oscillatory (rather than evanescent) incident rays. It will become clear that this necessitates guided body modes.

In this case, r_2 is complex. In accordance with ray theory, the real part gives the ratio of amplitudes of the reflected and incident rays, and the imaginary part gives a phase shift that the incident ray undergoes upon reflection (Born and Wolf, 1999). The reflection coefficient r_2 given by Equation (3.39) has complex argument

$$\phi_2 = -2 \arctan\left(\frac{L_2}{\Lambda_0}\right). \tag{3.40}$$

This is the phase shift that the incident ray undergoes after total internal reflection on the interface between plasma 0 and 2. Similarly, the phase shift that an incident ray undergoes after total internal reflection on the interface between plasma 0 and 1 is

$$\phi_1 = -2 \arctan\left(\frac{L_1}{\Lambda_0}\right). \tag{3.41}$$

Figure 3.3 illustrates the internal reflection of an MHD ray starting from the left-hand side. The ray (dashed line) travels through plasma region 0 at an

angle of θ to the until it reflects off the interface between region 0 and region 2. The reflected ray reflects again off the other interface at point C and again off the first interface at point D. The wavefront associated with the ray just before it reaches point C (dotted line) is at a right angle to the direction of the phase ray, by definition.

A second ray is travelling parallel to the first. The point on the second ray with equal phase as the first ray at point C is denoted by point A and it is incident on the interface between region 0 and 1 at point B. By construction, the phase difference of the first ray between points C and D is equal to the phase difference of the second ray between points A and B. The phase difference of the first ray between points C and D is a sum of the phase difference accumulated by travelling the distance between C and D with that accumulated through each of the two internal reflections.

The geometrical distance CD is calculated using geometry of the right-angled triangle CDD',

$$CD = \frac{2x_0}{\sin\theta}. \tag{3.42}$$

By normalising the refractive index within the slab to 1, the optical distance that the ray travels between points C and D is equal to the geometrical distance.

Calculating the optical distance that the second ray travels between points A and B is more involved, but still a geometrical exercise. By the geometry of the right-angled triangle BDD',

$$BD' = 2x_0 \tan\theta. \tag{3.43}$$

By the geometry of the right-angled triangle CDD',

$$CD' = 2x_0 \cot\theta. \tag{3.44}$$

Therefore,

$$CB = CD' - BD' = 2x_0(\cot\theta - \tan\theta). \tag{3.45}$$

Geometry of the right-angled triangle CAB yields

$$AB = CB\cos\theta = 2x_0\cos\theta(\cot\theta - \tan\theta) = \frac{2x_0}{\sin\theta}(\cos^2\theta - \sin^2\theta). \tag{3.46}$$

Again, by normalising the refractive index in the slab to 1, the optical distance between points A and B is equal to the geometrical distance, that is, AB.

For the first ray at point D to be in phase with the second ray at point B it is required that

$$CDk_i + \phi_2 + \phi_1 = ABk_i + 2N\pi, \tag{3.47}$$

where $N \in \mathbb{Z}$. This is known as the self-consistency condition[3]. It is this self-consistency rule that ensures that there are only a discrete set of angles for rays that are associated with guided modes. Using basic trigonometry, $1 - (\cos^2\theta_i - \sin^2\theta_i) = 2\sin^2\theta_i$, therefore, Equation (3.47) becomes

$$\arctan\left(\frac{L_2}{\Lambda_0}\right) + \arctan\left(\frac{L_1}{\Lambda_0}\right) = 2x_0 k_i \sin\theta - N\pi. \tag{3.48}$$

Applying tan to this equation, using the identity $\tan(\arctan a + \arctan b) = (a+b)/(1-ab)$, and noticing that $k_i \sin\theta_i = k_{ix} = im_0$, yields

$$\tan(2im_0x_0) = \frac{\Lambda_0(L_1 + L_2)}{\Lambda_0^2 - L_1L_2}. \tag{3.49}$$

Recall that $\Lambda_2 = iL_2$ and $\Lambda_1 = iL_1$, therefore, using the fact that $\tan(i\theta) = i\tanh\theta$ (Abramowitz and Stegun, 1965), the above equation can be rewritten as

$$\Lambda_0(\Lambda_1 + \Lambda_2) + (\Lambda_0^2 + \Lambda_1\Lambda_2)\tanh(2m_0x_0) = 0, \tag{3.50}$$

where $m_0^2 < 0$. This is precisely the dispersion relation for MHD body modes guided by an asymmetric magnetic slab.

The procedure in this subsection of matching amplitudes is analogous to the analysis of left-handed slab waveguides of electromagnetic waves. The discrete spectrum of guided MHD modes is equivalent to the discrete set of angles for rays to ensure total internal reflection.

3.4.2 Surface modes

Next, we consider the case when Λ_0 is imaginary. In this case, k_{ix} is imaginary, therefore Equation (3.17) tells us that this corresponds to evanescent incident rays. It will become clear that this is leads to guided surface modes.

Let $\Lambda_0 = iL_0$, then the reflection coefficient in Equation (3.39) becomes

$$r_2 = \frac{L_0 - L_2}{L_0 + L_2}, \tag{3.51}$$

which is purely real. This is the amplitude change that the incident ray undergoes when it is reflected. No phase shift occurs because r_2 has no imaginary part. Instead, the self-consistency condition must be imposed on the amplitudes. Referring to Figure 3.3, let the amplitude of the evanescent ray at point

[3]The self-consistency condition is also known as the *transverse resonance condition* in the study of optical waveguides (Syms and Cozens, 1992) or the *Bohr-Sommerfeld quantization condition* in quantum mechanics (Messiah, 1961).

C be A_C. The amplitude at point D is then $A_D = e^{-2m_0x_0}A_C$. This ray is reflected, which modulates the amplitude by r_1 and is incident again on the interface between regions 0 and 2. When this ray is incident on this interface, its amplitude is $A_E = e^{-2m_0x_0}A_D = e^{-4m_0x_0}A_C$. It undergoes amplitude modulation of r_2 upon reflection. Now, the self-consistency condition imposes that this doubly reflected ray must have the same amplitude as the initial ray at point C, that is

$$e^{-4m_0x_0}r_1r_2 = 1. \tag{3.52}$$

By definition, for any x,

$$\tanh x = \frac{1 - e^{-2x}}{1 + e^{-2x}}. \tag{3.53}$$

Therefore,

$$\tanh 2m_0x_0 = \frac{1 - e^{-4m_0x_0}}{1 + e^{-4m_0x_0}} \tag{3.54}$$

$$= \frac{r_1r_2 - 1}{r_1r_2 + 1} \tag{3.55}$$

$$= -\frac{\Lambda_0(\Lambda_1 + \Lambda_2)}{\Lambda_0^2 + \Lambda_1\Lambda_2}. \tag{3.56}$$

This equation is rearranged into

$$\Lambda_0(\Lambda_1 + \Lambda_2) + (\Lambda_0^2 + \Lambda_1\Lambda_2)\tanh(2m_0x_0) = 0, \tag{3.57}$$

where $m_0^2 > 0$, which is the dispersion relation for MHD surface modes guided by an asymmetric magnetic slab.

The procedure in this subsection of matching amplitudes is analogous to the analysis of left-handed slab waveguides of electromagnetic waves.

3.5 Leaky modes

The condition imposed after Equation (3.32), where total internal reflection is supposed, restricts the dispersion relation to guided modes only. If this condition is relaxed, then a portion of the incident energy is transmitted into the external medium. Energy *leaks* from the waveguide. The ray theory approach to leaky modes gives an intuitive explanation of energy leakage and a simple method of computing the power loss per unit length of the waveguide.

Let k_{tx} be real. Then, the transmitted ray is spatially oscillatory. In this case, it is physically impossible for the incident ray (and hence the reflected ray) to be evanescent. This is because evanescent rays do not transport energy in the evanescent direction, so there would be no energy source for the leakage

in the external region (Goedbloed and Poedts, 2004). Hence, if k_{tx} is real, then so is k_{ix} (and k_{rx}). Therefore, $\Lambda_{0,2}$ are real. Hence, the reflection coefficient r is real.

Let the power lost per unit length transverse to the waveguide through the first and second interfaces be ΔP_1 and ΔP_2. Concentrating on the first interface initially, the power reflection coefficient, that is, the proportion of power that is reflected, is $r_{P1} = |r_1|^2$, where r_1 is the change in amplitude of the reflected ray compared to the incident ray (Marcuse, 1974). Therefore, the proportion of power transmitted into the external region 1 is $1 - |r_1|^2$. It follows that the power leaked in into the external plasma region is

$$\Delta P_1 = (1 - |r_1|^2) F \sin\theta \tag{3.58}$$

$$= \frac{4\Lambda_0\Lambda_1}{(\Lambda_0 + \Lambda_1)^2} F \sin\theta, \tag{3.59}$$

where F is the magnitude of the energy flux per unit area of the internal ray and θ is its angle of incidence. The power carried by the plane wave that remains in the waveguide is

$$P = 2x_0 F \cos\theta. \tag{3.60}$$

Therefore, the power loss coefficient for a leaky wave in an asymmetric slab is

$$\alpha_P = \frac{\Delta P_1 + \Delta P_2}{P} \tag{3.61}$$

$$= \frac{2k_x}{k_z x_0} \left(\frac{\Lambda_0\Lambda_1}{(\Lambda_0 + \Lambda_1)^2} + \frac{\Lambda_0\Lambda_2}{(\Lambda_0 + \Lambda_2)^2} \right). \tag{3.62}$$

For an asymmetric slab, the leakage can be asymmetric. That is, energy can leak out of one side of the waveguide compared to the other. In fact, it is possible that one side leaks energy whilst the other side does not. This occurs when, without loss of generality, m_1 is imaginary and m_2 is real. That is, in the intersection of the frequency ranges

$$c_{T1} < \frac{\omega}{k_z} < \min\{c_1, v_{A1}\} \quad \text{or} \quad \max\{c_1, v_{A1}\} < \frac{\omega}{k_z}, \tag{3.63}$$

and

$$\frac{\omega}{k_z} < c_{T2} \quad \text{or} \quad \min\{c_2, v_{A2}\} < \frac{\omega}{k_z} < \max\{c_2, v_{A2}\}. \tag{3.64}$$

In this case, the power loss coefficient is

$$\alpha_P = \frac{2k_x}{k_z x_0} \frac{\Lambda_0\Lambda_1}{(\Lambda_0 + \Lambda_1)^2}. \tag{3.65}$$

Most notable is the inverse proportionality between the power loss coefficient and the non-dimensionalised slab width, $k_z x_0$. The thinner the slab is compared to the wavelength, the greater the proportion of power lost to the surrounding medium via lateral wave leakage.

3.6 Chapter conclusions

In this chapter, we have made use of a mathematical approach known as ray theory to asymmetric MHD waves. In ray theory, a wave is modelled as having only a speed and a direction. MHD waves have two notions of direction, defined by the phase velocity and the group velocity. In general, these two directions are not parallel. This presents two options for defining the ray direction in a ray theory approach to MHD waves. We used the phase velocity to define the ray direction in this chapter because it allows us to impose a quantisation condition on the rays after reflecting of the interfaces that bound the waveguide.

Using the phase ray approach, we first derived the dispersion relation for MHD waves in a zero-beta asymmetric slab. In a zero-beta plasma, the slow magneto-acoustic mode degenerates and the fast magneto-acoustic mode propagated isotropically. Given this isotropic propagation, the phase and group velocities are parallel so ray direction is not ambiguous. Next, we derived the dispersion relation for MHD waves in finite-beta plasma. In this more general case, we utilised anisotropic ray theory to derive the dispersion relation for an asymmetric slab. This demonstrates a novel technique for deriving dispersion relations in MHD that does not require the solution of sophisticated differential equations.

Leaky modes are intuitive in the ray theory framework. Leaky modes occur when total internal reflection is not achieved by rays propagating within the waveguide. Instead, upon intersecting the interface, the ray splits into two. One ray reflects back into the waveguide, and the other is refracted through the interface and propagates into the half-planar plasma region outside the slab. This external ray is not free to propagate energy from the oscillating slab laterally away. After each internal reflection, the energy of the internal ray is diminished, as more and more energy is leaked as kinetic energy in the surrounding plasma.

CHAPTER 4

Initial value problem

4.1 Chapter introduction

Eigenmodes are rightfully considered the building blocks of linear oscillations of complex MHD models. They define natural oscillation frequencies and describe how wave power is spatially distributed across a waveguide. However, when solving an MHD wave problem using an EVP approach, such as was used in Section 2, we use a Fourier decomposition in time, so that the eigenmodes have time dependence proportional to $\exp(i\omega t)$. This is a simple time-dependence: a sinusoidal oscillation with frequency ω, and allows an effectively time-independent amplitude to be found. Whilst this approach is useful for understanding the spatial properties of the wave, eigenmodes do not paint the whole picture. A more complete description involves studying the time-evolution by solving the associated initial value problem (IVP).

The IVP approach to MHD wave problems has been utilised by several authors, developing the theory of time-dependant wave phenomena including phase mixing and resonant absorption. The first use of an IVP approach to solar MHD waveguides was by Sedláček (1971) who, quite ahead of their time, showed that the discrete spectrum[1] of the cold magnetic cylindrical waveguide contains more than just eigenmodes. They derived the existence of exponentially damped collective oscillations. The damping mechanism of these oscillations was later shown to be lateral wave leakage due to the waveguide not fully trapping the collective oscillation (Ruderman and Roberts, 2006*b*).

The IVP approach has been particularly useful for studying leaky modes. Cally (2003) catalogued the possible types of wave leakage that a cylindrical waveguide could have, with their associated damping rate, by solving the IVP of a cold magnetic flux tube. Of particular note is what Cally (2003) described as the "principal leaky kink mode", which is the leaky analogue of the principal

[1] The term spectrum is being used here in the functional analytical sense.

kink mode, that is, the first-order trapped kink body mode. Ruderman and Roberts (2006*b*) showed that it is not possible to observe this proposed leaky mode because it is not a physical solution of the dispersion equation. More precisely, it is a solution that is found only on the non-physical Riemann sheet. After some debate (Cally, 2006; Ruderman and Roberts, 2006*a*), it has been shown numerically and later analytically that the principal leaky kink mode does not contribute to the IVP solution. In particular, Terradas et al. (2006) solved the IVP numerically and in doing so demonstrated that the principal leaky kink mode does not contribute to the solution for the initial conditions that they tested and Andries and Goossens (2007) used spectral theory to show that the principal leaky kink mode is not part of the physical spectrum.

The timescale of amplitude attenuation due to wave leakage is much longer than the damping timescale of resonant absorption (Roberts, 2019). This has quite rightly led the solar physics community to focus on resonant absorption as the more plausible mechanism for the damping of coronal loop oscillations. It is worth noting, however, that waveguide curvature can amplify wave leakage (Selwa et al., 2007).

The utility of the IVP approach in the present chapter is to determine a time-scale over which collective and coherent asymmetric oscillations can be expected to develop following an initial perturbation of an MHD waveguides. The structure of this chapter is as follows. Leaky waves play a key role in IVPs in MHD waveguides so Section 4.2 discusses leaky waves in the IVP context. In Section 4.3, we solve the IVP for an interface between two plasmas, correcting several significant errors made in previous research of other authors. In Section 4.4, we solve the MHD IVP for a symmetric slab and discuss how this generalises to an asymmetric slab.

4.2 Leaky waves

Small-amplitude MHD waves guided by an isolated plasma inhomogeneity are made up of *trapped* and *leaky* wave components. Trapped waves maintain a constant (when averaged over a period) amplitude through time and are spatially evanescent away from the waveguide. Trapped waves were the subject of the analysis in Chapter 2. One can then ask whether there can exist any modes with attenuated amplitude through time. Without any damping mechanism[2], there is no way for this energy to be converted into heat. The energy is not

[2]The discontinuous Alfvén speed profile used in the asymmetric slab model avoids resonant absorption and phase mixing and neglecting viscosity avoids viscous damping.

lost, rather, it is *transported*. Energy must be transported orthogonal to the propagation direction.

To see this mathematically, consider the *Poynting flux*, which represents the directional energy flux of a magnetic field. The Poynting flux is defined as $\mathbf{S} = (\mathbf{E}\times\mathbf{B})/\mu_0$ (see, for example, Priest, 2014). In ideal MHD, Ohm's law tells us that the electric field is $\mathbf{E} = -(\mathbf{v}\times\mathbf{B})$. Therefore, using a standard vector calculus identity, the Poynting flux can be written as $\mathbf{S} = [B^2\mathbf{v} - (\mathbf{v}\cdot\mathbf{B})\mathbf{B}]/\mu_0$. Under the assumption that the wave is temporally attenuating, the angular frequency must be complex (with a negative imaginary part), $\omega = \omega_R + i\omega_I$. The time-averaged Poynting flux over a wave period, $T = 2\pi/\omega_R$, is a more instructive quantity because it neglects the small changes in energy flux that do not contribute to the energy flux over time-scales longer than a wave period. The velocity perturbation time-averaged from an initial time t_0 is

$$\langle\mathbf{v}\rangle = \frac{1}{T}\int_{t_0}^{t_0+T} \mathbf{v}\ dt \tag{4.1}$$

$$= \frac{1}{T}\int_{t_0}^{t_0+T} \widehat{\mathbf{v}}e^{i(kz-\omega t)}\ dt \tag{4.2}$$

$$= \frac{i}{\omega T}\widehat{\mathbf{v}}e^{i(kz-\omega t_0)}(e^{\omega_I T}-1). \tag{4.3}$$

To linear order, the time-averaged Poynting flux due to an MHD wave in our model is

$$\langle\mathbf{S}\rangle = \frac{1}{\mu_0}[B_0^2\langle\mathbf{v}\rangle - (\langle\mathbf{v}\rangle\cdot\mathbf{B}_0)\mathbf{B}_0] \tag{4.4}$$

$$= \frac{iB_0^2}{\omega T\mu_0}\widehat{v}_x e^{i(kz-\omega t_0)}(e^{\omega_I T}-1)\widehat{\mathbf{x}}. \tag{4.5}$$

For trapped waves, the frequency is purely real, *i.e.* $\omega_I = 0$, hence $\langle\mathbf{v}\rangle = \mathbf{0}$, giving a vanishing time-averaged Poynting flux (to linear order). Equation (4.5) shows that for non-trapped waves, the time-averaged Poynting flux is in the x-direction, orthogonal to the direction of propagation. Energy leaks laterally away from the waveguide, balancing the amplitude attenuation in the propagation direction. Waves of this type are known as *leaky*.

As discussed in Chapter 3, wave leakage can occur for incidence angles greater then the critical angle for total internal reflection. A proportion of the energy is transmitted into the external plasma. When posed as an eigenvalue problem, the leaky modes have eigenfunctions that are spatially oscillatory in the external plasma (Figure 4.1b) as opposed to trapped modes, which have eigenfunctions that are evanescent in the external plasma (Figure 4.1a).

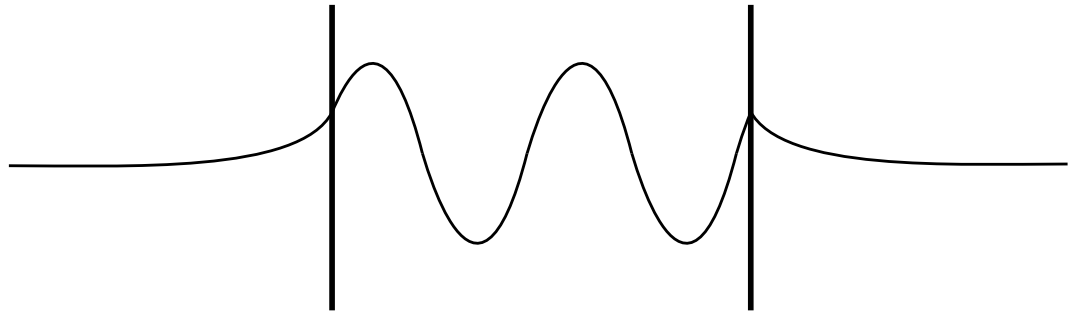

(a) Trapped

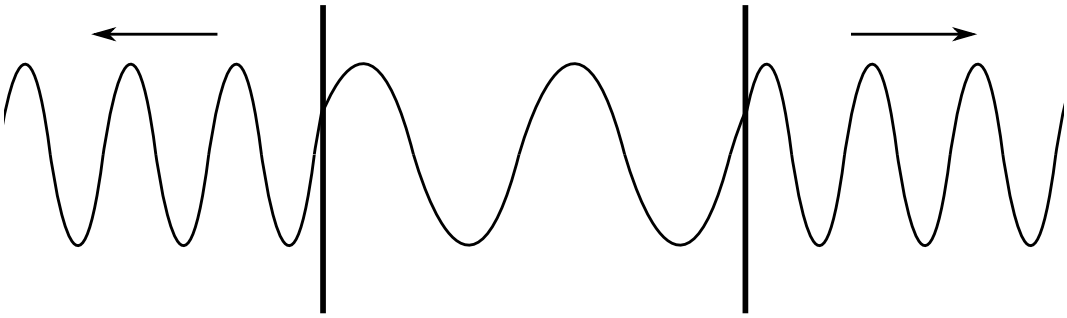

(b) Leaky

Figure 4.1: Typical eigenfunctions for trapped and leaky modes of an MHD waveguide. The arrows denote the direction of energy flux.

Leaky modes are not normal eigenmodes of the true sense, in that they do not contribute to the orthogonal set of elements of the MHD Hilbert space. This is equivalent to the frequencies of leaky modes not being elements of the discrete spectrum[3]. This is clearly seen by the fact that they perturb plasma at an arbitrary distance from the waveguide, therefore input an infinite amount of energy on the plasma. Instead, they contribute to the continuous spectrum[4]. For the slab waveguide, the spectral measure associated with the continuous spectrum has peaks at specific frequencies. These peaks are the allowed frequencies of the leaky modes. This gives the erroneous impression that they contribute to the discrete spectrum. Leaky modes of a slab waveguide are analysed in more detail from the perspective of spectral theory by Andries and Goossens (2007).

The physical nature of leaky modes is that they can dominate the time-dependent solution for intermediate time scales, *i.e.* much longer than the pe-

[3]The spectrum of a bounded operator on a Hilbert space is the set of scalars λ such that the operator $\mathbf{F} - \lambda\mathbf{I}$ does not have a bounded inverse on the Hilbert space. Here, $\mathbf{F}$ and $\mathbf{I}$ are the ideal MHD force operator and the identity operator, respectively. The discrete spectrum is made up of the eigenvalue of the operator $\mathbf{F}$. The spectrum is a generalisation of the set of eigenvalues of an operator in the sense that the discrete spectrum is a subset of the spectrum.

[4]The continuous spectrum is the subset of the spectrum whose elements λ are dense.

riod of the dominant eigenmode and less than (or of the order of) the timescale of damping due to energy leakage, and at intermediate length scales from the waveguide (Ruderman and Roberts, 2006*b*, 2002). This means that they contribute a finite amount of energy, rather than an infinite amount if they were superposed as a standard eigenmode. This is shown in Section 4.4.2 for an MHD slab.

4.3 Wave evolution on a tangential interface

In seminal research, and one of the earlier uses of the IVP approach to an MHD wave problem, Rae and Roberts (1981) modelled surface waves propagating along an isolated tangential interface, parallel to the z-axis, separating two distinct plasmas. In this section, we bring to attention several ways in which the derivation and results of that paper are incorrect and correct the analysis. To our knowledge, this is the first time these errors have been reported.

Consider a stationary, inviscid plasma that is stratified in the x-direction only that has unidirectional magnetic field $\mathbf{B} = (0, 0, B(x))$. Following Rae and Roberts (1981), we let the plasma be incompressible. First, taking Fourier components in the z-direction[5]

$$v_x(x, z, t) = \widehat{v}_x(x, t)e^{ikz}, \tag{4.6}$$

the linearised ideal incompressible MHD equations can be simplified to a single equation for the transverse velocity perturbation, namely (Priest, 2014)

$$\frac{\partial}{\partial x}\left\{\rho_0\left(\frac{\partial^2}{\partial t^2} + k^2 v_A^2\right)\frac{\partial \widehat{v}_x}{\partial x}\right\} - k^2\rho_0\left(\frac{\partial^2}{\partial t^2} + k^2 v_A^2\right)\widehat{v}_x = 0. \tag{4.7}$$

Next, we take the Laplace transform[6], of this equation, where we define

$$\tilde{v}_x(x) = \mathcal{L}\{\widehat{v}_x(x, t)\} = \int_0^\infty \widehat{v}_x(x, t)e^{i\omega t}dt. \tag{4.8}$$

Firstly,

$$\mathcal{L}\left\{\frac{\partial^2 \widehat{v}_x}{\partial t^2}\right\} = \left[\dot{\widehat{v}}_x e^{i\omega t}\right]_0^\infty - i\omega\int_0^\infty \dot{\widehat{v}}_x e^{i\omega t}dt \tag{4.9}$$

$$= -\dot{\widehat{v}}_{x0} - i\omega\left[\widehat{v}_x e^{i\omega t}\right]_0^\infty - \omega^2\int_0^\infty \widehat{v}_x e^{i\omega t}dt \tag{4.10}$$

$$= i\omega\widehat{v}_{x0} - \dot{\widehat{v}}_{x0} - \omega^2\tilde{v}_x, \tag{4.11}$$

[5]To maintain consistency with the remainder of this thesis, we look for parameters proportional to e^{ikz} instead of e^{-ikz} as was taken by Rae and Roberts (1981).

[6]The choice of Laplace transform convention is discussed in Appendix C.

where $\dot{\widehat{v}}_x = d\widehat{v}_x/dt$, and we have used the assumption that $\lim_{t\to\infty} \dot{\widehat{v}}_x(x,t) = \lim_{t\to\infty} \widehat{v}_x(x,t) = 0$, for all x. Therefore, Equation (4.7) becomes

$$\begin{aligned}\frac{d}{dx}\left[\rho_0\left(\left\{i\omega\widehat{v}'_{x0} - \dot{\widehat{v}}'_{x0} - \omega^2\tilde{v}'_x\right\} + k^2 v_A^2\tilde{v}'_x\right)\right] \\ - k^2\rho_0\left(\left\{i\omega\widehat{v}_{x0} - \dot{\widehat{v}}_{x0} - \omega^2\tilde{v}_x\right\} + k^2 v_A^2\tilde{v}_x\right) = 0,\end{aligned}$$

where $\tilde{v}'_x = d\tilde{v}_x/dx$. By defining $\epsilon = \epsilon(x) = \rho_0(x)(k^2 v_A(x)^2 - \omega^2)$, this equation is equivalent to

$$\begin{aligned}\frac{d}{dx}\left[\epsilon\tilde{v}'_x\right] - k^2\epsilon\tilde{v}_x &= -\rho_0 k^2\left(\dot{\widehat{v}}_{x0} - i\omega\widehat{v}_{x0}\right) + \frac{\partial}{\partial x}\left[\rho_0\left(\dot{\widehat{v}}'_{x0} - i\omega\widehat{v}'_{x0}\right)\right] \\ &= -\rho_0 k^2\left(\dot{\widehat{v}}_{x0} - i\omega\widehat{v}_{x0}\right) + \rho_0\left(\dot{\widehat{v}}''_{x0} - i\omega\widehat{v}''_{x0}\right) + \frac{d\rho_0}{dx}\left(\dot{\widehat{v}}'_{x0} - i\omega\widehat{v}'_{x0}\right) \\ &= \rho_0\left[\left(\dot{\widehat{v}}''_{x0} - k^2\dot{\widehat{v}}_{x0}\right) - i\omega\left(\widehat{v}''_{x0} - k^2\widehat{v}_{x0}\right)\right] + \frac{d\rho_0}{dx}\left(\dot{\widehat{v}}'_{x0} - i\omega\widehat{v}'_{x0}\right)\end{aligned} \tag{4.12}$$

Two equations that will help simplify this equation are derived from the assumption of incompressibility and the definition of vorticity:

- $\nabla\cdot\mathbf{v} = 0$, from which it follows that $\widehat{v}'_x = -ik\widehat{v}_z$.
- The vorticity, defined by $\Omega(\mathbf{x},t)\widehat{\mathbf{y}} = \widehat{\Omega}(x,t)e^{ikz}\widehat{\mathbf{y}} = \nabla\times\mathbf{v}(\mathbf{x},t)$, is given by

$$\widehat{\Omega}(x,t) = -\frac{i}{k}\left(\widehat{v}''_x - k^2\widehat{v}_x\right). \tag{4.13}$$

Using the above two equations, Equation (4.12) simplifies to

$$\frac{d}{dx}\left[\epsilon\frac{d\tilde{v}_x}{dx}\right] - k^2\epsilon\tilde{v}_x = f(x), \tag{4.14}$$

where

$$f(x) = ik\left\{\rho_0\left[\dot{\widehat{\Omega}}_0 - i\omega\widehat{\Omega}_0\right] - \frac{d\rho_0}{dx}\left(\dot{\widehat{v}}_{z0} - i\omega\widehat{v}_{z0}\right)\right\}. \tag{4.15}$$

This function is the corrected version of Equations (11)-(13) of Rae and Roberts (1981). The red operator is the corrected version. However, because Rae and Roberts (1981) assumed that $\partial\rho_0/\partial x = 0$, this error was inconsequential. Additionally, a typographical error was made in the above equation, where they wrote subscript x in place of our subscript z. Note that there is a factor of -1 discrepancy between this function and that of Rae and Roberts (1981) due to taking different Fourier forms. For future utility, we define $\Psi_0 = \Psi(x,0)$ by function $\Psi(x,t) = k[\rho_0\widehat{\Omega}(x,t) - \rho'_0\widehat{v}_z(x,t)]$ so that $f(x,\omega) = \omega\Psi_0 + i\frac{\partial\Psi_0}{\partial t}$.

Consider an equilibrium structuring of this plasma with magnetic field and density profiles given by

$$B(x) = \begin{cases} B_- & \text{for } x \leq 0, \\ B_+ & \text{for } x > 0, \end{cases} \quad \text{and} \quad \rho(x) = \begin{cases} \rho_- & \text{for } x \leq 0, \\ \rho_+ & \text{for } x > 0, \end{cases} \tag{4.16}$$

where B_j and ρ_j are uniform for $j = -, +$. In this equilibrium, Equation (4.14) tells us that transverse velocity perturbation is related to initial perturbations by

$$\frac{d^2\tilde{v}_x}{dx^2} - k^2\tilde{v}_x = \begin{cases} f(x)/\epsilon_-, & \text{for } x \leq 0, \\ f(x)/\epsilon_+, & \text{for } x > 0, \end{cases} \tag{4.17}$$

and satisfies the boundary conditions

$$\lim_{x\to-\infty} \tilde{v}_x(x) = \lim_{x\to\infty} \tilde{v}_x(x) = 0 \text{ and } \lim_{x\to0^-} \tilde{v}_x(x) = \lim_{x\to0^+} \tilde{v}_x(x). \tag{4.18}$$

The first of these boundary conditions ensures that plasma far from the interface is unaffected by its oscillation. The second ensure that the plasma at the interface remains connected. The latter these is referred to as the *kinematic boundary condition* for a free surface in fluid mechanics (Goedbloed and Poedts, 2004).

The problem given by Equation (4.17) with boundary conditions (4.18) is a *Sturm-Liouville problem* (Boyce and DiPrima, 2012). Sturm-Liouville theory tells us that the Green's function, $G(x; s)$, corresponding to Equation (4.17) must satisfy

$$\frac{\partial^2 G}{\partial x^2} - k^2 G = \delta(x - s), \quad G(-\infty; s) = G(\infty; s) = 0, \tag{4.19}$$

where δ denotes the Dirac delta function. It is instructive to piecewise define the Green's function as

$$G(x; s) = \begin{cases} G_-(x; s), & \text{for } x \leq 0, \\ G_+(x; s), & \text{for } x > 0. \end{cases} \tag{4.20}$$

The general solution of the equation for G_- for $x < 0$ is

$$G_-(x; s) = c_1 e^{kx} + c_2 e^{-kx}, \tag{4.21}$$

where c_1 and c_2 are constants with $c_2 = 0$ for $x < s$ and $c_1 = 0$ for $x > s$. Ensuring that G_- and $\partial G_-/\partial x$ have respective jumps of 0 and 1 at $x = s$ determines c_1 and c_2, so that $G_-(x; s)$ is

$$\begin{aligned} G_-(x; s) &= -\frac{1}{2k} \begin{cases} e^{kx}e^{-ks}, & \text{for } -\infty < x < s, \\ e^{-kx}e^{ks}, & \text{for } s < x < 0, \end{cases} \\ &= -\frac{1}{2k} \left[e^{ks}e^{-kx}H(x - s) + e^{-ks}e^{kx}H(s - x) \right], \end{aligned} \tag{4.22}$$

The Sturm-Liouville problem for each plasma ($x < 0$ and $x > 0$) has an inhomogeneous boundary condition at the interface. Therefore, we must add to the standard Green's function solution a term that is a solution to the homogeneous version of Equation (4.17) with inhomogeneous boundary conditions. In this manner, we find that the solution for $x < 0$ is

$$\tilde{v}_x(x) = \tilde{A}_- e^{kx} + \frac{1}{\epsilon_-} \int_{-\infty}^{0} G(x;s) f(s) ds. \tag{4.23}$$

Similarly, the solution for $x > 0$ is

$$\tilde{v}_x(x) = \tilde{A}_+ e^{-kx} + \frac{1}{\epsilon_+} \int_{0}^{\infty} G(x;s) f(s) ds. \tag{4.24}$$

where

$$G(x;s) = -\frac{1}{2k} \left[e^{ks} e^{-kx} H(x-s) + e^{-ks} e^{kx} H(s-x) \right]. \tag{4.25}$$

Equation (4.23) is the corrected version of Equation (16) in Rae and Roberts (1981). In Rae and Roberts (1981), they have a $-$ instead of a $+$. The erroneous solution is shown to not satisfy Equation (4.17) in Appendix B.

By imposing continuity of transverse velocity perturbation, we can determine the constants A_- and A_+ to be

$$\tilde{A}_+ = \frac{1}{k(\epsilon_- + \epsilon_+)} \left[- \int_{-\infty}^{0} f(s) e^{ks} ds - \frac{1}{2} \left(1 - \frac{\epsilon_-}{\epsilon_+} \right) \int_{0}^{\infty} f(s) e^{-ks} ds \right], \tag{4.26}$$

$$\tilde{A}_- = \frac{1}{k(\epsilon_- + \epsilon_+)} \left[- \int_{0}^{\infty} f(s) e^{-ks} ds - \frac{1}{2} \left(1 - \frac{\epsilon_+}{\epsilon_-} \right) \int_{-\infty}^{0} f(s) e^{ks} ds \right], \tag{4.27}$$

which differs to that given by Rae and Roberts (1981) by the red operators.

The solution in time is found by taking the inverse Laplace transform of Equations (4.23) and (4.24). This is not possible for arbitrary initial conditions. In the following subsection, we derive the solution for several specific initial conditions.

4.3.1 Solution for specific initial conditions

The corrected solutions for specific initial conditions used by Rae and Roberts (1981) are given below:

1. *Vorticity constant everywhere at* $t = 0$. When the initial vorticity is constant with respect to x, *i.e.* $\Omega(x,0) = \Omega_0$, Equation (B.12) tells us that the velocity perturbation is

$$\tilde{v}_x = -\frac{\rho_0 \omega \Omega_0}{k} \begin{cases} \left(1 + \frac{\epsilon_- - \epsilon_+}{\epsilon_- + \epsilon_+} e^{kx} \right) / \epsilon_-, & \text{for } x \leq 0, \\ \left(1 + \frac{\epsilon_+ - \epsilon_-}{\epsilon_- + \epsilon_+} e^{-kx} \right) / \epsilon_+, & \text{for } x > 0. \end{cases} \tag{4.28}$$

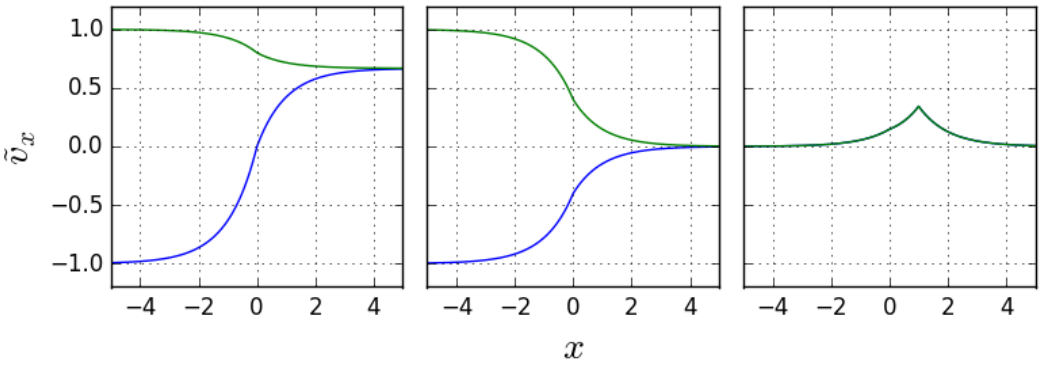

Figure 4.2: Original Rae and Roberts (1981) (blue) and corrected (green) solutions for the velocity perturbation, $\tilde{v}_x$, for initial condition 1 (left), 2 (middle), and 3 (right). The blue and green curves are the same in the right panel.

2. *Step function vorticity at* $t = 0$. When the initial vorticity is given by $\Omega(x, 0) = \Omega_0 H(-x)$, Equation (B.12) tells us that the velocity perturbation is

$$\tilde{v}_x = -\frac{\rho_0 \omega \Omega_0}{k} \begin{cases} \left(1 - \frac{\epsilon_+}{\epsilon_- + \epsilon_+} e^{kx}\right) / \epsilon_-, & \text{for } x \leq 0, \\ \frac{1}{\epsilon_- + \epsilon_+} e^{-kx}, & \text{for } x > 0. \end{cases} \tag{4.29}$$

3. *Impulsive vorticity at* $t = 0$. When the initial vorticity[7] is given by $\Omega(x, 0) = \Omega_0 \delta(k(x - x_0))$, for $x_0 > 0$, Equation (B.12) tells us that the velocity perturbation is

$$\tilde{v}_x = -\frac{\rho_0 \omega \Omega_0}{k} \begin{cases} \frac{1}{\epsilon_- + \epsilon_+} e^{-k(x_0 - x)}, & \text{for } x \leq 0, \\ \frac{\epsilon_+ - \epsilon_-}{2\epsilon_+(\epsilon_- + \epsilon_+)} e^{-k(x + x_0)} + \frac{e^{-k(x_0 - x)}}{2\epsilon_+}, & \text{for } 0 < x \leq x_0, \\ \frac{\epsilon_+ - \epsilon_-}{2\epsilon_+(\epsilon_- + \epsilon_+)} e^{-k(x + x_0)} + \frac{e^{-k(x - x_0)}}{2\epsilon_+}, & \text{for } x > x_0. \end{cases} \tag{4.30}$$

Figure 4.2 illustrates the solutions for the transverse velocity perturbation, $\tilde{v}_x$, for the three specific initial conditions given above, showing both the original and corrected initial transverse velocities.

The full solution for the transverse velocity, $v_x(x, z, t) = \widehat{v}_x(x, t) e^{ikz}$ is found by taking the inverse Laplace transform of $\tilde{v}_x$, such that

$$\widehat{v}_x(x, t) = \frac{1}{2\pi} \lim_{L \to \infty} \int_{-L + i\sigma}^{L + i\sigma} \tilde{v}_x(x) e^{-i\omega t} d\omega, \tag{4.31}$$

where σ is real and such that all the singularities of the integrand lie below the contour of integration in the complex plane. The singularities in the solutions

[7] Note that Rae and Roberts (1981) incorrectly use the impulsive initial condition $\Omega(x, 0) = \Omega_0 \delta(x - x_0)$. This can be shown to be erroneous by considering that the dimensions of the left-hand side, $\Omega(x, 0)$, are [Time^{-1}] and therefore not equal to the dimensions of the right-hand side, $\Omega_0 \delta(x - x_0)$, namely [Distance^{-1}Time^{-1}]. They also omit, without explanation, the density, ρ_0, from their solutions. Neither of these errors are consequential.

in Laplace space are all poles. Therefore, using Cauchy's Residue Theorem, it follows that

$$\widehat{v}_x(x,t) = -i \sum \text{Res}\left\{\tilde{v}_x e^{-i\omega t}\right\}, \tag{4.32}$$

where the summation is over all the poles of the argument.

Considering initial condition 1, with uniform vorticity, the singularities of this function occur at $\epsilon_- = 0$, $\epsilon_+ = 0$, and $\epsilon_- + \epsilon_+ = 0$. This corresponds to simple poles at $\omega = \pm k v_{A-}$, $\omega = \pm k v_{A+}$, and $\omega = \pm k v_s$, respectively, where

$$v_s = \sqrt{\frac{v_{A-}^2 + v_{A+}^2}{2}}. \tag{4.33}$$

The residues associated with each singularity are

$$\text{Res}\left\{\tilde{v}_x e^{-i\omega t}; \pm k v_{A+}\right\} = \frac{\Omega_0}{2k} e^{\mp i k v_{A+} t} \begin{cases} 0, & \text{for } x \leq 0, \\ 1 - e^{-kx}, & \text{for } x > 0, \end{cases} \tag{4.34}$$

$$\text{Res}\left\{\tilde{v}_x e^{-i\omega t}; \pm k v_{A-}\right\} = \frac{\Omega_0}{2k} e^{\mp i k v_{A-} t} \begin{cases} 1 - e^{kx}, & \text{for } x \leq 0, \\ 0, & \text{for } x > 0, \end{cases} \tag{4.35}$$

$$\text{Res}\left\{\tilde{v}_x e^{-i\omega t}; \pm k v_s\right\} = \frac{\Omega_0}{2k} e^{\mp i k v_s t} \begin{cases} e^{kx}, & \text{for } x \leq 0, \\ e^{-kx}, & \text{for } x > 0. \end{cases} \tag{4.36}$$

By summing these residues,

$$\widehat{v}_x(x,t) = -\frac{i\Omega_0}{k} \begin{cases} \cos(k v_{A-} t)\left(1 - e^{kx}\right) + \cos(k v_s t) e^{kx}, & \text{for } x \leq 0, \\ \cos(k v_{A+} t)\left(1 - e^{-kx}\right) + \cos(k v_s t) e^{-kx}, & \text{for } x > 0. \end{cases} \tag{4.37}$$

This solution differs from that given by Rae and Roberts (1981) most notably by a contribution from surface waves (second term), not just body waves (first term). The solution given by Rae and Roberts (1981) contained only body modes.

The full solution for v_x when the initial disturbance is of the form of a single wave, is recovered by multiplying the above expression by e^{ikz}. In reality, an initial disturbance will be of finite extent. Solutions for such a disturbance are the subject of the following subsection.

4.3.2 Solution for an initial disturbance of finite extent

The response to a disturbance of finite extent is obtained by a superposition over all the Fourier modes. That is, we must integrate over the wavenumber k using the inverse Fourier transform, namely

$$v_x(x,z,t) = \frac{1}{2\pi} \int_{-\infty}^{\infty} \widehat{v}_x(x,t) e^{ikz} \, dk. \tag{4.38}$$

Let's consider an initial impulse that has uniform vorticity with respect to x and is uniform over a finite range $[-z_0, z_0]$, outside of which it is zero. Precisely, the initial velocity is

$$v_x(x,z,0) = \frac{v_0}{2z_0}\left[H(z+z_0) - H(z-z_0)\right], \tag{4.39}$$

where H is the Heaviside step function and v_0 is constant. The division by $2z_0$ ensures that the integral of the initial velocity is not dependent on the size of the domain of the initial disturbance, $2z_0$. In particular, it means that in the limit as $z_0 \to 0$, the initial velocity is a Dirac delta function of z. Therefore, the initial vorticity is

$$\Omega(x,z,0)\widehat{\mathbf{y}} = \nabla \times \mathbf{v} = \frac{v_0}{2z_0}\left[\delta(z+z_0) - \delta(z-z_0)\right]\widehat{\mathbf{y}}, \tag{4.40}$$

which has Fourier transform

$$\widehat{\Omega}(x,0) = \int_{-\infty}^{\infty} \Omega(x,z,0)e^{-ikz}\,dz = i\frac{v_0}{z_0}\sin(kz_0). \tag{4.41}$$

The temporal evolution of this initial velocity pulse over a finite z-domain is, for the region $\pm x > 0$,

$$\begin{aligned} v_x &= -\frac{v_0}{2\pi z_0}\int_{\infty}^{\infty}\frac{1}{k}\sin(kz_0)[(\cos(kv_{A\pm}t) - \cos(kv_s t))e^{-|k||x|} \\ &\qquad - \cos(kv_{A\pm}t)]e^{ikz}\,dk \\ &= -\frac{v_0}{\pi z_0}\int_0^{\infty}\frac{1}{k}[\sin(k(z+z_0)) - \sin(k(z-z_0))] \\ &\qquad \left[(\cos(kv_{A\pm}t) - \cos(kv_s t))e^{-k|x|} - \cos(kv_{A\pm}t)\right]\,dk. \end{aligned} \tag{4.42}$$

Here, we have used the fact that an odd function integrated over the real line vanishes and an even function integrated over the real line is twice its integral over the positive real line. We also used the product-to-sum identity $2\cos\theta\sin\phi = \sin(\theta+\phi) - \sin(\theta-\phi)$. Further, by use of the similar identity $2\sin\theta\cos\phi = \sin(\theta+\phi) + \sin(\theta-\phi)$, Equation (4.42) can be reduced to a series of integrals of the form

$$\int_0^{\infty}\frac{1}{k}\sin(k(z+z_0+v_{A\pm}))e^{-k|x|}\,dk, \tag{4.43}$$

and

$$\int_0^{\infty}\frac{1}{k}\sin(k(z+z_0+v_{A\pm}))\,dk. \tag{4.44}$$

Both of these are known integrals (see, for example, Abramowitz and Stegun, 1965). The general form of the first integral can be evaluated like

$$\int_0^{\infty}\frac{1}{x}\sin(ax)e^{-bx}\,dx = \tan^{-1}\left(\frac{a}{b}\right), \tag{4.45}$$

for $b > 0$. The second of these is a limiting case of the *sine integral*, $\mathrm{Si}(x)$, which can be evaluated in its general form as

$$\int_0^\infty \frac{1}{t}\sin(at)\ dt = \lim_{x\to\infty}\int_0^{ax}\frac{1}{t}\sin t\ dt \tag{4.46}$$

$$= \lim_{x\to\infty}\mathrm{Si}(ax) \tag{4.47}$$

$$= \begin{cases} -\pi/2, & \text{if } a<0, \\ 0, & \text{if } a=0, \\ \pi/2, & \text{if } a>0, \end{cases} \tag{4.48}$$

$$= \frac{\pi}{2}\left[2H(a)-1\right]. \tag{4.49}$$

Using the above results leads us to the solution

$$\begin{aligned} v_x = \frac{v_0}{4\pi z_0}\Bigg[&-\tan^{-1}\left(\frac{z+z_0+v_{A\pm}t}{|x|}\right) - \tan^{-1}\left(\frac{z+z_0-v_{A\pm}t}{|x|}\right) \\ &+\tan^{-1}\left(\frac{z-z_0+v_{A\pm}t}{|x|}\right) + \tan^{-1}\left(\frac{z-z_0-v_{A\pm}t}{|x|}\right) \\ &+\tan^{-1}\left(\frac{z+z_0+v_s t}{|x|}\right) + \tan^{-1}\left(\frac{z+z_0-v_s t}{|x|}\right) \\ &-\tan^{-1}\left(\frac{z-z_0+v_s t}{|x|}\right) - \tan^{-1}\left(\frac{z-z_0-v_s t}{|x|}\right) \\ &+\pi\left\{H(z+z_0+v_{A\pm}t) + H(z+z_0-v_{A\pm}t)\right. \\ &\left.-H(z-z_0+v_{A\pm}t) - H(z-z_0-v_{A\pm}t)\right\}\Bigg]. \end{aligned} \tag{4.50}$$

By taking $t = 0$ in Equation (4.50), the initial velocity profile is recovered.

The solution given by Equation (4.50) is plotted in Figure 4.3. The initial perturbation is illustrated in the upper left panel, showing a band of constant velocity between $-z_0 < z < z_0$, where $z_0 = 1$. It is clear that the waves in the left half-plane are propagating more slowly than the waves in the right half-plane. This is because the Alfvén speed in the left half-plane, v_{A-}, is half that of the right, v_{A+}.

The solution is made up of a superposition of several wave modes:

1. The body wave pulses propagating at speed $v_{A\pm}$, depending on the side of the interface. These waves correspond to the four Heaviside functions in Equation (4.50). They can be seen in Figure 4.3 as the propagating bands of positive velocity (blue).

2. The wakes at the front and back on the body waves, which correspond to the first four $\tan^{-1}$ functions in Equation (4.50). They can be seen

in Figure 4.3 as the regions of weakly positive velocity (blue) in front of the body waves and regions of weakly negative velocity (red) behind the body waves.

3. The surface wave pulses propagating at speed v_s. These waves correspond to the last four $\tan^{-1}$ functions in Equation (4.50). They can be seen in Figure 4.3 as the regions of positive velocity (blue) close to the interface, propagating at an intermediate speed between the two Alfvén speeds.

Each wave mode propagates in the positive and negative z-directions because the system has reflectional symmetry about the $z = 0$ axis.

A limiting case that allows for direct comparison with Rae and Roberts (1981) is that of an infinitely thin initial pulse at $z = 0$. We can recover this limit from Equation (4.50). In the limit as $z_0 \to 0$, the initial velocity becomes $v_x(x, z, 0) = v_0\delta(z)$, and its evolution obeys

$$\begin{aligned} v_x(x,z,t) = \frac{v_0}{2\pi}\Bigg[&- \frac{|x|}{x^2 + (z + v_{A\pm}t)^2} - \frac{|x|}{x^2 + (z - v_{A\pm}t)^2} \\ &+ \frac{|x|}{x^2 + (z + v_s t)^2} + \frac{|x|}{x^2 + (z - v_s t)^2} \\ &+ \pi\{\delta(z + v_{A\pm}t) + \delta(z - v_{A\pm}t)\}\Bigg]. \end{aligned} \tag{4.51}$$

In deriving the above limit we have used the results that, by definition of the Dirac delta function,

$$\lim_{z_0 \to 0}\left[\frac{1}{2z_0}\{H(z + z_0) - H(z - z_0)\}\right] = \delta(z), \tag{4.52}$$

and, by L'Hopital's rule,

$$\begin{aligned} &\lim_{z_0\to 0}\left[\frac{1}{2z_0}\left\{\tan^{-1}\left(\frac{z + z_0 + v_{A\pm}t}{|x|}\right) - \tan^{-1}\left(\frac{z - z_0 + v_{A\pm}t}{|x|}\right)\right\}\right] \\ &= \frac{1}{2}\lim_{z_0\to 0}\frac{d}{dz_0}\left[\tan^{-1}\left(\frac{z + z_0 + v_{A\pm}t}{|x|}\right) - \tan^{-1}\left(\frac{z - z_0 + v_{A\pm}t}{|x|}\right)\right] \\ &= \frac{1}{2}\lim_{z_0\to 0}\left[\frac{|x|}{x^2 + (z + z_0 + v_{A\pm}t)^2} + \frac{|x|}{x^2 + (z - z_0 + v_{A\pm}t)^2}\right] \\ &= \frac{|x|}{x^2 + (z + v_{A\pm}t)^2}. \end{aligned} \tag{4.53}$$

Equation (4.51), where we can see the contribution from the surface mode as well as the body mode, is the corrected version of Equation (34) in Rae and Roberts (1981).

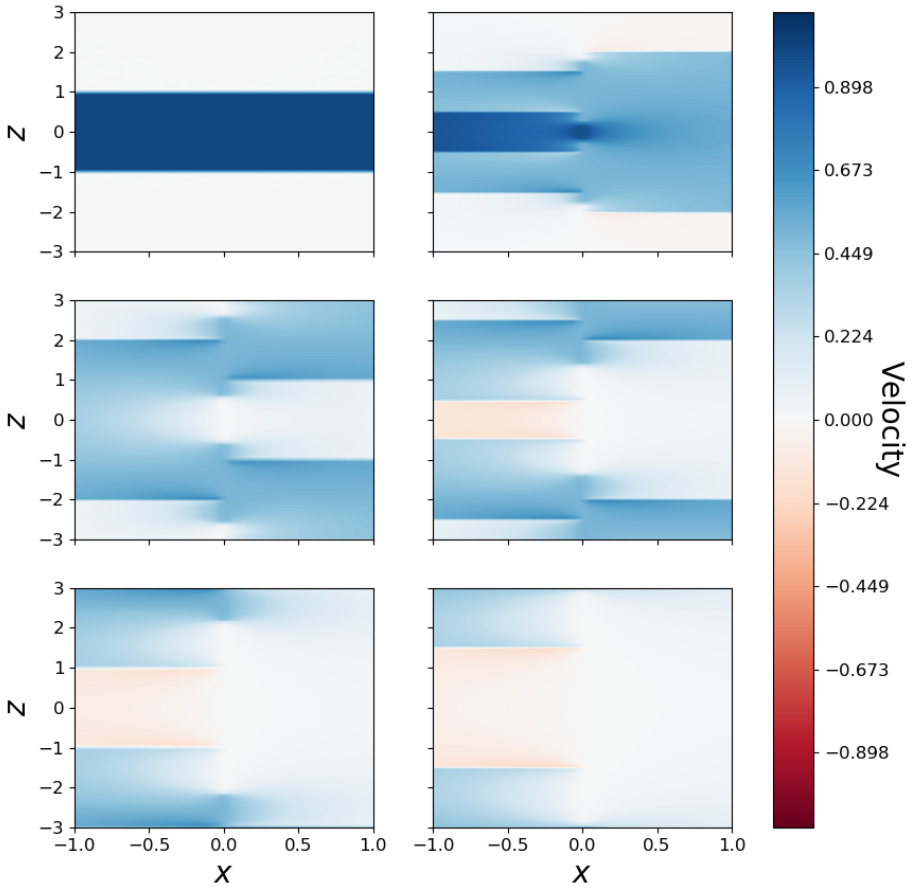

Figure 4.3: Evolution of waves propagating along a tangential interface between incompressible plasmas. Time increases along the rows and down the columns. The interface is at $x = 0$ and the initial perturbation is a constant velocity confined to the band $-z_0 < z < z_0$, where $z_0 = 1$. The Alfvén speeds in each half-plane are related by $v_{A+} = 2v_{A-}$.

4.4 Wave evolution in a slab waveguide

Building up the complexity of IVP, we next derive the evolution of plasma in an initially perturbed slab waveguide. We begin with an asymmetric slab of incompressible plasma (Section 4.4.1) and later introduce compressibility (Section 4.4.2).

4.4.1 Incompressible asymmetric slab

Consider equilibrium magnetic field and density profiles given by

$$B(x) = \begin{cases} B_1, & \text{if } x < -x_0, \\ B_0, & \text{if } |x| \le x_0, \\ B_2, & \text{if } x > x_0, \end{cases} \quad \text{and} \quad \rho(x) = \begin{cases} \rho_1, & \text{if } x < -x_0, \\ \rho_0, & \text{if } |x| \le x_0, \\ \rho_2, & \text{if } x > x_0, \end{cases} \tag{4.54}$$

Perturbation to the transverse velocity perturbations are related to initial perturbations of this equilibrium by

$$\frac{d^2\tilde{v}_x}{dx^2} - k^2\tilde{v}_x = \begin{cases} f(x,\omega)/\epsilon_1, & \text{if } x < -x_0, \\ f(x,\omega)/\epsilon_0, & \text{if } |x| \le x_0, \\ f(x,\omega)/\epsilon_2, & \text{if } x > x_0, \end{cases} \tag{4.55}$$

under the boundary conditions

$$\lim_{x\to-\infty} \tilde{v}_x(x) = \lim_{x\to\infty} \tilde{v}_x(x) = 0, \text{ and } \lim_{x\to\pm x_0^-} \tilde{v}_x(x) = \lim_{x\to\pm x_0^+} \tilde{v}_x(x). \tag{4.56}$$

Sturm-Liouville Theory tells us that the Green's function, $G(x;s)$, corresponding to Equation (4.55) must satisfy

$$\frac{\partial^2 G}{\partial x^2} - k^2 G = \delta(x-s), \quad G(-x_0;s) = G(x_0;s) = 0. \tag{4.57}$$

It is instructive to piecewise define the Green's function as

$$G(x;s) = \begin{cases} G_1(x;s), & \text{if } x < -x_0, \\ G_0(x;s), & \text{if } |x| \le x_0, \\ G_2(x;s), & \text{if } x_0 < x. \end{cases} \tag{4.58}$$

The general solution, for $|x| \le x_0$, of the equation for G_0 is

$$G_0(x;s) = c_1 \sinh(k(x-x_0)) + c_2 \sinh(k(x+x_0)), \tag{4.59}$$

where $c_1 = 0$ for $x < s$ and $c_2 = 0$ for $x > s$. Ensuring G_0 and $\partial G_0/\partial x$ have jumps of 0 and 1, respectively, at $x = s$ determines c_1 and c_2, so that $G_0(x;s)$ is

$$G_0(x;s) = \frac{1}{k\sinh(2kx_0)} \begin{cases} \sinh(k(s-x_0))\sinh(k(x+x_0)), & \text{if } -x_0 < x < s, \\ \sinh(k(x-x_0))\sinh(k(s+x_0)), & \text{if } s < x < x_0. \end{cases} \tag{4.60}$$

The boundary conditions at the interfaces are inhomogeneous, therefore we must add to the standard Green's function solution a term that is a solution to the homogeneous equation and the inhomogeneous boundary conditions. In this manner, we find that the solution within the slab is

$$\begin{aligned}\tilde{v}_x(x) =& \frac{1}{\sinh 2kx_0}\left[\tilde{A}_1 \sinh(k(x_0 - x)) + \tilde{A}_2 \sinh(k(x_0 + x))\right] \\ &+ \frac{1}{\epsilon_0}\int_{-x_0}^{x_0} G_0(x;s) f(s,\omega) ds,\end{aligned} \tag{4.61}$$

where $\tilde{A}_1 = \tilde{v}_x(-x_0)$ and $\tilde{A}_2 = \tilde{v}_x(x_0)$.

Similarly, we find that the Green's function for the plasma outside the slab is

$$G_1(x;s) = \frac{1}{k}\begin{cases} e^{k(x+x_0)}\sinh(k(s+x_0)), & \text{if } x < s, \\ e^{k(s+x_0)}\sinh(k(x+x_0)), & \text{if } s < x < -x_0, \end{cases} \tag{4.62}$$

for $x < -x_0$, and

$$G_2(x;s) = -\frac{1}{k}\begin{cases} e^{-k(s-x_0)}\sinh(k(x-x_0)), & \text{if } x_0 < x < s, \\ e^{-k(x-x_0)}\sinh(k(s-x_0)), & \text{if } s < x, \end{cases} \tag{4.63}$$

for $x > x_0$. Therefore, the solution outside the slab is

$$\tilde{v}_x(x) = \tilde{A}_1 e^{k(x_0+x)} + \frac{1}{\epsilon_1}\int_{-\infty}^{-x_0} G_1(x;s) f(s,\omega) ds, \tag{4.64}$$

for $x < -x_0$, and

$$\tilde{v}_x(x) = \tilde{A}_2 e^{k(x_0-x)} + \frac{1}{\epsilon_2}\int_{x_0}^{\infty} G_2(x;s) f(s,\omega) ds, \tag{4.65}$$

for $x > x_0$.

To establish physically relevant solutions, we require that the transverse velocity and the total pressure are continuous over each interface. The construction of Equations (4.61), (4.64), and (4.65) ensures that the transverse velocity is automatically continuous over the boundaries. Using Equation (2.15), the perturbation in the total pressure for a compressible plasma is given by $\tilde{p}_T(x) = \Lambda \tilde{v}_x'/m$. When the plasma is incompressible, $m^2 \to k^2$. Therefore, continuity in total pressure is equivalent to continuity in $\epsilon(x)\tilde{v}_x'(x)$ for an incompressible plasma. Applying this boundary condition gives

$$\tilde{A}_1(\omega) = \frac{T_1(\omega)}{kD(\omega)}, \quad \tilde{A}_2(\omega) = \frac{T_2(\omega)}{kD(\omega)}, \tag{4.66}$$

where

$$D(\omega) = \epsilon_0(\epsilon_1 + \epsilon_2)\cosh(2kx_0) + (\epsilon_0^2 + \epsilon_1\epsilon_2)\sinh(2kx_0) \tag{4.67}$$

is called the *dispersion function* and $T_{1,2}$ are functionals given by

$$T_1(\omega) = T_1[f](\omega) = -(I_0^- + I_1)\left[\epsilon_0 \cosh(2kx_0) + \epsilon_2 \sinh(2kx_0)\right] - \epsilon_0\left(I_0^+ + I_2\right), \tag{4.68}$$

$$T_2(\omega) = T_2[f](\omega) = -\epsilon_0\left(I_0^- + I_1\right) - \left(I_0^+ + I_2\right)\left[\epsilon_0 \cosh(2kx_0) + \epsilon_1 \sinh(2kx_0)\right], \tag{4.69}$$

where

$$I_0^{\pm} = I_0^{\pm}[f](\omega) = \int_{-x_0}^{x_0} \frac{\sinh(k(x_0 \pm s))}{\sinh(2kx_0)} f(s,\omega) ds, \tag{4.70}$$

$$I_1 = I_1[f](\omega) = \int_{-\infty}^{-x_0} e^{k(x_0+s)} f(s,\omega) ds, \tag{4.71}$$

$$I_2 = I_2[f](\omega) = \int_{x_0}^{\infty} e^{k(x_0-s)} f(s,\omega) ds. \tag{4.72}$$

4.4.1.1 Solution in time

To recover the transverse velocity, $v_x(x,t)$, we employ the inverse Laplace transform. Focusing firstly on the region $x < -x_0$, the solution is

$$v_x = \mathcal{L}^{-1}\left\{\tilde{A}_1 e^{k(x+x_0)} + \frac{1}{\epsilon_1}\int_{-\infty}^{-x_0} G_1(x;s) f(s,\omega) ds\right\}, \tag{4.73}$$

$$= e^{k(x+x_0)}\mathcal{L}^{-1}\left\{\tilde{A}_1\right\} + \int_{-\infty}^{-x_0} G_1(x;s)\mathcal{L}^{-1}\left\{\frac{f(s,\omega)}{\epsilon_1}\right\} ds, \tag{4.74}$$

$$= e^{k(x+x_0)}\mathcal{L}^{-1}\left\{\tilde{A}_1\right\} \tag{4.75}$$

$$+ \int_{-\infty}^{-x_0} G_1(x;s)\left[\Psi(s,0)\mathcal{L}^{-1}\left\{\frac{\omega}{\epsilon_1}\right\} + i\frac{\partial \Psi}{\partial t}(s,0)\mathcal{L}^{-1}\left\{\frac{1}{\epsilon_1}\right\}\right] ds. \tag{4.76}$$

We evaluate each of the three inverse Laplace transforms in turn.

The first inverse Laplace transform,

$$\mathcal{L}^{-1}\{\tilde{A}_1\} = \frac{1}{2\pi}\lim_{L\to\infty}\int_{-L+i\sigma}^{L+i\sigma} \tilde{A}_1 e^{-i\omega t}\, d\omega, \tag{4.77}$$

is calculated as follows. The functions $\epsilon_{0,1,2}$ are quadratic in ω, and are therefore entire. The integrals $I_{1,2}$ and $I_0^{\pm}$ are, in general, linear functions of ω so also contribute no singularities. Therefore, T_1 and T_2 are entire functions. Hence, the singularities of $\tilde{A}_1$ are precisely the zeros of the dispersion function, $D(\omega)$.

The zeros of $D(\omega)$ are determined by firstly noting that $D = 0$ is the dispersion relation of the corresponding eigenvalue problem solved in Chapter 2 and by Zsámberger et al. (2018). To recap, the dispersion relation governing

transverse wave propagation parallel to the magnetic field in an asymmetric slab of compressible plasma is given by

$$2(\Lambda_0^2 + \Lambda_1\Lambda_2) + \Lambda_0(\Lambda_1 + \Lambda_2)[\tanh(m_0x_0) + \coth(m_0x_0)] = 0, \tag{4.78}$$

where

$$\Lambda_j = -\frac{i\rho_j(k^2v_{Aj}^2 - \omega^2)}{\omega m_j}, \quad \text{and} \quad m_j^2 = \frac{(k^2c_j^2 - \omega^2)(k^2v_{Aj}^2 - \omega^2)}{(c_j^2 + v_{Aj}^2)(k^2c_{Tj}^2 - \omega^2)}, \tag{4.79}$$

for $j = 0, 1, 2$. When compressibility is neglected, such that the sound speeds, c_j, approach infinity, we have $c_{Tj}^2 \to v_{Aj}^2$, $m_j^2 \to k^2$, and therefore $\Lambda_j = -i\rho_j(k^2v_{Aj}^2 - \omega^2)/\omega k = -i\epsilon_j/\omega k$, for $j = 0, 1, 2$. Therefore, Equation (4.78) can be reduced to the dispersion relation for an incompressible magnetic slab, which is

$$2\left(\epsilon_0^2 + \epsilon_1\epsilon_2\right) + \epsilon_0(\epsilon_1 + \epsilon_2)[\tanh(m_0x_0) + \coth(m_0x_0)] = 0. \tag{4.80}$$

This equation can easily to shown to be equivalent to $D(\omega) = 0$, where $D(\omega)$ is given by Equation (4.67). It follows that the zeros of $D(\omega)$ are precisely the eigenvalues of the asymmetric incompressible magnetic slab. This is a specific case of the powerful general result that the solutions of eigenvalue problems contribute to solutions of initial value problems. This is explored in the MHD setting by Goedbloed and Poedts (2004), Chapter 10.2.

The zeros of D are found by writing the equation $D(\omega) = 0$ as

$$\epsilon_0(\epsilon_1 + \epsilon_2) + \left(\epsilon_0^2 + \epsilon_1\epsilon_2\right)\tanh(2kx_0) = 0 \tag{4.81}$$

and substituting expressions for $\epsilon(x)$, which gives

$$\begin{aligned}&\rho_0\left(k^2v_{A0}^2 - \omega^2\right)\left[\rho_1\left(k^2v_{A1}^2 - \omega^2\right) + \rho_2\left(k^2v_{A2}^2 - \omega^2\right)\right] \\ &+ \left[\rho_0^2\left(k^2v_{A0}^2 - \omega^2\right)^2 + \rho_1\rho_2\left(k^2v_{A1}^2 - \omega^2\right)\left(k^2v_{A2}^2 - \omega^2\right)\right]\tanh(2kx_0) = 0.\end{aligned} \tag{4.82}$$

The above equation can be rewritten as a quadratic in $(\omega/k)^2$, namely

$$a\left(\frac{\omega}{k}\right)^4 + b\left(\frac{\omega}{k}\right)^2 + c = 0, \tag{4.83}$$

which has solutions

$$\left(\frac{\omega_{0\pm}}{k}\right)^2 = \frac{-b \pm \sqrt{b^2 - 4ac}}{2a}, \tag{4.84}$$

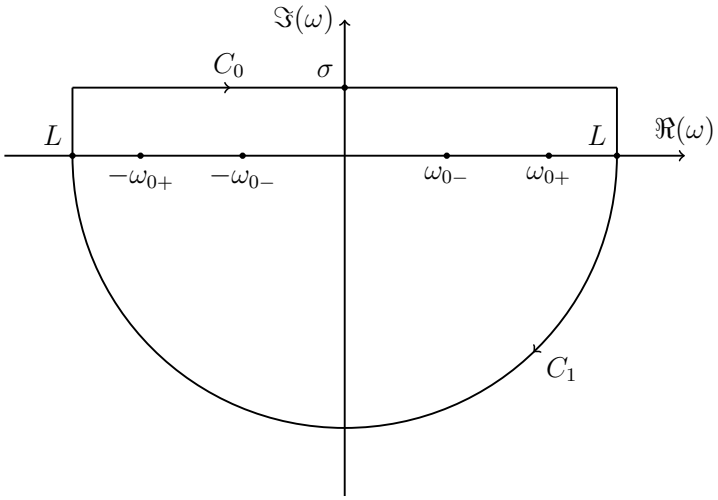

Figure 4.4: Bromwich contour for the complex integration of $\tilde{A}_{1,2}$.

where

$$a = \left(\rho_0^2 + \rho_1\rho_2\right)\tanh(2kx_0) + \rho_0(\rho_1 + \rho_2), \tag{4.85}$$

$$b = -\left(2\rho_0^2 v_{A0}^2 + \rho_1\rho_2\left(v_{A1}^2 + v_{A2}^2\right)\right)\tanh(2kx_0) - \rho_0\left\{\rho_1\left(v_{A0}^2 + v_{A1}^2\right) + \rho_2\left(v_{A0}^2 + v_{A2}^2\right)\right\}, \tag{4.86}$$

$$c = (\rho_0^2 v_{A0}^4 + \rho_1\rho_2 v_{A1}^2 v_{A2}^2)\tanh(2kx_0) + \rho_0 v_{A0}^2(\rho_1 v_{A1}^2 + \rho_2 v_{A2}^2). \tag{4.87}$$

The solutions, $\pm\omega_{0\pm}$, must be real (Goedbloed and Poedts, 2004). They are zeroes of the function $D(\omega)$ of order 1 so are simple poles of the integrand $\widehat{A}_1 e^{-i\omega t}$. Additionally, the solutions corroborate with the corresponding incompressible eigenfrequencies for an interface and a symmetric slab, shown in Appendices D.1 and D.2, respectively.

With the location of the singularities of the integrand in hand, we can evaluate the first integral in Equation (4.76) by making use of the *Residue Theorem* of complex analysis. For this theorem to apply, we must integrate around a closed contour instead of the infinite line in Equation (4.76). To accomplish this, we can choose a sequence of contours (known as Bromwich contours) such that the limit of the integrals over these contours is equal to the integral over the infinite line. We use the fact that the function $T_1(\omega)$ is entire to construct a Bromwich contour, $C = C_0 + C_1$, where C_0 is a straight line from $(-L, \sigma)$ to (L, σ), and C_1 connects $(-L, \sigma)$ and (L, σ) via a semi-circle to ensure that C encloses the zeros at $\pm\omega_{0\pm}$ (Figure 4.4). In the limit $L \to \infty$, we recover the desired integral.

Considering first the integral along C_1, the integrand in question behaves like $T_1(\omega)/kD(\omega) = \mathcal{O}(|\omega|^{-2})$, as $|\omega| \to \infty$. Therefore, the integral around the

semi-circle vanishes, *i.e.*

$$\lim_{L\to\infty}\int_{C_1}\frac{T_1(\omega)}{kD(\omega)}e^{-i\omega t}d\omega = 0. \tag{4.88}$$

Next, since the integral along contour C is integrated in the clockwise direction, it is equal to $-2\pi i$ multiplied by the sum of the residues of the poles at $\omega = \pm\omega_{0\pm}$. The residues are evaluated using L'Hopital's Rule (the requirements ensuring the validity L'Hopital's Rule in this case are verified in Appendix E). For an arbitrary choice of initial condition, $f(x,\omega)$, the residue at $\omega = \omega_{0+}$ is

$$\begin{aligned}
\text{Res}\left\{\frac{T_1(\omega)}{kD(\omega)}e^{-i\omega t};\omega=\omega_{0+}\right\} &= \lim_{\omega\to\omega_{0+}}\frac{(\omega-\omega_{0+})T_1(\omega)}{kD(\omega)}e^{-i\omega t}\\
&= \lim_{\omega\to\omega_{0+}}\frac{1}{kD'(\omega)}[T_1(\omega)+(\omega-\omega_{0+})T_1'(\omega)-it(\omega-\omega_{0+})T_1(\omega)]e^{-i\omega t}\\
&= \lim_{\omega\to\omega_{0+}}\frac{1}{kD'(\omega)}T_1\left[\omega\Psi_0+i\frac{\partial\Psi_0}{\partial t}\right](\omega)e^{-i\omega t}\\
&= \lim_{\omega\to\omega_{0+}}\frac{1}{kD'(\omega)}\left\{\omega T_1[\Psi_0](\omega)+iT_1\left[\frac{\partial\Psi_0}{\partial t}\right](\omega)\right\}e^{-i\omega t}\\
&= \left\{\omega_{0+}\chi_{1+}[\Psi_0]+i\chi_{1+}\left[\frac{\partial\Psi_0}{\partial t}\right]\right\}e^{-i\omega_{0+}t},
\end{aligned} \tag{4.89}$$

where $\chi_{1+}[g] := T_1[g](\omega_{0+})/kD'(\omega_{0+})$ is a functional mapping an arbitrary function g to the real numbers. Similarly, the residues at $\omega = -\omega_{0+}$ and $\omega = \pm\omega_{0-}$ are

$$\text{Res}\left\{\frac{T_1(\omega)}{kD(\omega)}e^{-i\omega t};\omega=-\omega_{0+}\right\} = \left\{\omega_{0+}\chi_{1+}[\Psi_0]-i\chi_{1+}\left[\frac{\partial\Psi_0}{\partial t}\right]\right\}e^{i\omega_{0+}t}, \tag{4.90}$$

$$\text{Res}\left\{\frac{T_1(\omega)}{kD(\omega)}e^{-i\omega t};\omega=\pm\omega_{0-}\right\} = \left\{\omega_{0-}\chi_{1-}[\Psi_0]\pm i\chi_{1-}\left[\frac{\partial\Psi_0}{\partial t}\right]\right\}e^{\mp i\omega_{0-}t}, \tag{4.91}$$

respectively, where we define $\chi_{1-}[g] = T_1[g](\omega_{0-})/kD'(\omega_{0-})$. To derive these residues, we have used the fact that D' is an odd function of ω, and D and $T_1[g]$ are even functions of ω when the function g that is constant with respect to ω.

Compiling the above results, the solution of the first inverse Laplace Trans-

form in Equation (4.76) is

$$\mathcal{L}^{-1}\left\{\tilde{A}_1\right\} = \frac{1}{2\pi}\lim_{L\to\infty}\int_{C_0}\frac{T_1(\omega)}{kD(\omega)}e^{-i\omega t}d\omega \tag{4.92}$$

$$\begin{aligned}
&= \frac{1}{2\pi}\lim_{L\to\infty}\int_{C}\frac{T_1(\omega)}{kD(\omega)}e^{-i\omega t}d\omega \\
&= -i\sum \text{Res}\left\{\frac{T_1(\omega)}{kD(\omega)}e^{-i\omega t};\omega=\pm\omega_{0\pm}\right\} \\
&= -i\left\{\omega_{0+}\chi_{1+}[\Psi_0]\left(e^{-i\omega_{0+}t}+e^{i\omega_{0+}t}\right)+i\chi_{1+}\left[\frac{\partial\Psi_0}{\partial t}\right]\left(e^{-i\omega_{0+}t}-e^{i\omega_{0+}t}\right)\right. \\
&\qquad \left.+\omega_{0-}\chi_{1-}[\Psi_0]\left(e^{-i\omega_{0-}t}+e^{i\omega_{0-}t}\right)+i\chi_{1-}\left[\frac{\partial\Psi_0}{\partial t}\right]\left(e^{-i\omega_{0-}t}-e^{i\omega_{0-}t}\right)\right\} \\
&= -2\left\{i\omega_{0+}\chi_{1+}[\Psi_0]\cos(\omega_{0+}t)-\chi_{1+}\left[\frac{\partial\Psi_0}{\partial t}\right]\sin(\omega_{0+}t)\right. \\
&\qquad \left.+i\omega_{0-}\chi_{1-}[\Psi_0]\cos(\omega_{0-}t)-\chi_{1-}\left[\frac{\partial\Psi_0}{\partial t}\right]\sin(\omega_{0-}t)\right\}.
\end{aligned} \tag{4.93}$$

The second inverse Laplace transform in Equation (4.76) is calculated as follows.

$$\begin{aligned}
\mathcal{L}^{-1}\left\{\frac{\omega}{\epsilon_1}\right\} &= \frac{1}{2\pi}\lim_{L\to\infty}\int_{i\sigma-L}^{i\sigma+L}\frac{\omega e^{-i\omega t}}{\epsilon_1}\,d\omega \\
&= \frac{1}{2\pi\rho_1}\lim_{L\to\infty}\int_{i\sigma-L}^{i\sigma+L}\frac{\omega e^{-i\omega t}}{(kv_{A1}+\omega)(kv_{A1}-\omega)}\,d\omega,
\end{aligned} \tag{4.94}$$

whose integrand has simple poles at $\omega = \pm kv_{A1}$. From Jordan's Lemma it follows that the integrand vanishes as $\omega \to \infty$. Therefore, we can construct a Bromwich contour as shown in Figure 4.5. The residues of the integrand at the poles are

$$\text{Res}\left\{\frac{\omega e^{-i\omega t}}{k^2v_{A1}^2-\omega^2};\omega=\pm kv_{A1}\right\} = \lim_{\omega\to\pm kv_{A1}}\frac{(\omega\mp kv_{A1})\omega e^{-i\omega t}}{k^2v_{A1}^2-\omega^2} \tag{4.95}$$

$$= -\frac{1}{2}e^{\mp ikv_{A1}t}. \tag{4.96}$$

Therefore, the second inverse Laplace transform in Equation (4.76) is

$$\mathcal{L}^{-1}\left\{\frac{\omega}{\epsilon_1}\right\} = -\frac{i}{\rho_1}\sum \text{Res}\left\{\frac{\omega e^{-i\omega t}}{k^2v_{A1}^2-\omega^2};\omega=\pm kv_{A1}\right\} = \frac{i}{\rho_1}\cos kv_{A1}t. \tag{4.97}$$

The third and final inverse Laplace transform in Equation (4.76) is calculated as follows.

$$\begin{aligned}
\mathcal{L}^{-1}\left\{\frac{1}{\epsilon_1}\right\} &= \frac{1}{2\pi}\lim_{L\to\infty}\int_{i\sigma-L}^{i\sigma+L}\frac{e^{-i\omega t}}{\epsilon_1}\,d\omega, \\
&= \frac{1}{2\pi\rho_1}\lim_{L\to\infty}\int_{i\sigma-L}^{i\sigma+L}\frac{e^{-i\omega t}}{(kv_{A1}+\omega)(kv_{A1}-\omega)}\,d\omega,
\end{aligned} \tag{4.98}$$

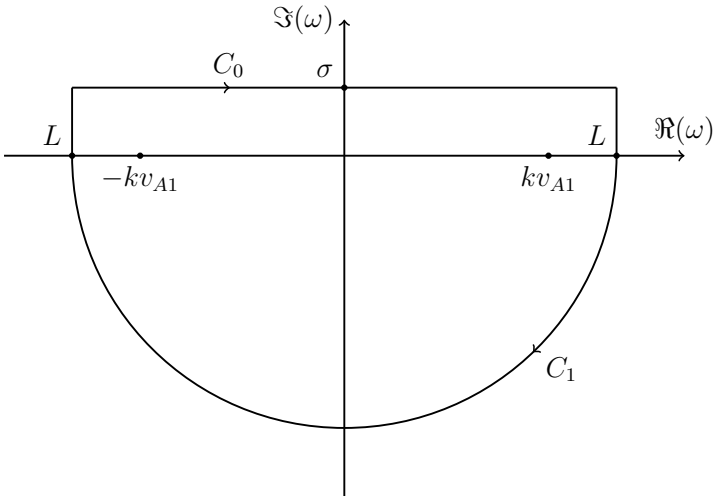

Figure 4.5: Bromwich contour for the complex integration of the integrand of J_1.

whose integrand has simple poles at $\omega = \pm kv_{A1}$. Again, the integrand vanishes as $\omega \to \infty$, so we can integrate around the Bromwich contour as shown in Figure 4.5. The residues of the integrand at the poles are

$$\begin{aligned} \text{Res}\left\{\frac{e^{-i\omega t}}{k^2 v_{A1}^2 - \omega^2}; \omega = \pm kv_{A1}\right\} &= \lim_{\omega \to \pm kv_{A1}} \frac{(\omega - kv_{A1})e^{-i\omega t}}{k^2 v_{A1}^2 - \omega^2} \\ &= \mp \frac{1}{2kv_{A1}} e^{\mp ikv_{A1}t}. \end{aligned} \tag{4.99}$$

Therefore, the final inverse Laplace transform in Equation (4.76) is

$$\begin{aligned} \mathcal{L}^{-1}\left\{\frac{1}{\epsilon_1}\right\} &= -\frac{i}{\rho_1} \sum \text{Res}\left\{\frac{e^{-i\omega t}}{k^2 v_{A1}^2 - \omega^2}; \omega = \pm kv_{A1}\right\} \\ &= \frac{1}{\rho_1 kv_{A1}} \sin kv_{A1} t. \end{aligned} \tag{4.100}$$

Combining the above expressions for the three inverse Laplace transforms, the transverse velocity solution for $x < -x_0$ is

$$v_x(x,t) = -2e^{k(x+x_0)} \left\{ i\omega_{0+}\chi_{1+}[\Psi_0]\cos(\omega_{0+}t) - \chi_{1+}\left[\frac{\partial \Psi_0}{\partial t}\right]\sin(\omega_{0+}t) \right. \tag{4.101}$$

$$\left. + i\omega_{0-}\chi_{1-}[\Psi_0]\cos(\omega_{0-}t) - \chi_{1-}\left[\frac{\partial \Psi_0}{\partial t}\right]\sin(\omega_{0-}t) \right\} \tag{4.102}$$

$$+ \frac{i}{\rho_1}\int_{-\infty}^{-x_0} G_1(x;s)\left[\Psi(s,0)\cos kv_{A1}t + \frac{\partial \Psi}{\partial t}(s,0)\frac{\sin kv_{A1}t}{kv_{A_1}}\right] ds. \tag{4.103}$$

Similarly, the transverse velocity for the region $x > x_0$ is

$$\begin{aligned} v_x(x,t) = &- 2e^{k(x_0-x)} \left\{ i\omega_{0+}\chi_{2+}[\Psi_0]\cos(\omega_{0+}t) - \chi_{2+}\left[\frac{\partial\Psi_0}{\partial t}\right]\sin(\omega_{0+}t) \right. \\ &\left. + i\omega_{0-}\chi_{2-}[\Psi_0]\cos(\omega_{0-}t) - \chi_{2-}\left[\frac{\partial\Psi_0}{\partial t}\right]\sin(\omega_{0-}t) \right\} \\ &+ \frac{i}{\rho_2}\int_{x_0}^{\infty} G_2(x;s)\left[\Psi(s,0)\cos kv_{A2}t + \frac{\partial\Psi}{\partial t}(s,0)\frac{\sin kv_{A2}t}{kv_{A_2}}\right]\, ds. \end{aligned} \tag{4.104}$$

Finally, for the region $|x| \leq x_0$, it is

$$\begin{aligned} v_x(x,t) = &- \frac{2}{\sinh 2kx_0}\left[\left\{ i\omega_{0+}\chi_{1+}[\Psi_0]\cos(\omega_{0+}t) - \chi_{1+}\left[\frac{\partial\Psi_0}{\partial t}\right]\sin(\omega_{0+}t) \right. \right. \\ &\left. + i\omega_{0-}\chi_{1-}[\Psi_0]\cos(\omega_{0-}t) - \chi_{1-}\left[\frac{\partial\Psi_0}{\partial t}\right]\sin(\omega_{0-}t) \right\}\sinh(k(x_0-x)) \\ &+ \left\{ i\omega_{0+}\chi_{2+}[\Psi_0]\cos(\omega_{0+}t) - \chi_{2+}\left[\frac{\partial\Psi_0}{\partial t}\right]\sin(\omega_{0+}t) \right. \\ &\left. \left. + i\omega_{0-}\chi_{2-}[\Psi_0]\cos(\omega_{0-}t) - \chi_{2-}\left[\frac{\partial\Psi_0}{\partial t}\right]\sin(\omega_{0-}t) \right\}\sinh(k(x_0+x)) \right] \\ &+ \frac{i}{\rho_0}\int_{-x_0}^{x_0} G_0(x;s)\left[\Psi(s,0)\cos kv_{A0}t + \frac{\partial\Psi}{\partial t}(s,0)\frac{\sin kv_{A0}t}{kv_{A0}}\right]\, ds. \end{aligned} \tag{4.105}$$

These solutions are not particularly illuminating in there general form, so we evaluate the solutions using specific initial conditions in the next subsections.

4.4.1.2 Uniform initial vorticity

Let $\Omega(x,0) = \Omega_0$ be constant. Therefore, $\Psi_0 = k\rho_0\Omega_0$ and $\partial\Psi_0/\partial t = 0$. To evaluate the solution, we evaluate the Green's function integral for each regions of the waveguide separately. Firstly, for $x < -x_0$,

$$\begin{aligned} \int_{-\infty}^{-x_0} G_1(x;s)\Psi_0\, ds &= \Omega_0\rho_1\left[\sinh(k(x+x_0))\int_{-\infty}^{x} e^{k(s+x_0)}\, ds \right. \\ &\qquad \left. + e^{k(x+x_0)}\int_{x}^{-x_0}\sinh(k(s+x_0))\, ds\right] \\ &= \frac{\Omega_0\rho_1}{k}\left[e^{k(x+x_0)} - 1\right]. \end{aligned} \tag{4.106}$$

Secondly, for $|x| \leq x_0$,

$$\int_{-x_0}^{x_0} G_0(x;s)\Psi_0 \, ds = \frac{\Omega_0\rho_0}{\sinh 2kx_0}\left[\sinh(k(x-x_0))\int_{-x_0}^{x}\sinh(k(s+x_0))\, ds \right. \\ \left. + \sinh(k(x+x_0))\int_{x}^{x_0}\sinh(k(s-x_0))\, ds\right], \\ = \frac{\Omega_0\rho_0}{k}\left(\frac{\cosh kx}{\cosh kx_0} - 1\right). \tag{4.107}$$

Finally, for $x > x_0$,

$$\int_{x_0}^{\infty} G_2(x;s)\Psi_0 \, ds = -\Omega_0\rho_2\left[e^{-k(x-x_0)}\int_{x_0}^{x}\sinh(k(s-x_0))\, ds \right. \\ \left. + \sinh(k(x-x_0))\int_{x}^{\infty} e^{-k(s-x_0)}\, ds\right], \\ = \frac{\Omega_0\rho_2}{k}\left[e^{-k(x-x_0)} - 1\right]. \tag{4.108}$$

The other integrals that need to be evaluated are

$$I_0^{\pm} = \frac{\Omega_0\omega\rho_0 k}{\sinh 2kx_0}\int_{-x_0}^{x_0}\sinh(k(s\pm x_0))ds, \tag{4.109}$$

$$= \pm\frac{\Omega_0\omega\rho_0}{\sinh 2kx_0}(\cosh 2kx_0 - 1), \tag{4.110}$$

$$I_1 = \Omega_0\omega\rho_1 k\int_{-\infty}^{-x_0} e^{k(s+x_0)}ds, \tag{4.111}$$

$$= \Omega_0\omega\rho_1, \tag{4.112}$$

and

$$I_2 = \Omega_0\omega\rho_2 k\int_{x_0}^{\infty} e^{k(x_0-s)}ds, \tag{4.113}$$

$$= \Omega_0\omega\rho_2. \tag{4.114}$$

Using the above integrals, the transverse velocity through time for an initially constant vorticity is

$$v_x = -\frac{i}{k}\begin{cases} 2e^{k(x+x_0)}A_1^* + \Omega_0\left\{1 - e^{k(x+x_0)}\right\}\cos kv_{A1}t & \text{for } x < -x_0, \\ \frac{2}{\sinh 2kx_0}\left[A_1^*\sinh(k(x_0-x)) + A_2^*\sinh(k(x_0+x))\right] & \\ +\Omega_0\left(1 - \frac{\cosh kx}{\cosh kx_0}\right)\cos kv_{A0}t & \text{for } x < |x_0|, \\ 2e^{k(x_0-x)}A_2^* + \Omega_0\left\{1 - e^{k(x_0-x)}\right\}\cos kv_{A2}t & \text{for } x > x_0, \end{cases} \tag{4.115}$$

where

$$A_{1,2}^* = \omega_{0+}\frac{T_{1,2}[\psi_0](\omega_{0+})}{D'(\omega_{0+})}\cos(\omega_{0+}t) + \omega_{0-}\frac{T_{1,2}[\psi_0](\omega_{0-})}{D'(\omega_{0-})}\cos(\omega_{0-}t), \tag{4.116}$$

and

$$T_{1,2}[\Psi_0](\omega) = -\Omega_0\{(\rho_0 \tanh(kx_0) + \rho_{1,2})(\epsilon_0 \cosh(2kx_0) + \epsilon_{2,1} \sinh(2kx_0)) + \epsilon_0(\rho_0 \tanh(kx_0) + \rho_{2,1})\}. \tag{4.117}$$

When $\rho_1 = \rho_2 = \rho_0$ and $x_0 = 0$, the solution given by Equation (4.115) reduces with that of a tangential interface, Equation (4.37).

The time-dependant evolution of a perturbation of an incompressible asymmetric magnetic slab are thus purely superposition of normal modes. There is no contribution from the continuous spectrum. There is instantaneous set-up of coherently oscillating collective modes. It is the introduction of compressibility that introduces a continuous spectrum, and therefore a leaky component to the oscillation. This is the subject of the following subsection.

4.4.2 Compressible slab

In this subsection, we solve the initial value problem of a compressible asymmetric slab.

The more general compressible version of Equation (4.12) is

$$\tilde{v}_x'' - m^2 \tilde{v}_x = g(x, \omega), \tag{4.118}$$

where

$$g(x,\omega) = \frac{1}{(c_0^2 + v_A^2)(\omega_T^2 - \omega^2)} \left[(\omega_0^2 - \omega^2)\left(\dot{\widehat{v}}_{x0} - i\omega \widehat{v}_{x0}\right) + ikc_0^2\left(\dot{\widehat{v}}'_{z0} - i\omega \widehat{v}'_{z0}\right)\right]. \tag{4.119}$$

This equation can be reduced to the corresponding equation for incompressible plasma in the limit of infinite sound speed, *i.e.* $c_0 \to \infty$. Equation (4.119) corroborates with the general initial value problem considered by Andries and Goossens (2007), although some algebra is required to transform between velocity and total pressure coordinates.

Considering a magnetic slab in a non-magnetic environment, we have

$$m_0^2 = \frac{(\omega_0^2 - \omega^2)(\omega_A^2 - \omega^2)}{(c_0^2 + v_A^2)(\omega_T^2 - \omega^2)}, \quad m_{1,2}^2 = \frac{\omega_{1,2}^2 - \omega^2}{c_{1,2}^2}, \tag{4.120}$$

$$g_{1,2}(x,\omega) = \frac{1}{c_0^2\omega^2}\left[(\omega_0^2 - \omega^2)\left(\dot{\widehat{v}}_{x0} - i\omega \widehat{v}_{x0}\right) + ikc_0^2\left(\dot{\widehat{v}}'_{z0} - i\omega \widehat{v}'_{z0}\right)\right]. \tag{4.121}$$

4.4.2.1 Solution in Laplace space

For the solution inside the slab, $|x| \leq x_0$, $\tilde{v}_x(x)$ satisfies

$$\left(\frac{\partial^2}{\partial x^2} - m_0^2\right)\tilde{v}_x = g_0(\omega, x), \tag{4.122}$$

under the boundary conditions $\tilde{v}_x(-x_0) = \tilde{A}_1$ and $\tilde{v}_x(-x_0) = \tilde{A}_2$. To solve this we construct the Green's function, $G_0(x;s)$ that satisfies

$$\frac{d^2G_0}{dx^2} - m_0^2 G_0 = \delta(x-s), \quad G_0(-x_0;s) = G_0(x_0;s) = 0. \tag{4.123}$$

The general solution of this equation is

$$G_0(x;s) = c_1 \sinh(m_0(x-x_0)) + c_2 \sinh(m_0(x+x_0)), \tag{4.124}$$

where $c_1 = 0$ for $x < s$ and $c_2 = 0$ for $x > s$. Ensuring G_0 and $\partial G_0/\partial x$ have jumps of 0 and 1 at $x = s$, respectively, determines c_1 and c_2 so that $G_0(x;s)$ is

$$G_0 = \frac{-1}{m_0 \sinh(2m_0x_0)} \begin{cases} \sinh(m_0(x_0-s))\sinh(m_0(x_0+x)), & \text{if } -x_0 < x < s, \\ \sinh(m_0(x_0-x))\sinh(m_0(x_0+s)), & \text{if } s < x < x_0. \end{cases} \tag{4.125}$$

Then the solution of Equation (4.122) is

$$\begin{aligned} \tilde{v}_x(x) =& \frac{1}{m_0 \sinh 2m_0x_0}\left[\tilde{A}_1 \sinh(m_0(x_0-x)) + \tilde{A}_2 \sinh(m_0(x_0+x))\right] \\ &+ \int_{-x_0}^{x_0} G_0(x;s) g_0(\omega, s)\, ds. \end{aligned} \tag{4.126}$$

This is the sum of the Green's function term and a two terms that are independent solutions to the homogeneous version of Equation (4.122) that ensure that the inhomogeneous boundary conditions are satisfied.

For the solution outside and to the left of the slab, $x < -x_0$, $\tilde{v}_x(x)$ satisfies

$$\left(\frac{d^2}{dx^2} - m_1^2\right)\tilde{v}_x = g_1(\omega, x), \tag{4.127}$$

and the boundary conditions $\tilde{v}_x(-\infty) = 0$, $\tilde{v}_x(-x_0) = \tilde{A}_1$. By following a Green's function method, the solution of this Sturm-Liouville system is

$$\tilde{v}_x(x) = \tilde{A}_1 e^{m_1(x_0+x)} + \int_{-\infty}^{-x_0} G_1(x;s) g_1(\omega, s) ds, \tag{4.128}$$

where $\mathrm{Re}\{m_1\} > 0$ and the Green's function, G_1, is defined by

$$G_1(x;s) = \frac{1}{m_1} \begin{cases} e^{m_1(x_0+x)} \sinh(m_1(x_0+s)), & \text{if } x < s, \\ e^{m_1(x_0+s)} \sinh(m_1(x_0+x)), & \text{if } s < x < -x_0. \end{cases} \tag{4.129}$$

Similarly, the solution outside and to the right of the slab, $x > x_0$, is

$$\tilde{v}_x(x) = \tilde{A}_2 e^{m_2(x_0-x)} + \int_{x_0}^{\infty} G_2(x;s) g_2(\omega,s)\, ds, \tag{4.130}$$

where $\mathrm{Re}\{m_2\} > 0$ and the Green's function, G_2, is defined by

$$G_2(x;s) = \frac{1}{m_2} \begin{cases} e^{m_2(x_0-s)} \sinh(m_2(x_0-x)), & \text{if } x_0 < x < s, \\ e^{m_2(x_0-x)} \sinh(m_2(x_0-s)), & \text{if } s < x. \end{cases} \tag{4.131}$$

Putting all of this together, the Laplace transform of the transverse velocity is

$$\tilde{v}_x(x) = \begin{cases} \tilde{A}_1 e^{m_1(x_0+x)} + \int_{-\infty}^{-x_0} G_1(x;s) g_1(\omega,s)\, ds, & \text{if } -\infty < x < -x_0, \\ \frac{1}{\sinh 2m_0 x_0} \Big[\tilde{A}_1 \sinh(m_0(x_0-x)) & \\ + \tilde{A}_2 \sinh(m_0(x_0+x)) \Big] & \\ + \int_{-x_0}^{x_0} G_0(x;s) g_0(\omega,s)\, ds, & \text{if } |x| \le x_0, \\ \tilde{A}_2 e^{m_2(x_0-x)} + \int_{x_0}^{\infty} G_2(x;s) g_2(\omega,s)\, ds, & \text{if } x_0 < x < \infty. \end{cases} \tag{4.132}$$

4.4.2.2 Matching solutions

For physically relevant solutions, we require that the transverse velocity and the total pressure be continuous across the interfaces at $x = \pm x_0$.

Continuity in transverse velocity, $\tilde{v}_x$, is satisfied automatically by considering the solutions inside and outside the slab given by Equations (4.132), and our definition of $\tilde{A}_1 = \tilde{v}_x(-x_0)$ and $\tilde{A}_2 = \tilde{v}_x(x_0)$.

Continuity in total pressure can be dealt with as follows. The perturbation in total pressure is related to the velocity gradient by[8]

$$\frac{\partial p_T}{\partial t} = -\rho \left[\left(c_0^2 + v_A^2\right) \frac{\partial v_x}{\partial x} + c_0^2 \frac{\partial v_z}{\partial z} \right]. \tag{4.133}$$

Looking for solutions proportional to $\exp ikz$ and taking Laplace transforms in time leads to

$$\tilde{p}_T = -\frac{i\rho}{\omega} \frac{(c_0^2 + v_A^2)(\omega_T^2 - \omega^2)}{(\omega_0^2 - \omega^2)} \tilde{v}_x' + \frac{i}{\omega} \widehat{p}_{T0} + \frac{\rho\omega^2}{k\omega(\omega_0^2 - \omega^2)} \left(\dot{\widehat{v}}_{z0} - i\omega \widehat{v}_{z0} \right). \tag{4.134}$$

Therefore, if we make the simplification[9] to the prescribed initial conditions such that

$$\widehat{p}_{T0} - \frac{\rho\omega_0^2}{k(\omega_0^2 - \omega^2)} \left(i\widehat{v}_{z0} + \omega \dot{\widehat{v}}_{z0} \right) = 0, \tag{4.135}$$

[8] Found by combining that induction equation with the momentum equation, see, for example, the bottom row of Equation (2) by Andries and Goossens (2007).

[9] This simplification is not as strict as it might first seem. For example, any pressure perturbation-free transverse kick, such as you might expect from a nearby flare, would do.

then the continuity in total pressure boundary condition is equivalent to

$$\left[\left[\frac{\Lambda}{m}\frac{\partial \tilde{v}_x}{\partial x}\right]\right]_{x=\pm x_0} = 0, \tag{4.136}$$

where double brackets indicate a jump in the quantity,

$$[[f]]_{x=x_0} = \lim_{\epsilon\to 0}[f(x_0+\epsilon) - f(x_0-\epsilon)]. \tag{4.137}$$

Substituting the solutions given by Equation (4.132) into these boundary conditions gives

$$\tilde{A}_1(\omega) = \frac{T_1(\omega)}{D(\omega)}, \quad \tilde{A}_2(\omega) = \frac{T_2(\omega)}{D(\omega)}, \tag{4.138}$$

where

$$\begin{aligned} T_1(\omega) =& -(\Lambda_0\cosh 2m_0x_0 + \Lambda_2\sinh 2m_0x_0)(\Lambda_0 I_0^- + \Lambda_1 I_1) \\ & - \Lambda_0(\Lambda_0 I_0^+ + \Lambda_2 I_2), \qquad (4.139)\\ T_2(\omega) =& -(\Lambda_0\cosh 2m_0x_0 + \Lambda_1\sinh 2m_0x_0)(\Lambda_0 I_0^+ + \Lambda_2 I_2) \\ & - \Lambda_0(\Lambda_0 I_0^- + \Lambda_1 I_1), \qquad (4.140)\\ D(\omega) =& \Lambda_0(\Lambda_1+\Lambda_2)\cosh(2m_0x_0) + (\Lambda_0^2 + \Lambda_1\Lambda_2)\sinh(2m_0x_0), \qquad (4.141) \end{aligned}$$

where $\Lambda_j = \rho_j(\omega^2 - \omega_{Aj}^2)/m_j$, for $j = 0, 1, 2$, and

$$I_0^{\pm} = I_0^{\pm}[f] = \frac{1}{m_0}\int_{-x_0}^{x_0} \frac{\sinh(m_0(x_0 \pm s))}{\sinh(2m_0x_0)} f(\omega, s)\, ds, \tag{4.142}$$

$$I_1 = I_1[f] = \frac{1}{m_1}\int_{-\infty}^{-x_0} e^{m_1(s+x_0)} f(\omega, s)\, ds, \tag{4.143}$$

$$I_2 = I_2[f] = \frac{1}{m_2}\int_{x_0}^{\infty} e^{m_2(x_0-s)} f(\omega, s)\, ds. \tag{4.144}$$

4.4.2.3 Solution in time

To recover the transverse velocity, $v_x(x,t)$, we employ the inverse Laplace transform (non-standard, discussed in Appendix C), such that

$$\widehat{v}_x(x,t) = \mathcal{L}^{-1}\{\tilde{v}_x(x)\} = \frac{1}{2\pi}\lim_{L\to\infty}\int_{i\sigma-L}^{i\sigma+L} \tilde{v}_x(x)e^{-i\omega t}d\omega, \tag{4.145}$$

where σ is a real number such that all the singularities of the integrand are below the contour of integration to ensure that all singularities contribute to the integral. The integral is evaluated along an infinite horizontal line in the upper half of the complex plane and is dependent on the singularities (with

respect to ω) of $\tilde{v}_x$, whose residues determine the value of the contour integral. Focusing firstly on the region $x < -x_0$, the solution is

$$\widehat{v}_x(x,t) = \mathcal{L}^{-1}\left\{\tilde{A}_1 e^{m_1(x+x_0)} + \int_{-\infty}^{-x_0} G_1(x;s) f_1(\omega,s) ds\right\}, \tag{4.146}$$

$$= \mathcal{L}^{-1}\left\{\tilde{A}_1 e^{m_1(x+x_0)}\right\} + \mathcal{L}^{-1}\left\{\int_{-\infty}^{-x_0} G_1(x;s) f_1(\omega,s) ds\right\}. \tag{4.147}$$

To study the time-dependent behaviour of the transverse velocity, we start by studying the asymptotic behaviour of

$$A_1(t) = v_x(-x_0,t) = \frac{1}{2\pi}\lim_{L\to\infty}\int_{i\sigma-L}^{i\sigma+L} \frac{T_1(\omega)}{D(\omega)} e^{-i\omega t} d\omega. \tag{4.148}$$

Since the problem of finding the solution is now reduced to solving a complex integral, it is dependent on the singularities (with respect to ω) of T_1, T_2, and D and the zeros of D. Identifying the singularities allows us to modify the contour so that it is confined to a single-valued branch and the zeroes of D are poles of the integrand whose residues determine the value of the modified contour integral.

To determine the singularities of T_1, T_2, and D, we determine the singularities of the constituent functions, as follows:

- The functions Λ_j^2 are rational functions of ω with simple poles at $\omega = \pm\omega_{0j}$, for $j = 0, 1, 2$.
- Λ_j, for $j = 0, 1, 2$, involve radicals and have branch points at $\omega = \pm\omega_{Aj}$, $\pm\omega_{0j}$, and $\pm\omega_{Tj}$, respectively.[10]
- The functions $\cosh z$ and $\sinh z$ are entire functions of z with only even and odd terms in their respective series expansions. Therefore, $\cosh z$ and $z\sinh z$ are entire functions of z^2. Hence, $\cosh 2m_0x_0$ and $\Lambda_0 \sinh 2m_0x_0$ have only simple poles at $\omega = \pm\omega_{T0}$.
- The integrands of $I_0^{\pm}$ are integrated with respect to s. Therefore, the singularities of $I_{1,2}$ are precisely the singularities of the integrands. The function $g(z) = \sinh(az)/\sinh(bz)$, for constants a and $b \neq 0$ are entire functions of z, containing only even powers (once g has been redefined as to remove the removable singularity at $z = 0$). Therefore, for another complex function h, the singularities of the composition $g \cdot h$ are precisely

[10] More precisely, $\omega = \pm\omega_{Aj}$, $\pm\omega_{0j}$, and $\pm\omega_{Tj}$ are the ramification points corresponding to the branch points $\Lambda_j(\omega)$, each with ramification index 2. However, the language used in the main text is common shorthand that is considered synonymous.

the singularities of the function $h(z^2)$. Hence, by letting $h(\omega) = m_0$, $a = s \pm x_0$, and $b = 2x_0$, it follows that $\sinh(m_0(s - x_0))/\sinh(2m_0x_0)$ has simple poles at $\omega = \pm\omega_{T0}$.

- To determine the singularities of $I_{1,2}$, we need consider the singularities of the integrands. The functions $e^{\pm a\sqrt{z}}$, for constant $a \neq 0$ have branch points at $z = 0$ that are algebraic (of ramification index 2). Therefore, by setting $a = x_0 \pm s$, it follows that the functions $e^{m_j(x_0 \pm s)}$, and therefore I_j, have algebraic branch points at $\omega = \pm\omega_{Aj}$, $\pm\omega_{0j}$, and $\pm\omega_{Tj}$.

The set of branch points of a sum of functions is the union of the branch points of the constituent functions. Therefore, the branch points of both T_1, T_2, and D are $\omega = \pm\omega_{A0,1,2}$, $\pm\omega_{00,1,2}$, $\pm\omega_{T0,1,2}$.

T_1 and T_2 have no other singularities. Therefore, the poles of $\tilde{A}_1$ and $\tilde{A}_2$ are precisely the zeroes of the dispersion function D. The subset of these zeroes that are real are the eigenfrequencies of the asymmetric slab studied in Chapter 2 and the subset that are complex are the leaky modes. There is a rich spectrum of eigenmodes which, in the absence of any simplification to the model, are not possible to describe analytically.

The integrand has 18 branch points and an infinite number of poles that are not possible to describe analytically. This is a very difficult problem to solve analytically. Therefore, we will instead solve the simplified problem of a thin symmetric slab with zero-beta plasma. From there, we will study what would happen when symmetry is broken (Section 4.4.3).

4.4.2.4 Solving a simplified case - thin zero-beta symmetric slab

When simplifying to a symmetric slab, we use the notation subscript e to denote the symmetric *external* environment, rather than subscripts 1 and 2. Now that we are considering a symmetric slab, the parameters on each side of the slab are equal. Under the zero-beta approximation, the tube speed is identical to the sound speed, both of which are zero. Therefore, the branch points at $\omega = \pm\omega_{00,e}$ and $\omega = \pm\omega_{T0,e}$ degenerate. The remaining branch points are $\omega = \pm\omega_{Ae}$.

Under the zero-beta approximation, the dispersion relation for a symmetric slab simplifies to

$$\rho_e v_{Ae}^2 m_e \begin{pmatrix} \tan \\ -\cot \end{pmatrix} (n_0 x_0) = -\rho_0 v_{A0}^2 n_0, \tag{4.149}$$

where $n_0^2 = -m_0^2 \approx \omega^2/v_{A0}^2 - k^2$ and $m_e^2 \approx k^2 - \omega^2/v_{Ae}^2$. Edwin and Roberts (1982) noticed that this is precisely the dispersion relation for Love waves, which are horizontally polarized surface wave that appears in Earth seismology (Love, 1911). Equilibrium pressure balance requires that $\rho_e v_{Ae}^2 = \rho_0 v_{A0}^2$, therefore, the dispersion relation reduces to

$$\begin{pmatrix} \tan \\ -\cot \end{pmatrix} (n_0 x_0) = -\frac{n_0}{m_e}. \tag{4.150}$$

The tan version of this equation describes sausage modes and the cot version describes kink modes.

With the aim of finding solutions to this dispersion relation, we start with the equation describing kink modes. By letting the non-dimensional slab width, kx_0, be small, we can expand the eigenfrequencies of the first-order kink body mode as a polynomial in kx_0, the largest two terms of which are

$$\omega = \pm k v_{Ae} \left[1 - \frac{1}{2} \left(\frac{v_{Ae}^2}{v_{A0}^2} - 1 \right) (kx_0)^2 \right]. \tag{4.151}$$

This is the only eigenmode of the low-beta slab. It is equivalent to the fast principal kink mode in a magnetic flux tube described by Cally (2003). For this reason, we refer to this mode as the fast principal kink mode of a magnetic slab. The other zeros have non-zero imaginary part and therefore have a decreasing amplitude over time. They are leaky modes. To find these, we must first investigate on which Riemann sheet we expect them to be. In this case, the branch points are due to the square root functions in m_e and n_0. These functions are double-valued so each contribute two branches. The branches of the function m_e determine the behaviour of the velocity outside the slab. Outside the slab, the transverse velocity has the form $\tilde{v}_x = \tilde{A}_1 e^{m_e(x_0+x)}$ plus terms due to the inverse Laplace transform of the Green's function term (Equation 4.132). Trapped modes require that $v_x \to 0$ as $x \to \infty$. This is only possible when $\mathrm{Re}\{m_e\} > 0$, which for trapped modes simplifies to $m_e > 0$. For the trapped mode, we have $\omega < \omega_{Ae}$, therefore to ensure that $m_e > 0$, we must take the positive square root in the definition of m_e. This ensures that the trapped modes are physical, by which we mean that they do not perturb plasma far from the slab. Therefore, we define the positive branch of m_e as the *principal sheet*[11].

[11] Due to it's physically relevant solutions, the equivalent of this sheet in the cylindrical problem has been labelled as the *physical sheet* (Ruderman and Roberts, 2006*b*).

On the other hand, for leaky modes, we require that $v_x \nrightarrow 0$ as $x \to \infty$. Therefore, these modes must exist on the Riemann sheet defined by the negative square root in m_e. This is the *non-principal sheet*[12].

Leaky kink modes on the non-principal sheet are complex solutions to the equation

$$\tan\left(kx_0\sqrt{\frac{\omega^2}{\omega_0^2}-1}\right) = -\frac{\sqrt{1-\frac{\omega^2}{\omega_e^2}}}{\sqrt{\frac{\omega^2}{\omega_0^2}-1}}. \tag{4.152}$$

This equation admits solutions where the argument of the tan function remains finite as $kx_0 \to \infty$. For this to be satisfied, the solution must be of the form $\omega = \nu/kx_0$, where ν is independent of kx_0. Substituting this ansatz into the above equation and using the fact that tan is π-periodic, we find that the leaky kink mode solutions, for small kx_0, are

$$\omega = \frac{v_{A0}}{x_0}\left[n\pi - i\tanh^{-1}\left(\frac{v_{A0}}{v_{Ae}}\right)\right], \tag{4.153}$$

for $n \in \mathbb{Z}$.

Similarly, the leaky sausage modes on the non-principal sheet are complex solutions to the equation

$$\tan\left(kx_0\sqrt{\frac{\omega^2}{\omega_0^2}-1}\right) = \frac{\sqrt{\frac{\omega^2}{\omega_0^2}-1}}{\sqrt{1-\frac{\omega^2}{\omega_e^2}}} \tag{4.154}$$

and are given by

$$\omega = \frac{v_{A0}}{x_0}\left[(n+\frac{1}{2})\pi - i\tanh^{-1}\left(\frac{v_{A0}}{v_{Ae}}\right)\right], \tag{4.155}$$

for small kx_0 and for $n \in \mathbb{Z}$. It is easy to see that, for each pole, one can construct an open ball centred on the pole that contains no other poles, therefore all the poles are isolated. These sausage and kink leaky modes are the slab versions of the "leaky trig mode" defined in a magnetic flux tube by Cally (2003).

The integrals in question given in Equation (4.148) can be calculated using the Bromwich contour in Figure 4.6. To ensure that the contour remains on a single Riemann surface, it is modified around the branch cuts so as to encircle the poles. The closed contour C is a sum of the following sub-contours:

- C_0: the horizontal line with imaginary part σ.

[12] Also known as the *non-physical sheet* (Ruderman and Roberts, 2006*b*)

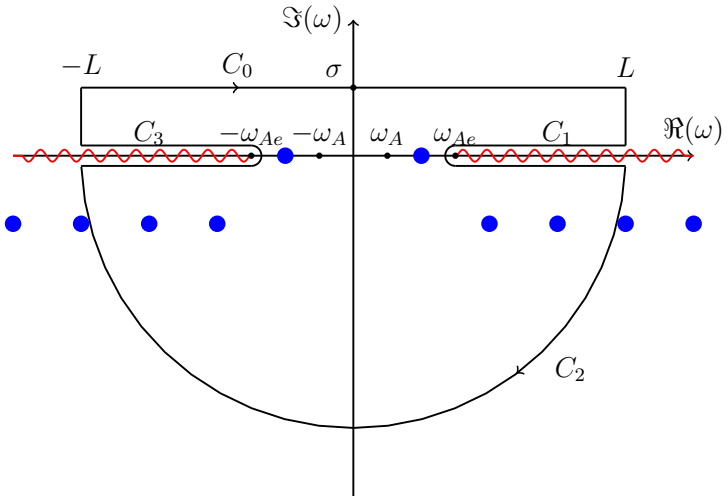

Figure 4.6: The Bromwich contour, $C = \sum_{n=0}^{5} C_n$, for the complex integration of $\tilde{A}_{1,2}$ in the inverse Laplace transform in Equation (4.148). The radius of the large semicircle is L and the radius of the small semicircles around the points $\pm\omega_0$ and $\pm\omega_T$ is δ. The blue circles are the poles and the red lines indicate the branch cuts.

- C_1: the horizontal line from $L + \delta i$ to $\omega_{Ae} + \delta i$, round the semicircle of radius δ and back along the horizontal line from $\omega_{Ae} - \delta i$ to $L - \delta i$.
- C_2: the vertical lines from $\pm L + \sigma i$ to $\pm L + \delta i$ and the arcs of the large semicircle centred at the origin with radius L.
- C_3: the horizontal line from $-L - \delta i$ to $-\omega_{Ae} - \delta i$, round the semicircle of radius δ and back along the horizontal line from $-\omega_{Ae} + \delta i$ to $-L + \delta i$.

The integral in the inverse Laplace transform along the horizontal line is the same as the integral along the closed contour minus the integrals along the other constituent contours, *i.e.* $C_0 = C - \sum_{n=1}^{3} C_n$. The integrals along each of the contours C and C_1 to C_3 are calculated in the following subsections.

4.4.2.5 Integral along C

The contour C is closed and has been chosen such that the integrand can be made to be meromorphic on this contour, given a particular choice of Riemann sheet. Therefore, we would like to use the Residue Theorem to calculate this integral. While the Residue Theorem is often quoted with a restriction to a finite number of isolated poles, it is also valid when there are infinitely many isolated poles (Ahlfors, 1979).

The residue of the principal kink mode is calculated as follows. First, we must determine the order of the pole. The order of the pole is equivalent to

the order of the corresponding zero of the dispersion function. The dispersion function for a symmetric slab can be factorised into a product of a functions governing sausage and kink modes, namely

$$D(\omega) = -2\rho_0^2 v_{A0}^4 \frac{\cosh 2m_0 x_0}{\tanh m_0 x_0 + \coth m_0 x_0} D_s(\omega) D_k(\omega), \tag{4.156}$$

where

$$D_s(\omega) = m_0 + m_e \tanh m_0 x_0 \quad \text{and} \quad D_k(\omega) = m_0 + m_e \coth m_0 x_0. \tag{4.157}$$

Denote the principal kink eigenfrequency by ω_k. We know that $D_s(\omega_k) \neq 0$. We can expand the function D_k as a Taylor series about the frequency ω_k as

$$D_k(\omega) = D_k(\omega_k) + D_k'(\omega)(\omega - \omega_k) + O((\omega - \omega_k)^2). \tag{4.158}$$

Then, the order of ω_k as a zero of D_k (and hence of D) is determined by the order of the first derivative of D_k that is not small when evaluated at ω_k. First, we check the order of $D_k'(\omega_k)$. Using the product and chain rules,

$$D_k'(\omega) = \omega \left[\frac{1}{v_{A0}^2 m_0} (m_e \mathrm{csch}^2 m_0 x_0 - 1) - \frac{1}{v_{Ae}^2 m_e} \coth m_0 x_0 \right]. \tag{4.159}$$

Evaluated at $\omega = \omega_k$, it can easily be shown that $D_k'(\omega_k) = O(1)$ with respect to the small quantity kx_0. In particular, $D_k'(\omega_k)$ is not small. Therefore, ω_k is a simple pole of the integrand.

The residues of the forwards and backwards propagating principal kink modes are thus

$$\begin{aligned}
\mathrm{Res}\left\{ \frac{T_1}{D} e^{-i\omega t}; \omega = \omega_k \right\} &= \lim_{\omega \to \omega_k} (\omega - \omega_k) \frac{T_1(\omega)}{D(\omega)} e^{-i\omega t} \\
&= \lim_{\omega \to \omega_k} \frac{1}{D'(\omega)} [T_1(\omega) + (\omega - \omega_k) T_1'(\omega) - it(\omega - \omega_k) T_1(\omega)] e^{-i\omega t} \\
&= \lim_{\omega \to \omega_k} \frac{T_1(\omega)}{D'(\omega)} e^{-i\omega t} \\
&= \chi_1^{(k)} e^{-i\omega_k t},
\end{aligned} \tag{4.160}$$

where $\chi_1^{(k)} = T_1(\omega_k)/D(\omega_k)$. L'Hopital's rule was used in the above derivation. Similarly,

$$\mathrm{Res}\left\{ \frac{T_1}{D} e^{-i\omega t}; \omega = -\omega_k \right\} = -\chi_1^{(k)} e^{i\omega_k t}, \tag{4.161}$$

because T_1 is an even functions of ω and D' is an odd function of ω. The sum of these two residues is

$$-2i\chi_1^{(k)} \sin \omega_k t. \tag{4.162}$$

The residues at the leaky kink modes can be calculated as follows. We denote the eigenfrequency of the nth leaky kink mode as ω_{kn}. Following the same line of reasoning as for the principal kink mode, $D'(\omega_{kn}) = O(1)$ with respect to kx_0, so $D'(\omega_{kn})$ is not small. Therefore, these poles are simple. The residue at ω_{kn}, for $n \in \mathbb{Z}$, is

$$\text{Res}\left\{\frac{T_1}{D}e^{-i\omega t};\omega=\omega_{kn}\right\} = \chi_1^{(kn)}e^{-i\omega_{kn}t}, \tag{4.163}$$

where $\chi_1^{(kn)} = T_1(\omega_{kn})/D(\omega_{kn})$. Since, ω_{kn} is complex, it is instructive to split it up into its real and imaginary parts by writing the residue as

$$\chi_1^{(kn)} \exp\left\{-i\pi tn\frac{v_{A0}}{x_0}\right\} e^{-\gamma t}, \tag{4.164}$$

where $\gamma = \frac{v_{A0}}{x_0}\tanh^{-1}(v_{A0}/v_{Ae})$.

Similarly, we denote the eigenfrequencies of the leaky sausage modes by ω_{sn}, for $n \in \mathbb{Z}$. These poles have resides

$$\text{Res}\left\{\frac{T_1}{D}e^{-i\omega t};\omega=\omega_{sn}\right\} = \chi_1^{(sn)} \exp\left\{-i\pi t\left(n+\frac{1}{2}\right)\frac{v_{A0}}{x_0}\right\} e^{-\gamma t}, \tag{4.165}$$

where $\chi_1^{(sn)} = T_1(\omega_{sn})/D(\omega_{sn})$.

In the residues for the leaky sausage and kink modes, the first exponential has an imaginary argument and therefore contributes an oscillatory component. The second exponential has a negative real argument and therefore contributes a decaying component with decrement γ.

4.4.2.6 Integral along C_1 and C_3

In the limit as $\delta \to 0$, the integral along the semicircular part of C_1 vanishes because the integrand is analytic in this limit and the length of the contour approaches zero.

As $L \to \infty$ the integrals along the horizontal parts of C_1 become

$$I_{C_1} = \int_{\infty}^{\omega_{Ae}} \frac{T_1^+}{D^+}e^{-i\omega t}d\omega + \int_{\omega_{Ae}}^{\infty} \frac{T_1^-}{D^-}e^{-i\omega t}d\omega \tag{4.166}$$

$$= \int_{\omega_{Ae}}^{\infty}\left(\frac{T_1^-}{D^-} - \frac{T_1^+}{D^+}\right)e^{-i\omega t}d\omega, \tag{4.167}$$

where superscripts $+$ and $-$ indicate the value of the function above and below the horizontal branch cut $[\omega_{Ae}, \infty)$, respectively. For values of ω close to the branch cut, the integrand is analytic, except at the branch point. In particular,

the integrand is analytic except at the endpoint of the integral, therefore, we can use integration by parts to show that

$$I_{C_1} = \frac{i}{t}\left\{\left[\left(\frac{T_1^-}{D^-} - \frac{T_1^+}{D^+}\right)e^{-i\omega t}\right]_{\omega_{Ae}}^{\infty} - \int_{\omega_{Ae}}^{\infty}\frac{d}{d\omega}\left(\frac{T_1^-}{D^-} - \frac{T_1^+}{D^+}\right)e^{-i\omega t}d\omega\right\}. \tag{4.168}$$

Given that $T_1^+/D^+ = T_1^-/D^-$ when evaluated at the branch point and that $T_1^{\pm}(\omega)/D^{\pm}(\omega) \to 0$ as $|\omega| \to \infty$, the first term on the right hand side vanishes. On the second term, we can perform integration by parts again to see that the $I_{C_1} = O(t^{-2})$ as $t \to \infty$.

Similarly, $I_{C_3} = \mathcal{O}(t^{-2})$ as $t \to \infty$.

4.4.2.7 Integral along C_2

Points on the curve C_2 will behave like $|\omega| \to \infty$ as $L \to \infty$. When $|\omega| \to \infty$, $T_1 = \mathcal{O}(|\omega|)$ and $D = \mathcal{O}(|\omega|^2)$ (except when the contour intersects one or more of the poles), therefore the integrands behave like $T_1/D = \mathcal{O}(1/|\omega|)$. Therefore, the integral around C_2 approaches 0 as $L \to \infty$.

Since there is an infinite number of isolated poles that stretch out infinitely in the positive and negative imaginary direction, it is possible to choose a sequence of contours where $L \to \infty$ such that the above result does not hold. Any sequence of contours such that an infinite number of contours pass through poles as $L \to \infty$ would suffice for this. Given that we are free to choose the sequence of contours, we can choose a sequence that does not contain an infinite number of contours that pass through poles.

4.4.2.8 Combining integrals to derive velocity solution

We can combine these integrals to show that

$$A_1(t) = -2\chi_1^{(k)}\sin\omega_k t - iS_1 e^{-\gamma t} + \mathcal{O}(t^{-2}), \tag{4.169}$$

where

$$S_1 = \sum_{n\in\mathbb{Z}}\left(\chi_1^{(kn)}\exp\left\{-i\pi t n\frac{v_{A0}}{x_0}\right\} + \chi_1^{(sn)}\exp\left\{-i\pi t\left(n+\frac{1}{2}\right)\frac{v_{A0}}{x_0}\right\}\right). \tag{4.170}$$

Referring back to the Equation (4.147), which for a symmetric slab waveguide looks like[13]

$$\widehat{v}_x(x,t) = \mathcal{L}^{-1}\left\{\tilde{A}_1 e^{m_e(x+x_0)}\right\} + \mathcal{L}^{-1}\left\{\int_{-\infty}^{-x_0} G_1(x;s) f_1(\omega,s) ds\right\}. \tag{4.171}$$

The first of the inverse Laplace transforms is related to A_1 as follows. $\tilde{A}_1 e^{m_e(x+x_0)}$ has the same analytical properties as $\tilde{A}_1$ in the sense that they have the same singularities and hence the same Riemann surface. Therefore, the first inverse Laplace transform is given by Equation (4.169) but where each term is multiplied by $e^{m_e(x+x_0)}$ evaluated at that term's corresponding frequency. The function $m_e(\omega)$ evaluated at ω_{kn} or ω_{sn} does not have simply analytical form, however, evaluated at ω_k, we have

$$m_e(\omega_k) = k\left(\frac{v_{Ae}^2}{v_{A0}^2} - 1\right)(kx_0). \tag{4.172}$$

Therefore, the first inverse Laplace transform is

$$\begin{aligned}\mathcal{L}^{-1}\left\{\tilde{A}_1 e^{m_e(x+x_0)}\right\} = &-2\chi_1^{(k)} \sin\omega_k t \exp\left\{k(x+x_0)\left(\frac{v_{Ae}^2}{v_{A0}^2} - 1\right)(kx_0)\right\} \\ &- iS_1' e^{-\gamma t} + \mathcal{O}(t^{-2}),\end{aligned} \tag{4.173}$$

where

$$S_1' = \sum_{n\in\mathbb{Z}}\left(\chi_1^{(kn)} \exp\left\{-i\pi t n\frac{v_{A0}}{x_0} + m_e(\omega_{kn})(x+x_0)\right\}\right. \tag{4.174}$$

$$\left. + \chi_1^{(sn)} \exp\left\{-i\pi t\left(n+\frac{1}{2}\right)\frac{v_{A0}}{x_0} + m_e(\omega_{sn})(x+x_0)\right\}\right). \tag{4.175}$$

Finally, we need to determine an asymptotic form for the inverse Laplace transform of the Green's function term in Equation (4.171). This term is a double integral where the inner integral is with respect to s and outer is the inverse Laplace transform which is an integral with respect to ω. The functions $G_1(x,s)f_1(\omega,s)$ and $e^{-i\omega t}$ are continuous functions of s and ω, therefore we are free to switch the order of integration. After doing so, the inner integral is

$$\int_{i\sigma-\infty}^{i\sigma+\infty} G_1(x,s) f_1(\omega,s) e^{-i\omega t}\, d\omega. \tag{4.176}$$

If we restrict the initial condition to being only horizontal, *i.e.* $\widehat{v}_{z0} = \dot{\widehat{v}}_{z0} = 0$, then f is linear in ω and the integrand of this integral has branch points

[13]The Green's function G_1 and the initial condition function f_1 retain their subscript 1 rather than e because the initial condition imposed on the symmetric waveguide could still be asymmetric.

at $\pm\omega_{Ae}$ and no poles. Therefore, with branch cuts along the real axis on the set $(-\infty, -\omega_{Ae}] \cup [\omega_{Ae}, \infty)$ we can use a Bromwich contour that has two horizontal modifications around the branch cuts. Because the integrand has no poles, the integral around the closed contour vanishes, the integral along the large semicircle vanishes, and in the integrals along the horizontal contours are $\mathcal{O}(t^{-2})$. Therefore, the term in the horizontal velocity solution is $\mathcal{O}(t^{-2})$ as $t \to \infty$.

Putting all of this together, we find that

$$\begin{aligned}\widehat{v}_x(x,t) = &- 2\chi_1^{(k)} \sin\omega_k t \exp\left\{k(x+x_0)\left(\frac{v_{Ae}^2}{v_{A0}^2} - 1\right)(kx_0)\right\} \\ &- iS_1' e^{-\gamma t} + \mathcal{O}(t^{-2}),\end{aligned} \tag{4.177}$$

which is valid for $x < -x_0$. Similarly, we can derive the asymptotic solution for the regions $|x| \leq x_0$ and $x > x_0$, but their functional form is the same so we focus just on the solution given by Equation (4.177).

The solution is made up of three parts. The first term is an undamped sinusoid in time and corresponds to the contribution from the trapped kink body mode. There are no trapped sausage modes in the zero-beta slab, so they have no contribution to the solution. The second term is an exponentially decreasing term due to wave leakage in the form of leaky sausage and kink body modes. The terms that are $\mathcal{O}(t^{-2})$ as $t \to \infty$ are not due to collective modes but, instead, represent the propagation of an initial velocity impulse across the waveguide before collective modes are set up. It gives an indication as to the set up time of collective modes.

Like the magnetic flux tube (Ruderman and Roberts, 2006*b*; Terradas et al., 2006), the temporal evolution of a magnetic slab follows three phases: the *initial phase*, the *impulsive phase*, and the *stationary phase*. The initial phase is dominated by the distribution of the initial disturbance. The impulsive phase is dominated by the leaky modes. The stationary phase is dominated by the trapped modes.

The decrement $\gamma = \mathcal{O}((kx_0)^{-1})$ is large, therefore, the amplitude of the leaky modes attenuates rapidly. In general, these terms will decay faster than the $\mathcal{O}(t^{-2})$ terms. This means that, in general, the impulsive phase will be short or possibly non-existent. In particular, the impulsive phase of the magnetic slab is, in general, significantly shorter than the impulsive phase for a magnetic flux tube, whose decrement $\gamma = \mathcal{O}(kx_0)$ is small (Ruderman and Roberts, 2006*b*).

However, the initial conditions have a strong effect on the relative contributions of each of the terms and hence on the duration of each of the three phases (Terradas et al., 2006, 2007). This can be to such an extent that the contribution of any individual mode could be zero or any of the three phases might not exist. For example, a symmetric initial condition will induce only kink modes and an anti-symmetric initial condition will induce only kink modes. Higher order modes are induced by initial conditions that have a shorter characteristic length scale (Terradas et al., 2007).

4.4.3 Generalising to an asymmetric slab

The solution found in the previous section is valid for a symmetric slab. The main affect that waveguide asymmetry has on the evolution of an initial disturbance is that the principal kink mode, which is trapped by a symmetric slab, is leaky for thin asymmetric slabs. This has been shown by the presence of a cut-off value for trapped modes in the dispersion diagrams in Chapter 2 and by Allcock and Erdélyi (2017) and Zsámberger et al. (2018). This means that a thin asymmetric slab of cold plasma will not have a stationary phase for any initial condition because there are no trapped modes. All the energy from the initial condition is leaked out of the waveguide.

It is worth comparing the principal kink mode in this problem to the "principal leaky mode" whose physical relevance has been the subject of debate (Cally, 2003; Ruderman and Roberts, 2006*b*; Cally, 2006; Ruderman and Roberts, 2006*a*). Cally (2003) claimed that in addition to the trapped principal kink mode, which is indisputably physical, there exists a corresponding leaky mode whose real part of its frequency is equal to the principal kink frequency. This leaky mode was later shown to be unphysical by Ruderman and Roberts (2006*b*). In the present chapter, the principal kink mode, which becomes leaky when the slab is asymmetric, is not the mode that Cally (2003) labelled the "principal leaky mode". Instead, it is the principal trapped kink mode that has become leaky due to the waveguide asymmetry.

4.5 Chapter conclusions

In this chapter, we have used mathematical methods to investigate the temporal evolution of MHD waves in simple models of solar waveguides.

First, we focussed on the evolution of incompressible MHD waves along a tangential interface. The main result from this analysis was to correct an error

in one of the key articles using the initial value approach in MHD (Rae and Roberts, 1981), showing that surface modes, not just body modes, are induced by a uniform vorticity initial condition.

Next, we investigated the evolution of incompressible MHD waves along an asymmetric slab. Under the incompressible approximation, there is no initial phase or impulsive phase. There is only a stationary phase. That is to say that the initial impulse is propagated away instantly as purely trapped collective modes. Mathematically, this is equivalent to there being no branch points of the integrand of the inverse Laplace transform. The poles, whose residues give the contribution of the trapped eigenmodes, are the only singularities of the integrand.

Finally, we investigated the evolution of MHD wave in a slab of cold plasma. The solution evolves, in general, through three phases: the initial phase, the impulsive phase, and the stationary phase. These are the same phases through which an initially perturbed magnetic flux tube evolves (Ruderman and Roberts, 2006*b*). The main difference between the slab and flux tube is that the impulsive phase for a magnetic slab is significantly shorter. When a thin slab of cold plasma is asymmetric, the stationary phase is no longer present because the trapped kink mode becomes leaky. After some time, all the energy will be leaked from the slab.

CHAPTER 5

Solar magneto-seismology

5.1 Chapter introduction

In this chapter, we derive two novel techniques for spatial seismology that use an asymmetric slab waveguide to approximate background parameters. This has applications to solar atmospheric structures that are locally slab-like which have been observed to guide MHD oscillations, such as elongated magnetic bright points (Yuan et al., 2014), prominences (Arregui et al., 2012), and light bridge surges (Roy, 1973; Shimizu et al., 2009) (which have also been named light walls by, *e.g.* Yang et al., 2015, 2017; Zhang et al., 2017).

We showed in Chapter 2 that a magnetic slab, with non-magnetic, but asymmetric density and temperatures outside the slab has eigenmodes which can be described as either quasi-sausage or quasi-kink. For quasi-sausage (quasi-kink) modes, the oscillations on each slab interface are in anti-phase (phase). They differ in character from traditional (symmetric) sausage and kink modes by their asymmetry about the centre of the slab due to the amplitude of oscillation on each interface being unequal caused by the asymmetric external environment. This results in quasi-kink modes not necessarily retaining their cross-sectional area and quasi-sausage modes not necessarily having reflection symmetric about the centre line of the slab. The spatial distribution of these waves across the slab, and therefore the extent to which they are modified from the traditional sausage and kink modes, is dependent on the asymmetric background plasma parameters. Consequently, we can use the spatial distribution of these waves to diagnose the waveguide. This is the focus of the present chapter: to derive expressions for proxy parameters that encapsulate this asymmetric spatial distribution and discuss the application to SMS.

Sections 5.1.1 and 5.1.2 give a definition and brief history of SMS. Sections 5.2 and 5.3 introduce two new SMS techniques: the amplitude ratio

method and the minimum perturbation shift method. Section 5.4 discusses in more depth the numerical inversion procedure required to apply these two techniques without having to resort to additional approximations. Section 5.5 discusses where these techniques can be appropriately applied and Section 5.6 records the first use of the amplitude ratio method on solar observations.

5.1.1 What is solar magneto-seismology?

Perpetual bubbling, erupting, and turbulent buffeting of plasma drive ubiquitous magneto-acoustic waves throughout the solar atmosphere. The topology and strength of the magnetic field determines the type and properties of waves present in a given structure. Therefore, by observing these waves and solving an inverse problem, it is possible to make a diagnosis of unknown plasma parameters - a class of techniques known as *solar magneto-seismology* (SMS) (Erdélyi, 2006; Andries et al., 2009; Arregui, 2012; De Moortel and Nakariakov, 2012). This in turn equips us with more realistic parameters for numerical simulations and give us a better understanding of conditions that lead to, for example, wave energy dissipation, instability, magnetic reconnection, and heating.

SMS techniques can be categorised as either *temporal* or *spatial*. Temporal seismology refers to techniques that estimate a plasma parameter by using the observed frequency, or equivalently the period, of waves. Spatial seismology refers to techniques that estimate a plasma parameter by comparing the observed spatial wave power distribution with the eigenfunctions from a theoretical model. Mathematically, the distinction is that temporal seismology techniques use temporal wave parameters (eigenfrequency) only whereas spatial seismology techniques use spatial or a combination of temporal and spatial wave parameters (eigenfunction).

The flowchart in Figure 5.1 illustrates the causal chain from identifying wave and equilibrium parameters in observations, combining these with eigenmode analysis from models of the physical system, and using SMS techniques to diagnose previously unknown equilibrium parameters.

Several temporal seismology methods have been employed successfully. Rosenberg (1970) first suggested that the frequency of oscillations, observed through the fluctuation of synchrotron radiation due to the presence of MHD waves, could be used to diagnose background parameters. Further theoretical development has led to more sophisticated temporal methods including local

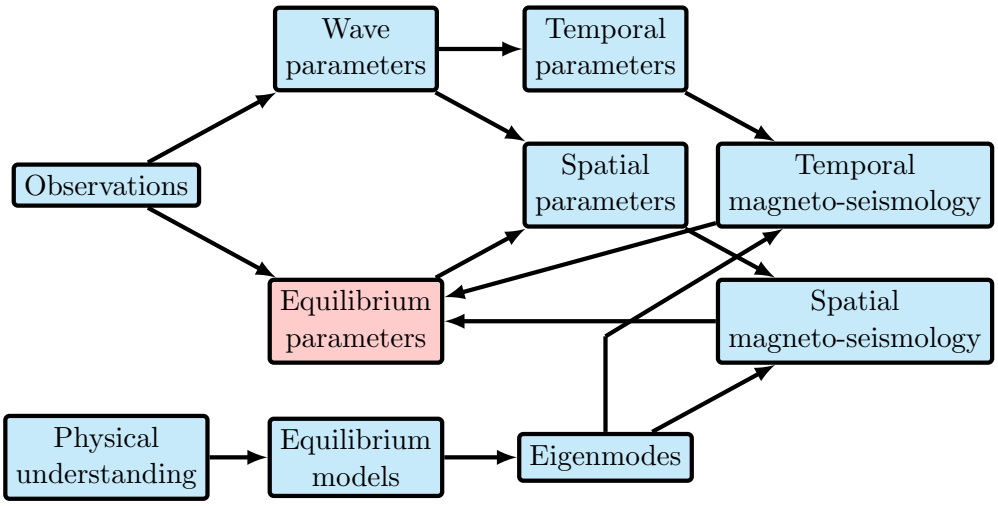

Figure 5.1: A flow chart illustrating the causal chain of solar magneto-seismology.

coronal magnetic field strength estimates using standing kink modes in coronal loops by Roberts et al. (1984); Nakariakov and Ofman (2001), and using slow sausage and kink modes by Erdélyi and Taroyan (2008). The ratio of periods of the fundamental and the first harmonic standing kink mode and its dependence on density stratification has also been well studied (Banerjee et al., 2007; Erdélyi et al., 2014; Yu et al., 2016).

Spatial seismology techniques have more recently started demonstrating their efficacy in estimating solar parameters. Uchida (1970) estimated the coronal magnetic structure by comparing Moreton wave observations with the theoretical influence that the coronal magnetic field has on the shape of the Moreton wavefront. More recent eigenfunction methods include utilising the anti-node shift of standing modes in a magnetic flux tube to diagnose its inhomogeneous density stratification (Erdélyi and Verth, 2007; Verth et al., 2007; Erdélyi et al., 2014).

In this thesis, we particularly focus on diagnosis of the magnetic field. This is because out of all the solar atmospheric features, the magnetic field is often the most elusive and amongst the most dominant in governing solar atmospheric phenomena. It is insightful to consider SMS techniques as part of the larger group of solar magnetometry techniques, so that the most appropriate technique can be chosen for a given purpose. No solar magnetometry technique is suitable for all solar structures and a thorough understanding of the advantages and disadvantages of each is recommended before choosing. Besides SMS, other solar magnetometry techniques include spectral inversion from Stokes' parameters (Stenflo, 2013; Lites et al., 1993), the Zeeman effect (Alissandrakis

and Chiuderi Drago, 1995), the Hanle effect (Raouafi et al., 2016), Faraday rotation (Mancuso and Garzelli, 2007), and photospheric extrapolation (Inoue, 2016).

5.1.2 A brief history of solar magneto-seismology

To motivate this chapter's focus on developing new temporal seismology techniques, we list a selection of the major advancements in SMS since its development in Table 5.1. In this chronology, there are nine major developments in temporal seismology compared to two major developments in spatial seismology. Whilst this is by no means a scientific review of the literature, the dominance of the development of temporal seismology techniques over temporal seismology techniques is striking. Whilst temporal seismology is growing into a mature field, spatial seismology is in its infancy.

Why has spatial seismology lagged behind? There are several plausible answers to this questions. Both ground-based and space-bourne solar telescopes suffer from limitations in spatial resolution. The most significant increases in spatial resolution come from increasing telescope's aperture size. Space-bourne telescopes are limited in this regard because larger aperture size means a larger spacecraft is required to deliver the telescope into orbit. This comes at significant extra cost. Ground-based telescopes suffer from limitations on their spatial resolution from seeing effects and that some electromagnetic wavelengths do not reach the Earth's surface, although the first of these has been partially overcome in the era of adaptive optics. These limitations have allowed faster improvements in temporal resolution compared to spatial resolution, therefore the measurement errors in temporal parameters tend to be lower than those in spatial parameters. This means that temporal seismology inversions tend to have lower errors that propagate through from input errors than spatial seismology inversions.

A second plausible explanation is that the development of spatial seismology techniques tends to require more sophisticated MHD wave modelling than temporal seismology techniques. In general, spatial seismology techniques exploit some observational consequence of a deviation of a waveguide from its most simple counterpart to estimate an unknown parameter. For example, the anti-node shift method uses the shift in position (observational consequence of density non-uniformity) of the anti-nodes of standing modes of coronal loops, due to enhanced density in the loop foot-points (deviation from simple model of a uniform flux tube) to estimate the foot-point density (unknown parameter)

Date	Author	Description	Type
1970	Rosenberg	Pulsations in synchrotron radiation caused by MHD waves.	T
1970	Uchida	Moreton wavefront morphology used to diagnose coronal magnetic structure.	S
1984	Roberts et al.	Introduced the theory of coronal seismology.	T
1995	Tandberg-Hanssen	Prominence seismology.	T
1999	Aschwanden et al. Nakariakov et al.	First observations of coronal loop oscillations using TRACE.	N
2001	Nakariakov et al.	Period of standing kink mode used to diagnose magnetic field strength in coronal loops.	T
2002	Ruderman and Roberts	Damping time scales (assuming exponential damping profile) used to estimate density variation across a coronal loop.	T
2005	Andries et al.	Density stratification deduced from the period ratio of the first two standing kink harmonics.	T
2007	Verth et al.	Anti-node shift used to diagnose density stratification along the loop.	S
2008	Erdelyi et al.	Seismology of slow standing modes in coronal loops.	T
2011	Arregui et al.	Probabilistic coronal seismology inversion using Bayesian statistics.	N
2013	Pascoe et al.	A combination of Gaussian and exponential damping of kink modes used to estimate loop density.	T
2017	Long et al.	Dynamic coronal seismology, *i.e.* diagnosing the magnetic field strength changing in time and across a large portion of the solar atmosphere. Using the methodology developed by Morton et al. (2015).	T

Table 5.1: History of solar magneto-seismology development. The *type* column refers to whether the development is in temporal seismology (T), spatial seismology (S), or neither (N).

(Erdélyi and Verth, 2007). An interpretation the techniques we will develop in Sections 5.2 and 5.3 using this framing is that these techniques use the amplitude ratio or minimum perturbation shift (observational consequences of waveguide asymmetry) which exist due to the asymmetry of the waveguide (deviation from the simple symmetric slab model) which are proxies for the strength of the magnetic field (unknown parameter).

5.2 Amplitude ratio method

The aim of this section is to derive an expression for the ratio of the oscillation amplitude on each interface of an asymmetric magnetic slab in terms of the wave parameters and plasma parameters of the system, then demonstrate how this parameter can be utilised to diagnose background parameters. We focus on estimating the Alfvén speed since it is one of the most difficult of all the background parameters to measure using traditional methods. We do this by first deriving expressions for the eigenfunctions[1] of quasi-sausage and quasi-kink modes, using them to derive expressions for the amplitude ratio, and then by making suitable approximations, we can solve the inverse problem for the Alfvén speed. Numerical inversion procedures for the amplitude ratio method are discussed in Section 5.4.

5.2.1 Deriving an expression for the amplitude ratio

Consider an asymmetric magnetic slab in a non-magnetic environment, as studied in Section 2.3 and by Allcock and Erdélyi (2017). In this section, we denote the Alfvén speed inside the slab as v_{A} rather than v_{A0} for brevity because it is the only Alfvén speed in the system since we have let the external plasma be non-magnetic.

In Section 2.3, it was shown that trapped magneto-acoustic modes propagating along an asymmetric magnetic slab have velocity perturbation in the x-direction given by $v_x(x,z,t) = \widehat{v}_x(x)e^{i(kz-\omega t)}$, where ω and k are the angular frequency and wavenumber, and

$$\widehat{v}_x(x) = \begin{cases} A(\cosh m_1 x + \sinh m_1 x) & \text{if } x < -x_0, \\ B\cosh m_0 x + C\sinh m_0 x & \text{if } |x| \leq x_0, \\ D(\cosh m_2 x - \sinh m_2 x) & \text{if } x > x_0, \end{cases} \tag{5.1}$$

[1] That is, the distribution of the oscillation amplitude across the waveguide.

where

$$m_0^2 = \frac{(k^2 v_{\rm A}^2 - \omega^2)(k^2 c_0^2 - \omega^2)}{(c_0^2 + v_{\rm A}^2)(k^2 c_{T0}^2 - \omega^2)}, \qquad c_{T0}^2 = \frac{c_0^2 v_{\rm A}^2}{c_0^2 + v_{\rm A}^2}, \tag{5.2}$$

$$m_j^2 = k^2 - \frac{\omega^2}{c_j^2}, \quad \text{for } j = 1, 2, \tag{5.3}$$

and A, B, C, and D are arbitrary constants (with respect to x). Therefore, to derive expressions for the eigenfunctions, we need to determine these constants. They can be determined, to within one degree of freedom, using the boundary conditions of continuity in total pressure and transversal velocity component across the slab boundaries at $x = \pm x_0$. Applying these four boundary conditions retrieves four coupled linear homogeneous algebraic equations in the four unknowns, namely

$$\begin{pmatrix} c_1 - s_1 & -c_0 & s_0 & 0 \\ 0 & c_0 & s_0 & s_2 - c_2 \\ \Lambda_1(c_1 - s_1) & \Lambda_0 s_0 & -\Lambda_0 c_0 & 0 \\ 0 & \Lambda_0 s_0 & \Lambda_0 c_0 & -\Lambda_2(s_2 - c_2) \end{pmatrix} \begin{pmatrix} A \\ B \\ C \\ D \end{pmatrix} = \begin{pmatrix} 0 \\ 0 \\ 0 \\ 0 \end{pmatrix}, \tag{5.4}$$

where

$$\Lambda_0 = -\frac{i\rho_0(k^2 v_{\rm A}^2 - \omega^2)}{m_0 \omega}, \quad \Lambda_1 = \frac{i\rho_1 \omega}{m_1}, \quad \text{and} \quad \Lambda_2 = \frac{i\rho_2 \omega}{m_2}, \tag{5.5}$$

and $c_i = \cosh m_i x_0$ and $s_i = \sinh m_i x_i$, for $i = 0, 1, 2$. Ensuring that this matrix has a vanishing determinant gives us the dispersion relation,

$$(\Lambda_0 c_0 + \Lambda_2 s_0)(\Lambda_0 s_0 + \Lambda_1 c_0) + (\Lambda_0 c_0 + \Lambda_1 s_0)(\Lambda_0 s_0 + \Lambda_2 c_0) = 0. \tag{5.6}$$

By satisfying this relation, we gain one degree of freedom in the system of Equations (5.4), which leaves one of the constants B or C arbitrary. This leads to two types of solution: *quasi-sausage* and *quasi-kink* modes.

Firstly, for quasi-sausage modes, by letting C be arbitrary the other constants A, B, and D can be determined as

$$A = \frac{1}{c_1 - s_1}(Bc_0 - Cs_0), \tag{5.7}$$

$$D = \frac{1}{c_2 - s_2}(Bc_0 + Cs_0), \tag{5.8}$$

where

$$B = \frac{\Lambda_0 c_0 + \Lambda_1 s_0}{\Lambda_0 s_0 + \Lambda_1 c_0} C = -\frac{\Lambda_0 c_0 + \Lambda_2 s_0}{\Lambda_0 s_0 + \Lambda_2 c_0} C. \tag{5.9}$$

The second formulation of B in Equation (5.9) is found by utilising the dispersion relation, Equation (5.6). A substitution of these values, using the

first form of B in Equation (5.9), into the velocity solution, Equation (5.1), evaluated at the slab boundaries, yields

$$\widehat{v}_x(x_0) = Bc_0 + Cs_0 = \frac{2\Lambda_1 + \Lambda_0\left(\tau_0 + \frac{1}{\tau_0}\right)}{\Lambda_0 + \Lambda_1\frac{1}{\tau_0}}Cc_0, \tag{5.10}$$

$$\widehat{v}_x(-x_0) = Bc_0 - Cs_0 = \frac{\Lambda_0}{\Lambda_0 + \Lambda_1\frac{1}{\tau_0}}C/s_0, \tag{5.11}$$

where $\tau_0 = \tanh m_0 x_0$. Similarly, using the second form of B in Equation (5.9) yields

$$\widehat{v}_x(x_0) = \frac{-\Lambda_0}{\Lambda_0 + \Lambda_2\frac{1}{\tau_0}}C/s_0, \tag{5.12}$$

$$\widehat{v}_x(-x_0) = \frac{-2\Lambda_2 - \Lambda_0\left(\tau_0 + \frac{1}{\tau_0}\right)}{\Lambda_0 + \Lambda_2\frac{1}{\tau_0}}Cc_0. \tag{5.13}$$

These forms are equivalent. Notice that the horizontal velocity perturbation amplitude, $\widehat{v}_x$, is, more precisely, the *signed* amplitude, where a positive (negative) value indicates perturbation in the positive (negative) x-direction. This will be important for the inversion procedure.

Secondly, for quasi-kink modes, by letting B be arbitrary, the other constants A, C, and D can be determined in terms of B as

$$A = \frac{1}{c_1 - s_1}(Bc_0 - Cs_0), \tag{5.14}$$

$$D = \frac{1}{c_2 - s_2}(Bc_0 + Cs_0), \tag{5.15}$$

where

$$C = \frac{\Lambda_0 s_0 + \Lambda_1 c_0}{\Lambda_0 c_0 + \Lambda_1 s_0}B = -\frac{\Lambda_0 s_0 + \Lambda_2 c_0}{\Lambda_0 c_0 + \Lambda_2 s_0}B. \tag{5.16}$$

A substitution of these values, using the first form of C in Equation (5.16), into Equation (5.1), evaluated at the slab boundaries, yields

$$\widehat{v}_x(x_0) = \frac{2\Lambda_1 + \Lambda_0\left(\tau_0 + \frac{1}{\tau_0}\right)}{\Lambda_0 + \Lambda_1\tau_0}Bs_0, \tag{5.17}$$

$$\widehat{v}_x(-x_0) = \frac{\Lambda_0}{\Lambda_0 + \Lambda_1\tau_0}B/c_0. \tag{5.18}$$

Using the second form of C in Equation (5.16) yields

$$\widehat{v}_x(x_0) = \frac{\Lambda_0}{\Lambda_0 + \Lambda_2\tau_0}B/c_0, \tag{5.19}$$

$$\widehat{v}_x(-x_0) = \frac{2\Lambda_2 + \Lambda_0\left(\tau_0 + \frac{1}{\tau_0}\right)}{\Lambda_0 + \Lambda_2\tau_0}Bs_0. \tag{5.20}$$

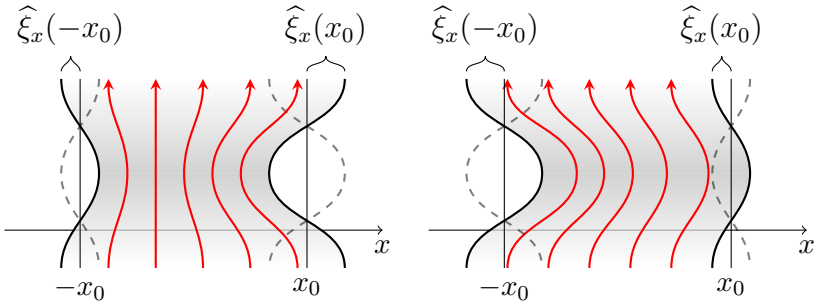

Figure 5.2: Illustration of the difference in amplitude of oscillation on each boundary of the slab for (a) quasi-sausage and (b) quasi-kink modes.

We now define the *amplitude ratio*, $R_\mathrm{A} := \widehat{\xi}_x(x_0)/\widehat{\xi}_x(-x_0)$, as the ratio of the amplitude of oscillation of the left interface ($x = x_0$) to that of the right interface ($x = -x_0$) (see Figure 5.2). Given that $\widehat{\xi}_x(x) = i\widehat{v}_x(x)/\omega$, we also have $R_\mathrm{A} = \widehat{v}_x(x_0)/\widehat{v}_x(-x_0)$. Firstly, using Equations (5.11) and (5.12), the amplitude ratio for quasi-sausage modes is

$$\begin{aligned} R_A &= -\frac{\Lambda_0 + \Lambda_1 \frac{1}{\tau_0}}{\Lambda_0 + \Lambda_2 \frac{1}{\tau_0}} \\ &= -\frac{\rho_1 m_2}{\rho_2 m_1}\left[\frac{(k^2 v_\mathrm{A}^2 - \omega^2) m_1 \frac{\rho_0}{\rho_1} - \omega^2 m_0 \coth m_0 x_0}{(k^2 v_\mathrm{A}^2 - \omega^2) m_2 \frac{\rho_0}{\rho_2} - \omega^2 m_0 \coth m_0 x_0}\right]. \end{aligned} \tag{5.21}$$

Using Equations (5.18) and (5.19), the corresponding expression for quasi-kink modes can be obtained, namely

$$\begin{aligned} R_\mathrm{A} &= \frac{\Lambda_0 + \Lambda_1 \tau_0}{\Lambda_0 + \Lambda_2 \tau_0} \\ &= \frac{\rho_1 m_2}{\rho_2 m_1}\left[\frac{(k^2 v_\mathrm{A}^2 - \omega^2) m_1 \frac{\rho_0}{\rho_1} - \omega^2 m_0 \tanh m_0 x_0}{(k^2 v_\mathrm{A}^2 - \omega^2) m_2 \frac{\rho_0}{\rho_2} - \omega^2 m_0 \tanh m_0 x_0}\right]. \end{aligned} \tag{5.22}$$

As expected, Equations (5.21) and (5.22) reduce to $R_\mathrm{A} = -1$ and $R_\mathrm{A} = 1$ for sausage and kink modes, respectively, when the slab is symmetric.

To obtain an approximation for the Alfvén speed analytically, an approximation such as these must be applied. The following subsections give the analytical inversion for the Alfvén speed, v_A, of equations (5.21) and (5.22) under the thin slab, wide slab, incompressible plasma, and low-beta approximations. A numerical inversion procedure that requires no further approximation is discussed in Section 5.4. Note that we restrict the parameter inversions to surface modes only, thereby omitting body modes, because the eigenfrequencies and eigenfunctions of body modes are not significantly effected by asymmetry in

the external plasma (see Section 2.3) so they are not useful for parameter inversion.

5.2.2 Thin slab approximation

For surface modes in the thin slab approximation, $kx_0 \ll 1$, Roberts (1981*b*) showed that $m_0 x_0 \ll 1$. Therefore, to quadratic order, $\tanh m_0 x_0 \approx m_0 x_0$, and the amplitude ratio for a quasi-sausage surface mode in a thin slab reduces to

$$R_{\mathrm{A}} = -\frac{\rho_1 m_2}{\rho_2 m_1}\left[\frac{(k^2 v_{\mathrm{A}}^2 - \omega^2) m_1 x_0 \frac{\rho_0}{\rho_1} - \omega^2}{(k^2 v_{\mathrm{A}}^2 - \omega^2) m_2 x_0 \frac{\rho_0}{\rho_2} - \omega^2}\right], \tag{5.23}$$

which can be rearranged to give the analytical expression

$$v_{\mathrm{A}}^2 = \frac{\omega^2}{k^2}\left[1 + \frac{1}{x_0}\left(\frac{R_{\mathrm{A}} \frac{\rho_2}{\rho_0 m_2} + \frac{\rho_1}{\rho_0 m_1}}{R_{\mathrm{A}} + 1}\right)\right]. \tag{5.24}$$

The amplitude ratio for a thin slab quasi-kink surface mode reduces to

$$R_{\mathrm{A}} = \frac{\rho_1 m_2}{\rho_2 m_1}\left[\frac{(k^2 v_{\mathrm{A}}^2 - \omega^2) m_1 \frac{\rho_0}{\rho_1} - \omega^2 m_0^2 x_0}{(k^2 v_{\mathrm{A}}^2 - \omega^2) m_2 \frac{\rho_0}{\rho_2} - \omega^2 m_0^2 x_0}\right], \tag{5.25}$$

which can be rearranged to give the analytical expression

$$v_{\mathrm{A}}^2 = \frac{\omega^2}{k^2}\left[\frac{c_0^2}{c_0^2 - \frac{\omega^2}{k^2}} + k^2 x_0 \left(\frac{R_{\mathrm{A}} \frac{\rho_2}{\rho_0 m_2} - \frac{\rho_1}{\rho_0 m_1}}{R_{\mathrm{A}} - 1}\right)\right]. \tag{5.26}$$

In a thin asymmetric slab, the fast quasi-kink surface mode degenerates due to a cut-off by the external sound speeds becoming distinct (Allcock and Erdélyi, 2017) and the slow quasi-kink surface mode has a phase speed that approaches zero in the thin slab limit (see Section 2.3.1.4). Therefore, to a good approximation, the phase speed is much less than the internal sound speed ($\omega/k \ll c_0$) therefore Equation (5.26) simplifies to

$$v_{\mathrm{A}}^2 = \frac{\omega^2}{k^2}\left[1 + k^2 x_0 \left(\frac{R_{\mathrm{A}} \frac{\rho_2}{\rho_0 m_2} - \frac{\rho_1}{\rho_0 m_1}}{R_{\mathrm{A}} - 1}\right)\right]. \tag{5.27}$$

5.2.3 Wide slab approximation

The wide slab approximation applies when the slab width is much larger than the wavelength, that is when $kx_0 \gg 1$. In Section 2.3.1.5, we showed that the surface mode solutions of a wide asymmetric slab are just the surface modes that propagate along each interface independently.

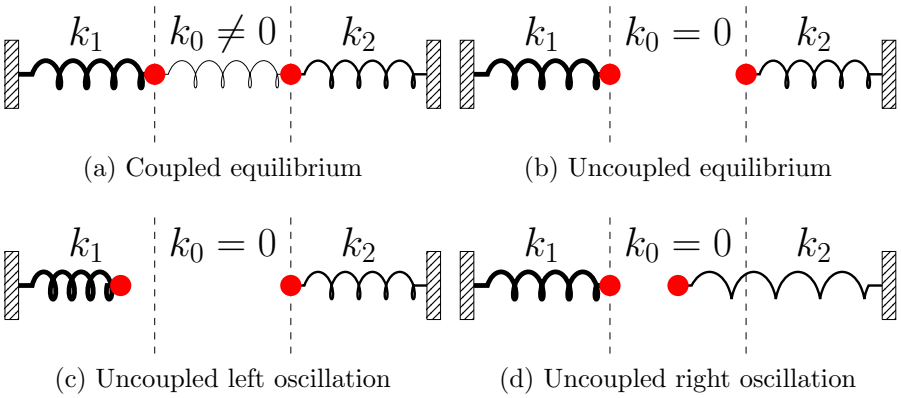

(a) Coupled equilibrium (b) Uncoupled equilibrium

(c) Uncoupled left oscillation (d) Uncoupled right oscillation

Figure 5.3: Mechanical example showing weak and zero coupling between the masses. This provides an analogy to the wide slab approximation of an asymmetric magnetic slab, in which case the interfaces on each side of the slab oscillate independently.

This is analogous to the mechanical example introduced in Section 2.3.3. When the two masses are decoupled by removing the middle spring, equivalently setting $k_0 = 0$, each mass oscillates independently at the natural frequency of that side of the spring-mass system (Figure 5.3). This decoupling provides a good analogy to the wide slab limit for the magnetic slab. In a wide slab, each interface is effectively *decoupled* and oscillates at its own natural frequency, independent of the other interface. Given that we are considering magneto-acoustic waves, there are two restoring forces, the magnetic tension force and the pressure gradient force, which means that each independent interface has two natural frequencies, corresponding to the fast and slow magneto-acoustic modes. With this understanding of the modes in the wide slab limit, the amplitude ratio, R_{A}, is either 0 or $\pm\infty$, depending on which interface the wave is propagating and is therefore not useful for magneto-seismology.

5.2.4 Incompressible approximation

If the plasma is incompressible, the sound speeds become unbounded, so that $m_j \approx k$ for $j = 0, 1, 2$. Under this approximation, the amplitude ratios for quasi-sausage modes (top) and quasi-kink modes (bottom) reduce to

$$R_{\mathrm{A}} = \left(\begin{smallmatrix}-\\+\end{smallmatrix}\right) \frac{\rho_1}{\rho_2} \left[\frac{(k^2 v_{\mathrm{A}}^2 - \omega^2) k \frac{\rho_0}{\rho_1} - \omega^2 k \begin{pmatrix}\coth\\\tanh\end{pmatrix}(kx_0)}{(k^2 v_{\mathrm{A}}^2 - \omega^2) k \frac{\rho_0}{\rho_2} - \omega^2 k \begin{pmatrix}\coth\\\tanh\end{pmatrix}(kx_0)} \right]. \tag{5.28}$$

These equations have solutions for $v_{\rm A}$ given by

$$v_{\rm A}^2 = \frac{\omega^2}{k^2}\left[1 + \left(\frac{R_{\rm A}\frac{\rho_2}{\rho_0}\binom{+}{-}\frac{\rho_1}{\rho_0}}{R_{\rm A}\binom{+}{-}1}\right)\binom{\coth}{\tanh}(kx_0)\right]. \tag{5.29}$$

5.2.5 Low-beta approximation

For a low-beta plasma ($\beta = 2\mu_0 p_0/B_0^2 \ll 1$), the magnetic pressure dominates the kinetic plasma pressure and the Alfvén speed, $v_{\rm A}$, dominates the sound speed, c_0. Therefore, $m_0^2 \approx k^2 - \omega^2/v_{\rm A}^2$. For waves with phase speed much less than the Alfvén speed, a further approximation of $m_0^2 \approx k^2$ can be made, in which case, the amplitude ratios for quasi-sausage modes (top) and quasi-kink modes (bottom) reduce to

$$R_{\rm A} = \binom{-}{+}\frac{\rho_1 m_2}{\rho_2 m_1}\left[\frac{(k^2v_{\rm A}^2 - \omega^2)m_1\frac{\rho_0}{\rho_1} - \omega^2 k\binom{\coth}{\tanh}(kx_0)}{(k^2v_{\rm A}^2 - \omega^2)m_2\frac{\rho_0}{\rho_2} - \omega^2 k\binom{\coth}{\tanh}(kx_0)}\right]. \tag{5.30}$$

These equations can be solved for $v_{\rm A}$ to give

$$v_{\rm A}^2 = \frac{\omega^2}{k^2}\left[1 + k\left(\frac{\frac{\rho_1}{\rho_0 m_1}\binom{+}{-}R_{\rm A}\frac{\rho_2}{\rho_0 m_2}}{1\binom{+}{-}R_{\rm A}}\right)\binom{\coth}{\tanh}(kx_0)\right]. \tag{5.31}$$

We will return to a discussion of the inversion of the amplitude ratio in Section 5.4.

5.3 Minimum perturbation shift method

A second spatial magneto-seismology technique uses the shift in the position of minimum wave power from the centre of the slab due to the asymmetry in the external plasma regions as a diagnostic parameter for estimating the slab Alfvén speed.

5.3.1 Deriving an expression for the minimum perturbation shift

For a symmetric sausage or kink mode, the position of minimum wave power is the central axis of the slab, at $x = 0$. We define $\Delta_{\rm min}$ to be the displacement (from the central axis of the waveguide) of the position of minimum wave power inside an asymmetric magnetic slab (Figure 5.4). For quasi-sausage modes, $\Delta_{\rm min}$ is the solution to $\widehat{v}_x(x) = 0$ under the constraint $|x| \leq x_0$, and

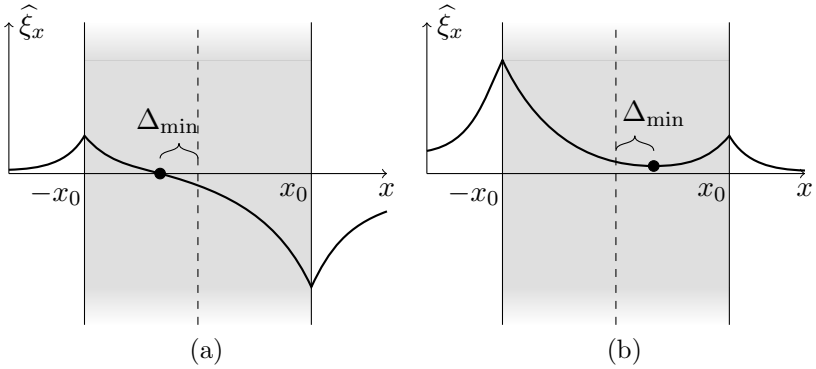

Figure 5.4: Illustration of the minimum perturbation shift, $\Delta_{\min}$, within the slab (shaded) for (a) quasi-sausage and (b) quasi-kink modes.

for quasi-kink modes, $\Delta_{\min}$ is the solution to $\mathrm{d}\widehat{v}_x(x)/\mathrm{d}x = 0$ under the same constraint $|x| \leq x_0$. The constraint restricts the solutions to being within the slab.

Firstly, for quasi-sausage modes, using the solution for the transversal velocity amplitude given by Equation (5.1) and the expressions for the variables within given by equation (5.9), the minimum perturbation shift can be calculated as follows. The solution for the transversal velocity amplitude within the slab is

$$\widehat{v}_x(x) = B\cosh m_0 x + C\sinh m_0 x = 0, \tag{5.32}$$

where B is given by Equation (5.9) and C is arbitrary. This equation is solved for x to give

$$x = \frac{1}{m_0}\tanh^{-1}\left(-\frac{B}{C}\right). \tag{5.33}$$

Therefore, the minimum perturbation shift for quasi-sausage modes is

$$\Delta_{\min} = \frac{1}{m_0}\tanh^{-1}\left[-\frac{(k^2{v_{\mathrm{A}}}^2-\omega^2)m_1\frac{\rho_0}{\rho_1}-\omega^2 m_0\tanh m_0x_0}{(k^2{v_{\mathrm{A}}}^2-\omega^2)m_1\frac{\rho_0}{\rho_1}\tanh m_0x_0-\omega^2 m_0}\right]. \tag{5.34}$$

Similarly, for quasi-kink modes, using Equations (5.1) and (5.16), we calculate the minimum perturbation shift to be

$$\Delta_{\min} = \frac{1}{m_0}\coth^{-1}\left(-\frac{(k^2{v_{\mathrm{A}}}^2-\omega^2)m_1\frac{\rho_0}{\rho_1}-\omega^2 m_0\tanh m_0x_0}{(k^2{v_{\mathrm{A}}}^2-\omega^2)m_1\frac{\rho_0}{\rho_1}\tanh m_0x_0-\omega^2 m_0}\right). \tag{5.35}$$

The dependence of the minimum perturbation shifts on the external plasma region with subscript 2 is implicit in the determination of the eigenfrequency ω when solving the dispersion relation.

The concept of minimum perturbation shift is exclusive to surface modes. The eigenfunctions of surface modes in a magnetic slab are significantly more sensitive to the external plasma parameters than body modes (Allcock and Erdélyi, 2017). This makes intuitive sense given that the energy in a surface mode is localised to the boundaries of the slab whereas the energy in a body mode is largely isolated within the slab. There is a shift in the spatial nodes and anti-nodes in body mode perturbations within a slab due to changing external plasma parameters, however, it is too small to be an effective observational tool.

Akin to the amplitude ratio method for solar magneto-seismology prescribed in Section 5.2, we can invert Equation (5.34) or (5.35) for the the Alfvén speed, v_{A}, and hence get an estimate the magnetic field strength of inhomogeneous solar magnetic structures. This can be done either numerically, using an iterative root finding method, or analytically, under an appropriate approximation. In each of the following subsections, we discuss the analytical inversion procedure under the thin slab (Section 5.3.2), wide slab (Section 5.3.3), incompressible (Section 5.3.4), and low-beta (Section 5.3.5) approximations.

5.3.2 Thin slab approximation

Under the thin slab approximation, that is $kx_0 \ll 1$, we have $m_0 x_0 \ll 1$ for surface modes (Section 2.3.1.4). By definition, $|\Delta_{\mathrm{min}}| < x_0$, therefore, $m_0|\Delta_{\mathrm{min}}| \ll 1$, so that $\tanh m_0\Delta_{\mathrm{min}} \approx m_0\Delta_{\mathrm{min}}$. Firstly, for quasi-sausage modes in a thin slab, Equation (5.34) can be solved for v_{A} to give

$$v_{\mathrm{A}}^2 = \frac{\omega^2}{k^2}\left[\frac{\rho_1}{\rho_0 m_1}(x_0+\Delta_{\mathrm{min}}) + \frac{1}{1+(\omega/kc_0)^2} + k^2 x_0 \Delta_{\mathrm{min}}\right]. \tag{5.36}$$

For quasi-kink modes in a thin slab, Equation (5.35) can be solved for v_{A} to give

$$v_{\mathrm{A}}^2 = \frac{\omega^2}{k^2}\left[\frac{-b \pm \sqrt{b^2-4ac}}{2a}\right], \tag{5.37}$$

where

$$a = m_1\frac{\rho_0}{\rho_1}(k^2c_0^2-\omega^2)(x_0+\Delta_{\mathrm{min}}), \tag{5.38}$$

$$b = -m_1\frac{\rho_0}{\rho_1}(2k^2c_0^2-\omega^2)(x_0+\Delta_{\mathrm{min}}) - (k^2c_0^2-\omega^2), \tag{5.39}$$

$$c = c_0^2 m_1\frac{\rho_0}{\rho_1}(x_0+\Delta_{\mathrm{min}}) + c_0^2 + \omega^2 x_0\Delta_{\mathrm{min}}. \tag{5.40}$$

5.3.3 Wide slab approximation

The concept of minimum perturbation shift is ill-defined under the wide slab approximation, that is, when $kx_0 \gg 1$. In this case, each interface oscillates independently at its own eigenfrequency. Therefore the nomenclature of quasi-sausage and quasi-kink mode breaks down. In the wide slab limit, the eigenfunctions have no local minimum in the slab, instead the perturbations are evanescent away from the oscillating interface, therefore there is no local minimum of wave power within the slab.

5.3.4 Incompressible approximation

When the plasma is incompressible, the sound speeds are unbounded, so that $m_j = k$, for $j = 0, 1, 2$. The minimum perturbation shift for a quasi-sausage mode (top) and quasi-kink (bottom) in an incompressible slab is

$$\Delta_{\min} = \frac{1}{k} \begin{pmatrix} \tanh^{-1} \\ \coth^{-1} \end{pmatrix} \left(- \frac{(k^2 {v_{\rm A}}^2 - \omega^2) \frac{\rho_0}{\rho_1} - \omega^2 \tanh kx_0}{(k^2 {v_{\rm A}}^2 - \omega^2) \frac{\rho_0}{\rho_1} \tanh kx_0 - \omega^2} \right), \tag{5.41}$$

which can be solved for $v_{\rm A}$ to give

$$v_{\rm A}^2 = \frac{\omega^2}{k^2} \left[1 + \frac{\rho_1}{\rho_0} \begin{pmatrix} \tanh \\ \coth \end{pmatrix} (k(x_0 + \Delta_{\min})) \right]. \tag{5.42}$$

5.3.5 Low-beta approximation

In a low-beta plasma, the minimum perturbation shift for a quasi-sausage mode (top) and quasi-kink (bottom) is given by

$$\Delta_{\min} = \frac{1}{k} \begin{pmatrix} \tanh^{-1} \\ \coth^{-1} \end{pmatrix} \left(- \frac{(k^2 {v_{\rm A}}^2 - \omega^2) m_1 \frac{\rho_0}{\rho_1} - \omega^2 k \tanh kx_0}{(k^2 {v_{\rm A}}^2 - \omega^2) m_1 \frac{\rho_0}{\rho_1} \tanh kx_0 - \omega^2 k} \right), \tag{5.43}$$

which can be solved for $v_{\rm A}$ to give

$$v_{\rm A}^2 = \frac{\omega^2}{k^2} \left[1 + \frac{k\rho_1}{m_1 \rho_0} \begin{pmatrix} \tanh \\ \coth \end{pmatrix} (k(x_0 + \Delta_{\min})) \right]. \tag{5.44}$$

Mode	Approximation of $k^2 v_{\rm A}^2/\omega^2$ using the amplitude ratio, $R_{\rm A}$		
	Thin slab	Incompressible	Low-beta
Quasi-sausage surface	$1+\frac{1}{x_0}\left(\frac{R_{\rm A}\frac{\rho_2}{\rho_0 m_2}+\frac{\rho_1}{\rho_0 m_1}}{R_{\rm A}+1}\right)$	$1+\left(\frac{R_{\rm A}\frac{\rho_2}{\rho_0}+\frac{\rho_1}{\rho_0}}{R_{\rm A}+1}\right)\coth kx_0$	$1+k\left(\frac{R_{\rm A}\frac{\rho_2}{\rho_0 m_2}+\frac{\rho_1}{\rho_0 m_1}}{R_{\rm A}+1}\right)\coth kx_0$
Quasi-kink surface	$1+k^2 x_0\left(\frac{R_{\rm A}\frac{\rho_2}{\rho_0 m_2}-\frac{\rho_1}{\rho_0 m_1}}{R_{\rm A}-1}\right)$	$1+\left(\frac{R_{\rm A}\frac{\rho_2}{\rho_0}-\frac{\rho_1}{\rho_0}}{R_{\rm A}-1}\right)\tanh kx_0$	$1+k\left(\frac{R_{\rm A}\frac{\rho_2}{\rho_0 m_2}-\frac{\rho_1}{\rho_0 m_1}}{R_{\rm A}-1}\right)\tanh kx_0$

Table 5.2: Magneto-seismology inversion using the amplitude ratio, $R_{\rm A}$, to approximate the Alfvén speed, $v_{\rm A}$.

Mode	Approximation of $k^2 v_{\rm A}^2/\omega^2$ using the minimum perturbation shift, $\Delta_{\rm min}$		
	Thin slab	Incompressible	Low-beta
Quasi-sausage surface	$\frac{\rho_1}{\rho_0 m_1}(x_0+\Delta_{\rm min})+\frac{1}{1+(\omega/kc_0)^2}+k^2 x_0\Delta_{\rm min}$	$1+\frac{\rho_1}{\rho_0}\tanh k(x_0+\Delta_{\rm min})$	$1+\frac{k\rho_1}{m_1\rho_0}\tanh k(x_0+\Delta_{\rm min})$
Quasi-kink surface	$\frac{-b\pm\sqrt{b^2-4ac}}{2a}$, defined in Section 5.3.2	$1+\frac{\rho_1}{\rho_0}\coth k(x_0+\Delta_{\rm min})$	$1+\frac{k\rho_1}{m_1\rho_0}\coth k(x_0+\Delta_{\rm min})$

Table 5.3: Magneto-seismology inversion using the minimum perturbation shift, $\Delta_{\rm min}$, to approximate the Alfvén speed, $v_{\rm A}$.

5.4 Numerical inversion procedure

We have introduced the amplitude ratio and the minimum perturbation shift which quantify the spatial asymmetry in magnetic slab eigenmodes. These expressions can be applied to determine the Alfvén speed, for a given set of observed equilibrium parameters, providing us a novel method to diagnose information about the background plasma, thus advancing the field of spatial magneto-seismology.

A summary of the analytical expressions for estimating the Alfvén speed, v_{A}, within an asymmetric magnetic slab is given in Tables 5.2 and 5.3, utilising the amplitude ratio method and the minimum perturbation shift method, respectively. With these analytical inversions, theoretical simplicity comes at the cost of having to use an additional approximation.

A second option is to solve the inverse problem numerically. In practice, a numerical procedure could be made relatively simple and computationally inexpensive by making use of a standard root finding method once the observed parameters have been prescribed.

5.4.1 Estimating a single parameter

The diagnosis procedure for one background parameter - the Alfvén speed, for example - is as follows:

1. Observe an oscillating asymmetric MHD waveguide in the solar atmosphere.

2. Decompose into asymmetric MHD wave modes.

3. Measure wave parameters: angular frequency and wavelength.

4. Measure background parameters: waveguide width, density, and temperature (and hence sound speed).

5. Measure a diagnostic parameter: amplitude ratio or minimum perturbation shift.

6. Use a root-finding technique to solve the diagnostic equation (Equation (5.21), (5.22), (5.34), or (5.35), depending on the mode identified and the diagnostic parameter used) for the Alfvén speed.

In practice, Step 3 is often extremely difficult. In addition to the Alfvén speed, the density across the waveguide is very difficult to measure (Warren and Brooks, 2009). One way around this is to estimate multiple parameters simultaneously, as discussed in Section 5.4.2.

Figure 5.5 illustrates the dependency of the amplitude ratio and minimum perturbation shift on the (non-dimensionalised half) slab width, kx_0, and the density ratio, ρ_1/ρ_0, of one external plasma density to the slab density, holding the other external density fixed. Varying one density ratio in this way is equivalent to changing the degree of asymmetry of the waveguide. The amplitude ratio is positive (negative) for quasi-kink (quasi-sausage) modes, because the oscillations on each boundary are in phase (anti-phase). Figures 5.5a and 5.5b further show that, for a given background parameter regime, the boundary with the highest amplitude is different for quasi-kink and quasi-sausage modes. This is demonstrated by the absolute value of the amplitude ratio being greater than 1 for quasi-sausage modes when it is less than 1 for quasi-kink modes, and *vice versa*. This is in agreement with the properties of the eigenmodes of the analogous spring-mass system introduced by Allcock and Erdélyi (2017) and discussed in Section 2.3.3. Figures 5.5c and 5.5d demonstrate that the position of minimum perturbation for quasi-kink modes is shifted in the opposite direction to that of quasi-sausage modes.

5.4.2 Estimating multiple parameters

It is often the case that not all the non-magnetic parameters characterising a waveguide are well-observable. In particular, the density distribution across the waveguide is, like the Alfvén speed, often impossible to determine. Thankfully, a combination of the amplitude ratio method and minimum perturbation shift method can be employed to diagnose multiple unknown background parameters. Using a combination of observables to be able to estimate multiple background parameters has been explored by Arregui et al. (2007); Goossens et al. (2008).

The motivation for this combined technique is as follows. The dispersion relation, the amplitude ratio method, and minimum perturbation shift method give us a set of three functions where the zeros of each function correspond to solutions of the respective equation. Denoting the wave parameters and background parameters by p_{w} and p_{bg}, respectively, these functions (for a

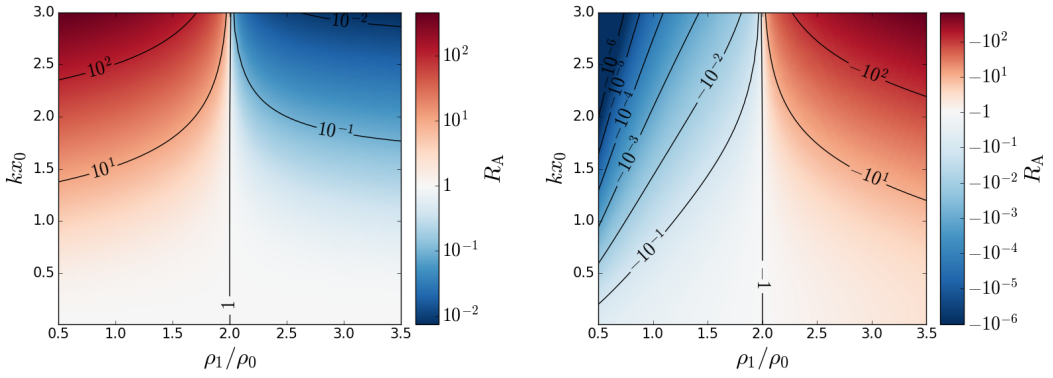

(a) Quasi-kink

(b) Quasi-sausage

(c) Quasi-kink

(d) Quasi-sausage

Figure 5.5: (a, b) The amplitude ratio, R_A, and (c, d) the minimum perturbation shift, $\Delta_{\min}$, as a function of the slab width, non-dimensionalised to kx_0, and the density ratio, ρ_1/ρ_0, for slow (a, c) quasi-kink and (b, d) quasi-sausage surface modes. The other density ratio is set to $\rho_2/\rho_0 = 2$, the characteristic speed ordering inside the slab is $v_A = 1.3c_0$, and the sound speed outside the slab is determined to ensure equilibrium pressure balance.

quasi-sausage mode) are

$$D(p_{\mathrm{w}}, p_{\mathrm{bg}}) = (\Lambda_0 c_0 + \Lambda_2 s_0)(\Lambda_0 s_0 + \Lambda_1 c_0) \tag{5.45}$$

$$+ (\Lambda_0 c_0 + \Lambda_1 s_0)(\Lambda_0 s_0 + \Lambda_2 c_0), \tag{5.46}$$

$$f_{\mathrm{AR}}(R_{\mathrm{A}}, p_{\mathrm{w}}, p_{\mathrm{bg}}) = R_A + \frac{\rho_1 m_2}{\rho_2 m_1}\left[\frac{(k^2 v_{\mathrm{A}}^2 - \omega^2) m_1 \frac{\rho_0}{\rho_1} - \omega^2 m_0 \coth m_0 x_0}{(k^2 v_{\mathrm{A}}^2 - \omega^2) m_2 \frac{\rho_0}{\rho_2} - \omega^2 m_0 \coth m_0 x_0}\right], \tag{5.47}$$

$$f_{\mathrm{MPS}}(\Delta_{\mathrm{min}}, p_{\mathrm{w}}, p_{\mathrm{bg}}) = \Delta_{\mathrm{min}} \tag{5.48}$$

$$- \frac{1}{m_0} \tanh^{-1}\left[-\frac{(k^2 {v_{\mathrm{A}}}^2 - \omega^2) m_1 \frac{\rho_0}{\rho_1} - \omega^2 m_0 \tanh m_0 x_0}{(k^2 {v_{\mathrm{A}}}^2 - \omega^2) m_1 \frac{\rho_0}{\rho_1} \tanh m_0 x_0 - \omega^2 m_0}\right]. \tag{5.49}$$

$$\tag{5.50}$$

The zeros of each of these functions correspond to solutions of Equations (5.6), (5.21), and (5.34). The single parameter estimation involves using a single-variable root-finding scheme (such as the secant method) to find the zeros of either f_{AR} or f_{MPS}, depending on whether the diagnostic parameter is the amplitude ratio or the minimum perturbation shift (see Section 5.4.1). Alternatively, notice that setting Equations (5.46)-(5.49) to zero forms a system of three coupled equations. Therefore, given measurements of one or two diagnostic parameters, R_{A} or Δ_{min}, all but up to three background parameters, p_{bg}, we can use a multivariate root-finding algorithm to solve up to three of these equations. Effectively, the extra diagnostic parameter and the dispersion relation each reduce the number of degrees of freedom. Thus, we can estimate up to three parameters.

As an example, the procedure to estimate the Alfvén speed and both the density ratios is as follows:

1. Observe an oscillating asymmetric MHD waveguide in the solar atmosphere.
2. Decompose into asymmetric MHD wave modes.
3. Measure wave parameters: angular frequency and wavelength.
4. Measure background parameters: waveguide width and temperature (and hence sound speed).
5. Measure diagnostic parameters: amplitude ratio and minimum perturbation shift.

6. Use a multi-variate root-finding algorithm to find the values of the Alfvén speed and the two density ratios for which the functions (5.46)-(5.49) are zero.

As an example, Figure 5.6 shows the inversion curves for a particular parameter regime typical of a slow surface mode. It is plotted by prescribing (as if they were observed quantities) all plasma parameters except the Alfvén speed, v_{A}, and one of the density ratios, ρ_1/ρ_0, then simultaneously solving the dispersion relation, Equation (5.6), with the equations for the amplitude ratio, Equation (5.21) or (5.22), or the minimum perturbation shift, Equation (5.34) or (5.35). The solution curves were calculated numerically using Powell's Method, which is an efficient algorithm for calculating the minimum of a multivariate function when the partial derivatives are not available analytically (Powell, 1964).

The ability to diagnose multiple parameters simultaneously could, in some cases, get around the hurdle of uncertain density measurements. However, the cost of this is that by estimating several parameters, we are more likely to encounter multiple roots (Section 5.4.4).

5.4.3 Error analysis

Every measurement comes with error, and when assessing the efficacy of a new measurement technique, an analysis of the errors must be undertaken. There are two kinds of error in a diagnosis made using the AR and MPS methods: *propagated errors* that are due to errors in them measurement of the input parameters, and *systematic errors* that are due to the asymmetric waveguide model approximating the real structure less than perfectly.

To analyse the propagated error, we determine which input parameters are most uncertain and hence are likely to contribute the most uncertainty to the diagnosed parameters. When density is used as an input parameter, it is often the case that the error in its measurement dominates the errors in all other input parameters. Errors in spatial parameters, such as the waveguide width, and temporal parameters, such as the angular frequency, are generally much smaller. The propagation of the error in the density is reduced by a factor of two by the square root that is introduced when inverting v_A from $k^2 v_A^2/\omega^2$ (in a similar way to Nakariakov and Ofman, 2001). That is, a relative error of 10% in the density leads to a relative error of approximately 5% in the Alfvén speed estimation. Furthermore, with high precision methods using density-sensitive

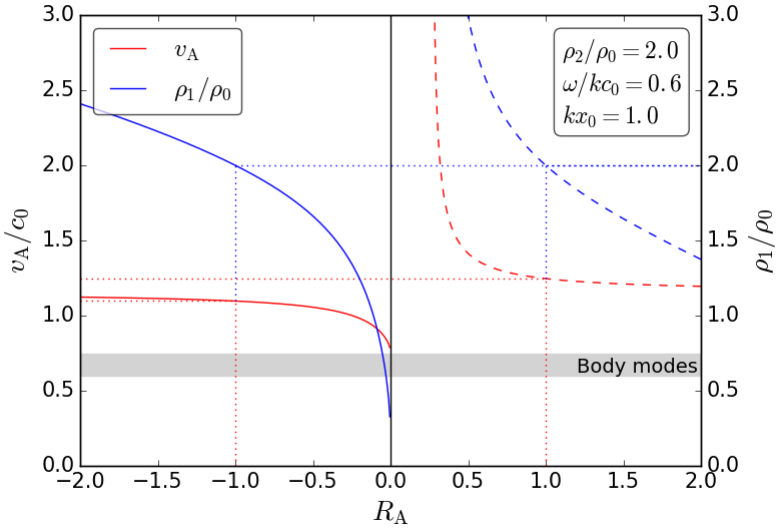

(a) Amplitude ratio inversion

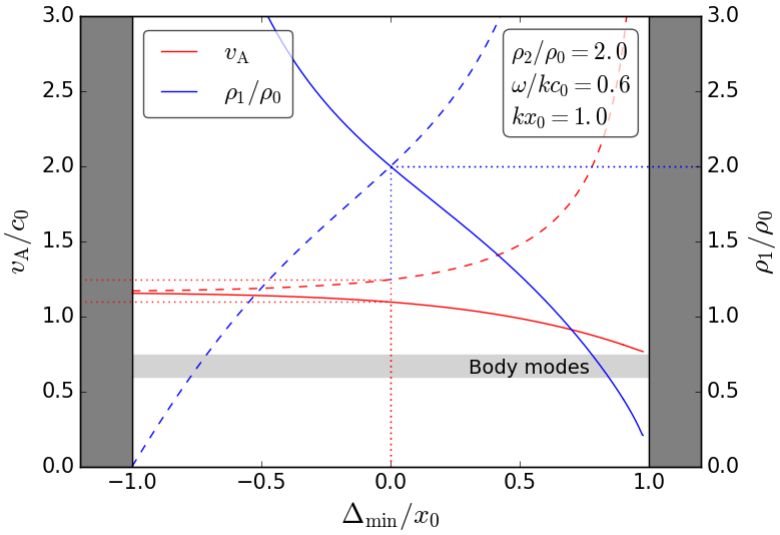

(b) Minimum perturbation shift inversion

Figure 5.6: Using prescribed values for (a) the amplitude ratio, R_A, or (b) the minimum perturbation shift, Δ_{min}, a numerical inversion is used to approximate the background equilibrium parameters, in this case the Alfvén speed, v_A, and one of the density ratios, ρ_1/ρ_0, for slow magneto-acoustic modes. Dashed (solid) lines correspond to the inversion curves for slow quasi-kink (quasi-sausage) surface modes. The dotted lines indicate the inversion for symmetric kink and sausage modes. The light-shaded area indicates the values of the Alfvén speed which correspond to body modes, rather than surface modes, so are not important for SMS application. The dark shaded region in Figure (b) illustrates the region outside the slab, outside the bounds of the minimum perturbation shift.

emission lines (Young et al., 2009), the propagation of density measurement errors can be reduced.

As we have seen in Section 5.4.2, the density need not be an input parameter if both the amplitude ratio and the minimum perturbation shift are observable. In this case, I expect that the input parameter with the highest uncertainty would be the minimum perturbation shift. This is because . Nevertheless, in the same way as the error in density, the relative error in the measurement of the minimum perturbation shift reduces by a factor of two when propagated through to the relative uncertainty in the estimated parameters.

The systematic error is more difficult to analyse quantitatively. The main sources of systematic error include:

1. The waveguide is not well-modelled as an asymmetric slab,
2. The wave is significantly nonlinear,
3. The wrong solution is found to the parameter inversion.

Error sources 1 and 3 are discussed in Sections 5.5 and 5.4.4, respectively. Regarding error source 2, unfortunately, a thorough study into the effects of MHD wave nonlinearity on seismology inversions is yet to be conducted. For this reason, it is unclear to what extent neglecting nonlinearity contributes to the errors in the present seismological inversion.

5.4.4 Dealing with multiple solutions

A common pitfall when solving inverse problems is identifying the *wrong* solution[2]. Even the most simple functions can have a multivalued inverse. For example, the function $f(x) = x^2$ has inverse function $f^{-1}(x) = \sqrt{x}$, which is multivalued, for example, $f^{-1}(1) = 1$ or -1. If we were looking specifically for the solution 1 but found only the solution -1, we'd have found the *wrong* solution. The original function does not preserve the complete information of the input, so there is no way of getting the missing information when given only the output.

Solar magneto-seismology techniques can lead to problems of a multivalued inverse. In theory, there can be multiple values of the background parameters that will lead to a given observational signature of MHD waves. Therefore,

[2]The *wrong* solutions are not wrong in the sense that they don't mathematically solve the equations, rather they are wrong in the sense that they do not map to reality.

given only the observational signature, is not always possible to find an unambiguous solution to the inverse problem. Sometimes we cannot be sure that our estimation of the background parameters is the correct one, leading to significant systematic error. This problem is more likely to raise its head when attempting to estimate multiple background parameters, such as described in Section 5.4.2. This is due to there being more dimensions over which the original function can be non-injective. Non-injectivity of the original function is sufficient to guarantee that its inverse function is multivalued. It is even possible for there to be infinitely many solutions to the seismological inverse problems that are all equally likely.

One way around the problem of the multivalued inverse is to use prior information about the MHD waveguide to inform our choice of the correct solution. This is the domain of Bayesian statistics (Arregui and Asensio Ramos, 2011; Arregui, 2018). Bayesian statistics can provide a mathematically precise formulation of multivalued inverse problems in probabilistic terms. It can be used to determine which seismological solution is *more likely* to be correct. For example, let's say we are solving an inverse problem to estimate the magnetic field strength in a quiescent prominence. If we lived in a world where we knew nothing at all about the conditions in a prominence, we would have no way to preference one solution to the inverse problem over another. However, we do not live in that world. Based on several decades worth of of solar observations from tens of solar observatories, we have prior understanding of the range of parameter values we'd expect to observe. We would be more surprised to find a value of 0.01 Gauss or 1000 Gauss than we would be for a value of, say, 10 Gauss. Bayesian statistic formalises this probabilistic reasoning. The posterior distribution gives the *degree of belief* of the parameter of interest.

As well as helping to determine which parameter values are more likely to be correct, Bayesian statistics can be useful for model comparison (Arregui, 2018). This is a method of quantitatively assessing which of several models is favoured by the data. It provides a well defined degree of belief in each of the models. This is a promising way to reduce the systematic error in seismological inversions.

5.4.5 Sensitivity to input parameters

The amplitude ratio has a strong sensitivity to the changes in the external densities, and therefore the external asymmetry, whereas the minimum perturbation shift has a weaker dependency. Therefore, the amplitude ratio is

likely to be a more effective parameter for diagnosing background parameters. Furthermore, observations of the location of the minimum wave power within a solar magnetic slab will be fraught with noise, potentially causing the detection of a false minimum. Noise in amplitude ratio measurements is less likely to introduce large errors because the locations of the slab boundaries are a more obvious features and can be identified by the steep gradients in the wavelength of observed light, for example, and is stable to larger noise signals.

Both the amplitude ratio and minimum perturbation shift are more sensitive to small changes in the background equilibrium parameters, *i.e.* the asymmetry in the background plasma, than the eigenfrequencies are. On a theoretical level, this corroborates with the result that eigenfunctions of linear operators on a Hilbert space are often more sensitive to small perturbations of the operator than their corresponding eigenvalues (Kato, 1995). The amplitude ratio and minimum perturbation shift parameters depend on the eigenfunctions, $\widehat{v}_x(x)$, as well as the eigenvalues, ω^2. This means that spatial seismology techniques can be theoretically more effective than temporal techniques for many solar structure. Therefore, we are excited to see a push for increased spatial resolution with next-generational observational instrumentation such as the Daniel K. Inouye Solar Telescope (DKIST). Upon completion, this will equip us to be able to use the magneto-seismology techniques developed here to better understand the diagnostic properties of asymmetric slab-like solar atmospheric structures such as elongated magnetic bright points, prominences, and sunspot light walls.

5.5 Discussion of the application of these techniques

The amplitude ratio method and minimum perturbation shift method present interesting and novel approaches to solar magneto-seismology. Their application is appropriate only to solar atmospheric waveguides that approximate the slab waveguide model. The simplicity of the model used to derive these techniques means that we are restricted in their application. In this section, we outline several solar atmospheric structures that could lend themselves to analysis by the seismological methods introduced in this thesis, namely, chromospheric fibrils, magnetic bright points, quiescent prominences, and light walls.

Large magnetic bright points (MBPs), with characteristic length $L > 500$ km, along inter-granular lanes are often rather elongated (Crockett et al., 2010). The application of SMS techniques to MBPs is limited by the low spatial resolution of current observations. DKIST is going to have a spatial resolution of 19 km for structures on the solar surface (Tritschler et al., 2015), sufficient enough to resolve oscillations in MBPs. This unprecedented resolution will hopefully give the sufficient number of pixels (5-10) across an MBP to determine whether their oscillations have maximum power at the boundaries of or within the waveguide, that is, to differentiate between the transverse eigenfunctions of surface and body MHD modes, respectively. This is crucial for the accurate employment of these SMS techniques, and would build upon previous work on mode identification such as the surface modes that were identified in photospheric pores (Morton et al., 2015).

Quiescent prominences, which are large long-lived magnetic formations of cool dense plasma elevated into the hot and rarefied coronal atmosphere, can be approximated by magnetic slabs and have been regularly observed to guide MHD waves (Arregui et al., 2012). A basic slab model of prominences, as illustrated by *e.g.* Joarder and Roberts (1992*a*,*b*), is of a symmetric slab, however, a small asymmetry could easily be caused by adjacent inhomogeneities. Even a small asymmetry in density ($|1-\rho_1/\rho_2| < 0.1$) can cause a significant (factor of 2 or more) asymmetry in the eigenmode (Figure 5.5), except for in thin slabs. This makes prominences a good candidate for applying the SMS techniques developed here. One issue that one has to bear in mind for the employment of these techniques is that the approximation of simple asymmetric magnetic slab may be insufficient to capture some important aspects of prominence oscillations, in particular, prominences are likely to have a sheared magnetic field and may have significant flows, which are neglected in the asymmetric slab model (Van Ballegooijen and Martens, 1989; Zirker et al., 1994; Ballester, 2005; Oliver, 2009; Arregui et al., 2012).

Light bridge surges also present a possible application. Rooted in sunspot light bridges, these clusters of recurrent chromospheric surges observed as bright structures in *e.g.* IRIS 1330 Å line, as observed by Yang et al. (2016) are formed by either magnetic reconnection just above the light bridge (Toriumi et al., 2015; Robustini et al., 2016) or by leakage of p-modes from beneath the underlying photosphere (Yang et al., 2015; Zhang et al., 2017). They have been demonstrated to guide MHD waves driven by nearby disturbances (Yang

et al., 2016, 2017). While the asymmetric magnetic slab could be a valid approximation for the actual geometry of light walls, the strong magnetic field in the low solar atmosphere above a sunspot umbra (the plasma each side of the light bridge) may put into question the full validity of the non-magnetic external plasma in the current model. However, what matters is the relative strength of the magnetic force compared to the pressure gradient force, that is, the value of plasma-beta. The value of beta above magnetic pores and sunspots is uncertain, but has been shown to be rather high in some cases (Bourdin, 2017), and has therefore been used in models of the low atmosphere (Mumford et al., 2015). With improved observations, it may turn out that the plasma surrounding light walls has a low-beta, in which case, we suggest that a future generalisation of the methods described here which involves an asymmetric magnetic plasma outside the slab will be a more appropriate method for the first magneto-seismology diagnosis of sunspot light walls.

Of course, these methods have limits of applicability due to the fact that we have modelled the slab as infinitely long, yet there do not exist any infinitely long waveguides in the solar atmosphere. However, if the length, L, of the cross section of an observed solar waveguide is much greater than its width, x_0, say $L/x_0 = 5-10$, then this model of an infinitely long slab may be a valid approximation. Furthermore, if the wavelength of the observed wave, λ, is such that $L \gg \lambda \gg x_0$, then the thin slab approximation holds (Sections 5.2.2 and 5.3.2), therefore an analytical diagnosis of the Alfvén speed within the waveguide can be made using Table 5.2 or 5.3.

5.5.1 Alternative causes of asymmetry

As a word of warning before we demonstrate a first use of these new SMS techniques, the observed asymmetry of solar MHD waves may not always be a consequence of underlying asymmetry in the background plasma. There are three mechanisms other than asymmetry in the equilibrium plasma that can plausibly explain observed asymmetry of MHD waves:

1. Local oscillations,
2. Collective oscillations of a larger waveguide,
3. Multiple overlying oscillating waveguides.

In the following paragraphs, we explain the mechanism and discuss their plausibility as alternative hypotheses.

The first alternative possibility is that when we observe asymmetry in MHD waves, we are actually observing a symmetric MHD structure that is oscillating locally rather than as a whole. The eigenmodes described in Section 2 are oscillations of the waveguide as a whole. This type of oscillation is known as a *collective* or *global* oscillation. If the waveguide's characteristic length-scale (which is equal to the slab width for a magnetic slab) is much greater than the wave's characteristic length-scale, then a portion of the structure can oscillate without perturbing the rest of the structure. For example, each interface of a symmetric slab can oscillate independently with a wave whose wavelength is much shorter than the slab width[3]. Two parallel interfaces oscillating independently with different amplitudes could be erroneously interpreted as a collective asymmetric oscillation of the whole waveguide. It is unclear how likely this hypothesis is to be true over the hypothesis of asymmetric equilibrium parameters.

Secondly, the structure that appears to be oscillating asymmetrically could be oscillation as part of a larger structure. For example, a symmetric magnetic slab or axisymmetric flux tube could oscillate collectively with several adjacent structures to form a larger scale asymmetric waveguide (as studied by Shukhobodskaia and Erdélyi (2018) for a slab as part of a larger system of several parallel interfaces and by Van Doorsselaere, Ruderman and Robertson (2008) for a flux tube oscillating with an adjacent flux tube). It is conceivable that if part of the larger waveguide is obfuscated from view, that the symmetric visible part (say, a structure approximating a symmetric slab or axisymmetric flux tube) is oscillating asymmetrically. This seems highly unlikely to explain many asymmetric waves observation due to the improbability of the equilibrium set-up.

A third alternative possibility to explain the observed asymmetry is that we are observing several overlying structures. When observing in a optically thick spectral line, each pixel is made up of the integral of light emitted by plasma along the line-of-sight. For example, an observation of the chromosphere made with the commonly used Hα emission line is made up of a light emitted from the multiple overlying structures between the telescope and the photosphere. It is impossible to isolate how much each structure contributes to the emission[4]. For this reason, observed asymmetry of an MHD wave could be due to several

[3]This was shown analytically in Section 2.3.1.5.

[4]With multiple telescopes observing the same point in three-dimensional space but from different angles, we can get much closer to isolating the light emission from a single structure. This is the project of the Stereo mission (NASA, 2018).

overlying structures moving in a way that appears like a single asymmetric oscillation. That is, it could be an observational artefact due to the optically thick plasma rather than due to asymmetry in the equilibrium structure. This strikes us as an implausible mechanism. This is because the combination of emission from overlying structures would be far more likely to combine into an incoherent oscillation in the optically thick line. For example, in the chromospheric Hα data analysed in Section 5.6.1, most of the observational domain is a sea of incoherently oscillating fibrils. We identify this as being due to overlying structures obscuring coherently oscillating waveguide. We also see many structures oscillating coherently for several periods, all of which demonstrate some degree of asymmetry. Were this asymmetry due to overlying structures, we would expect them to not oscillate coherently for as long, and to be much smaller in number. Therefore, we reject this possibility.

5.6 Diagnosing the Alfvén speed of chromospheric fibrils

The Alfvén speed in the chromospheric quiet Sun is highly inhomogeneous, due to the many magnetic structures that make up the magnetic canopy, and undergoes a steep gradient from 15 km s^{-1} in photospheric flux tubes to 1000 km s^{-1} in the corona (Van Ballegooijen et al., 2011). The Alfvén speed in specific chromospheric structures is very hard to determine using current techniques. At best, we can use extrapolations from the photospheric magnetic field, but since the chromosperic magnetic field is non-potential (Woodard and Chae, 1999; Wiegelmann et al., 2014), the errors are significant. In this section, we apply the amplitude ratio method to make an estimate of the Alfvén speed in several chromospheric fibrils.

5.6.1 Data

The data were taken from observations close to the disk centre with a narrow-band 0.25 Å Hα core (6562.8 Å) filter on the 29th September 2010 using the Rapid Oscillations in the Solar Atmosphere (ROSA) imager on the Dunn Solar Telescope (Jess et al., 2010). The data show a dynamic sea of dark dense fibrils that map, at least partially, the inter-network magnetic field overlying the bright and less dense plasma that permeates the quiet Sun (Leenaarts et al., 2012). The implementation of the amplitude ratio method involves resolving sub-fibril structure, for which the ROSA instrument's high spatial (150 km)

and temporal resolution (7.68 s) were just barely sufficient, with 10-20 pixels (width ∼50 km) across each fibril.

More information about the observations is detailed by Morton et al. (2012), who originally used the same data for the analysis of ubiquitous MHD waves in the chromosphere. They interpreted the observed fibril oscillations as concurrent sausage and kink modes of circular cross-sectional magnetic flux-tubes. In the present analysis, we propose an alternative interpretation that the oscillations are MHD oscillations in asymmetric waveguides. The strong phase relationship between and the similar phase speeds measured for the oscillations in each of the transverse axial displacement, the cross-sectional width, and the integrated intensity across the fibrils (see Morton et al., 2012), is some evidence for the present interpretation. However, we wish to make it clear that this interpretation is taken mainly to demonstrate a new SMS technique which depends on the existence of waveguide asymmetry. The evidence for or against either interpretation (concurrent modes in symmetric waveguides or individual modes in asymmetric waveguides) is too weak to be conclusive.

5.6.2 Methodology

In the absence of MHD wave theory in more realistic asymmetric geometries, we model each fibril as an isolated magnetic slab whose boundaries are parallel discontinuities between the uniform internal plasma and the asymmetric external plasma (Figure 2.1). Only sufficiently isolated fibrils that maintain their structure for at least a full period were analysed. A primary slit is placed perpendicularly across each fibril and time-distance data produced from an average of the intensities across the primary slit and two parallel neighbouring slits, placed at a distance of 1 pixel either side (Figure 5.7a). This technique of averaging over several slits is used to increase the signal-to-noise ratio.

5.6.2.1 Boundary tracking

To find the fibril boundaries so that the boundary oscillation amplitudes can be determined, we fit a Gaussian function to each time frame of the time-distance data. The boundaries are taken to be the positions along the slit at which the fitted Gaussian reaches half-maximum. Due to the limited number of datapoints across each fibril, the high signal-to-noise ratio, and to improve the fitting stability, for time frames where the Gaussian fitting failed, the fitting domain was reduced to 10 pixels either side of the boundaries on the previous time step.

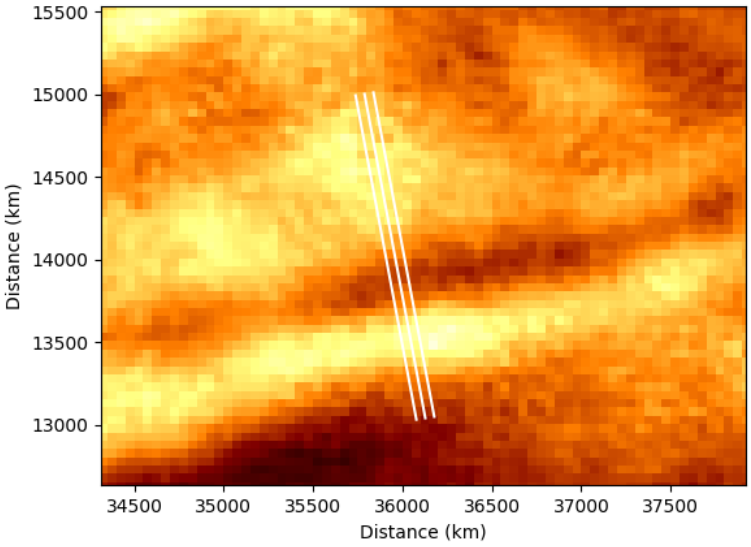

(a)

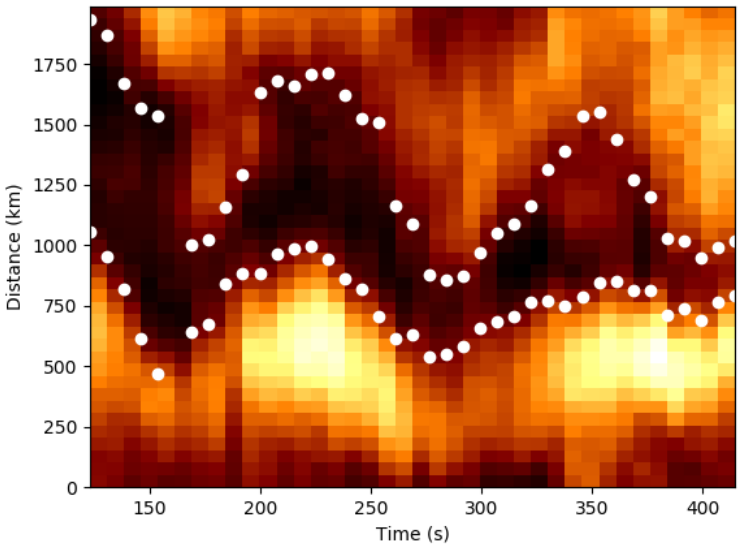

(b)

Figure 5.7: (a) A typical example of a ROSA Hα fibril taken at $t = 399.36$ s from the start of the observational window. The middle slit is placed perpendicular to the fibril. The mean of the intensities along the middle slit and two parallel slits at a pixel each side at each time step is plotted in Panel (b). The white dots correspond to the boundaries of the fibril, calculated as the position of half-maximum of the fitted Gaussian. Axis values are in units from the bottom left of the observational domain.

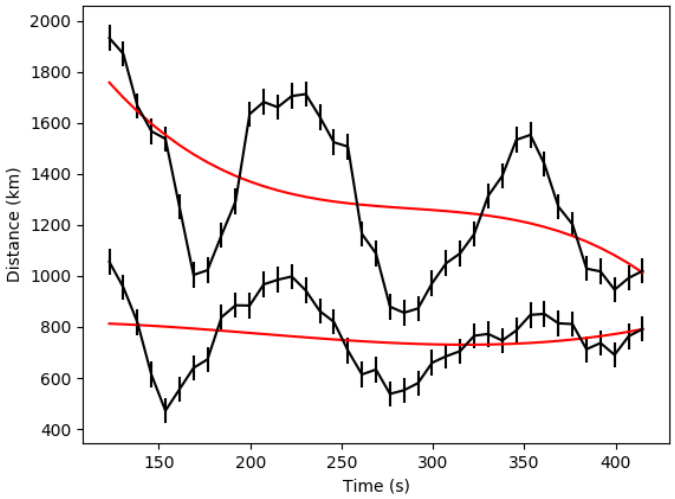

Figure 5.8: The boundary data (black), with cubic polynomial trend (red) overlaid. The error bars refer to the uncertainty in the boundary position due to spatial resolution limits.

Fibrils for which the stabilized Gaussian fitting failed on a significant proportion of time steps were omitted from the analysis. The boundaries were cross-checked and the small number of isolated anomalous points were smoothed over using a linear interpolation between the previous and next time frames. The width of each fibril is taken as the mean distance between the boundaries throughout the time window for which the stabilized Gaussian fitting was successful.

5.6.2.2 Frequency and amplitude measurement

For each fibril, both sets of boundary data were detrended with a cubic polynomial fit by least-squares regression. The detrended boundaries are then fit with a sinusoidal curve (Figure 5.9). The frequency of each wave is given by the average of the frequencies of both boundary sinusoids. The amplitude ratio is the signed ratio of the amplitudes of the boundary sinusoids.

5.6.2.3 Phase speed measurement

For each fibril, we plotted the cross-sectional width variation through time at five parallel slits, each five pixels apart and perpendicular the fibril. The widths at each time-step were calculated as the position of half-maximum of the fitted Gaussian function along each slit. The intensity along each of the five slits used for the phase speed measurement, as described in Section 5.6.2.1,

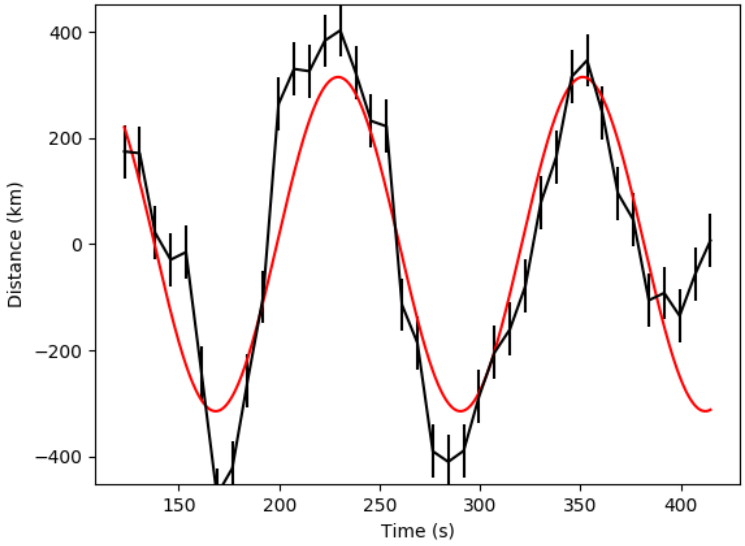

(a)

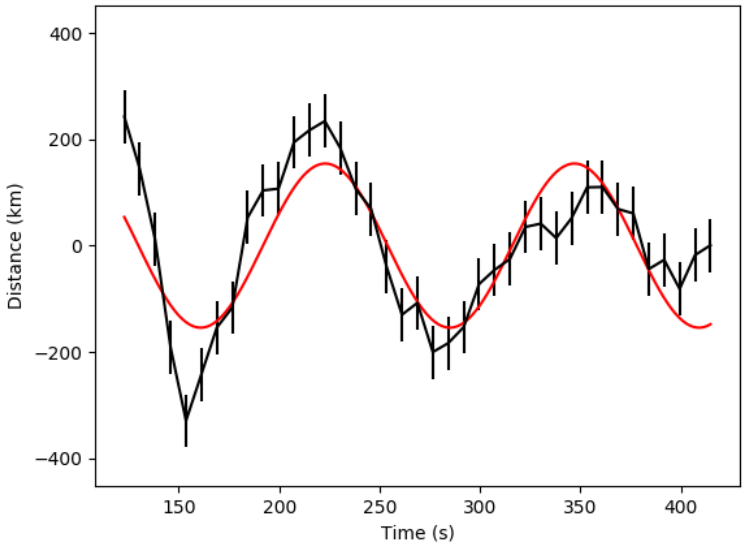

(b)

Figure 5.9: (a) Top and (b) bottom boundary positions along the averaged slits given in Figure 5.7a (black line), detrended with a cubic polynomial. The error bounds on each point are the pixel size and therefore correspond to the error in the observations rather than the error in the trend fitting so represent a lower bound on the total error. The boundaries are fitted with a sinusoid (red line).

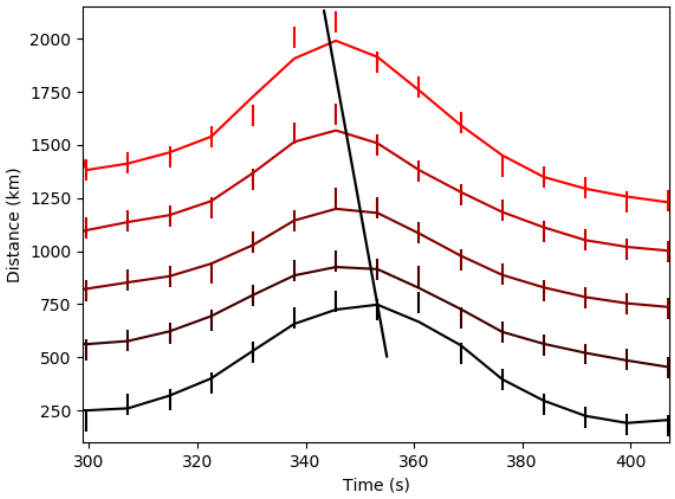

Figure 5.10: Five parallel slits, spaced by five pixels, are placed perpendicular to each fibril. The widths, calculated from the fitted Gaussian along each slit, are plotted and displaced in the y-direction by five pixels = 250 km, the distance between each slit. The peaks and trough of the width oscillations are fitted by a straight line, the gradient of which is approximately the phase speed.

is the mean of the intensities across three parallel slits spaced a pixel apart. The width variation was smoothed with a 3-point box-car function and the temporal lag in the smoothed width variation was fitted with a straight line (see Figure 5.10). The gradient of this line is the estimated phase speed.

The measured phase speeds assume that the fibril waveguides are parallel to the plane of sky. However, in reality, the waveguides are inclined at some angle θ to the plane of sky. Therefore, the true phase speed will be a factor of $\sec(\theta)$ greater than the measured phase speed. Unfortunately, using the given data it is impossible to infer the angle θ. The best we can do is use the fact that the fibrils tend to track the magnetic field of the chromospheric magnetic canopy, which is dominated by a horizontal magnetic field component, to motivate the assumption that θ is small. Under this assumption, we can take $\sec(\theta) \approx 1$, to leading order. From this it follows that the true phase speed is approximately equal to the measured phase speed in the observational plane.

Additionally, it might appear that we have assumed that the oscillations are polarized in the plane of sky because the amplitudes are measured in the observational place. However, the amplitudes only enter the inversion calculation as a ratio, eliminating any projection effects.

5.6.3 Inversion procedure

Using the technique from Section 5.4, we employed a numerical inversion procedure to estimate the Alfvén speed within the fibrils. First, for each fibril oscillation, the mode of oscillation (quasi-sausage or quasi-kink) was identified by assessment of the phase-shift between the oscillations on each boundary. After prescribing all the parameters apart from the internal Alfvén speed, v_{A1}, in Equation (5.21) or (5.21) (depending on the mode identified), the secant method was used to estimate the Alfvén speed inside each fibril.

For each inversion, we specified an internal sound speed of $c_0 = 10$ km s^{-1} and density ratios of $\rho_1/\rho_0 = 0.1$ and $\rho_2/\rho_0 = 0.2$, and vice versa depending on which side had the largest amplitude. In the absence of any density-sensitive proxies from the data, they were chosen to match the order of magnitude difference between the densities external and internal to the fibrils as expected from previous fibril observations (Leenaarts et al., 2012; Morton et al., 2012).

To reduce the chance of finding the wrong root when the inverse problem is multi-valued, a hundred initial values for v_{A} equally spaced between 1 and 200 km s^{-1} were tried and only fibrils which have a consistent inversion were included in the analysis. This range of initial values was chosen because it covers the expected range of Alfvén speed values.

5.6.4 Results

We made a successful inversion of five chromospheric fibrils and recorded the parameters in Table 5.4. Two of the fibrils were identified as oscillating in the quasi-kink mode and three in the quasi-sausage mode. Fibril 1 exhibited a change in direction of propagation before breaking up. The other fibril oscillations propagated in the same direction for the duration of the time for which Gaussian fitting was successful. The inverted Alfvén speeds agree with expected values for chromospheric fibrils (Morton et al., 2012). However, even the *expected* values for chromospheric Alfvén speed are highly uncertain.

We reiterate the advice from Leenaarts et al. (2015), that chromospheric seismology inversions should be taken with caution due to the partial mapping between the fibril intensity oscillations and the underlying magnetic field dynamics. The present results serve as a proof-of-concept of the novel solar magneto-seismology technique and we expect the errors to be significant.

Table 5.4: A table of measured parameters, identified mode, and estimated local Alfvén speed of five chromospheric fibrils.

Fibril	Width km	Frequency s^{-1}	Phase speed km s^{-1}	Amplitude ratio	Asymmetric eigenmode	Estimated Alfvén Speed km s^{-1}
1	463	0.0285	63 (and -63)	1.29	Quasi-kink	30.5
2	997	0.0328	63	-0.407	Quasi-sausage	91.7
3	1120	0.0800	63	-3.42	Quasi-sausage	75.5
4	530	0.0198	31	-3.13	Quasi-sausage	49.4
5	551	0.0511	129	2.04	Quasi-kink	63.1

5.7 Chapter conclusions

In this chapter, we started with an overview of the emerging field of SMS. Tracking the major developments highlights that while temporal seismology has received a large amount of attention, spatial seismology has lagged behind. This motivates the need for new SMS techniques that harness the observational power of spatial signatures of MHD waves.

We have derived two new techniques for spatial seismology: the amplitude ratio method and the minimum perturbation shift method. These techniques exploit observational proxies of the asymmetric background plasma, namely, the deviation of the ratio of boundary amplitudes from unity and the deviation of the position of minimum perturbation from the centre of the waveguide, to estimate unknown background parameters. Analytical inversion is possible when a further approximation to the plasma is made. We derived the analytical inversion under the thin slab, incompressible, and zero-beta approximations. To avoid the need to make these further approximations to the already over-simplified model, we can implement a numerical inversion scheme instead.

The analytical inversions are useful to demonstrate how the error associated with input parameter measurements propagates through to errors in the diagnosed parameters. We demonstrate the relative errors in the density ratio (the input parameters that will most often introduce the largest error) are halved when propagated through the inversion scheme for both of the techniques introduced in this chapter.

It is very often the case that multiple plasma parameters in the solar atmosphere are unknown. In addition to these techniques being used independently to estimate a single unknown parameter, we can combine these techniques to estimate up to three unknown parameters. The cost of this is the greater possibility of identifying incorrect solutions to the inversion problem. Whilst this source of error can be minimised by using a range of initial values in the numerical inversion scheme, other sources of systematic error are significant and difficult to quantify.

Finally, we carried out the first application of the amplitude ratio method on solar observational data. Analysing Hα data obtained from the Dunn Solar Telescope, we used the numerically inversion procedure to estimate the Alfv'en speed in five chromospheric fibrils. We found values in the range 30 - 92 km s^{-1}. The Alfvén speed in chromospheric fibrils and other waveguides in

the solar atmosphere is often impossible to measure using other magnetometry methods as each method, including the novel techniques introduced in this chapter, require very special conditions for valid implementation. Therefore, the development of these SMS techniques broadens the set of solar objects for which we can estimate previously unknown plasma parameters.

CHAPTER 6
Conclusions

The magnetic field of the solar atmosphere can support plasma structures in equilibrium. Stable perturbations of these structures may propagate as MHD waves. Many previous mathematical models of these waveguides utilised either reflectional symmetry or axisymmetry for mathematical simplicity, yet this assumption is not valid for a wide range of solar structures. Breaking the symmetry of solar waveguide models increases the mathematical difficulty but provides valuable insights into these asymmetric solar waveguides. Given that this thesis is the first exploration of asymmetry in solar waveguide models, we focussed on the most simple asymmetric MHD model: the asymmetric slab.

Firstly, studying the asymmetric slab as an eigenvalue problem (EVP), the dispersion relation has solutions which are the waveguide's eigenfrequencies, have mixed properties of the traditional (symmetric) sausage and kink modes (Allcock and Erdélyi, 2017). Distinguishing features of the traditional sausage and kink modes are that the sausage mode perturbs the waveguide's cross-sectional width and leaves the waveguide's axis unperturbed, whereas the kink mode leaves the cross-sectional width unperturbed and perturbs the axis. In contrast, all of the eigenmodes of the asymmetric slab perturb both the axis and the cross-sectional width. However, we can define two categories of asymmetric eigenmodes using the phase relationship of the waveguide boundaries. Asymmetric eigenmodes are described as quasi-sausage (quasi-kink) if the oscillations of the waveguide boundaries are in anti-phase (phase). This suggests that the phase relationship of the waveguide boundaries is a fundamental characteristic on which to describe MHD eigenmodes, rather than the presence of cross-sectional width or axial perturbation. The mixed nature of the asymmetric eigenmodes is expressed mathematically by the fact that the dispersion relation does not decouple into separate equations for sausage and kink eigenfrequencies. This makes the dispersion relation for the asymmetric

slab mathematically distinct from the dispersion relation for a symmetric slab (Roberts, 1981*b*; Edwin and Roberts, 1982).

We identify a concern that the mixed properties of asymmetric eigenmodes could lead to the incorrect identification of MHD modes in the solar atmosphere. In particular, since both the quasi-sausage and quasi-kink modes perturb the cross-sectional width and the waveguide axis, these modes would have similar observational features to nonlinear symmetric modes or a superposition of linear symmetric eigenmodes. Therefore, identification must include the phase relationship of the boundary oscillations rather than either the cross-sectional width or the axial perturbations.

A second way in which asymmetric modes could be misidentified is through the existence of quasi-symmetric eigenmodes (Zsámberger et al., 2018). We describe eigenmodes of an asymmetric waveguide as quasi-symmetric when they appear to be symmetric, in the sense that the amplitudes on each waveguide boundary are equal. In the simplest case where the only restoring forces are the magnetic force and the pressure gradient force, this occurs when the sum of the magnetic and pressure gradient restoring forces is equal on both sides of an asymmetric waveguide. We derived necessary and sufficient conditions for this phenomenon to occur. The key implication of this is that merely observing a symmetric wave in a solar waveguide is insufficient to deduce without ambiguity that the background parameters are symmetric.

The main difference in the dispersion diagram of the asymmetric eigenmodes in comparison to the symmetric eigenmodes is the presence of a cut-off frequency. Collective oscillations with frequency above the cut-off frequency in a sufficiently thin slab are not trapped by the waveguide. Instead, these oscillations leak energy laterally into the external plasma regions. Due to the asymmetry of the waveguide, the leakage occurs asymmetrically in the sense that energy is leaked at a different rate on each side. The asymmetry can be so stark that part of the wave is be completely trapped on one side of the waveguide whilst leaking out of the other.

Asymmetric wave leakage can be described more intuitively by *ray theory*. Ray theory is a mathematical description of waves as having only a speed and a direction for each point in time. By defining a phase-ray, the dispersion relation for the asymmetric slab is derived using a different approach to that of the eigenvalue problem. In this derivation, the ray is assumed to undergo total internal reflection when incident on the waveguide boundaries. Relaxing this requirement allows for some portion of the wave energy to be transmitted

into the external plasma, leading to attenuation of the collective wave. The simplicity of ray theory in dispersion relation derivation and its intuitive explanation for phenomena such as leaky modes shows that the potential for this approach is perhaps underutilised in MHD theory.

The temporal evolution of a series of initially perturbed MHD waveguides was investigated. Initially perturbed waveguides that are not subject to any damping mechanism are known to evolve through a series of three phases: the *initial phase*, the phase before collective modes are excited; the *impulsive phase*, where leaky modes can dominate; and the *stationary phase*, where trapped modes dominate for an indefinite time period (see, for example, Ruderman and Roberts (2006*b*)). In this thesis, we studied the initial value problem of an incompressible tangential interface. This relatively simple problem was first studied nearly 40 years ago by Rae and Roberts (1981). The key result from our solution to this problem is to correct a mistake that was made early in the original paper. We showed that the tangential interface which is initially perturbed with constant vorticity drives both surface and body modes, rather than just body modes as claimed by Rae and Roberts (1981). Since this problem was studied for an incompressible plasma, there is no wave leakage and any incompressible initial condition excites trapped modes instantaneously, so only the stationary phase exists in this case.

Next, we solved the initial value problem for an incompressible asymmetric slab. Again, only the stationary phase exists because only trapped eigenmodes are excited, of which the time-dependent solution is a linear summation.

Finally, we solved the initial value problem for a cold symmetric slab. The analysis resulted in an asymptotic solution that is valid for large values of time. The solution is made up of three groups of terms corresponding to the three phases of evolution, as expected. We showed that the impulsive phase is much shorter in duration than for a similar initial condition in a cold magnetic flux tube. Of course, the precise nature of the three phases is highly dependent on the initial conditions. Generalising this result to an asymmetric slab, we showed that for a sufficiently thin slab, the trapped principal kink mode becomes leaky. This means that for a sufficiently thin cold asymmetric slab, the impulsive phase is non-existent because all the excited collective modes are leaky. In this case, all the energy from the initial disturbance will eventually we transferred laterally into the background plasma, rather than continuing to propagate along the waveguide.

The major application of the theory of asymmetric MHD waveguides developed in this thesis is in solar magneto-seismology (Allcock and Erdélyi, 2018*b*). We developed two new techniques that use the eigenmode asymmetry as a proxy for the background magnetic field strength, which is difficult to measure using traditional methods. The amplitude ratio method uses the ratio of the boundary amplitudes as a proxy for asymmetry and the minimum perturbation shift method uses the shift of the position of minimum perturbation as a proxy for asymmetry. We applied the amplitude ratio method to a series of 5 chromospheric fibrils observed by the ROSA instrument on the Dunn Solar Telescope in 2012 (Allcock et al., 2019). The estimated Alfvén speeds range from 30 to 92 kms^{-1}. These values fit in the ball-park of previous estimates using different techniques.

CHAPTER 7

Future work

7.1 Compiling a solar catalogue of observations of asymmetric MHD waves

The bulk of this thesis is focussed on developing the theory of solar MHD waves. One promising direction would be to approach this concept from an observational point of view. A key first step in this direction is to catalogue the array of asymmetric wave observations. With a large enough sample, this could answer questions such as

- To what extent are solar MHD waves asymmetric?
- Do different types of solar structures exhibit different degrees of asymmetry?
- Is the asymmetry due to asymmetry of the waveguide, the initial perturbation or driver, or something else?

In this thesis, we discussed several mechanisms through which MHD waves in the solar atmosphere could appear asymmetric, for example, the wave could be guided by an asymmetric waveguide, it could be a symmetric waveguide that has been asymmetrically perturbed, or it could be a localised wave rather than a collective wave. A large enough observational study, coupled with an understanding of the observational signatures of each of these mechanisms, would shed light on which mechanism is the most dominant in different solar structures.

Asymmetry of solar MHD waves has not been addressed widely from an observational point of view due to the high spatial resolution needed to resolve the variation in wave power across a waveguide. The modern fleet of solar observational instrumentation (for example, the Swedish Solar Telescope and the Daniel K. Inouye Solar Telescope) is now able to accomplish this, although

the quality of image in the required scale is still poor. This will become less of a problem in the coming years as the next generation of Earth-based telescopes with improved spatial resolution are utilised.

7.2 Realistic asymmetric waveguides

The main drawback of the present work is the simplicity of the asymmetric waveguide model. Whilst this approach has allowed for increased mathematical tractability using a range of different mathematical techniques, it has to trade-off against the applicability of the waveguide model. Going forward, modelling more realistic asymmetric waveguides would lead to a better understanding of the asymmetric waves in the solar atmosphere and allow for the development of more accurate magneto-seismological techniques. Two more realistic asymmetric waveguides that would be valuable to study are:

- *An asymmetric slab with transitional regions.* Replacing the strict discontinuities imposed at the boundaries of an asymmetric slab with a continuous monotonic function would introduce phase-mixing and resonant absorption in the transitional regions. These otherwise well-studied dissipation mechanisms would presumably lead to differential heating across the waveguide. Differential waveguide heating is yet to be studied but could explain observations of localised heating due to MHD wave dissipation in solar structures.

- *A magnetic flux tube in a non-uniform background.* Many of the waveguides in the solar atmosphere have a closer resemblance to cylindrical models, rather than slab models. Cylindrical waveguides may still guide asymmetric waves, in the sense that the waves could have different amplitudes on two sides of the cylindrical cross-section. A cylindrical waveguide embedded in a non-uniform background plasma could provide an accurate model of this. However, the background parameter gradient would apply differential pressure around the flux tube boundary. Therefore, for the flux tube to remain in equilibrium, the boundary of the tube must be non-circular and, presumably, a parameter gradient would be induced inside the tube. Merely deriving a mathematical description of the equilibrium would be quite some task, as one can see.

APPENDIX A

Eigenmodes of an asymmetric spring-mass oscillator

In this appendix, we prove that the breathing mode has its highest amplitude on the mass connected to the external spring with lowest spring constant and the sloshing mode has highest amplitude on the mass connected to the external spring with highest spring constant.

Without loss of generality, let $\omega_2 > \omega_1$, so that the spring on the right has higher spring constant than the spring on the left. First, consider the case when $W < 1$. For the breathing mode, which has eigenfrequency ω_+,

$$\left|\frac{\hat{x}_1}{\hat{x}_2}\right| = \frac{1}{2W}\left(1+\sqrt{1+4W^2}\right) \tag{A.1}$$

$$> \frac{1}{2}\left(1+\sqrt{1}\right), \quad \text{since } 0 < W < 1, \tag{A.2}$$

$$= 1. \tag{A.3}$$

Therefore, the oscillation amplitude of the mass on the left is higher. For the sloshing mode, which has eigenfrequency ω_-,

$$\left|\frac{\hat{x}_1}{\hat{x}_2}\right| = \frac{1}{2W}\left|1-\sqrt{1+4W^2}\right| \tag{A.4}$$

$$= \frac{1}{2W}\left(\sqrt{1+4W^2}-1\right) \tag{A.5}$$

$$\leq \frac{1}{2W}\left(\sqrt{1}+\sqrt{4W^2}-1\right), \quad \text{by the triangle inequality,} \tag{A.6}$$

$$= 1. \tag{A.7}$$

Therefore, the oscillation amplitude of the mass on the right is higher.

Next, consider the case when $W > 1$. For the breathing mode,

$$\left|\frac{\hat{x}_1}{\hat{x}_2}\right| = \frac{1}{2W}\left(1 + \sqrt{1 + 4W^2}\right) \tag{A.8}$$

$$\geq \frac{1}{2W}\sqrt{2 + 4W^2}, \quad \text{by the triangle inequality,} \tag{A.9}$$

$$= \sqrt{\frac{1}{2W} + 1} \tag{A.10}$$

$$> 1, \quad \text{since } W > 0. \tag{A.11}$$

Therefore, the oscillation amplitude of the mass on the left is higher. For the sloshing mode,

$$\left|\frac{\hat{x}_1}{\hat{x}_2}\right| = \frac{1}{2W}\left(\sqrt{1 + 4W^2} - 1\right) \tag{A.12}$$

$$\leq \frac{1}{2W}\left(\sqrt{1 + 4W^2 - 1}\right), \quad \text{by the reverse triangle inequality,} \tag{A.13}$$

$$= 1. \tag{A.14}$$

Therefore, the oscillation amplitude of the mass on the right is higher.

Finally, it is trivial to show the same result holds in the case where $W = 1$. This completes the proof that the breathing mode has highest amplitude on the mass connected to the external spring with lowest spring constant and the sloshing mode has highest amplitude on the mass connected to the external spring with highest spring constant.

APPENDIX B

Proof of the error in Rae and Roberts (1981)

Rae and Roberts (1981) claim that the solution to the above system of equations is given by

$$\tilde{v}_x(x) = \begin{cases} A_- e^{kx} + \dfrac{1}{\epsilon_-}\displaystyle\int_{-\infty}^{0} G(x;s)f(x)ds, & \text{if } x \leq 0, \\ A_+ e^{-kx} - \dfrac{1}{\epsilon_+}\displaystyle\int_{0}^{\infty} G(x;s)f(x)ds, & \text{if } x > 0, \end{cases} \tag{B.1}$$

where

$$G(x;s) = \frac{1}{2k}[e^{ks}e^{-kx}H(x-s) + e^{-ks}e^{kx}H(s-x)] \tag{B.2}$$

and H is the Heaviside step function. By requiring continuity of transverse perturbation, Equation (4.18), the authors determine the constants A_- and A_+ to be

$$A_- = \left[+\int_{-\infty}^{0} f(s)e^{ks}ds - \frac{1}{2}\left(1 - \frac{\epsilon_-}{\epsilon_+}\right)\int_{0}^{\infty} f(s)e^{-ks}ds\right]/k(\epsilon_- + \epsilon_+), \tag{B.3}$$

$$A_+ = \left[-\int_{0}^{\infty} f(s)e^{-ks}ds + \frac{1}{2}\left(1 - \frac{\epsilon_+}{\epsilon_-}\right)\int_{-\infty}^{0} f(s)e^{ks}ds\right]/k(\epsilon_- + \epsilon_+). \tag{B.4}$$

The red operators in Equations (B.1) and (B.4) are incorrect.

Let's see whether Equation (B.1) satisfies Equation (4.17). First, we find that

$$\begin{aligned} \frac{d^2}{dx^2}G(x;s) = \frac{1}{2k}[&e^{ks}e^{-kx}(k^2H(x-s) - 2k\delta(x-s) + \delta'(x-s)) + \\ &e^{-ks}e^{kx}(k^2H(s-x) - 2k\delta(s-x) + \delta'(s-x))]. \end{aligned} \tag{B.5}$$

It is also useful to recall the following delta function identities:

$$\int_{-\epsilon}^{\epsilon}\delta(x)f(x)dx = f(0), \quad \text{and} \quad \int_{-\epsilon}^{\epsilon}\delta'(x)f(x)dx = -f(0), \tag{B.6}$$

for any $\epsilon > 0$ and function f. Using the equations above, we find that

$$\frac{d^2\tilde{v}_x}{dx^2} = k^2 A_- e^{kx} + \frac{1}{\epsilon_-}\int_{-\infty}^{0} \frac{d^2G}{dx^2}(x;s)f(s)ds \tag{B.7}$$

$$= k^2 A_- e^{kx} + \frac{1}{2k\epsilon_-}\left[k^2\left\{\int_{-\infty}^{x} e^{ks}e^{-kx}f(s)ds + \int_{x}^{0} e^{-ks}e^{kx}f(s)ds\right\}\right. \tag{B.8}$$

$$\left. -4kf(x) + [(e^{ks}e^{-kx} - e^{-ks}e^{kx})f(s)]'_{s=x}\right] \tag{B.9}$$

$$= k^2 A_- e^{kx} + \frac{1}{2k\epsilon_-}\left[k^2\int_{-\infty}^{0} G(x;s)f(s)ds - 2kf(x)\right] \tag{B.10}$$

$$= k^2\tilde{v}_x - \frac{1}{\epsilon_-}f(x). \tag{B.11}$$

Therefore, the solution given by Equation (B.1) does not satisfy Equation (4.17). It does, however, if the red plus were a minus, making the correct solution

$$\tilde{v}_x(x) = \begin{cases} A_- e^{kx} - \dfrac{1}{\epsilon_-}\displaystyle\int_{-\infty}^{0} G(x;s)f(x)ds, & \text{if } x \le 0, \\ A_+ e^{-kx} - \dfrac{1}{\epsilon_+}\displaystyle\int_{0}^{\infty} G(x;s)f(x)ds, & \text{if } x > 0, \end{cases} \tag{B.12}$$

where A_- and A_+ are given by

$$A_- = \left[-\int_{-\infty}^{0} f(s)e^{ks}ds - \frac{1}{2}\left(1 - \frac{\epsilon_-}{\epsilon_+}\right)\int_{0}^{\infty} f(s)e^{-ks}ds\right]/k(\epsilon_- + \epsilon_+), \tag{B.13}$$

$$A_+ = \left[-\int_{0}^{\infty} f(s)e^{-ks}ds - \frac{1}{2}\left(1 - \frac{\epsilon_+}{\epsilon_-}\right)\int_{-\infty}^{0} f(s)e^{ks}ds\right]/k(\epsilon_- + \epsilon_+). \tag{B.14}$$

APPENDIX C

Non-standard Laplace transform

Consider a function $f(t)$, whose standard Laplace transform, $F_1(\omega)$, and non-standard Laplace transform, $F_2(\omega)$, are

$$F_1(\omega) = \int_0^\infty f(t)e^{-\omega t}dt, \quad \text{and} \quad F_2(\omega) = \int_0^\infty f(t)e^{i\omega t}dt. \tag{C.1}$$

Trivially, $F_1(-i\omega) = F_2(\omega)$. Using the standard inverse Laplace transform, and letting σ be real and greater than the real part of all the singularities of $F_1(\omega)$, the original function $f(t)$ can be written

$$f(t) = \frac{1}{2\pi i} \lim_{T\to\infty} \int_{\sigma-iT}^{\sigma+iT} F_1(\omega)e^{\omega t}d\omega, \tag{C.2}$$

$$= \frac{1}{2\pi i} \lim_{T\to\infty} \int_{i\sigma-T}^{i\sigma+T} F_1(-i\omega)e^{-i\omega t}(-id\omega), \tag{C.3}$$

$$= \frac{1}{2\pi} \lim_{T\to\infty} \int_{i\sigma-T}^{i\sigma+T} F_2(\omega)e^{-i\omega t}d\omega. \tag{C.4}$$

Therefore, the inverse transform of the non-standard Laplace transform is

$$f(t) = \frac{1}{2\pi} \lim_{T\to\infty} \int_{i\sigma-T}^{i\sigma+T} F_2(\omega)e^{-i\omega t}d\omega. \tag{C.5}$$

APPENDIX D

Corroboration of incompressible solutions with previous results

D.1 Corroboration of the eigenfrequencies with an interface

When we let the width of an asymmetric slab vanish, we recover the traditional interface geometry. Letting $x_0 \to 0$, the parameters a, b, and c, from Equations (4.85), (4.86), and (4.87), reduce to

$$a = \rho_0(\rho_1 + \rho_2), \tag{D.1}$$

$$b = -\rho_0 v_{A0}^2(\rho_1 + \rho_2) - \rho_0(\rho_1 v_{A1}^2 + \rho_2 v_{A2}^2), \tag{D.2}$$

$$c = \rho_0 v_{A0}^2(\rho_1 v_{A1}^2 + \rho_2 v_{A2}^2). \tag{D.3}$$

Therefore, when the slab width vanishes, the eigenmodes given by Equation (4.84) reduce to

$$\left(\frac{\omega_0}{k}\right)^2 = \frac{-b \pm \sqrt{b^2 - 4ac}}{2a} = \begin{cases} v_{A0}^2, \\ \frac{\rho_1 v_{A1}^2 + \rho_2 v_{A2}^2}{\rho_1 + \rho_2}. \end{cases} \tag{D.4}$$

The first solution above is degenerate because, while the parameter v_{A0} makes sense in the limit as the slab width vanishes, it is meaningless in an interface system constructed without an inner region. The second solution corroborates with the surface eigenfrequencies of an interface, as expected (Roberts, 1981*a*).

D.2 Corroboration of the eigenfrequencies with a symmetric slab

By letting the parameters on each external plasma region be equal (*i.e.* $\rho_1 = \rho_2 = \rho_e$, and similar for the magnetic field and Alfvén speed) the asymmetric

slab is reduced to a symmetric slab. In this limit, the parameters a, b, and c, from Equations (4.85), (4.86), and (4.87), can be reduced to

$$a = \frac{2}{\tau_0 + c_0}\left[\rho_0^2 + \rho_e^2 + \rho_0\rho_e(\tau_0 + c_0)\right], \tag{D.5}$$

$$b = \frac{-2}{\tau_0 + c_0}\left[2(\rho_0^2 v_{A0}^2 + \rho_e^2 v_{Ae}^2) + \rho_0\rho_e(v_{A0}^2 + v_{Ae}^2)(\tau_0 + c_0)\right], \tag{D.6}$$

$$c = \frac{2}{\tau_0 + c_0}\left[\rho_0^2 v_{A0}^4 + \rho_e^2 v_{Ae}^4 + \rho_0\rho_e v_{A0}^2 v_{Ae}^2(\tau_0 + c_0)\right], \tag{D.7}$$

where $\tau_0 = \tanh kx_0$ and $c_0 = \coth kx_0$. The discriminant in the solution, Equation (4.84), reduces to

$$b^2 - 4ac = 4\rho_0^2\rho_e^2(v_{A0}^2 - v_{Ae}^2)^2\left(\frac{\tau_0 - c_0}{\tau_0 + c_0}\right)^2. \tag{D.8}$$

Therefore, the eigenfrequencies reduce to

$$\left(\frac{\omega_0}{k}\right)^2 = \frac{-b \pm \sqrt{b^2 - 4ac}}{2a} = \begin{cases} \frac{\rho_0 v_{A0}^2 + \rho_e v_{Ae}^2 c_0}{\rho_0 + \rho_e c_0}, \\ \frac{\rho_0 v_{A0}^2 + \rho_e v_{Ae}^2 \tau_0}{\rho_0 + \rho_e \tau_0}, \end{cases} \tag{D.9}$$

which corroborates with Equation (12) in Roberts (1981*b*).

D.3 Corroboration of the velocity solution with an interface

When $\rho_1 = \rho_2 = \rho_0$,

$$T_{1,2}[\Psi_0](\omega) = -2\Omega_0\rho_0 e^{kx_0}(\epsilon_0 \cosh kx_0 + \epsilon_{2,1} \sinh kx_0). \tag{D.10}$$

When $\rho_1 = \rho_2 = \rho_0$ and $x_0 = 0$, we expect that the solution will reduce to (the corrected version of) Equation (25) in Rae and Roberts (1981). Let's check that this is the case.

When the above conditions hold, the dispersion function reduces to $D(\omega) = \epsilon_0(\epsilon_1 + \epsilon_2)$ and its zeroes reduce to $\omega_{0+} = kv_{A0}$ and $\omega_{0-} = kv_{AS} = k\sqrt{(v_{A1}^2 + v_{A2}^2)/2}$. Therefore, the functionals reduce to

$$T_{1,2}[\Psi_0](\omega) = -2\Omega_0\rho_0\epsilon_0, \quad \chi_{1,2}[\Psi_0](\omega_{0+}) = 0, \quad \chi_{1,2}[\Psi_0](\omega_{0-}) = \frac{\Omega_0}{2k^2 v_{AS}}. \tag{D.11}$$

Therefore, the transverse velocity solution reduces to

$$v_x = -\frac{i\Omega_0}{k}\begin{cases} (1 - e^{kx})\cos kv_{A1}t + e^{kx}\cos kv_{AS}t & \text{for } x \leq 0, \\ (1 - e^{-kx})\cos kv_{A2}t + e^{-kx}\cos kv_{AS}t & \text{for } x > 0, \end{cases} \tag{D.12}$$

which corroborates with (the corrected version of) the result from Rae and Roberts (1981).

APPENDIX E
Validation of L'Hopital's rule

L'Hopital's Rule is a powerful tool for evaluating limits of quotients of functions, provided that these functions satisfy certain necessary criteria. L'Hopital's Rule (for function of complex variables) states that, for functions f and g which are analytic at a point z_0, if $f(x_0) = g(z_0) = 0$, $g'(z_0) \neq 0$ then

$$\lim_{z \to z_0} \frac{f(z)}{g(z)} = \frac{f'(z)}{g'(z)}. \tag{E.1}$$

Applied to the present problem, the requirements for L'Hopital's rule to hold are:

1. The functions $(\omega - \omega_{0+})T_1(\omega)e^{-i\omega t}$ and $kD(\omega)$ are analytic at ω_{0+},
2. $[(\omega - \omega_{0+})T_1(\omega)e^{-i\omega t}]|_{\omega=\omega_{0+}} = kD(\omega_{0+}) = 0$,
3. $kD'(\omega_{0+}) \neq 0$.

Below, we validate that each of these conditions holds:

1. Functions $T_1(\omega)$ and $D(\omega)$ are polynomials and hence are analytic. Since products of analytic functions are also analytic, $(\omega - \omega_{0+})T_1(\omega)e^{-i\omega t}$ and $kD(\omega)$ are analytic. In particular, they are analytic at ω_{0+}.
2. The point ω_{0+} is a zero of $D(\omega)$ (by definition of ω_{0+}) and $T_1(\omega)$ is regular at ω_{0+}, therefore $[(\omega - \omega_{0+})T_1(\omega)e^{-i\omega t}]|_{\omega=\omega_{0+}} = kD(\omega_{0+}) = 0$.
3. The function $D'(\omega)$ can be rewritten as

$$D'(\omega) = 2k^2\omega \left[2a\frac{\omega^2}{k^2} + b\right], \tag{E.2}$$

where a and b are given by Equations (4.85) and (4.86). The above equation has zeros at $\omega = 0$ and $\omega = \pm\omega_0$, where

$$\frac{\omega_0^2}{k^2} = -\frac{b}{2a}. \tag{E.3}$$

Therefore, the zeros of the function D are always at least a factor of i away from the zeros of D' (and are a factor of exactly i away if and only if $d = b^2 - 4ac = 0$). The result follows.

Bibliography

Abdelatif, T. E. (1990), 'Magneto-atmospheric waves', *Solar Phys.* **129**, 201–219.

Abramowitz, M. and Stegun, I. A. (1965), *Handbook of mathematical functions with formulas, graphs, and mathematical tables*, Cambridge University Press.

Ahlfors, L. V. (1979), *Complex analysis: an introduction to the theory of analytic functions of one complex variable*, McGraw-Hill.

Alfvén, H. (1942), 'Existence of Electromagnetic-Hydrodynamic Waves', *Nature* **150**, 405–406.

Alissandrakis, C. A. and Chiuderi Drago, F. (1995), 'Coronal Magnetic Fields from Faraday Rotation Observations', *Solar Phys.* **160**(1), 171–179.

Allcock, M. and Erdélyi, R. (2017), 'Magnetohydrodynamic Waves in an Asymmetric Magnetic Slab', *Solar Phys.* **292**, 35.

Allcock, M. and Erdélyi, R. (2018*a*), 'Magneto-hydrodynamic waveguides - magnetic slab', http://swat.group.shef.ac.uk/slab.html.

Allcock, M. and Erdélyi, R. (2018*b*), 'Solar Magnetoseismology with Magnetoacoustic Surface Waves in Asymmetric Magnetic Slab Waveguides', *Astrophys. J.* **855**(2), 90.

Allcock, M., Shukhobodskaia, D., Zsámberger, N. K. and Erdélyi, R. (2019), 'Magnetohydrodynamic waves in multi-layered asymmetric waveguides: solar magneto-seismology theory and application', *Frontiers in Astronomy and Space Sciences* **6**, 48.

Andries, J., Arregui, I. and Goossens, M. (2005), 'Determination of the Coronal Density Stratification from the Observation of Harmonic Coronal Loop Oscillations', *Astrophys. J. Lett.* **624**(1), L57–L60.

Andries, J. and Goossens, M. (2007), 'On the continuous spectrum of leaky magnetohydrodynamic modes and the associated quasimodes', *Physics of Plasmas* **14**(5), 052101.

Andries, J., Van Doorsselaere, T., Roberts, B., Verth, G., Verwichte, E. and Erdélyi, R. (2009), 'Coronal Seismology by Means of Kink Oscillation Overtones', *Space Sci. Rev.* **149**, 3–29.

Arregui, I. (2012), 'Inversion of Physical Parameters in Solar Atmospheric Seismology', *Astrophysics and Space Science Proceedings* **33**, 159.

Arregui, I. (2018), 'Bayesian coronal seismology', *Advances in Space Research* **61**(2), 655–672.

Arregui, I., Andries, J., Van Doorsselaere, T., Goossens, M. and Poedts, S. (2007), 'MHD seismology of coronal loops using the period and damping of quasi-mode kink oscillations', *Astron. Astrophys.* **463**, 333–338.

Arregui, I. and Asensio Ramos, A. (2011), 'Bayesian Magnetohydrodynamic Seismology of Coronal Loops', *Astrophys. J.* **740**(1), 44.

Arregui, I., Oliver, R. and Ballester, J. L. (2012), 'Prominence Oscillations', *Living Rev. Solar Phys.* **9**, 2.

Aschwanden, M. J., Fletcher, L., Schrijver, C. J. and Alexander, D. (1999), 'Coronal Loop Oscillations Observed with the Transition Region and Coronal Explorer', *Astrophys. J.* **520**(2), 880–894.

Aschwanden, M. J., Nightingale, R. W. and Alexand er, D. (2000), 'Evidence for Nonuniform Heating of Coronal Loops Inferred from Multithread Modeling of TRACE Data', *Astrophys. J.* **541**(2), 1059–1077.

Ashour, H. (2013), 'TE Modal Dispersion in Dielectric Slab Waveguide with Lossy Left-Handed Metamaterial', *Journal of Modern Physics* **4**(9), 1165–1170.

Ballester, J. L. (2005), 'Theoretical Advances in Prominence Seismology', *Space Sci. Rev.* **121**, 105–113.

Banerjee, D., Erdélyi, R., Oliver, R. and O'Shea, E. (2007), 'Present and Future Observing Trends in Atmospheric Magnetoseismology', *Solar Phys.* **246**, 3–29.

Barbulescu, M. and Erdélyi, R. (2018), 'Magnetoacoustic Waves and the Kelvin-Helmholtz Instability in a Steady Asymmetric Slab. I: The Effects of Varying Density Ratios', *Solar Phys.* **293**(6), 86.

Berthold, W. K., Harris, A. K. and Hope, H. J. (1960), 'World-Wide Effects of Hydromagnetic Waves Due to Argus', *J. Geophys. Res.* **65**, 2233.

Born, M. and Wolf, E. (1999), *Principles of Optics*, Cambridge University Press.

Bourdin, P.-A. (2017), 'Plasma Beta Stratification in the Solar Atmosphere: A Possible Explanation for the Penumbra Formation', *Astrophys. J. Lett.* **850**, L29.

Boyce, W. E. and DiPrima, R. C. (2012), *Elementary Differential Equations and Boundary Value Problems*, 10 edn, Wiley.

Cabinet Office (2015), 'National Risk Register for Civil Emergencies'.

Cally, P. S. (2003), 'Coronal Leaky Tube Waves and Oscillations Observed with Trace', *Solar Phys.* **217**, 95–108.

Cally, P. S. (2006), 'Note on the Initial Value Problem for Coronal Loop Kink Waves', *Solar Phys.* **233**, 79–87.

Cirtain, J. W., Golub, L., Lundquist, L., Van Ballegooijen, A., Savcheva, A., Shimojo, M., DeLuca, E., Tsuneta, S., Sakao, T., Reeves, K., Weber, M., Kano, R., Narukage, N. and Shibasaki, K. (2007), 'Evidence for Alfvén Waves in Solar X-ray Jets', *Science* **318**(5856), 1580.

Crockett, P. J., Mathioudakis, M., Jess, D. B., Shelyag, S., Keenan, F. P. and Christian, D. J. (2010), 'The Area Distribution of Solar Magnetic Bright Points', *Astrophys. J. Lett.* **722**, L188–L193.

Davila, J. M. (1985), 'A leaky magnetohydrodynamic waveguide model for the acceleration of high-speed solar wind streams in coronal holes', *Astrophys. J.* **291**, 328–338.

De Moortel, I. and Browning, P. (2015), 'Recent advances in coronal heating', *Philosophical Transactions of the Royal Society of London Series A* **373**(2042), 20140269–20140269.

De Moortel, I. and Nakariakov, V. M. (2012), 'Magnetohydrodynamic waves and coronal seismology: an overview of recent results', *Philosophical Transactions of the Royal Society of London Series A* **370**, 3193–3216.

DeForest, C. E. and Gurman, J. B. (1998), 'Observation of Quasi-periodic Compressive Waves in Solar Polar Plumes', *Astrophys. J. Lett.* **501**(2), L217–L220.

Defouw, R. J. (1976), 'Wave propagation along a magnetic tube.', *Astrophys. J.* **209**, 266–269.

Doschek, G. A., Feldman, U., Vanhoosier, M. E. and Bartoe, J. D. F. (1976), 'The emission-line spectrum above the limb of the quiet sun: 1175 - 1940 Å.', *Astrophys. J. Suppl.* **31**, 417–443.

Edwin, P. M. and Roberts, B. (1982), 'Wave propagation in a magnetically structured atmosphere. III - The slab in a magnetic environment', *Solar Phys.* **76**, 239–259.

Edwin, P. M. and Roberts, B. (1983), 'Wave Propagation in a Magnetic Cylinder', *Solar Phys.* **88**(1-2), 179–191.

Erdélyi, R. (2006), Magnetic seismology of the lower solar atmosphere, *in* 'Proceedings of SOHO 18/GONG 2006/HELAS I, Beyond the spherical Sun', Vol. 624 of *ESA Special Publication*, p. 15.

Erdélyi, R., Hague, A. and Nelson, C. J. (2014), 'Effects of Stratification and Flows on P $_1$/ P $_2$ Ratios and Anti-node Shifts Within Closed Loop Structures', *Solar Phys.* **289**, 167–182.

Erdélyi, R. and Morton, R. J. (2009), 'Magnetohydrodynamic waves in a compressible magnetic flux tube with elliptical cross-section', *Astron. Astrophys.* **494**(1), 295–309.

Erdélyi, R. and Taroyan, Y. (2008), 'Hinode EUV spectroscopic observations of coronal oscillations', *Astron. Astrophys.* **489**, L49–L52.

Erdélyi, R. and Verth, G. (2007), 'The effect of density stratification on the amplitude profile of transversal coronal loop oscillations', *Astron. Astrophys.* **462**, 743–751.

Foullon, C., Verwichte, E., Nakariakov, V. M., Nykyri, K. and Farrugia, C. J. (2011), 'Magnetic Kelvin-Helmholtz Instability at the Sun', *Astrophys. J. Lett.* **729**(1), L8.

Goedbloed, J. P. H. and Poedts, S. (2004), *Principles of Magnetohydrodynamics*, Cambridge University Press.

Goossens, M., Andries, J. and Aschwanden, M. J. (2002), 'Coronal loop oscillations. An interpretation in terms of resonant absorption of quasi-mode kink oscillations', *Astron. Astrophys.* **394**, L39–L42.

Goossens, M., Andries, J., Soler, R., Van Doorsselaere, T., Arregui, I. and Terradas, J. (2012), 'Surface Alfvén Waves in Solar Flux Tubes', *Astrophys. J.* **753**(2), 111.

Goossens, M., Arregui, I., Ballester, J. L. and Wang, T. J. (2008), 'Analytic approximate seismology of transversely oscillating coronal loops', *Astron. Astrophys.* **484**, 851–857.

Goossens, M. L., Arregui, I. and Van Doorsselaere, T. (2019), 'Mixed properties of MHD waves in non-uniform plasmas', *Frontiers in Astronomy and Space Sciences* **6**, 20.

Goossens, M., Terradas, J., Andries, J., Arregui, I. and Ballester, J. L. (2009), 'On the nature of kink MHD waves in magnetic flux tubes', *Astron. Astrophys.* **503**(1), 213–223.

Gu, Y. N. and Qiu, N. X. (1980), 'Kink instabilities of a plasma column with elliptical cross-section', *Acta Physica Sinica* **29**, 1367–1377.

Hashimoto, M. (1988), 'Principles for Modal Waves in Guided Wave Optics', *Electronics and Communications in Japan* **71**(10), 1455–1465.

Hess, H. D. and Hinsch, H. (1973), 'Propagation of Alfvén waves in bismuth', *Applied Physics* **2**(1), 27–30.

Heyvaerts, J. and Priest, E. R. (1983), 'Coronal heating by phase-mixed shear Alfven waves', *Astron. Astrophys.* **117**, 220–234.

Hu, J. and Menyuk, C. R. (2009), 'Understanding leaky modes: slab waveguide revisited', *Adv. Opt. Photon.* **1**(1), 58–106.

Inoue, S. (2016), 'Magnetohydrodynamics modeling of coronal magnetic field and solar eruptions based on the photospheric magnetic field', *Progress in Earth and Planetary Science* **3**(1), 19.

Ionson, J. A. (1978), 'Resonant absorption of Alfvénic surface waves and the heating of solar coronal loops.', *Astrophys. J.* **226**, 650–673.

Jafarzadeh, S., Solanki, S. K., Stangalini, M., Steiner, O., Cameron, R. H. and Danilovic, S. (2017), 'High-frequency Oscillations in Small Magnetic Elements Observed with Sunrise/SuFI', *Astrophys. J. Suppl.* **229**(1), 10.

Jess, D. B., Mathioudakis, M., Christian, D. J., Keenan, F. P., Ryans, R. S. I. and Crockett, P. J. (2010), 'ROSA: A High-cadence, Synchronized Multi-camera Solar Imaging System', *Solar Phys.* **261**, 363–373.

Jess, D. B., Mathioudakis, M., Erdélyi, R., Crockett, P. J., Keenan, F. P. and Christian, D. J. (2009), 'Alfvén Waves in the Lower Solar Atmosphere', *Science* **323**(5921), 1582.

Joarder, P. S. and Roberts, B. (1992*a*), 'The modes of oscillation of a prominence. I - The slab with longitudinal magnetic field', *Astron. Astrophys.* **256**, 264–272.

Joarder, P. S. and Roberts, B. (1992*b*), 'The modes of oscillation of a prominence. II - The slab with transverse magnetic field', *Astron. Astrophys.* **261**, 625–632.

Kato, T. (1995), *Perturbation Theory for Linear Operators*, 2 edn, Springer, Verlag Berlin Heidelberg.

Lee, D. and Kim, K. (2002), 'Reflection and Transmission of MHD Waves in an Inhomogeneous Magnetosphere', *Journal of the Korean Physical Society* **40**(2), 353–357.

Leenaarts, J., Carlsson, M. and Rouppe van der Voort, L. (2012), 'The Formation of the Hα Line in the Solar Chromosphere', *Astrophys. J.* **749**, 136.

Leenaarts, J., Carlsson, M. and Rouppe van der Voort, L. (2015), 'On Fibrils and Field Lines: the Nature of Hα Fibrils in the Solar Chromosphere', *Astrophys. J.* **802**, 136.

Lehnert, B. (1954), 'Magneto-Hydrodynamic Waves in Liquid Sodium', *Physical Review* **94**(4), 815–824.

Leonovich, A. S., Mishin, V. V. and Cao, J. B. (2003), 'Penetration of magnetosonic waves into the magnetosphere: influence of a transition layer', *Annales Geophysicae* **21**(5), 1083–1093.

Li, B., Habbal, S. R. and Chen, Y. (2013), 'The Period Ratio for Standing Kink and Sausage Modes in Solar Structures with Siphon Flow. I. Magnetized Slabs', *Astrophys. J.* **767**, 169.

Lites, B. W., Elmore, D. F., Seagraves, P. and Skumanich, A. P. (1993), 'Stokes Profile Analysis and Vector Magnetic Fields. VI. Fine Scale Structure of a Sunspot', *Astrophys. J.* **418**, 928.

Long, D. M., Valori, G., Pérez-Suárez, D., Morton, R. J. and Vásquez, A. M. (2017), 'Measuring the magnetic field of a trans-equatorial loop system using coronal seismology', *Astron. Astrophys.* **603**, A101.

Love, A. E. H. (1911), *Some Problems of Geodynamics*, Cambridge University Press, Cambridge.

Luna, M., Terradas, J., Oliver, R. and Ballester, J. L. (2008), 'Transverse Oscillations of Two Coronal Loops', *Astrophys. J.* **676**(1), 717–727.

Lundquist, S. (1949), 'Experimental Investigations of Magneto-Hydrodynamic Waves', *Physical Review* **76**(12), 1805–1809.

Mancuso, S. and Garzelli, M. V. (2007), 'Assessing the tilt of the solar magnetic field axis through Faraday rotation observations', *Astron. Astrophys.* **466**(2), L5–L8.

Marcuse, D. (1974), *Theory of dielectric optical waveguides*, Academic Press.

Mather, J. F. and Erdélyi, R. (2016), 'Magneto-Acoustic Waves in a Gravitationally Stratified Magnetized Plasma: Eigen-Solutions and their Applications to the Solar Atmosphere', *Astrophys. J.* **822**, 116.

Mathioudakis, M., Jess, D. B. and Erdélyi, R. (2013), 'Alfvén Waves in the Solar Atmosphere. From Theory to Observations', *Space Sci. Rev.* **175**, 1–27.

McKenzie, J. F. (1970), 'Hydromagnetic wave interaction with the magnetopause and the bow shock', *Planetary and Space Sci.* **18**(1), 1–23.

Messiah, A. (1961), *Quantum Mechanics*, Vol. 1, North-Holland Publishing Co.

Morton, R. J. and Ruderman, M. S. (2011), 'Kink and fluting modes of stratified coronal magnetic loops with elliptical cross-sections', *Astron. Astrophys.* **527**, A53.

Morton, R. J., Tomczyk, S. and Pinto, R. (2015), 'Investigating Alfvénic wave propagation in coronal open-field regions', *Nature Communications* **6**, 7813.

Morton, R. J., Verth, G., Jess, D. B., Kuridze, D., Ruderman, M. S., Mathioudakis, M. and Erdélyi, R. (2012), 'Observations of ubiquitous compressive waves in the Sun's chromosphere', *Nature Communications* **3**, 1315.

Mumford, S. J., Fedun, V. and Erdélyi, R. (2015), 'Generation of Magnetohydrodynamic Waves in Low Solar Atmospheric Flux Tubes by Photospheric Motions', *Astrophys. J.* **799**, 6.

Nakariakov, V. M. and Ofman, L. (2001), 'Determination of the coronal magnetic field by coronal loop oscillations', *Astron. Astrophys.* **372**, L53–L56.

Nakariakov, V. M., Ofman, L., Deluca, E. E., Roberts, B. and Davila, J. M. (1999), 'TRACE observation of damped coronal loop oscillations: Implications for coronal heating', *Science* **285**, 862–864.

Nakariakov, V. M. and Verwichte, E. (2005), 'Coronal Waves and Oscillations', *Living Rev. Solar Phys.* **2**, 3.

Nakariakov, V. M., Verwichte, E., Berghmans, D. and Robbrecht, E. (2000), 'Slow magnetoacoustic waves in coronal loops', *Astron. Astrophys.* **362**, 1151–1157.

Naqvi, K. R. and Brown, W. B. (1972), 'The non-crossing rule in molecular quantum mechanics', *International Journal of Quantum Chemistry* **6**(2), 271–279.

NASA (2018), 'Stereo: 3-d view of the sun and heliosphere', https://stereo.gsfc.nasa.gov/.

Nisticò, G., Nakariakov, V. M. and Verwichte, E. (2013), 'Decaying and decayless transverse oscillations of a coronal loop', *Astron. Astrophys.* **552**, A57.

Novotny, L. (2010), 'Strong coupling, energy splitting, and level crossings: A classical perspective', *American Journal of Physics* **78**, 1199–1202.

Núñez, M. (2018), 'Nonlinear effects in the propagation, reflection and refraction of magnetosonic waves', *EPL (Europhysics Letters)* **121**(6), 65001.

Núñez, M. (2020), 'On the second order geometric optics approximation to fast magnetosonic waves', *Communications in Nonlinear Science and Numerical Simulations* **82**, 105032.

Nye, A. H. and Thomas, J. H. (1976), 'Solar magneto-atmospheric waves. I. An exact solution for a horizontal magnetic field.', *Astrophys. J.* **204**, 573–588.

Ofman, L., Nakariakov, V. M. and DeForest, C. E. (1999), 'Slow Magnetosonic Waves in Coronal Plumes', *Astrophys. J.* **514**(1), 441–447.

Ofman, L., Nakariakov, V. M. and Sehgal, N. (2000), 'Dissipation of Slow Magnetosonic Waves in Coronal Plumes', *Astrophys. J.* **533**(2), 1071–1083.

Oliver, R. (2009), 'Prominence Seismology Using Small Amplitude Oscillations', *Space Sci. Rev.* **149**, 175–197.

Oxley, W., Zsámberger, N. K. and Erdélyi, R. (2020*a*), 'Standing MHD Waves in a Magnetic Slab Embedded in an Asymmetric Magnetic Plasma Environment: Surface Waves', *Astrophys. J.* **898**(1), 19.

Oxley, W., Zsámberger, N. K. and Erdélyi, R. (2020*b*), 'Standing MHD Waves in a Magnetic Slab Embedded in an Asymmetric Plasma Environment: Slow Surface Waves', *Astrophys. J.* **890**(2), 109.

Parnell, C. E. and De Moortel, I. (2012), 'A contemporary view of coronal heating', *Philosophical Transactions of the Royal Society of London Series A* **370**(1970), 3217–3240.

Pascoe, D. J., Hood, A. W., De Moortel, I. and Wright, A. N. (2013), 'Damping of kink waves by mode coupling. II. Parametric study and seismology', *Astron. Astrophys.* **551**, A40.

Powell, M. J. D. (1964), 'An efficient method for finding the minimum of a function of several variables without calculating derivatives', *The Computer Journal* **7**(2), 155–162.

Priest, E. (2014), *Magnetohydrodynamics of the Sun*, Cambridge University Press.

Rae, I. C. and Roberts, B. (1981), 'Surface waves and the heating of the corona', *Geophysical and Astrophysical Fluid Dynamics* **18**, 197–226.

Ramo, S., Whinnery, J. R. and Van Duzer, T. (1984), *Fields and Waves in Communications Electronics*, 2 edn, John Wiley and Sons.

Raouafi, N. E., Riley, P., Gibson, S., Fineschi, S. and Solanki, S. K. (2016), 'Diagnostics of Coronal Magnetic Fields Through the Hanle Effect in UV and IR Lines', *Frontiers in Astronomy and Space Sciences* **3**, 20.

Rast, M. P. (2003), 'The Scales of Granulation, Mesogranulation, and Supergranulation', *Astrophys. J.* **597**(2), 1200–1210.

Robbrecht, E., Verwichte, E., Berghmans, D., Hochedez, J. F., Poedts, S. and Nakariakov, V. M. (2001), 'Slow magnetoacoustic waves in coronal loops: EIT and TRACE', *Astron. Astrophys.* **370**, 591–601.

Roberts, B. (1981*a*), 'Wave propagation in a magnetically structured atmosphere. I - Surface waves at a magnetic interface.', *Solar Phys.* **69**, 27–38.

Roberts, B. (1981*b*), 'Wave Propagation in a Magnetically Structured Atmosphere. II - Waves in a Magnetic Slab', *Solar Phys.* **69**, 39–56.

Roberts, B. (2019), *MHD Waves in the Solar Atmosphere*, Cambridge University Press.

Roberts, B., Edwin, P. M. and Benz, A. O. (1984), 'On coronal oscillations', *Astrophys. J.* **279**, 857–865.

Robustini, C., Leenaarts, J., de la Cruz Rodriguez, J. and Rouppe van der Voort, L. (2016), 'Fan-shaped jets above the light bridge of a sunspot driven by reconnection', *Astron. Astrophys.* **590**, A57.

Rosenberg, H. (1970), 'Evidence for MHD Pulsations in the Solar Corona', *Astron. Astrophys.* **9**, 159.

Roy, J. R. (1973), 'The Magnetic Properties of Solar Surges', *Solar Phys.* **28**, 95–114.

Ruderman, M. S. (1992), 'Soliton propagation on multiple-interface magnetic structures', *J. Geophys. Res.* **97**, 16.

Ruderman, M. S. (2003), 'The resonant damping of oscillations of coronal loops with elliptic cross-sections', *Astron. Astrophys.* **409**, 287–297.

Ruderman, M. S. and Roberts, B. (2002), 'The Damping of Coronal Loop Oscillations', *Astrophys. J.* **577**(1), 475–486.

Ruderman, M. S. and Roberts, B. (2006*a*), 'Comment on "Note on the Initial Value Problem for Coronal Loop Kink Waves" By P. S. Cally', *Solar Phys.* **237**, 119–121.

Ruderman, M. S. and Roberts, B. (2006*b*), 'Leaky and non-leaky kink oscillations of magnetic flux tubes', *Journal of Plasma Physics* **72**, 285–308.

Ryutov, D. A. and Ryutova, M. P. (1976), 'Sound oscillations in a plasma with "magnetic filaments"', *Soviet Journal of Experimental and Theoretical Physics* **43**, 491.

Schunker, H. and Cally, P. S. (2006), 'Magnetic field inclination and atmospheric oscillations above solar active regions', *Mon. Not. Roy. Astron. Soc.* **372**(2), 551–564.

Sedláček, Z. (1971), 'Electrostatic oscillations in cold inhomogeneous plasma I. Differential equation approach', *Journal of Plasma Physics* **5**(2), 239–263.

Selwa, M., Murawski, K., Solanki, S. K. and Wang, T. J. (2007), 'Energy leakage as an attenuation mechanism for vertical kink oscillations in solar coronal wave guides', *Astron. Astrophys.* **462**(3), 1127–1135.

Shadrivov, I. V., Sukhorukov, A. A. and Kivshar, Y. S. (2003), 'Guided modes in negative-refractive-index waveguides', *Phys. Rev. E* **67**(5), 057602.

Shimizu, T., Katsukawa, Y., Kubo, M., Lites, B. W., Ichimoto, K., Suematsu, Y., Tsuneta, S., Nagata, S., Shine, R. A. and Tarbell, T. D. (2009), 'Hinode Observation of the Magnetic Fields in a Sunspot Light Bridge Accompanied by Long-Lasting Chromospheric Plasma Ejections', *Astrophys. J. Lett.* **696**, L66–L69.

Shukhobodskaia, D. and Erdélyi, R. (2018), 'Propagation of Surface Magnetohydrodynamic Waves in Asymmetric Multilayered Plasma', *Astrophys. J.* **868**(2), 128.

Srivastava, A. K., Shetye, J., Murawski, K., Doyle, J. G., Stangalini, M., Scullion, E., Ray, T., Wójcik, D. P. and Dwivedi, B. N. (2017), 'High-frequency torsional Alfvén waves as an energy source for coronal heating', *Scientific Reports* **7**, 43147.

Stenflo, J. O. (2013), 'Solar magnetic fields as revealed by Stokes polarimetry', *Astron. Astrophys. Rev.* **21**, 66.

Syms, R. and Cozens, J. (1992), *Optical Guided Waves and Devices*, Cambridge University Press.

Tandberg-Hanssen, E. (1995), *The nature of solar prominences*, Vol. 199, Springer Netherlands.

Terradas, J., Andries, J. and Goossens, M. (2007), 'On the Excitation of Leaky Modes in Cylindrical Loops', *Solar Phys.* **246**, 231–242.

Terradas, J., Oliver, R. and Ballester, J. L. (2006), 'Damped Coronal Loop Oscillations: Time-dependent Results', *Astrophys. J.* **642**, 533–540.

Tomczyk, S., McIntosh, S. W., Keil, S. L., Judge, P. G., Schad, T., Seeley, D. H. and Edmondson, J. (2007), 'Alfvén Waves in the Solar Corona', *Science* **317**(5842), 1192.

Toriumi, S., Katsukawa, Y. and Cheung, M. C. M. (2015), 'Light Bridge in a Developing Active Region. I. Observation of Light Bridge and its Dynamic Activity Phenomena', *Astrophys. J.* **811**, 137.

Tritschler, A., Rimmele, T. R., Berukoff, S., Casini, R., Craig, S. C., Elmore, D. F., Hubbard, R. P., Kuhn, J. R., Lin, H., McMullin, J. P., Reardon, K. P., Schmidt, W., Warner, M. and Woger, F. (2015), DKIST: Observing the Sun at High Resolution, *in* G. T. Van Belle and H. C. Harris, eds, '18th Cambridge Workshop on Cool Stars, Stellar Systems, and the Sun', Vol. 18 of *Cambridge Workshop on Cool Stars, Stellar Systems, and the Sun*, pp. 933–944.

Uchida, Y. (1970), 'Diagnosis of Coronal Magnetic Structure by Flare-Associated Hydromagnetic Disturbances', *Pub. Astron. Soc. Japan* **22**, 341.

Van Ballegooijen, A. A., Asgari-Targhi, M., Cranmer, S. R. and DeLuca, E. E. (2011), 'Heating of the Solar Chromosphere and Corona by Alfvén Wave Turbulence', *Astrophys. J.* **736**, 3.

Van Ballegooijen, A. A. and Martens, P. C. H. (1989), 'Formation and eruption of solar prominences', *Astrophys. J.* **343**, 971–984.

Van Doorsselaere, T., Debosscher, A., Andries, J. and Poedts, S. (2004), 'The effect of curvature on quasi-modes in coronal loops', *Astron. Astrophys.* **424**, 1065–1074.

Van Doorsselaere, T., Nakariakov, V. M. and Verwichte, E. (2008), 'Detection of Waves in the Solar Corona: Kink or Alfvén?', *Astrophys. J. Lett.* **676**(1), L73.

Van Doorsselaere, T., Ruderman, M. S. and Robertson, D. (2008), 'Transverse oscillations of two parallel coronal loops', *Astron. Astrophys.* **485**(3), 849–857.

Van Doorsselaere, T., Verwichte, E. and Terradas, J. (2009), 'The Effect of Loop Curvature on Coronal Loop Kink Oscillations', *Space Sci. Rev.* **149**(1-4), 299–324.

Veiras, F. E., Perez, L. I. and Garea, M. T. (2010), 'Phase shift formulas in uniaxial media: an application to waveplates', *Appl. Opt.* **49**(15), 2769–2777.

Verth, G., Van Doorsselaere, T., Erdélyi, R. and Goossens, M. (2007), 'Spatial magneto-seismology: effect of density stratification on the first harmonic amplitude profile of transversal coronal loop oscillations', *Astron. Astrophys.* **475**, 341–348.

Verwichte, E., Foullon, C. and Nakariakov, V. M. (2006*a*), 'Fast magnetoacoustic waves in curved coronal loops', *Astron. Astrophys.* **446**(3), 1139–1149.

Verwichte, E., Foullon, C. and Nakariakov, V. M. (2006*b*), 'Fast magnetoacoustic waves in curved coronal loops. II. Tunneling modes', *Astron. Astrophys.* **449**(2), 769–779.

Verzariu, P. (1973), 'Reflection and refraction of hydromagnetk waves at the magnetopause', *Planetary and Space Sci.* **21**(12), 2213–2225.

Vickers, E., Ballai, I. and Erdélyi, R. (2018), 'Propagation of Leaky MHD Waves at Discontinuities with Tilted Magnetic Field', *Solar Phys.* **293**(10), 139.

Walker, A. (2004), 'Magnetohydrodynamic Waves in Geospace', Magnetohydrodynamic Waves in Geospace. Series: Series in Plasma Physics.

Walker, A. D. M. (1977), 'The phase velocity, ray velocity, and group velocity surfaces for a magneto-ionic medium', *Journal of Plasma Physics* **17**(3), 467–486.

Wang, Z. H. and Li, S. P. (2008), 'Quasi-optics of the surface guided modes in a left-handed material slab waveguide', *Journal of the Optical Society of America B Optical Physics* **25**(6), 903.

Warren, H. P. and Brooks, D. H. (2009), 'The Temperature and Density Structure of the Solar Corona. I. Observations of the Quiet Sun with the EUV Imaging Spectrometer on Hinode', *Astrophys. J.* **700**(1), 762–773.

Wiegelmann, T., Thalmann, J. K. and Solanki, S. K. (2014), 'The magnetic field in the solar atmosphere', *Astronomy and Astrophysics Review* **22**, 78.

Withbroe, G. L. and Noyes, R. W. (1977), 'Mass and energy flow in the solar chromosphere and corona.', *Annual Review of Astronomy and Astrophysics* **15**, 363–387.

Wolfe, A. and Kaufmann, R. L. (1975), 'MHD wave transmission and production near the magnetopause', *J. Geophys. Res.* **80**(13), 1764.

Woodard, M. F. and Chae, J. (1999), 'Evidence for non-potential magnetic fields in the quiet Sun', *Solar Phys.* **184**, 239–247.

Yang, S., Zhang, J. and Erdélyi, R. (2016), 'Enhancement of a Sunspot Light Wall with External Disturbances', *Astrophys. J. Lett.* **833**, L18.

Yang, S., Zhang, J., Erdélyi, R., Hou, Y., Li, X. and Yan, L. (2017), 'Sunspot Light Walls Suppressed by Nearby Brightenings', *Astrophys. J. Lett.* **843**, L15.

Yang, S., Zhang, J., Jiang, F. and Xiang, Y. (2015), 'Oscillating Light Wall Above a Sunspot Light Bridge', *Astrophys. J. Lett.* **804**, L27.

Young, P. R., Watanabe, T., Hara, H. and Mariska, J. T. (2009), 'High-precision density measurements in the solar corona. I. Analysis methods and results for Fe XII and Fe XIII', *Astron. Astrophys.* **495**, 587–606.

Yu, H., Chen, S.-X., Li, B. and Xia, L.-D. (2016), 'Period ratios for standing kink and sausage modes in magnetized structures with siphon flow on the Sun', *Research in Astronomy and Astrophysics* **16**, 92.

Yuan, D., Nakariakov, V. M., Huang, Z., Li, B., Su, J., Yan, Y. and Tan, B. (2014), 'Oscillations in a Sunspot with Light Bridges', *Astrophys. J.* **792**, 41.

Zajtsev, V. V. and Stepanov, A. V. (1975), 'On the origin of pulsations of type IV solar radio emission. Plasma cylinder oscillations (I).', *Issledovaniia Geomagnetizmu Aeronomii i Fizike Solntsa* **37**, 3–10.

Zhang, J., Tian, H., He, J. and Wang, L. (2017), 'Surge-like Oscillations above Sunspot Light Bridges Driven by Magnetoacoustic Shocks', *Astrophys. J.* **838**, 2.

Zirker, J. B. (1993), 'Coronal Heating', *Solar Phys.* **148**(1), 43–60.

Zirker, J. B., Engvold, O. and Yi, Z. (1994), 'Flows in quiescent prominences', *Solar Phys.* **150**, 81–86.

Zsámberger, N. K., Allcock, M. and Erdélyi, R. (2018), 'Magneto-acoustic Waves in a Magnetic Slab Embedded in an Asymmetric Magnetic Environment: The Effects of Asymmetry', *Astrophys. J.* **853**, 136.

Zsámberger, N. K. and Erdélyi, R. (2020), 'Magnetoacoustic Waves in a Magnetic Slab Embedded in an Asymmetric Magnetic Environment. II. Thin and Wide Slabs, Hot and Cold Plasmas', *Astrophys. J.* **894**(2), 123.